Quantum simulation with electron spins in quantum dots

van Diepen, C.J.

DOI
10.4233/uuid:f7adb947-1d56-4326-aa99-13b5baa353f6

Publication date
2021

Document Version
Final published version

Citation (APA)
van Diepen, C. J. (2021). *Quantum simulation with electron spins in quantum dots*. [Dissertation (TU Delft), Delft University of Technology]. https://doi.org/10.4233/uuid:f7adb947-1d56-4326-aa99-13b5baa353f6

Quantum simulation with electron spins in quantum dots

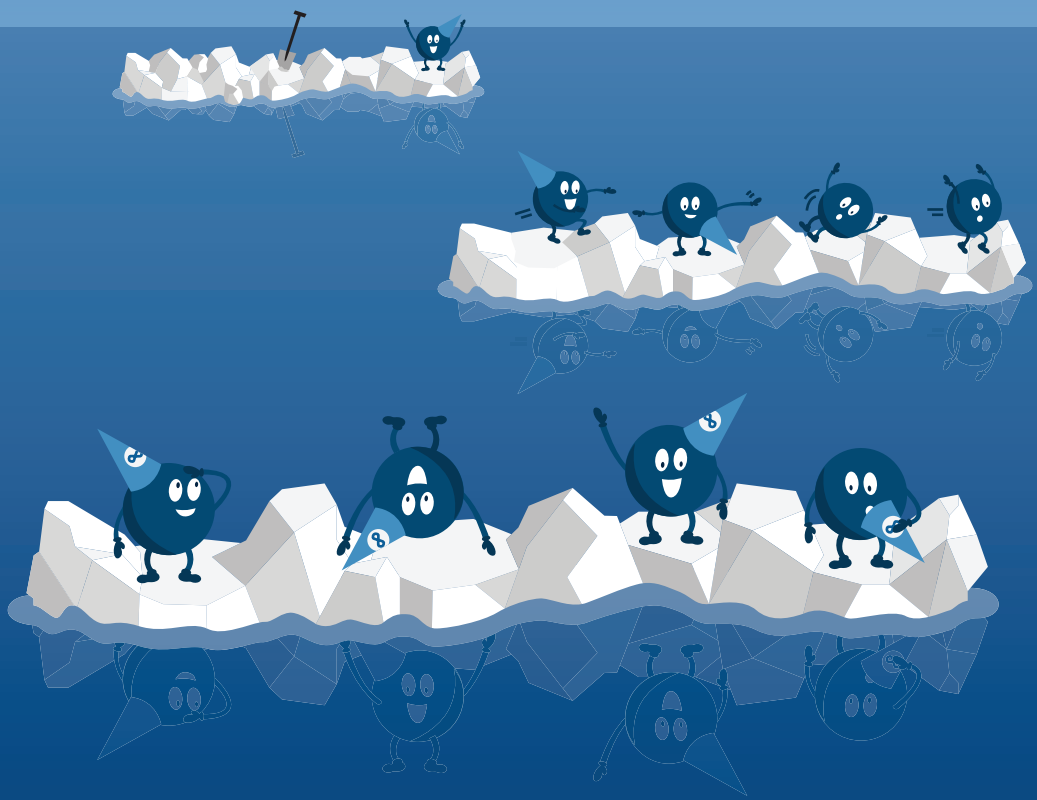

Sjaak van Diepen

QUANTUM SIMULATION WITH ELECTRON SPINS IN QUANTUM DOTS

QUANTUM SIMULATION WITH ELECTRON SPINS IN QUANTUM DOTS

Proefschrift

ter verkrijging van de graad van doctor
aan de Technische Universiteit Delft,
op gezag van de Rector Magnificus prof.dr.ir. T.H.J.J. van der Hagen,
voorzitter van het College voor Promoties,
in het openbaar te verdedigen op
donderdag 2 december 2021 om 12:30 uur

door

Cornelis Jacobus VAN DIEPEN

Master of Science in Physics & Climate Science,
Universiteit Utrecht, Nederland,
geboren te Alkmaar, Nederland.

Dit proefschrift is goedgekeurd door de promotor.

Samenstelling promotiecommissie:

Rector Magnificus,	voorzitter
Prof.dr.ir. L.M.K. Vandersypen,	Technische Universiteit Delft, promotor
Dr.ir. M. Veldhorst,	Technische Universiteit Delft, copromotor
Onafhankelijke leden:	
Prof.dr. A.F. Otte	Technische Universiteit Delft
Prof.dr. S. Bose	University College London
Dr. J.M. Nichol	University of Rochester
Dr.ir. S.J.J.M.F. Kokkelmans	Technische Universiteit Eindhoven
Prof.dr. G.A. Steele	Technische Universiteit Delft, reservelid

Keywords: quantum simulation, quantum dots, quantum computation, spin qubits

Printed by: Gildeprint, Enschede

Cover: Design by Marlien de Wit

Casimir PhD Series, Delft-Leiden 2021-32

ISBN 978-90-8593-498-1

An electronic version of this dissertation is available at
https://repository.tudelft.nl/.

CONTENTS

SUMMARY

More is more applies in particular to systems with interacting parts. These interactions enable the emergence of collective behaviour. Examples can be found among the behaviour of animals, such as the V-shaped formation of migrating geese and the flight of a flock of starlings. More examples are found among the electromagnetic properties of materials. For properties that rely on quantum-mechanical correlations it quickly becomes infeasible for classical numerical simulations to provide accurate results. An appealing alternative is to study these properties with quantum simulators, which mimic the material properties themselves. Besides being of scientific interest for the field of condensed matter physics, insights obtained from quantum simulations could in the future serve as input for the synthesis of novel materials.

Developing quantum simulators requires the engineering of quantum systems. One such quantum system is that of electrons in gate-defined quantum dots, which are formed by three-dimensional confinement at the nano-scale. Experiments with quantum dots have already demonstrated measurement and coherent control of both individual charges and spins, and their operation as quantum bits. The first quantum simulation experiments with quantum dots have been performed in the last couple of years. Further development of quantum dots as platform for quantum simulations forms the overarching motivation for this thesis.

The first experiment in this thesis describes the automated tuning of the tunnel coupling between quantum dots. This automation builds on previously developed automated tuning of double quantum dots. The automated tuning relies on image processing to extract parameters from measurement results. This step is part of a feedback loop in which the voltages on the gates are iteratively adjusted. This loop repeats until the target tunnel coupling is achieved.

The second experiment further studies the tuning of tunnel couplings. For operation of gate-defined quantum dots it is common practice to independently control chemical potentials with so-called virtual gates. These virtual gates compensate for crosstalk effects due to cross-capacitances of the physical gates. The control of multiple tunnel couplings similarly suffers from crosstalk, but efficient compensation techniques were lacking. This chapter reports an efficient calibration scheme for such crosstalk, and demonstrates independent control of tunnel couplings with enhanced virtual gates.

The third experiment demonstrates a method to measure charge and spin in large quantum dot arrays. The charge configuration of a quantum dot array is typically measured with a charge sensor, which is usually another quantum dot. To measure the spin configuration it is first mapped onto a charge configuration, which for singlet-triplet measurements is based on the Pauli exclusion principle. The charge measurement relies on Coulomb repulsion, which decays with distance, thus only charge and spin close to the sensor can be reliably measured. This chapter presents how, inspired by the effect of toppling dominoes, a cascade of hopping electrons induced by Coulomb repulsion

can effectively convert the information about motion of a distant charge to the motion of a charge close to the sensor. The benefit of cascade-based readout is demonstrated by comparing singlet-triplet measurements with or without the cascade activated.

The most involved experiment described in this thesis is a proof-of-principle quantum simulation of Heisenberg magnetism, which is one of the most famous models in condensed-matter physics. Specifically, this experiment demonstrates how a linear array of quantum dots can be operated as a Heisenberg spin chain. The first part of the experiment shows the characterization of the energy spectrum, which is based on degeneracies between spin states with different magnetization. From the energy spectroscopy the conditions are identified for which the exchange couplings are homogeneous. Next, the coherence is studied by inducing global exchange oscillations, and evolution in different subspaces of the Heisenberg Hamiltonian is demonstrated. The final step of the experiment consists of the adiabatic preparation of the low-energy global singlet state for a homogeneous chain, and its characterization with pairwise singlet-triplet measurements for each of the nearest-neighbours and correlations therein. These techniques and results form the basis for the operation of quantum dots to simulate larger spin systems and different lattice structures.

The final experiment, shifts the focus from spin-spin interactions to electron-electron interactions. For gate-defined quantum dots, the Coulomb repulsion results in both on-site and inter-site interactions between electrons. The interaction is experimentally characterized with a linear array of six dots in which the tunnel couplings are tuned to be homogeneous. The decay of the interaction as a function of distance is modelled with both the method of image charges, where the gate metal acts as screening layer, and with a Yukawa type potential as a heuristic model. The latter provides an intuitive interpretation for the decay of the interaction in terms of a screening length. The characterization of the long-range electron-electron interaction is relevant for the operation of quantum dot arrays as hosts of spin qubits, but also for quantum simulations in which the charge degree of freedom and electron-electron interactions play an important role. Some examples of many-body physics for which long-range interactions are essential, are quantum chemistry, Wigner crystallization, and high-temperature superconductivity.

Summarizing, this thesis reports novel techniques for the control and measurement of larger quantum dot arrays, the operation of such an array as quantum simulator of Heisenberg magnetism with control over the spin-spin interactions, and characterization of the electron-electron interactions. These results pave the way for future quantum simulations with quantum dots.

Sjaak van Diepen

SAMENVATTING

Meer is meer geldt in het bijzonder voor systemen met interagerende delen. Deze interacties maken het ontstaan van collectief gedrag mogelijk. Voorbeelden zijn te vinden onder het gedrag van dieren, zoals de V-vormige formatie van trekganzen en de vlucht van een zwerm spreeuwen. Meer voorbeelden zijn te vinden onder de elektromagnetische eigenschappen van materialen. Voor eigenschappen die afhankelijk zijn van kwantum-mechanische correlaties wordt het al snel onhaalbaar voor klassieke numerieke simulaties om nauwkeurige resultaten te leveren. Een aantrekkelijk alternatief is om deze eigenschappen te bestuderen met kwantum simulatoren, die de materiaal eigenschappen zelf nabootsen. Behalve dat ze van wetenschappelijk belang zijn voor de fysica van gecondenseerde materie, kunnen inzichten verkregen uit kwantum simulaties in de toekomst als input dienen voor de synthese van nieuwe materialen.

Het ontwikkelen van kwantum simulatoren vereist het bouwen van kwantum systemen. Een zo'n kwantum systeem is dat van elektronen in door elektrodes gedefinieerde "kwantumdots", die worden gevormd door drie-dimensionale opsluiting op de nanoschaal. Experimenten met kwantumdots hebben al de uitlezing en coherente aansturing van zowel individuele ladingen als spins aangetoond, en hun gebruik als kwantum bits. De eerste kwantum simulatie experimenten met kwantumdots zijn in de afgelopen jaren uitgevoerd. Verdere ontwikkeling van kwantumdots als platform voor kwantum simulaties vormt de overkoepelende motivatie voor dit proefschrift.

Het eerste experiment in dit proefschrift beschrijft de geautomatiseerde afstemming van de tunnelkoppeling tussen kwantumdots. Deze automatisering bouwt voort op eerder ontwikkelde geautomatiseerde afstemming van dubbele kwantumdots. De geautomatiseerde afstemming is afhankelijk van beeldverwerking om parameters uit meetresultaten te halen. Deze stap maakt deel uit van een terugkoppel lus waarin de spanningen op de elektrodes iteratief worden aangepast. Deze lus herhaalt zich totdat de beoogde tunnelkoppeling is bereikt.

Het tweede experiment bestudeert de afstemming van tunnelkoppelingen verder. Voor de werking van door elektrodes gedefinieerde kwantumdots is het gebruikelijk om chemische potentialen onafhankelijk te besturen met zogenaamde virtuele elektrodes. Deze virtuele elektrodes compenseren overspraak effecten als gevolg van kruiscapaciteiten van de fysieke elektrodes. De aansturing van meerdere tunnelkoppelingen heeft eveneens last van overspraak, maar efficiënte compensatietechnieken ontbraken. Dit hoofdstuk rapporteert een efficiënt kalibratieschema voor dergelijke overspraak en demonstreert onafhankelijke aansturing van tunnelkoppelingen met verbeterde virtuele elektrodes.

Het derde experiment demonstreert een methode om lading en spin te meten in grote kwantumdot roosters. De ladingsconfiguratie van een kwantumdot rooster wordt gewoonlijk gemeten met een ladingssensor, die meestal een andere kwantumdot is. Om de spin configuratie te meten, wordt deze eerst omgezet in een ladingsconfiguratie, die

voor singlet-triplet metingen is gebaseerd op het Pauli-uitsluitingsprincipe. De ladingsmeting is gebaseerd op Coulomb repulsie, die met de afstand afneemt, dus alleen lading en spin dicht bij de sensor kunnen betrouwbaar worden gemeten. Dit hoofdstuk laat zien hoe, geïnspireerd door het effect van omvallende dominostenen, een cascade van verspringende elektronen, geïnduceerd door Coulomb repulsie, de informatie over beweging van lading ver weg effectief kan omzetten in de beweging van lading dichtbij de sensor. Het voordeel van cascade-gebaseerde uitlezing wordt aangetoond door singlet-triplet metingen te vergelijken met en zonder geactiveerde cascade.

Het meest ingewikkelde experiment dat in dit proefschrift wordt beschreven, is een proof-of-principle kwantum simulatie van Heisenberg magnetisme, een van de beroemdste modellen in de fysica van de gecondenseerde materie. In het bijzonder laat dit experiment zien hoe een lineaire rij kwantumdots kan worden gebruikt als een Heisenberg spin keten. Het eerste deel van het experiment demonstreert de karakterisatie van het energiespectrum, dat gebaseerd is op ontaarding van spin toestanden met verschillende magnetisatie. Uit de energie spectroscopie worden de condities geïdentificeerd waarvoor de uitwissel interacties homogeen zijn. Vervolgens wordt de samenhang bestudeerd door globale uitwissel oscillaties te induceren, en wordt evolutie in verschillende deelruimten van de Heisenberg Hamiltoniaan gedemonstreerd. De laatste stap van het experiment bestaat uit de adiabatische initialisatie van de laag energetische globale singlet toestand voor een homogene keten, en de karakterisatie ervan met paarsgewijze singlet-triplet metingen voor elk van de naaste buren, en de correlaties hiertussen. Deze technieken en resultaten vormen de basis voor het gebruik van kwantumdots om grotere spin systemen en diverse roosters te simuleren.

Het laatste experiment verlegt de focus van spin-spin interacties naar elektron-elektron interacties. Voor kwantumdots gedefinieerd door elektrodes resulteert de Coulomb repulsie in zowel interacties tussen elektronen op dezelfde positie in het rooster als op verschillende posities. De interactie wordt experimenteel gemeten in een rij van zes kwantumdots waarin de tunnelkoppelingen homogeen zijn ingesteld. De afname van de interactie als functie van afstand wordt gemodelleerd met zowel de methode van beeldladingen, waarbij het elektrode metaal voor afscherming zorgt, alsook met een Yukawa-type potentiaal als heuristisch model. De laatste geeft een intuïtieve interpretatie van het verval van de interactie in termen van een afschermingsafstand. De karakterisatie van de lange afstand elektron-elektron interactie is relevant voor het gebruik van kwantumdots als spin kwantum bits, alsook voor kwantum simulaties waarin de lading vrijheidsgraad en elektron-elektron interacties een belangrijke rol spelen. Enkele voorbeelden van veel-deeltjes fysica waarvoor lange afstand interacties essentieel zij, zijn kwantumchemie, Wigner-kristallisatie en supergeleiding bij hoge temperaturen.

Samenvattend, dit proefschrift beschrijft nieuwe technieken voor de controle en meting van grotere kwantumdot roosters, de aansturing van een dergelijke rooster als kwantum simulator van Heisenberg magnetisme met controle over de spin-spin interacties, en karakterisatie van de elektron-elektron interacties. Deze resultaten maken de weg vrij voor toekomstige kwantum simulaties met kwantumdots.

Sjaak van Diepen

1

INTRODUCTION

1

1.1. MORE IS MORE

“Less is more” is often used as a guiding principle in finding happiness and perceiving beauty, but sometimes more really is more. Perhaps the first to make a similar statement was the Greek philosopher Aristotle: "The whole is greater than the sum of its parts". This statement applies in particular to systems of which the parts interact with each other. The interactions enable the emergence of collective behaviour, which can be qualitatively different from the behaviour of the separate constituents.

A zoo of examples can be found among the behaviour of animals, where behaviour as a group offers benefits compared to that of individual animals. The group behaviour can result in clearly ordered patterns, such as the V-shaped formation of migrating geese depicted in Fig. 1.1(a). Also more complex yet organized behaviour can emerge, such as the flight of a flock of starlings shown in Fig. 1.1(b). Surprisingly, the interactions between individual starlings can accurately be described by a simple set of rules [1], but those do not hint at the amazing patterns formed during the collective flight.

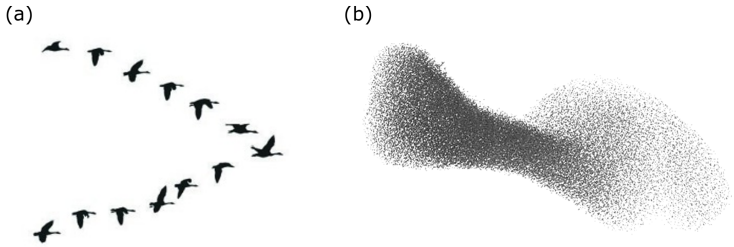

Figure 1.1: (a) Geese migrating in V-shape formation to improve energy efficiency. (b) Starlings in murmuration to protect the flock from a bird of prey.

1.2. A SPIN ON MAGNETISM

More examples of emergent behaviour can be found among the electromagnetic properties of materials. Let us focus on magnetism, which is a phenomenon known from how a bar magnet, shown in Fig. 1.2(a), attracts paper-clips or how two bar magnets orient such that opposite poles face each other. But what actually causes magnetic behaviour?

When we zoom in on a magnet we find that its macroscopic behaviour is a result of the underlying magnetic moments of electrons [2]. More specifically, the dominant component of the magnetic moment is the quantum-mechanical property called spin, which is visualized in Fig. 1.2(b). But how does the macroscopic magnetic behaviour arise from the individual electron spins? The answer lies in the collective behaviour arising from the interactions between the spins. What collective behaviour emerges depends on how the electron spins interact, which in turn depends on the type of atoms in the material, and how those atoms are configured with respect to each other. As one can imagine, there are many possible combinations and configurations of atoms, which manifests as a diversity of magnetic, and more generally, electromagnetic material properties.

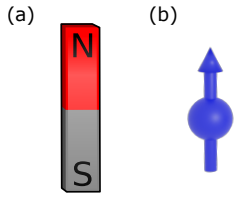

Figure 1.2: (a) A bar magnet with its north pole oriented upwards and its south pole pointing downwards. (b) Visualization of an electron spin and its associated magnetic moment.

1.3. QUANTUM SIMULATION

Many electromagnetic material properties are well understood, but open questions remain when the electrons interact and quantum effects are important, such as for high-temperature superconductors [3]. The search for answers has led to the engineering of artificial quantum matter [4], also referred to as a quantum simulator, which behaves according to the same physics as the system of interest [5, 6].

Several experimental platforms are being engineered as quantum simulators [5, 7]. The leading platform is probably that of ultracold atoms in optical lattices, for which multiple laser beams are interfered to form a pattern in which atoms are confined. Examples of other platforms are ions trapped in oscillating electrical fields, atoms and molecules positioned on a surface with a scanning tunnelling microscope, and electrical circuits with superconducting elements. Each of these platforms has different advantages and disadvantages. For example, beautiful experiments with ultracold atoms have demonstrated control over a large number of particles [8], but local control is limited, and access to the regime of unconventional superconductivity has been hindered by the relatively high temperature [9], because it washes out the quantum-mechanical correlations.

1.4. ARRAYS OF QUANTUM DOTS

One of the newest members to the family of quantum simulators is that of electrons confined in a semiconductor. For this thesis, we study electrons which effectively are two-dimensional due to tight confinement at the interface with another semiconductor or a dielectric. On top of these materials, a pattern of metallic structures, referred to as gates, is written. With voltages on the gates, the potential landscape at the interface is electrostatically shaped to induce confinement of the electrons in the other two dimensions, which is schematically depicted in Fig. 1.3. At the nano-scale such confinement, then referred to as a quantum dot, leads to a quantum-mechanical energy level structure, which resembles that of an atom.

Arrays of quantum dots are an interesting platform for quantum simulations [10, 11], because they host interacting electrons, and can be operated at temperatures where quantum effects can be resolved. In addition, dot arrays offer tunability of the potential landscape via the voltages on the gates, and flexibility in the lattice configuration, based on the freedom in design of gate patterns. Furthermore, the engineered quantum matter can be characterized by measurements of properties such as the charge and spin

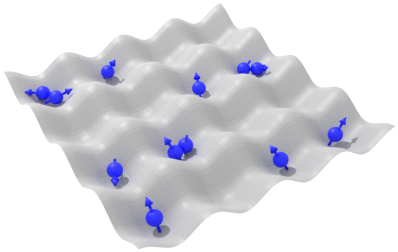

Figure 1.3: A two-dimensional potential landscape similar to an egg carton. This potential defines a 4x4 array of quantum dots with electrons in it.

in the quantum dot array.

1.5. THESIS OUTLINE

The research for this thesis is motivated by the question: "What is the potential of quantum dots as quantum simulator?" In addition, the results of this thesis are also expected to be relevant for quantum computation based on quantum dots. These results, as presented in the subsequent chapters, are briefly outlined below.

- **Chapter 2** provides an accessible overview of relevant concepts for gate-defined quantum dots, which forms the basis for understanding the experimental results in the subsequent chapters.

- **Chapter 3** describes a gate-defined quantum dot device, a characterization of its electrostatic disorder, the dilution refrigerator, and the electronics used for the experiments in this thesis.

- **Chapter 4** shows results on automation of device tuning, specifically for the tuning of the tunnel barrier between quantum dots. We used image processing on measurement data to obtain the tunnel coupling. This step is extended into an automated feedback routine, in which gate voltages are iteratively adjusted to achieve the target tunnel coupling.

- **Chapter 5** presents further work on the tuning of tunnel couplings, with the focus on crosstalk of gate voltages in the control of tunnel couplings. We developed an efficient calibration scheme to characterize such crosstalk, and apply this scheme to achieve independent tunnel coupling control.

- **Chapter 6** shifts gear from tuning tunnel couplings to measuring spin by using electron-electron interactions. We demonstrate how electron-electron interaction allows an initial charge transition to induce subsequent charge transitions, inducing a cascade of electron hops, like toppling dominoes. We use such a cascade to read out spins at a distance from the charge sensor, and show results with potential for high fidelity readout. We also discuss the application of cascade-based

spin readout to densely-packed two-dimensional quantum dot arrays with charge sensors placed at the periphery.

- **Chapter 7** builds on the tuning and spin measurements, and reports the most involved experiment in this thesis, which demonstrates the operation of quantum dots as a simulator of Heisenberg magnetism. Parts of this work are the development of experimental methods for energy spectroscopy and coherent oscillations of the global spin states in different Hamiltonian subspaces. We use these methods to engineer a spin chain with homogeneous exchange couplings. Then we prepare the low-energy global singlet eigenstate for the spin-chain and characterize the state with two-spin singlet-triplet readout on all nearest-neighbour pairs and correlations therein.

- **Chapter 8** returns from spin-spin interactions to electron-electron interactions, and presents a characterization of the fall-off with distance in a quantum dot device. The interactions were measured in a homogeneously tuned multi-dot array, and the interaction strengths are extracted from charge-stability diagrams for all dot pairs in the array. The interaction was found to be measurable for electrons up to four sites away, and the decay is explained by screening of the Coulomb repulsion due to the metal of the gates on the surface of the device.

- **Chapter 9** concludes this thesis by putting the results into broader perspective.

1

REFERENCES

[1] C. W. Reynolds, *Flocks, herds, and schools: A distributed behavioral model,* Proceedings of the 14th Annual Conference on Computer Graphics and Interactive Techniques (SIGGRAPH'87) **21**, 25 (1987).

[2] B. Cullity and C. Graham, *Introduction to magnetic materials* (John Wiley and Sons, 2009).

[3] P. W. Anderson, *Twenty-five years of high-temperature superconductivity - A personal review,* Journal of Physics: Conference Series **449**, 012001 (2013).

[4] R. P. Feynman, *Simulating physics with computers,* International Journal of Theoretical Physics **21**, 467 (1982).

[5] I. Buluta and F. Nori, *Quantum Simulators,* Science **326**, 108 (2009).

[6] J. I. Cirac and P. Zoller, *Goals and opportunities in quantum simulation,* Nature Physics **8**, 264 (2012).

[7] I. M. Georgescu, S. Ashhab, and F. Nori, *Quantum simulation,* Reviews of Modern Physics **86**, 153 (2014).

[8] C. Gross and I. Bloch, *Quantum simulations with ultracold atoms in optical lattices,* Science **357**, 995 (2017).

[9] A. Mazurenko, C. S. Chiu, G. Ji, M. F. Parsons, M. Kanász-Nagy, R. Schmidt, F. Grusdt, E. Demler, D. Greif, and M. Greiner, *A cold-atom Fermi-Hubbard antiferromagnet,* Nature **545**, 462 (2017).

[10] E. Manousakis, *A quantum-dot array as model for copper-oxide superconductors: A dedicated quantum simulator for the many-fermion problem,* Journal of Low Temperature Physics **126**, 1501 (2002).

[11] T. Byrnes, N. Y. Kim, K. Kusudo, and Y. Yamamoto, *Quantum simulation of Fermi-Hubbard models in semiconductor quantum-dot arrays,* Physical Review B **78**, 075320 (2008).

2

BACKGROUND FOR GATE-DEFINED QUANTUM DOTS

This chapter provides an accessible overview of the relevant concepts for gate-defined quantum dots, and forms the basis to understand the experimental chapters in this thesis. In the first section, the semiconductor material and the device components are introduced. The next sections introduce step-by-step the key concepts for gate-defined quantum dots. Then, the mapping between lattice models from condensed matter theory and quantum dot arrays is presented. This chapter ends with a didactic section about the technique referred to as virtual gates, which has facilitated the operation of multi-dot arrays as quantum simulator for lattice model physics.

2.1. MATERIALIZATION

Quantum dots are created at the nano-scale and provide electron or hole confinement in all three spatial dimensions. In this thesis, we focus on planar gate-defined quantum dots, which are implemented with a combination of band engineering and voltages on gates (for additional background see the reviews [1, 2] or the book [3]). The devices used for the results in this thesis are based on a stack of the III-V semiconductors AlGaAs ($Al_xGa_{1-x}As$ with $x \approx 0.3$ the Al concentration) and GaAs, grown with molecular-beam epitaxy, such as shown in Fig. 2.1(a). AlGaAs has a larger band gap than GaAs, which results in a step in the conduction band minimum. By n-doping the AlGaAs with Si, indicated by the thin red layer, the potential profile bends, and a two-dimensional electron gas (2DEG), indicated with the dashed blue line, forms at the interface between the two semiconductors. Ohmic contacts are added to serve as source and drain for electrical measurements of the device. Gates are patterned on top of the material stack, see Fig. 2.1(b) and Fig. 2.2(a), and with voltages on the gates the nearby electrons are pushed away, such that the 2DEG becomes locally depleted and quantum dots can be formed. To facilitate the control and measurement of the quantum states, the quantum dot devices are typically cooled to tens of millikelvin inside a dilution refrigerator (see Chapter 3).

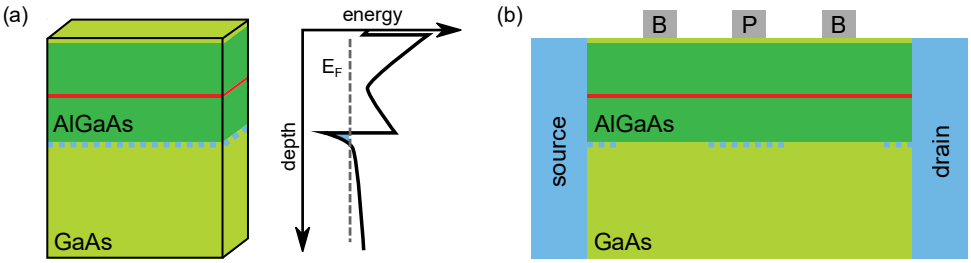

Figure 2.1: (a) Schematic of the material stack and corresponding energy diagram. The thin red layer indicates silicon dopants, while the blue dashed line indicates the location of electrons. The Fermi level, up to which states are occupied, is indicated with E_F. (b) Schematic side view of a device with gates patterned on top of the material stack. B corresponds to a barrier gate and P corresponds to a plunger gate. Source and drain contact to the electron gas and are used for electrical measurements of the device.

The last 5-10 years stacks based on the group-IV materials silicon and germanium [4] have quickly gained popularity. This popularity is due to the reduced presence and influence of nuclear spins, and envisioned compatibility with industrial processes tailored for group-IV materials. Only in the last few years the growth of these materials and the fabrication of the gate pattern, have reached the level of maturity, which allows the formation of multiple coupled quantum dots and control over several spin qubits. Note that, for silicon multi-layer gate patterns are used, because smaller pitches are required due to the larger effective mass, $0.19m_e$, compared to $0.067m_e$ in gallium-arsenide and $0.05m_e$ for germanium. These advances make that silicon and germanium are nowadays favoured for spin-qubits. However, the results presented in this thesis, achieved on the GaAs material stack, do not lose their merit when transferred to those other materials.

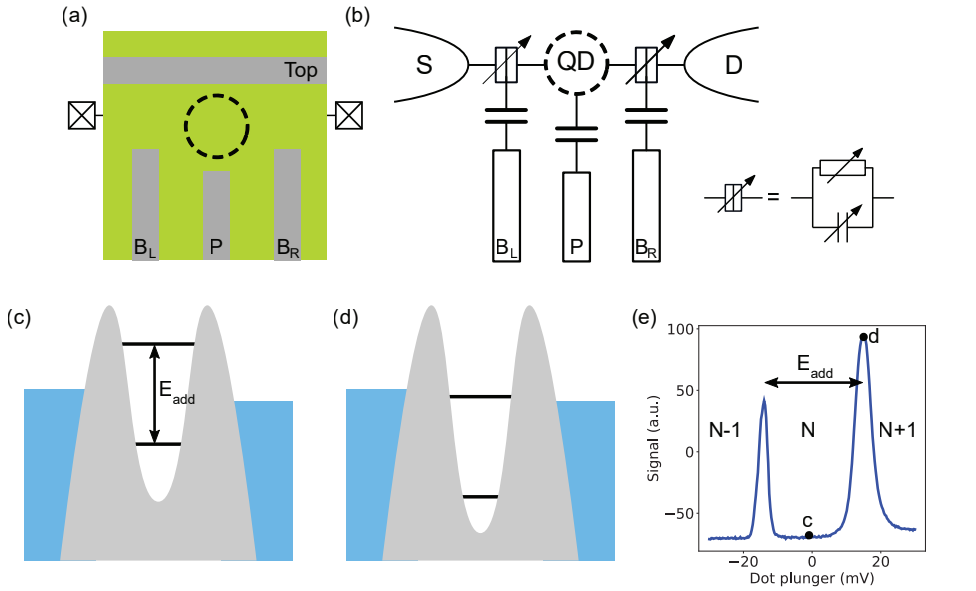

Figure 2.2: (a) Schematic top view of a device with a gate pattern for a single quantum dot. Boxes with crosses indicate the locations of ohmic contacts. (b) Schematic electrical diagram for a device with a single quantum dot and ohmic contacts which serve as source and drain. The capacitance and the resistance between the dot and the reservoirs are tunable with the gates, and so is the dot energy. (c) Schematic potential profile for a the quantum dot with the chemical potentials such that transport is not possible and (d) when it is possible. (e) Coulomb peaks appear in the signal, here measured with radio-frequency reflectometry (see Chapter 3), as function of plunger gate voltage, which controls a shift of the dot chemical potential and the number of charges on the dot.

2.2. SINGLE DOT: CONFINEMENT AND QUANTUM

Charges, such as electrons, can be trapped inside the confining potential of the quantum dot. The small size of the quantum dot results in a discrete energy level structure, which can be characterized by the energy needed to put an additional electron onto the quantum dot. This quantity is called the addition energy, E_{add}, (see Fig. 2.2) and consists of two components: the charging energy and the orbital energy. The charging energy, E_c, is a classical effect, which arises due to the Coulomb repulsion between charges, thus it essentially describes the energetic cost to add a charge to a quantum dot which already has charge in it. With the simplifying assumption that the charging energy remains constant under changes of gate voltages and dot occupation, commonly referred to as the constant-interaction model, the charging energy can be expressed as $E_c = e^2/C$, with C the sum of all capacitances to the dot, such as shown in Fig. 2.2(b). The orbital energy is a quantum-mechanical effect, and relates to the shape of the wave function for a confined particle, thus here to that of the electron in the quantum dot.

For circular quantum dots, when modelled as a metallic disk with radius r_{dot}, the charging energy scales as $\sim r_{dot}^{-1}$, and with a confinement potential shaped as an harmonic oscillator, the orbital energy scales with $\sim r_{dot}^{-2}$ [3]. For the gate-defined quantum dots operated in this thesis (~100 nm diameter) the charging energy is a few times larger

than the orbital energy. In practice, both the constant-interaction model and the energy scalings should be considered as a mere rule-of-thumb, because for the gate-defined quantum dots operated for this thesis these simplifying assumptions do not hold. Interesting to note is that quantum dots are sometimes also referred to as artificial atoms, because of the similarities in energy level structure and shell filling to real atoms [5].

The discrete energy spectrum of a quantum dot can be characterized with Coulomb peak measurements, such as shown in Fig. 2.2(c)-(e). For such measurements a small source-drain bias (~100 μV) is applied, and current can only flow if a quantum dot chemical potential lies within the bias window, which results in the Coulomb peaks.

The quantum states for the electrons on the dot have besides an orbital component also a spin component (neglecting valleys, which are relevant in silicon). The spin state can be expressed in terms of the single-electron spin states, which are naturally expressed in bra-ket notation as spin-up, $|\uparrow\rangle$, and spin-down, $|\downarrow\rangle$. To form a single-spin qubit, an external magnetic field is applied to energetically separate the spin-up and spin-down states with the Zeeman splitting. Manipulation of the single spin, and correspondingly single-qubit gates, have been achieved with microwave driving via magnetic control (referred to as electron-spin resonance: ESR) using an on-chip stripline [6] or electrical control (referred to as electron-dipole spin resonance: EDSR) via one of the gates and in the presence of a magnetic field gradient or spin-orbit coupling [7].

2.3. DOUBLE DOTS: CHARGE SENSING AND TUNNELLING

When quantum dots are near each other, two additional effects enter the picture [1, 8]. The first effect is referred to as inter-site interaction, which is just as the charging energy induced by the Coulomb repulsion, and corresponds to the energy cost to add charge to a dot, which is near a dot with charge on it. This effect is also referred to as the mutual capacitance [1] and is depicted in the schematic in Fig. 2.3(a).

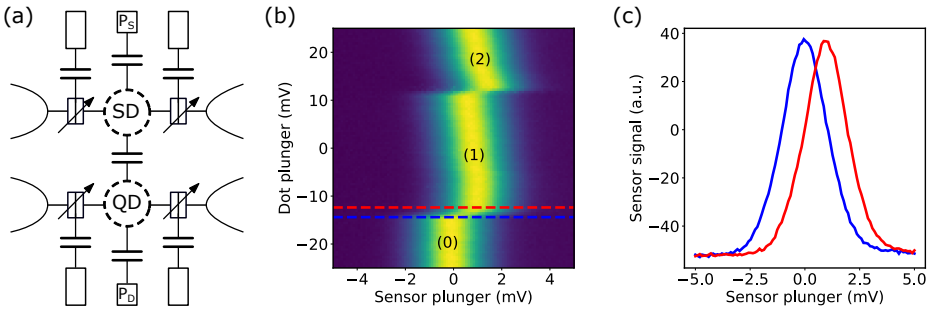

Figure 2.3: (a) Schematic electrical circuit diagram for a device with a quantum dot and a sensing dot, which are capacitively coupled. (b) Charge-sensing of a quantum dot with the sensor signal as function of sensor and dot plunger voltage, and (c) two traces for dot plunger settings just below and above a charge transition. The data shows that the Coulomb peak for the sensing dot shifts to more positive sensor plunger voltage due to the addition of an electron on the quantum dot. The number in round brackets indicates the number of charges on the quantum dot. Note that the position of the sensing dot Coulomb peak also shifts as a function of dot plunger voltage, which is a result of cross-capacitance (see Fig. 2.4 and Section 2.6).

The inter-site interaction forms the basis for the commonly used technique of charge-

sensing. A typical implementation of charge sensing is shown in Fig. 2.3(a), which relies on an additional quantum dot, referred to as the sensing dot, that is positioned in proximity of the quantum dot that is to be sensed. The sensing dot is tuned such that its signal, which is determined by its resistance, has a strong gate voltage dependence, which is the case on the flank of a Coulomb peak. In this way, the sensor signal depends on the charge distribution in its environment, such as the number of charges on a quantum dot (see Fig. 2.3). Chapter 6 demonstrates, inspired by the behaviour of toppling dominoes, how a sensing dot can be used to sense a distant quantum dot, far beyond the range where the inter-site interaction plays a role.

The second effect is that of electron tunnelling, which corresponds to the movement of an electron between two quantum dots, which are then referred to as a double dot, such as formed by D1 and D2 in Fig. 2.4(a). The effect of tunnelling is shown by the energy diagram in Fig. 2.5(a), where the tunnelling is captured in terms of the tunnel coupling, t. Due to tunnelling, the double dot eigenstates hybridize, which appears as an anti-crossing of states in the energy diagram, and the eigenstates form superpositions of the classical charge states. In bra-ket notation this can be expressed as $|\psi\rangle = \alpha|10\rangle + \beta|01\rangle = \alpha|L\rangle + \beta|R\rangle$, where $|L\rangle$ and $|R\rangle$ indicate the state with the charge on the left and the right dot respectively.

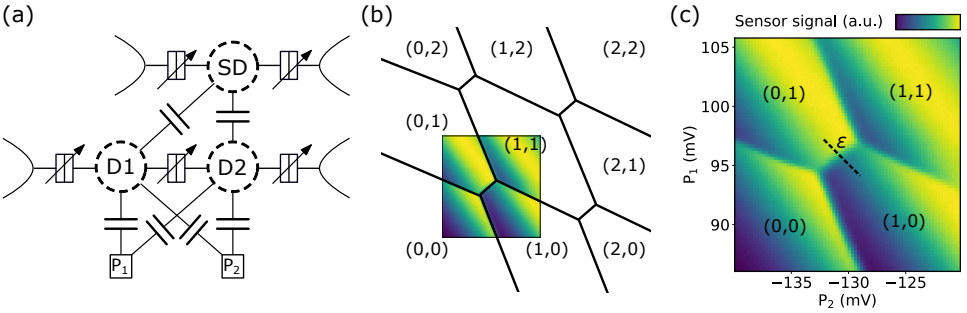

Figure 2.4: (a) Schematic electrical diagram for a double quantum dot with a sensing dot, which is capacitively coupled to both dots. Only the two dot plungers are indicated, while all other gates have been left out to reduce complexity. (b) Charge-stability diagrams of a double quantum dot with a schematic diagram with transition lines showing a larger part of the charge-stability space, which is overlaid on a (c) measured diagram that shows the sensor signal as function of dot plunger gate voltages. Numbers in round brackets indicate the charge occupation of the two dots.

Putting the above together, a charge-sensing measurement of a double quantum dot results in a so-called charge-stability diagram, such as shown in Fig. 2.4(b) and (c), which is also referred to as a honeycomb diagram due to its pattern. In this diagram, faces correspond to regions of gate voltages with the same charge occupation, indicated by numbers in round brackets, while lines correspond to charge transitions, either between quantum dots (inter-dot), or between a dot and a reservoir. The number of charges on a dot can be deduced, by starting from where the dot is fully emptied and then going upwards in voltage space while counting the number of dot-reservoir transition lines. The locations where the transition lines meet are referred to as triple points. Here the chemical potentials of the dots are aligned to one another and to the reservoirs. When

the double dot would be measured in transport, then this would occur near the triple points. The inter-site interaction between the two dots, just like that for a sensing dot and a quantum dot, appears in the double dot diagram as a shift of dot-reservoir transition lines between the triple points. The tunnelling, as it corresponds to hybridization of charge states, is visible in the charge-stability diagram as both a rounding of the triple points, and a broadening of the inter-dot transition line [9], such as shown in Fig. 2.5(b).

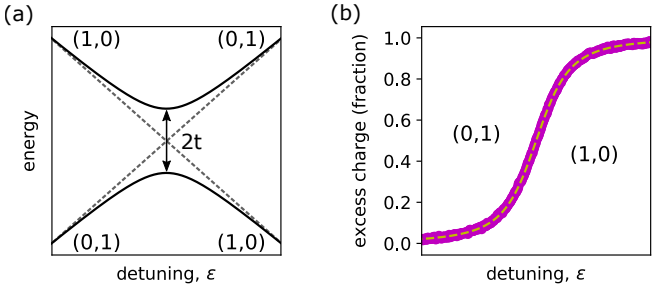

Figure 2.5: (a) Energy diagram as function of detuning, which corresponds to that the chemical potential of one dot increases while the chemical potential of the other dot decreases proportionally. Dashed lines correspond to the classical case, where there is no tunnel coupling, $t = 0$, while solid lines correspond to the tunnel coupled case for which the charge states hybridize, and the lines form an anti-crossing. (b) The fraction of excess charge as function of the detuning, which reveals the hybridization of the charge state via the broadening of the charge transition [9]. The dashed line is a fit to the data. More information is given in Chapter 4, from which this figure is adapted.

Note that the dot-reservoir transition lines are sloped, which is a result of the cross-capacitances between gates and quantum dots as indicated by the two diagonal capacitors in Fig. 2.4, and which will be further discussed in Section 2.6. Similarly, the signal gradient in the background of the charge-stability diagram is a result of cross-capacitance between the dot plungers and the sensing dot, but is not indicated in Fig. 2.4(a).

2.4. SPIN-TO-CHARGE CONVERSION

Besides measurements of the charge configuration, it is also common to measure the spin state. The spin of a single electron is very small, thus it is hard to measure directly. However, the spin configuration can be mapped onto a charge configuration, which is referred to as spin-to-charge conversion, and subsequently the charge configuration can be measured with charge sensing.

A popular method for spin-to-charge conversion, which was used for the results in Chapters 6 and 7, is called Pauli spin blockade [10–13], and is schematically depicted in Fig. 2.6(a). This method relies on the Pauli exclusion principle, which dictates that the total wave function of fermions should be anti-symmetric under the exchange of two particles. As a consequence, and as shown in the energy diagram in Fig. 2.6(b), for two electrons on a quantum dot, the spin-singlet state ($|S\rangle = \frac{1}{\sqrt{2}}(|\uparrow\downarrow\rangle - |\downarrow\uparrow\rangle)$) is energetically favoured, and the spin-triplet states ($|T^+\rangle = |\uparrow\uparrow\rangle$, $|T^0\rangle = \frac{1}{\sqrt{2}}(|\uparrow\downarrow\rangle + |\downarrow\uparrow\rangle)$, $|T^-\rangle = |\downarrow\downarrow\rangle$ are higher in energy, because one of the triplet electrons needs to occupy an excited orbital to maintain the antisymmetry of the total wave function. Actually, the singlet-triplet

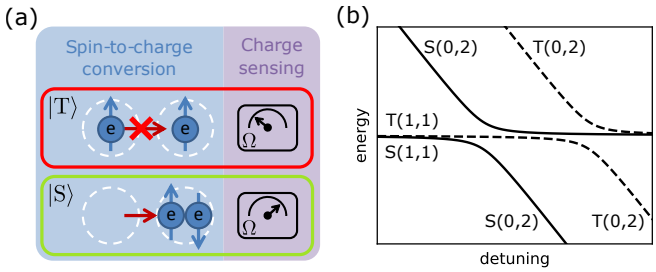

Figure 2.6: (a) Schematic of Pauli spin blockade readout. The transition is blocked for the triplet, $|T\rangle$, while it is allowed for the singlet, $|S\rangle$. In this way, the spin configuration is converted into a charge configuration, which is measured via the resistance of the charge sensor. (b) Double dot energy level diagram. Solid lines correspond to singlet states, while dashed lines correspond to triplet states. No external magnetic field is applied, thus the triplets are three-fold degenerate.

energy difference is smaller than the orbital energy, because the Coulomb energy is lower with one electron in the excited orbital [5]. In the energy diagram, for simplicity the tunnel coupling for the triplets is taken to be the same as for the singlet. In practice they typically differ, which can be understood from a difference in wave function overlap, because for a triplet one electron occupies an excited orbital.

In practice, to perform readout with Pauli spin blockade, two electrons, which were initially on separate dots, are conditionally moved onto the same dot by detuning the double dot with such an amount that the transition will only be allowed for electrons that form a spin-singlet, while for electrons in a spin-triplet the transition is energetically inaccessible, as explained above. In this way, the two-electron spin configuration is converted into a charge configuration, which can be measured with a sensing dot.

Note that, Pauli spin blockade can also be used for parity readout, which distinguishes parallel spin states ($|\uparrow\uparrow\rangle, |\downarrow\downarrow\rangle$) from anti-parallel spin states ($|\uparrow\downarrow\rangle, |\downarrow\uparrow\rangle$) [14, 15]. Parity readout can be achieved when the eigenstates at the readout point are not $|S\rangle$ and $|T_0\rangle$, but are $|\uparrow\downarrow\rangle$ and $|\downarrow\uparrow\rangle$. This is the case when the difference in Zeeman energy, for example due to (artificial) spin-orbit interaction or nuclear spins, dominates over the exchange coupling between spins (see Section 2.5 or Chapter 7).

Another popular spin-to-charge conversion method is commonly referred to as energy-selective readout or Elzerman readout [16]. For this method, an external magnetic field is applied to induce a Zeeman splitting between the spin-up and spin-down state. The quantum dot chemical potential is tuned such that the spin excited state is above the reservoir level and the spin ground state is below. Then, if the electron is in the excited spin state it will tunnel off the dot into the reservoir, which is followed by the tunnelling of an electron in the ground spin state into the empty dot, while if the electron was initially in the spin ground state no tunnelling occurs.

A benefit of the energy-selective method is that it allows to directly readout individual spins, while a limitation is that it requires the quantum dot to be tunnel coupled to a reservoir. More specifically, with a tunnel rate that is significantly lower than the measurement bandwidth, because otherwise tunnelling could occur without being detected and the incorrect spin state would be assigned. This requirement makes the energy-selective readout slow compared to Pauli spin blockade. A shorter readout time is not

only beneficial for faster calibration of the parameters of the quantum dot system, such as those for the spin manipulation and the exchange coupling between spins. In addition, for feedback routines, such as used for quantum error correction, it is key to achieve low latency, which demands fast readout.

2.5. MULTI-DOT ARRAYS AND LATTICE MODELS

Extending from a single dot, via double dots, to multi-dot arrays opens up opportunities for the exploration of quantum phases of matter. In condensed-matter physics, perhaps the most often studied model is the Fermi-Hubbard model, which describes mobile electrons on a lattice with the Hamiltonian

$$H_{FH} = U\sum_i n_{i\uparrow}n_{i\downarrow} - t\sum_{\langle i,j\rangle}\left(c_i^\dagger c_j + h.c.\right), \tag{2.1}$$

where U is the Coulomb interaction, $n_{i\sigma}$ the number operator for electrons with spin, σ, t corresponds to the tunnelling, and $c_i^\dagger$ and c_j are the creation and annihilation operators respectively. More intuitively, the first term describes the energy penalty for two electrons to occupy the same site, and the second term describes the movement of electrons. In the regime where interactions are strong, thus $U > t$, many-body effects can give rise to intricate phases of matter [17], such as a Mott-insulator, where all sites are occupied by one electron and movement is suppressed by the Coulomb interaction.

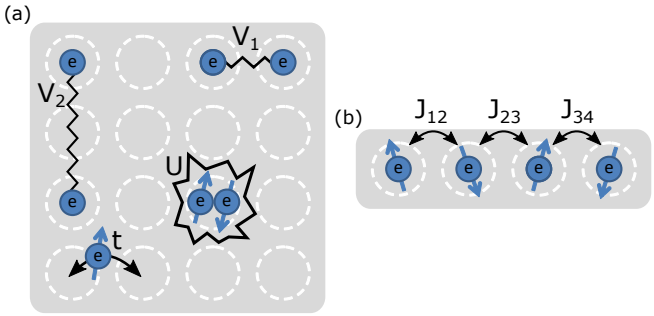

Figure 2.7: Schematics of quantum dot arrays (dashed circles) with visualizations of terms in (a) the Fermi-Hubbard model and (b) the Heisenberg model. The inter-site interactions, V_i, here have a single sub-index, which expresses the number of sites over which the electrons are separated.

Arrays of gate-defined quantum dots can be described with an extended form of the Fermi-Hubbard model [8, 18], which is visualized in Fig. 2.7(a), and for which the Hamiltonian is

$$H_{FH,qd} = -\sum_i \varepsilon_i n_i + \sum_i U_i n_{i\uparrow}n_{i\downarrow} + \sum_{i\neq j} V_{ij}n_i n_j - \sum_{\langle i,j\rangle} t_{ij}\left(c_i^\dagger c_j + h.c.\right), \tag{2.2}$$

with ε_i the local energy offset, U_i the Coulomb interaction for site i, V_{ij} the inter-site interaction and t_{ij} the tunnel coupling. Note that, each term in the Hamiltonian is now site-dependent, which expresses both the system disorder and tunability. As a rule-of-thumb, the interaction terms, U_i and V_{ij}, are considered to be reasonably fixed by the

parameter	value/range (meV)
ε_i	0 - 15
U_i	3
Δ_i	1
V_{ij}	0 - 1
t_{ij}	0 - 0.3
E_Z	0 - 0.3
T_e	≥ 0.005

Table 2.1: Typical values and ranges of the parameters for a gate-defined quantum dot array in GaAs. In addition to the Fermi-Hubbard parameters, typical values are shown for Δ_i, the orbital splitting, E_Z the Zeeman splitting, and T_e, the temperature of the electron reservoirs.

gate pattern, while the local energy offsets, ε_i, and the tunnel couplings, t_{ij}, are tunable with the gate voltages. Note that the model in eqn. (2.2) is single-band, thus it only includes the lowest orbital, while experiments with gate-defined quantum dots routinely involve the occupation of an excited orbital, for example with Pauli spin blockade. Nevertheless, this single-band model already covers a broad range of phenomena, and it provides an intuitive description of a gate-defined quantum dot array.

For a quantum dot array, typical values for the Fermi-Hubbard parameters, the orbital and Zeeman splitting, and the temperature of the electron reservoirs, T_e, are shown in Table 2.1. The tunnel coupling values, t_{ij}, are for nearest-neighbours. For the inter-site interaction, V_{ij}, the fall-off with distance was measured in a multi-dot array, and is presented in Chapter 8. From the parameter overview it follows that $U > t > T_e$, which corresponds to the regime where interactions are strong, and quantum effects dominate over temperature. This puts gate-defined quantum dot arrays in the most interesting regime of Fermi-Hubbard physics [17, 19–21], which is hard to study theoretically or with other quantum simulation platforms.

In the Mott-insulator regime, where the charge degree of freedom is frozen, only the spin degree of freedom remains. In this regime, the low-energy physics of the Fermi-Hubbard model can effectively be described by the Heisenberg model [22], for which the Hamiltonian is

$$H_{heis} = \sum_{\langle i,j \rangle} J_{ij} \left(\vec{S}_i \cdot \vec{S}_j - \frac{1}{4} \right), \tag{2.3}$$

with J_{ij} the exchange coupling between spins on sites i and j, and $\vec{S}_i$ the vector of spin operators for site i. The factor of $-\frac{1}{4}$ is subtracted as a convention, which sets the energy of two-spin triplets to zero.

From the Heisenberg model it follows that the exchange coupling is equal to the energy splitting between the two-spin singlet and triplet states. At the center of the (1,1) charge region, the so-called symmetric operating point [23, 24], the exchange coupling can be expressed as $J_{ij} = 4t_{ij}^2/U$, neglecting inter-site interactions, variations between U_i and differences between the singlet and triplet tunnel coupling and Coulomb energies [24]. In the detuned regime, thus closer to the inter-dot transition where two electrons in a spin-singlet can move to the same dot, see also the energy diagram in

Fig. 2.6(b), the exchange coupling can be approximated with $J_{ij} = \frac{1}{2}\left(-\varepsilon_{ij} + \sqrt{\varepsilon_{ij}^2 + 8t_{ij}^2}\right)$, with $\varepsilon_{ij} = \varepsilon_i - \varepsilon_j$, the detuning [25].

The exchange coupling is a key ingredient for quantum computation with spin-qubits, as it enables for example two-qubit gates between single-spin qubits [26, 27]. In the context of analog quantum simulation, the Heisenberg model is one of the key models to describe quantum magnetism, and covers a rich variety of magnetic phenomena [28–30]. Chapter 7 demonstrates how a quantum dot array can be used to emulate the behaviour of the Heisenberg model by implementing a spin chain, such as depicted in Fig. 2.7(b).

2.6. VIRTUAL GATES AND INDEPENDENT CONTROL

Control of multi-dot arrays is challenging due to disorder and crosstalk. See Section 3.1.3 for a characterization of the disorder for a device with a multi-dot array. In this section, the focus is on crosstalk and how to mitigate it. A more extensive discussion is presented in Chapter 5.

An effect of cross-capacitance is that each gate not only influences the local energy offset of its corresponding dot, but also those of nearby dots. This crosstalk results in sloped dot-reservoir transition lines in the charge-stability diagram, such as in Fig. 2.4. It is common practice to compensate for such cross-capacitances with the concept of virtual gates [18, 31]. A change in applied voltage on a virtual gate corresponds to a linear combination of changes in voltages on several physical gates, which can be captured in matrix form as

$$\begin{pmatrix}\delta P_1' \\ \delta P_2'\end{pmatrix} = \begin{pmatrix}1 & \alpha_{12} \\ \alpha_{21} & 1\end{pmatrix}\begin{pmatrix}\delta P_1 \\ \delta P_2\end{pmatrix}, \quad \begin{pmatrix}\delta\varepsilon_1 \\ \delta\varepsilon_2\end{pmatrix} = \begin{pmatrix}\alpha_1 & \alpha_2\end{pmatrix}\begin{pmatrix}\delta P_1' \\ \delta P_2'\end{pmatrix}, \tag{2.4}$$

with the cross-capacitance matrix elements $\alpha_{ij} = \frac{\partial\varepsilon_i}{\partial P_i} / \frac{\partial\varepsilon_i}{\partial P_j}$, and with α_i the so-called lever arm, here for the virtual gates. The lever arms offer a conversion between units of voltage and energy, and express how strongly a change in (virtual) gate voltage affects the quantum dot energy. The lever arms can be measured with various techniques, such as Coulomb diamonds, bias triangles, or photon-assisted tunnelling, of which the latter was regularly used for the results in this thesis (see for example Chapters 4 and 5). The α_{ij} can be obtained from the slopes of the dot-reservoir lines in a charge-stability diagram. By controlling the quantum dots with virtual gates, the dot-reservoir transition lines ideally become fully horizontal and vertical, such as in the charge-stability diagram in Fig. 2.8(a). Note that, without the incorporation of the lever arms into the virtual gates, even though the control of chemical potentials is independent, they only change proportionally and not identically if there are differences between the lever arms, which corresponds to an inter-dot transition line that is not fully diagonal.

In addition, there are cross-capacitances between gates and tunnel couplings. An apparent complexity is that the tunnel couplings depend exponentially on gate voltage changes [24] as

$$t_{ij} = t_{ij,0} \exp\left\{\sum_{kl} \Gamma_{kl}^{ij} \delta B_{kl}'\right\}, \tag{2.5}$$

with $t_{ij,0}$ the tunnel coupling before changing the gate voltages, and Γ_{kl}^{ij} the exponential coefficients for each gate. For simplicity, the effect of plungers on tunnel couplings is

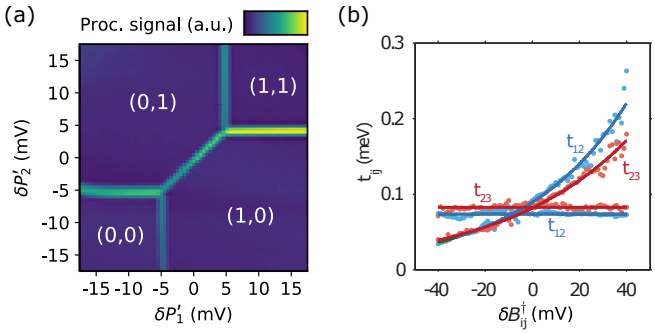

Figure 2.8: (a) Charge-stability diagram for a double dot, which is measured with virtual gates. Numbers in round brackets indicate the charge occupation. This subfigure is adapted from Chapter 4. (b) Tunnel couplings as function of voltage changes on enhanced virtual barriers. The data was taken in two experimental runs, thus one for which t_{12} was varied while t_{23} was kept fixed, and vice versa for the other run. This data was published in [18], and was acquired on the same triple dot device as presented in Chapter 4.

left out, and the barrier gates are already virtual in the sense that they are defined analogous to eqn. (2.4), which is explicitly described in Section 4.8.2. Despite the exponential dependence, the tunnel coupling crosstalk can still be compensated for with a linear transformation as

$$\begin{pmatrix} \delta B_{12}^{\dagger} \\ \delta B_{23}^{\dagger} \end{pmatrix} = \begin{pmatrix} 1 & \beta_{12} \\ \beta_{21} & 1 \end{pmatrix} \begin{pmatrix} \delta B'_{12} \\ \delta B'_{23} \end{pmatrix}, \quad t_{ij} = t_{ij,0} \exp\left\{ \Gamma_{ij}^{ij} \delta B_{ij}^{\dagger} \right\}, \tag{2.6}$$

with for example $\beta_{12} = \Gamma_{23}^{12}/\Gamma_{12}^{12}$, and where Γ_{ij}^{ij} can be considered as lever arms for the tunnel couplings. With these enhanced virtual gates, independent control over tunnel couplings can be achieved, such as shown in Fig. 2.8(b). Chapter 5 more extensively discusses cross-capacitances to tunnel couplings, shows the characterization of these cross-capacitances, and demonstrates an efficient calibration method for the enhanced virtual gates.

REFERENCES

[1] W. G. van der Wiel, *Electron transport through double quantum dots,* Reviews of Modern Physics **75**, 1 (2003).

[2] R. Hanson, L. P. Kouwenhoven, J. R. Petta, S. Tarucha, and L. M. K. Vandersypen, *Spins in few-electron quantum dots,* Reviews of Modern Physics **79**, 1217 (2007).

[3] T. Ihn, *Semiconductor Nanostructures - Quantum States and Electronic Transport* (Oxford University Press, 2010).

[4] G. Scappucci, *Semiconductor materials stacks for quantum dot spin qubits,* arXiv:2102.10897 (2021).

[5] L. P. Kouwenhoven, G. D. Austing, and S. Tarucha, *Few-electron quantum dots,* Reports on Progress in Physics **64**, 701 (2001).

[6] F. H. L. Koppens, C. Buizert, K. J. Tielrooij, I. T. Vink, K. C. Nowack, T. Meunier, L. P. Kouwenhoven, and L. M. K. Vandersypen, *Driven coherent oscillations of a single electron spin in a quantum dot,* Nature **442**, 766 (2006).

[7] K. C. Nowack, F. H. L. Koppens, Y. V. Nazarov, and L. M. K. Vandersypen, *Coherent Control of a Single Electron Spin with Electric Fields,* Science **318**, 1430 (2007).

[8] S. Yang, X. Wang, and S. Das Sarma, *Generic Hubbard model description of semiconductor quantum-dot spin qubits,* Physical Review B **83**, 161301(R) (2011).

[9] L. DiCarlo, H. J. Lynch, A. C. Johnson, L. I. Childress, K. Crockett, C. M. Marcus, M. P. Hanson, and A. C. Gossard, *Differential charge sensing and charge delocalization in a tunable double quantum dot,* Physical Review Letters **92**, 226801 (2004).

[10] K. Ono, D. G. Austing, Y. Tokura, and S. Tarucha, *Current rectification by Pauli exclusion in a weakly coupled double quantum dot system,* Science **297**, 1313 (2002).

[11] A. C. Johnson, J. R. Petta, A. Yacoby, M. D. Lukin, C. M. Marcus, M. P. Hanson, and A. C. Gossard, *Triplet – singlet spin relaxation via nuclei in a double quantum dot,* Nature **435**, 925 (2005).

[12] J. R. Petta, A. C. Johnson, J. M. Taylor, E. A. Laird, A. Yacoby, M. D. Lukin, C. M. Marcus, M. P. Hanson, and A. C. Gossard, *Coherent Manipulation of Coupled Electron Spins in Semiconductor Quantum Dots,* Science **309**, 2180 (2005).

[13] C. Barthel, D. J. Reilly, C. M. Marcus, M. P. Hanson, and A. C. Gossard, *Rapid single-shot measurement of a singlet-triplet qubit,* Physical Review Letters **103**, 160503 (2009).

[14] C. Barthel, J. Medford, H. Bluhm, A. Yacoby, C. M. Marcus, M. P. Hanson, and A. C. Gossard, *Relaxation and readout visibility of a singlet-triplet qubit in an Overhauser field gradient,* Physical Review B **85**, 035306 (2012).

[15] A. E. Seedhouse, T. Tanttu, R. C. Leon, R. Zhao, K. Y. Tan, B. Hensen, F. E. Hudson, K. M. Itoh, J. Yoneda, C. H. Yang, A. Morello, A. Laucht, S. N. Coppersmith, A. Saraiva, and A. S. Dzurak, *Pauli Blockade in Silicon Quantum Dots with Spin-Orbit Control,* PRX Quantum **2**, 010303 (2021).

[16] J. M. Elzerman, R. Hanson, L. H. W. van Beveren, B. Witkamp, L. M. K. Vandersypen, and L. P. Kouwenhoven, *Single-shot read-out of an individual electron spin in a quantum dot,* Nature **430**, 431 (2004).

[17] M. Imada, A. Fujimori, and Y. Tokura, *Metal-insulator transitions,* Rev. Mod. Phys. **70**, 1039 (1998).

[18] T. Hensgens, T. Fujita, L. Janssen, X. Li, C. J. Van Diepen, C. Reichl, W. Wegscheider, S. Das Sarma, and L. M. K. Vandersypen, *Quantum simulation of a Fermi-Hubbard model using a semiconductor quantum dot array,* Nature **548**, 70 (2017).

[19] E. Manousakis, *A quantum-dot array as model for copper-oxide superconductors: A dedicated quantum simulator for the many-fermion problem,* Journal of Low Temperature Physics **126**, 1501 (2002).

[20] T. Byrnes, N. Y. Kim, K. Kusudo, and Y. Yamamoto, *Quantum simulation of Fermi-Hubbard models in semiconductor quantum-dot arrays,* Physical Review B **78**, 075320 (2008).

[21] P. Barthelemy and L. M. K. Vandersypen, *Quantum Dot Systems: A versatile platform for quantum simulations,* Annalen der Physik **525**, 808 (2013).

[22] A. Auerbach, *Interacting Electrons and Quantum Magnetism* (Springer, 1994).

[23] F. Martins, F. K. Malinowski, P. D. Nissen, E. Barnes, S. Fallahi, G. C. Gardner, M. J. Manfra, C. M. Marcus, and F. Kuemmeth, *Noise Suppression Using Symmetric Exchange Gates in Spin Qubits,* Physical Review Letters **116**, 116801 (2016).

[24] M. D. Reed, B. M. Maune, R. W. Andrews, M. G. Borselli, K. Eng, M. P. Jura, A. A. Kiselev, T. D. Ladd, S. T. Merkel, I. Milosavljevic, E. J. Pritchett, M. T. Rakher, R. S. Ross, A. E. Schmitz, A. Smith, J. A. Wright, M. F. Gyure, and A. T. Hunter, *Reduced Sensitivity to Charge Noise in Semiconductor Spin Qubits via Symmetric Operation,* Physical Review Letters **116**, 110402 (2016).

[25] J. M. Taylor, J. R. Petta, A. C. Johnson, A. Yacoby, C. M. Marcus, and M. D. Lukin, *Relaxation, dephasing, and quantum control of electron spins in double quantum dots,* Physical Review B **76**, 035315 (2007).

[26] D. Loss and D. P. Divincenzo, *Quantum computation with quantum dots,* Physical Review A **57**, 120 (1998).

[27] T. Meunier, V. E. Calado, and L. M. K. Vandersypen, *Efficient controlled-phase gate for single-spin qubits in quantum dots,* Physical Review B **83**, 121403 (2011).

[28] P. W. Anderson, *The Resonating Valence Bond State in La_2CuO_4 and Superconductivity,* Science **235**, 1196 (1987).

[29] S. Sachdev, *Quantum magnetism and criticality,* Nature Physics **4**, 173 (2008).

[30] L. Balents, *Spin liquids in frustrated magnets,* Nature **464**, 199 (2010).

[31] K. C. Nowack, M. Shafiei, M. Laforest, G. E. D. K. Prawiroatmodjo, L. R. Schreiber, C. Reichl, W. Wegscheider, and L. M. K. Vandersypen, *Single-Shot Correlations and Two-Qubit Gate of Solid-State Spins,* Science **333**, 1269 (2011).

3

DEVICE AND EXPERIMENTAL SETUP

The first part of this chapter describes the device, and the second part the experimental setup. The section on the device first discusses the design and fabrication, then the testing and handling, and ends with characterization of the electrostatic disorder in the device. The section about the experimental setup describes the dilution refrigerator, its electrical wiring, the printed circuit board, radio-frequency reflectometry, the electronics at room temperature, and the software stack.

3.1. DEVICE FOR GATE-DEFINED QUANTUM DOTS

3.1.1. DESIGN AND FABRICATION

The device in Fig. 3.1, which is fabricated on a GaAs material stack, has a gate pattern for a linear array of eight dots. The design is strongly based on that of earlier devices, such as that for a triple dot (see Chapter 4). The width of all gates is 30 nm, the thickness of the gates is 25 nm, and the distance between dots is 160 nm, thus the gate pitch is 80 nm. The distance between the plungers and the top gate is 175 nm and the barriers reach 25 nm closer to the top gate. The device is equipped with two sensing dots, which are positioned slightly inwards to improve the sensing of the middle pair of dots, and each is opposite to one of the eight dots to prevent symmetry effects from lowering the sensitivity for inter-dot transitions.

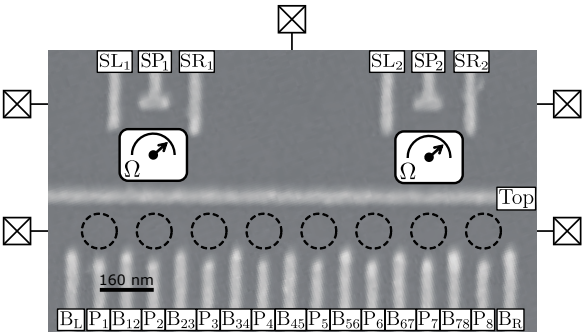

Figure 3.1: Scanning electron microscopy (SEM) image of the fine gate structure of a device for eight dots (indicated with black dashed circles) and two sensing dots (indicated as resistance meters by boxes labelled with Ω). Squares with crosses indicate ohmic contacts, which connect the electron gas to the outside world.

The devices were fabricated at the Van Leeuwenhoek Laboratory clean room at Delft University of Technology[1]. The device fabrication consists of a series of steps of which some important ones are described here (for more information see [1]). After several preparation steps [cleaning the wafer, placing alignment markers, etching a mesa] comes the placement of ohmic contacts, which are made of metal that is diffused into the material stack by annealing the device, such that the metal reaches the GaAs/AlGaAs interface and contacts the 2DEG. Next, are the fine gates, for which first a resist is spin-coated onto the device, then the gate pattern is lithographically written into the resist using an electron beam, after which the gate metal (5 nm titanium and 20 nm gold) is evaporated onto the exposed resist, and finally all unwanted metal is removed with lift-off. The last fabrication step follows a similar process flow as for the fine gates, and is the placement of bond-pads and coarse gates. The latter form the connections between the fine gates and the bond-pads, and the bond-pads [see Fig. 3.8(b)] are to connect to the outside world such that voltages can be applied to the gates.

In the later stage of this PhD, germanium devices[2] were tested. These devices had a

[1] The triple dot device, used for the experiment in Chapter 4, was fabricated by F. R. Braakman and the eight dot device, used for the results in the other chapters, was fabricated by U. Mukhopadhyay.

[2] These devices were fabricated by Will Lawrie and Chien-An Wang.

three-layer gate pattern, which was designed to define a ladder, formed with a four-by-two quantum dot array, and four sensing dots, which were each positioned at the corners of the ladder and also functioned as reservoirs. The devices had forty-eight gates and eight ohmic contacts. Whereas the initial devices had several issues, experiments with 4x2 Ge ladder devices are now underway.

3.1.2. TESTING AND HANDLING

The success of the fabrication can be assessed with various techniques. An optical microscope is commonly used for a coarse-grained check, such as shown in Fig. 3.8(b), but does not offer sufficient resolution to assess the most delicate structures. Scanning electron microscopy (SEM) offers high resolution, but the high-energy electrons used for the imaging can damage the device, thus it is common to inspect only one or sometimes a few devices of a fabrication batch, and to put aside the inspected devices. Alternatively, an atomic force microscope can be used to inspect the gate pattern of the device [see Fig. 3.2(a)] without damaging it. In this way, deviations such as interruptions in a gate or residual metal can be detected.

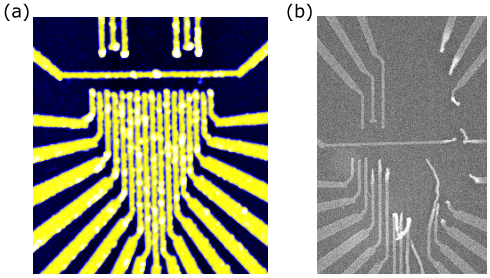

Figure 3.2: (a) Atomic force micrograph, which shows the height profile on the surface of the device. (b) SEM image of a device with the same gate design as in Fig. 3.1, but the metal of the fine gate structure looks as if it is blown up due to electrostatic discharge.

An important tool for electrical testing of the device at cryogenic temperatures is the so-called dip-stick, which is used to quickly cooldown the devices in a dewar with liquid helium. Typical testing with the dip-stick, besides checking for shorts, consists of the characterization of transport through the ohmic contacts, and pinch-off traces for the gates (see Fig. 3.3 and 3.4). For devices in other materials, such as those based on silicon and germanium, it is also common to characterize the voltage at which accumulation occurs, screen for effects such as gate leakage through the dielectric, and characterize potentially present drift and hysteresis. The dip-stick is also well-suited to test electrical components for proper operation at cryogenic temperatures, such as the printed circuit board and the home-built inductors, which are discussed in Section 3.2.3.

Electrostatic discharge (ESD) may cause serious damage to devices, such as visible in Fig. 3.2(b). To prevent ESD, various precautions are taken for safely handling the devices and making connections to it [admittedly, we did not systematically investigate whether each and everyone of these precautions makes a difference]:

- The person handling the device is grounded via a (wrist) grounding strap.

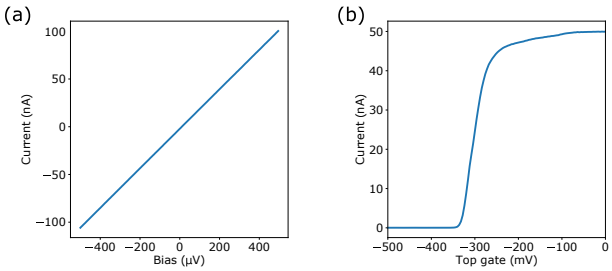

Figure 3.3: Typical measurements for electrical device testing at 4 K. (a) The current between the ohmic contacts in the bottom left and right of the device as a function of bias voltage, which indicates a resistance of 4.9 kΩ. The top gate is already set to −375 mV, which induces pinch-off between the top-half and bottom-half of the device. (b) The pinch-off trace for the top gate with the current as a function of gate voltage and with the bias between an ohmic in the top half and one in the bottom half set to 500 μV.

- The device and operator are grounded during wirebonding (see Section 3.2.3).
- An ionizer[3] is used during wirebonding.
- The wirebonded device, when not mounted in a setup, is connected to a shorting piece, which connects all lines together and to a ground plane.
- Devices are kept in ESD safe gel-packs.
- Grounding mats are on tables where devices are handled.
- ESD safe office chairs are used in the lab.
- Do not wear clothing with wool or fleece.
- Take into account that dry weather may result in an increased ESD risk.

3.1.3. CHARACTERIZATION OF ELECTROSTATIC DISORDER

The electrostatic disorder in the solid-state of quantum dot devices hinders the desired scaling up for quantum computation and simulation. A major source of disorder in the GaAs devices, such as those used for this thesis, are the charged impurities in the layer of dopants. For undoped systems, other sources are dominant, such as background impurities in the bulk, or charges at the surface and dielectric interface [2], where the latter two become more relevant for shallower two-dimensional electron gases [3].

For gate-defined quantum dots, the initially disordered landscape can often be sufficiently reshaped by tuning of each gate voltage, such that the target configuration of quantum dots, electrons and tunnel couplings can be achieved. Occasionally, a device, nominally identical to that in Fig. 3.1, suffered from disorder to such an extent, that tuning of gate voltages did not seem to suffice for the formation of a multi-dot array. Such device would subsequently be abandoned, thus disorder also impacts the yield in terms of successful device fabrication and growth. The required time for device tuning is

[3] Model 5802i from Simco-ion.

greatly reduced by the implementation and automation (see Chapter 4) of tuning strategies to achieve the target configuration [4]. However, to increase the number of qubits and optimize connectivity, the number of gates will increase and the gate patterns will evolve. Due to disorder, this scaling up will have to go hand-in-hand with the further development of tuning strategies, which restricts the pace of progress. Lower disorder will enable higher yield, and reduce the extend of required tuning, but is also considered to be a prerequisite for device operation with shared control [5] to achieve a lower average number of control lines per qubit.

Disorder is often expressed in terms of mobility or percolation density, which are useful parameters to assess the material quality [6], but offer limited insight into the disorder on the scale where quantum dots are formed. A set of data on disorder for a device with separately formed single dots, has been reported [7]. However, for the regime of tunnel-coupled multi-dot arrays in the single-electron regime, where spin-qubits are operated, the characterization of disorder has been hindered by the scarcity of success in tuning up such multi-dot arrays. Here, two sets of data are presented, of which one was obtained before any tuning, and one after fully tuning a homogeneously coupled multi-dot array in the single-electron regime. Both datasets were acquired at ~40 mK, and on the same device, which is nominally identical to that shown in Fig. 3.1.

The first set of data is obtained from the pinch-off curves for the gates of the (sensing) dots, which are shown in Fig. 3.4. These pinch-off curves are analysed with a method adopted from analysis of transistors [8]. A key characteristic for transistors is their threshold voltage, which is the gate voltage for which the transistor is at the verge of switching between being on and off. The threshold voltage is determined via extrapolation of a linear trend. This trend is taken at the point which is the local maximum in the first-order derivative for the transistor current as function of gate voltage. Analogously, threshold voltages were obtained from the pinch-off curves [see Fig. 3.5(a)]. For the pinch-off curves, the point for the linear trend was selected as the local maximum, which occurs at the lowest gate voltage. The pinch-off data was smoothed with a Gaussian filter to suppress analysis errors due to noise.

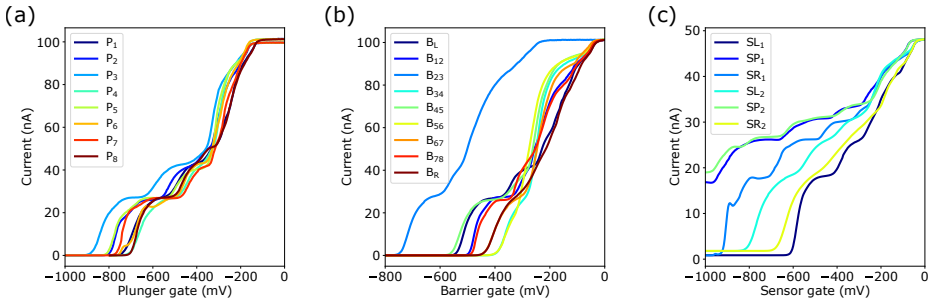

Figure 3.4: Pinch-off curves for the gates of the (sensing) dots, with in (a) the plunger gates and in (b) the barrier gates for the dots, and in (c) all gates for the sensing dots. The top gate was at −375 mV. The device was bias-cooled to reduce switching noise [9], with the plungers at 100 mV and all other gates at 200 mV.

The second set of data is taken from a homogeneously tuned sextuple dot in the middle of the device. The sextuple dot is tuned to have one electron on each dot, and such

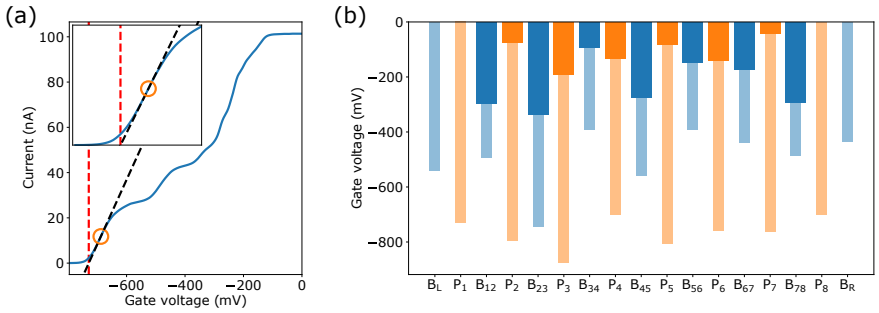

Figure 3.5: (a) Extraction of the threshold voltage from a pinch-off curve (here for gate P_1). The open circle indicates the point with the selected local maximum for the first-order derivative, the black dashed line shows the extrapolation of the linear trend, and the vertical dashed line shows the point where this linear extrapolation is at the zero-current level, which corresponds to the threshold voltage. The inset shows a zoom-in of the regime for the threshold voltage extraction. (b) Overview of gate voltages with thin, transparent bars the threshold voltages extracted from the pinch-off curves, and thick bars the voltages from a homogeneously tuned sextuple dot.

that all tunnel couplings are ~20 μeV. The voltages, at the center of the (111111) charge-region, which is where for each of the dots, the distance in gate-voltage space is equal to the previous and the next dot-reservoir transition, form the second data set.

Table 3.1 shows the means and standard deviations for the plunger and barrier gate voltages as obtained from the threshold analysis of the pinch-off curves, the homogeneously tuned multi-dot, and for the differences between the gate voltages in the two regimes. This data reveals two important insights about the extent of disorder in the homogeneously tuned multi-dot regime. First, for the plungers, the standard deviations, ≥ 50 mV, are larger than a typical voltage corresponding to the charging energy (~ 30 mV). This implies that a multi-dot array would have inhomogeneous filling, if such disorder would not be compensated for. Second, intuition for the disorder in tunnel couplings corresponding to the variation in barrier voltages, can be obtained from

$$\frac{t_{high}}{t_{low}} = \exp\left(\Gamma \delta B\right), \tag{3.1}$$

which expresses the ratio between the highest and lowest tunnel coupling values as a function of voltage variation, δB, and the tunnel coupling lever arm, Γ. If δB is set to the standard deviation, > 80 mV, and the tunnel coupling lever arm is set as $\Gamma = 0.04\,\mathrm{mV}^{-1}$, which is the lowest value reported in Chapter 5, then the tunnel coupling ratio is > 24. Thus the standard deviation in barrier voltages corresponds to a disorder in tunnel coupling values of more than an order of magnitude.

Interestingly, the standard deviations for the differences before any tuning and after fully tuning, as compared to either of the two tuning regimes, are similar for the plungers and about 30% smaller for the barriers. This indicates that there are weak correlations, slightly stronger for the barriers than the plungers, between the two regimes. This interpretation is based on that the variance for the differences between two uncorrelated variables is the sum of their variances.

In the above analysis the effect of cross-capacitances has not been taken into ac-

Gates (regime)	Mean (mV)	Standard deviation (mV)
Plungers (pinch-off)	-765.6	54.8
Plungers (homo. tuning)	-110.4	50.0
Plungers (difference)	672.1	59.3
Barriers (pinch-off)	-496.9	103.4
Barriers (homo. tuning)	-231.2	84.8
Barriers (difference)	268.5	66.5

Table 3.1: Statistics for the voltages for the plungers and the barriers obtained from the pinch-off curves and from the gate voltages for the homogeneously tuned sextuple dot as shown in Fig. 3.5. The differences correspond to the differences in voltages between the two regimes, for which only the gates used for the sextuple dot are included.

count, but it is expected to influence the results in the following ways: (1) For the data from the multi-dot array, gates closer to the end of the array are expected to require more negative voltages, because those gates have fewer other gates nearby, which would otherwise, through their negative voltages, contribute to achieve the required local electric fields. (2) Again for the multi-dot array, the gates for the sensors also had negative voltages applied, thus the nearby gates required relatively less negative voltage. (3) The measurements for both regimes were taken on a device that was bias cooled, which induces negative charges in the doping layer, thus less negative gate voltages are required. Due to cross-capacitance, the effect of bias cooling is expected to be weaker for gates closer to the outside of the array, following a similar reasoning as in (1).

In conclusion, from the data and analysis presented here, when the disorder would not be compensated for with gate voltages, then it would result in inhomogeneous filling and tunnel coupling variations of more than an order of magnitude. These variations are based on a single standard deviation of the voltages, but for multi-dot devices with many gates two standard deviations would probably be a more relevant parameter for homogeneity in gate voltages. Two standard deviations correspond to variations of more than three times the charging energy, and a disorder in tunnel couplings of almost three orders of magnitude. Such disorder is probably better understood as that the device configuration would be outside of the voltage space where the multi-dot array is formed.

Unfortunately, there are only weak correlations between the threshold voltages from the pinch-off measurements and the voltages for the homogeneously tuned multi-dot. Strong correlations would be helpful for the device tuning, because the initial voltages could be based on the pinch-off values such that part of the disorder would already be compensated for. Similarly, with lower disorder, an efficient tuning strategy could consist of setting initial homogeneous voltages for the plungers and similarly for the barriers, such that a multi-dot array is formed, albeit disordered. Then, the next step could be to fine-tune the voltages to correct for the disorder and achieve a homogeneously tuned multi-dot array.

Characterization of the electrostatic disorder such as presented here, could provide relevant insights and feedback to facilitate further improvements of the material growth and device fabrication. Furthermore, the disorder in other parameters, such as the cross-capacitance matrix elements, charging energies (see Chapter 8), and orbital energies,

could be analysed for additional insights. For the level of disorder shown here, gate patterns which enable individual control over tunnel couplings and chemical potentials are required to mitigate the initial disorder and form a multi-dot array. Moreover, further development of tuning strategies and automation therein will be important for scaling up of quantum dot arrays in an environment with such electrostatic disorder.

3.2. EXPERIMENTAL SETUP

3.2.1. DILUTION REFRIGERATOR

The quantum dot devices are cooled to a few tens of millikelvin in a 3He/4He dilution refrigerator. Most of the research for this PhD has been performed with a so-called wet refrigerator (Oxford Kelvinox 400HA), which is shown in Fig. 3.6(a). As alternative to the wet refrigerator, a dry refrigerator (Oxford Triton 400) with a bottom loader was used. The dry refrigerator facilitated faster device testing, and offered more space, which made it easier to equip it with a higher number of wires for electrical measurements of devices with a higher number of gates and ohmics.

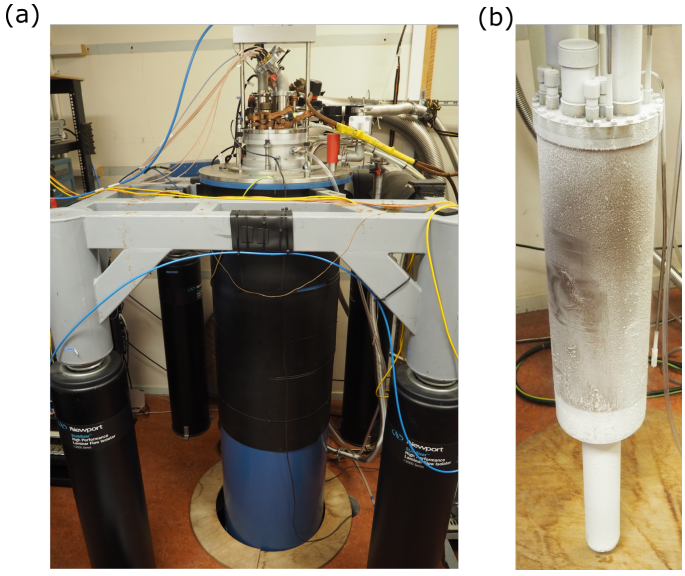

Figure 3.6: (a) Wet dilution refrigerator (Kelvinox 400HA), which hangs in a stabilizer frame and sticks through a hole in the floor, through which the refrigerator dewar can be lowered. On the top of the refrigerator are electric wires and gas pipes connected. (b) The vacuum can covered in frost, just after it has been taken out of the bath of liquid helium in the refrigerator dewar.

The cooling process of the dilution refrigerator can be divided into multiple cooling stages [10]. For the wet refrigerator, five main steps can be distinguished, which correspond to the steel flange and copper plates from top to bottom on the insert of the refrigerator, which is shown in Fig. 3.7(a). The first cooling step is submerging the vacuum can [Fig. 3.6(b)] and inserting it in a bath of liquid helium (4.2 K). The second step is provided by the 1K pot (1.7 K), which is continuously pumped on and sucks in liquid he-

lium from the bath. The third step cools (~ 0.7 K) by pumping on liquid 3He in the still. The fourth step is the cold stage (~100 mK) where heat is exchanged between incoming/warm and outgoing/cold 3He. The final step is the mixing chamber stage (~45 mK with cryogenic amplifier on the bottom of the steel flange energized), where cooling occurs via the "evaporation" of 3He from a concentrated phase to a dilute phase, from which 3He is extracted by the pumping on the still.

The wet refrigerator is equipped with a solenoid superconducting magnet, which is specified for normal operation up to 12 T. The magnet is not visible in Fig. 3.6, because it is inside the refrigerator dewar.

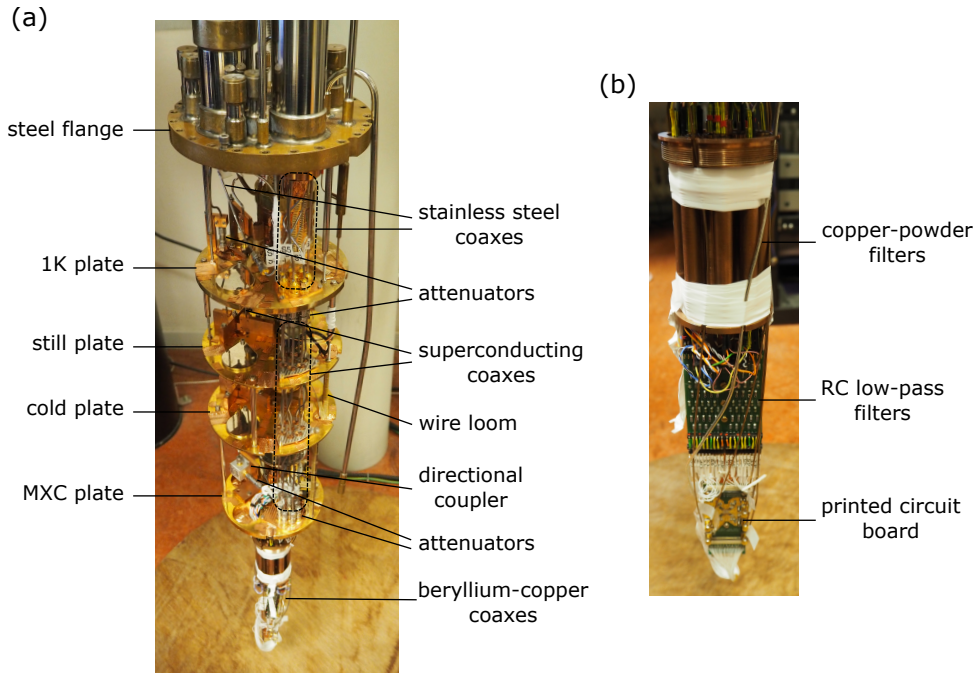

Figure 3.7: (a) The insert of the refrigerator, which is revealed after removing the vacuum can and a copper radiation shield below the mixing chamber plate. MXC stands for mixing chamber. (b) Bottom part of the insert, commonly referred to as the cold finger, which is below the mixing chamber plate, and is mounted with, the copper powder filters, the RC low-pass filters, and the printed circuit board with the device.

3.2.2. ELECTRICAL WIRING OF THE REFRIGERATOR

The refrigerator is equipped with two wire looms to apply direct current (DC) voltages on the gates and measure electrical transport. The material of the wires is copper or Constantan, where the first is used for ohmic contacts to achieve low Johnson noise because of its low resistance, and the latter is used for gates because of its low thermal conductivity. From below the 1K plate, one loom has wires made out of superconducting material to further reduce thermal conductivity, and the looms are thermally anchored by tightly wrapping them around copper posts on the plates. The wires are arranged in twisted

pairs to suppress picking up noise, and are low-pass filtered below the mixing chamber plate with copper-powder filters ($\lesssim$ 1 GHz), and RC-filters (cut-off of 1.3 MHz for gates and 20 Hz for ohmic contacts) [see Fig. 3.7(b)].

For the transmission of high-frequency signals (microwaves and voltage pulses) to the gates, the refrigerator is mounted with eight coaxial cables[4] (with component specifications up to ~20 GHz). Semi-rigid coaxial cables out of stainless steel[5] are used between room temperature and the 1K plate, where for the connection to the vacuum feedthroughs on the inside of the refrigerator, hand-formable coaxes[6] are used to facilitate (dis)assembling. Between the 1K plate and the mixing chamber plate, semi-rigid coaxes of niobium-titanium[7] are used, which is superconducting during refrigerator operation, and has low thermal conductivity. From the mixing chamber plate downwards, semi-rigid coaxes made out of beryllium-copper[8] or hand-formables[9] are used, which both have higher thermal conductivity, thus mediate cooling from the mixing chamber. The coaxes are attenuated with 20 dB[10] on the 1K plate and 6 dB[11] on the mixing chamber plate. These attenuation values are chosen as a trade-off between suppressing thermal noise, yet allowing sufficient signal transmission, while in addition the attenuators thermally anchor the coaxes to the respective stages of the refrigerator. On the other plates, coaxes are clamped for thermal anchoring, and just below the steel flange they are clamped in a copper block, which is connected to the flange with a copper braid.

Two additional coaxes are used for measurements based on radio-frequent (RF) reflectometry [11, 12] (see Section 3.2.4), for which a diagram of the circuit is shown in Fig. 3.9(a). One coax is used to transmit the ingoing RF signal, and the other for the reflected signal. The coax for the ingoing signal is attenuated with 20 dB[12] at both the 1K plate and the cold plate. The coaxes are combined at the mixing chamber plate via a directional coupler[13], which is mounted with the input port going to the device, such that the ingoing and reflected signal from there on run over the same coax. The returning signal is sent through a cryogenic amplifier[14] mounted on the bottom of the steel flange. On its input port is a DC block[15], which disconnects the inner conductor such that thermal contact is reduced. The coax for the ingoing signal is made from stainless steel[16] until the cryogenic amplifier, from there to the directional coupler it is made of a superconducting material[17], and below the directional coupler it is made of beryllium-copper[18].

[4] The coaxial wiring was designed together with Olaf Benningshof, mechanical parts were made by Nico Alberts, and connectors were soldered onto the coaxes by Erik van der Wiel, who works for DEMO at TU Delft.
[5] SC-219/50-SSS-SS and SC-119/50-SSS-SS from Coax Co.
[6] 415-0081 from Johnson - Cinch connectivity.
[7] SC-219/50-NbTi-NbTi from Coax Co.
[8] SC-119/50-B-B from Coax Co.
[9] 415-0082 from Johnson - Cinch connectivity.
[10] 2082-6418-20-cryo from XMA corp.
[11] 2082-6418-06-cryo from XMA corp.
[12] See footnote 10.
[13] ZEDC-15-2B from Mini-Circuits.
[14] CITLF2 from the Caltech Microwave Research group.
[15] PE8210 from Pasternack.
[16] SC-219/50-SSS-SS from Coax Co.
[17] SC-219/50-NbTi-NbTi from Coax Co.
[18] SC-119/50-B-B from Coax Co.

The coax with the reflected signal, for the section between the directional coupler and the 1K plate, is of the same type as superconducting coax as for the ingoing signal, and from there on upwards the same type of stainless steel coax is used.

3.2.3. PRINTED CIRCUIT BOARD

The DC lines and coaxes in the refrigerator are connected to a printed circuit board (PCB) [Fig. 3.8(a)], which serves as an interconnect to the device. This PCB has ten SMP connectors, of which one is designed for the RF reflectometry (see Section 3.2.4), and the others for high-frequency voltage pulses and microwaves to the gates. The DC and high-frequency signals are combined on the PCB via bias-tees. The bias-tees for the gates have a 10 MΩ resistor on the DC side, and two parallel capacitors of 56 pF and 47 nF on the high-frequency side, which corresponds to an RC-time constant of 470 ms, which is chosen as trade-off between quick settling of the DC voltages and performing long pulse sequences. The other bias-tees, used for the ohmic contacts connected to an inductor, have a 5 kΩ resistor and a 100 pF capacitor, giving an RC-time constant. The PCB has 48 DC lines that are routed to two flexible-flat-cable connectors, which are wired in parallel, such that via one side the PCB can be grounded while (dis)connecting the other side. All the DC lines are additionally high-frequency filtered on the PCB with a 100 pF capacitor to ground.

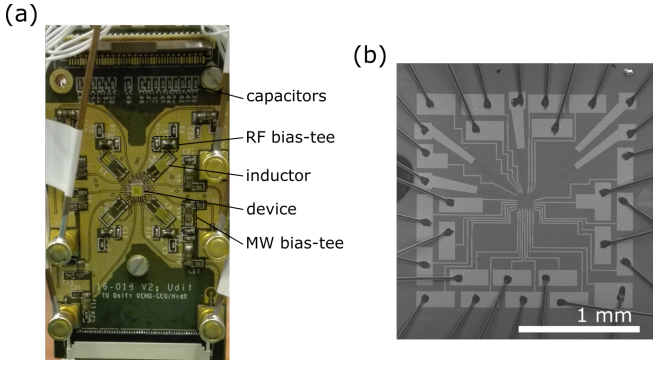

Figure 3.8: (a) The printed circuit board mounted and connected in the refrigerator, with in the centre the device. The radio-frequency (RF) bias-tees enable the combination of RF reflectometry with DC transport via the ohmic contacts, while the microwave (MW) bias-tees enable the combination of high-frequency signals and direct current voltages to the gates. (b) Optical microscope image of a device with wirebonds (somewhat smashed here) connected to the bond-pads for the gates and ohmics.

The device is glued onto the PCB with PMMA, and the PCB and the device are electrically connected with aluminium wirebonds [see Fig. 3.8(b)], which are made with a semi-automated Westbond bonder or fully-automated Bondtec bonder. For the RF read-out, two home-built inductors[19] of 1.3 µH and 3.9 µH, are glued onto the PCB, and wire-bonded to ohmic contacts for the sensing dots.

[19] Spiral inductors of niobium-titanium-nitride on quartz. [13]

3.2.4. RADIO-FREQUENT READOUT

The charge sensing relies on the dependence of the sensing dot resistance on the charge distribution in its environment [see Section 2.3]. The resistance of the charge sensor can be measured with DC transport, but better signal-to-noise ratios and a higher bandwidth can be achieved with RF readout [11, 14, 15]. For charge-sensing based on DC transport, the detection bandwidth is limited by the capacitance of the refrigerator wire to the room temperature amplifier and its input resistance. With RF readout, in addition to allowing a higher detection bandwidth, also the noise is reduced, because the noise floor is lower for the amplifier working at the carrier frequency, as compared to that of amplifiers working at baseband frequencies.

The reflection coefficient for an incident electromagnetic wave is

$$\Gamma = \frac{V^-}{V^+} = \frac{Z_L - Z_0}{Z_L + Z_0}, \tag{3.2}$$

with V^+ the incident signal, V^- the reflected signal, Z_L the impedance of the load and Z_0 the impedance of the transmission line with the incident signal. The charge sensor is most sensitive where $\frac{dR}{dq}$ is maximal. For a sensing dot this is typically the steepest point on the flank of a Coulomb peak measured in transport as function of sensing dot plunger voltage. Note that there can be deviations, because the resistance change due to the plunger voltage may not reliably represent the resistance change due to a change in charge configuration on the sensed dot(s). At the steepest point on its flank, the sensing dot impedance is typically about 150 kΩ. However, the transmission line components all have 50 Ω impedance, thus $Z_L >> Z_0$, and almost all signal would be reflected, resulting in a poor signal-to-noise.

Therefore RF reflectometry is implemented by transforming the load impedance of the charge sensor with an inductor and a capacitor to form a matching circuit. At its resonance frequency, $\omega = \frac{1}{\sqrt{LC}}$, this circuit has an equivalent impedance of $Z_{eq} = \frac{L}{RC}$. The capacitance is the parasitic capacitance, C_p, which is around 0.5 pF to 1 pF and consists of the capacitances of the bondwires, device and the line on the PCB, which connect the inductor and the device. With an inductor of around one to a few μH the equivalent impedance is brought close or even matched to the impedance of the transmission line, which is where the reflected signal is maximally sensitive to the resistance of the charge sensor (maximal $\frac{dV^-}{dR}$). The maximal sensitivity with respect to the sensed dot(s), $\frac{dV^-}{dq}$, is typically at a slightly different position on the Coulomb peak, because the matching is not perfect as to where $\frac{dR}{dq}$ is maximal. The carrier frequencies for the RF readout of the eight dot device were 97.2 MHz and 165.9 MHz, which correspond to the resonance dips in the amplitude of the reflected signal as shown in Fig. 3.9(b).

3.2.5. ROOM-TEMPERATURE ELECTRONICS

At room temperature, various home-built DC electronics are used, which come as separate modules that are put into a battery powered rack of either IVVI-type[20] or the newer SPI-type[21]. These modules include digital-to-analog converters, which are operated in

[20] http://qtwork.tudelft.nl/~schouten/ivvi/index-ivvi.htm
[21] http://qtwork.tudelft.nl/~mtiggelman/spi-rack.html.

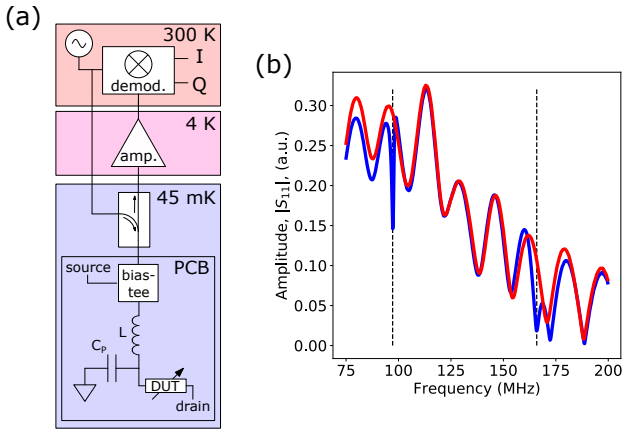

Figure 3.9: (a) Diagram of the radiofrequency reflectometry circuit for one carrier frequency. The readout circuit is frequency multiplexed for the experiments with two charge sensors. The multiplexing requires adding a signal source, doubling the demodulation electronics, and splitting the returning signal at room temperature and the ingoing signal on the PCB to matching circuits with different inductors. The bias-tee consists of a 5 kΩ resistance on the DC side and a 100 pF capacitor on the RF side. (b) The amplitude of the reflected signal shows two resonance dips, as indicated by the dashed lines, when the sensing dots are tuned up (blue), while those resonance dips are absent when the gates for the sensing dots are not biased (red).

a range from +2 V to -2 V for applying voltages on the gates and a source-drain bias. In addition, modules with current-to-voltage converters, which are connected to Keithley multimeters (2000 or 2700), are used to measure transport through the device.

High-frequency electronics are used to send voltage pulses and microwaves to the gates. The voltage pulses are generated with an arbitrary waveform generator (AWG). For the results in Chapters 4-6 a Tektronix AWG5014 was used, while for the other chapters the Keysight PXI system with AWG modules of type M3202A was used. The output of the AWGs are wired with low-pass filters[22] and common-mode chokes based on several loops of the room temperature coax through a ferrite ring. Both types of AWGs can go up to ~1 GHz sampling rate and have rise times slightly above 1 ns. As microwave source a Rohde Schwarz SMR40 is used, which can generate signals up to 40 GHz.

The RF signals (~100 MHz) for the reflectometry are generated with two Rohde Schwarz SMB100A. The outputs of the signal generators are both attenuated by 30 dB, and the signal is sent through a DC block, both at room temperature. The reflected RF signal is demodulated at room temperature as well, using a home-built demodulation box [13]. The input port of the demodulation box also has a DC block on it. The demodulated RF signals are acquired with a digitizer card. For Chapters 4-6 a Spectrum M4i was used, while for the other chapters a digitizer module M3102A in the Keysight system was used.

3.2.6. SOFTWARE

The code to perform the experiments is written in the programming language Python. The data storage is based on the Qcodes data-acquisition framework[23], just as the instru-

[22] SBLP-300+ from Mini-Circuits.
[23] https://github.com/QCoDeS/Qcodes

ment drivers for which several contributions were added to the framework. Part of the measurement and fitting routines are from, and also contributed to, the package QTT[24], of which the development is led by Pieter Eendebak. The Keysight system was controlled with a pulse library first developed by Stephan Philips and later expanded by Sander de Snoo[25]. Numerical simulations for this PhD are in general based on the package QuTiP[26] with extensions written by Steven van Gemert, while for Chapter 7 the time evolution simulations were based on the package DM solver, written by Stephan Philips[27].

[24] https://github.com/QuTech-Delft/qtt
[25] https://github.com/stephanlphilips/pulse_lib
[26] https://qutip.org
[27] https://github.com/stephanlphilips/DM_solver

REFERENCES

[1] U. Mukhopadhyay, *Quantum simulation using arrays of gate-defined quantum dots,* PhD thesis, Delft University of Technology (2019).

[2] P. Barthelemy and L. M. K. Vandersypen, *Quantum Dot Systems: A versatile platform for quantum simulations,* Annalen der Physik **525**, 808 (2013).

[3] F. A. Zwanenburg, A. S. Dzurak, A. Morello, M. Y. Simmons, L. C. L. Hollenberg, G. Klimeck, S. Rogge, S. N. Coppersmith, and M. A. Eriksson, *Silicon quantum electronics,* Reviews of Modern Physics **85**, 961 (2013).

[4] C. Volk, A. M. J. Zwerver, U. Mukhopadhyay, P. T. Eendebak, C. J. van Diepen, J. P. Dehollain, T. Hensgens, T. Fujita, C. Reichl, W. Wegscheider, and L. M. K. Vandersypen, *Loading a quantum-dot based "Qubyte" register,* npj Quantum Information **5**, 29 (2019).

[5] R. Li, L. Petit, D. P. Franke, J. P. Dehollain, J. Helsen, M. Steudtner, N. K. Thomas, Z. R. Yoscovits, K. J. Singh, S. Wehner, L. M. K. Vandersypen, J. S. Clarke, and M. Veldhorst, *A crossbar network for silicon quantum dot qubits,* Science Advances **4**, eaar3960 (2018).

[6] G. Scappucci, *Semiconductor materials stacks for quantum dot spin qubits,* arXiv:2102.10897 (2021).

[7] D. M. Zajac, T. M. Hazard, X. Mi, E. Nielsen, and J. R. Petta, *Scalable Gate Architecture for a One-Dimensional Array of Semiconductor Spin Qubits,* Physical Review Applied **6**, 054013 (2016).

[8] A. Ortiz-Conde, F. García-Sánchez, J. Liou, A. Cerdeira, M. Estrada, and Y. Yue, *A review of recent MOSFET threshold voltage extraction methods,* Microelectronics Reliability **42**, 583 (2002).

[9] M. Pioro-Ladrière, J. H. Davies, A. R. Long, A. S. Sachrajda, L. Gaudreau, P. Zawadzki, J. Lapointe, J. Gupta, Z. Wasilewski, and S. A. Studenikin, *Origin of switching noise in GaAs/Al_xGa_{1-x}As lateral gated devices,* Physical Review B **72**, 115331 (2005).

[10] G. Batey and G. Teleberg, *Principles of dilution refrigeration - a brief technoloy guide (Oxford Instruments),* (2015).

[11] D. J. Reilly, C. M. Marcus, M. P. Hanson, and A. C. Gossard, *Fast single-charge sensing with a rf quantum point contact,* Applied Physics Letters **91**, 162101 (2007).

[12] C. Barthel, M. Kjærgaard, J. Medford, M. Stopa, C. M. Marcus, M. P. Hanson, and A. C. Gossard, *Fast sensing of double-dot charge arrangement and spin state with a radio-frequency sensor quantum dot,* Physical Review B **81**, 161308(R) (2010).

[13] T. A. Baart, *CCD operating and long-range coupling of spins in quantum dot arrays,* PhD thesis, Delft University of Technology (2016).

[14] R. J. Schoelkopf, P. Wahlgren, A. A. Kozhevnikov, P. Delsing, and D. E. Prober, *The radio-frequency single-electron transistor (RF-SET): A fast and ultrasensitive electrometer*, Science **280**, 1238 (1998).

[15] L. Roschier, P. Hakonen, K. Bladh, P. Delsing, K. W. Lehnert, L. Spietz, and R. J. Schoelkopf, *Noise performance of the radio-frequency single-electron transistor*, Journal of Applied Physics **95**, 1274 (2004).

4

AUTOMATED TUNING OF INTER-DOT TUNNEL COUPLING IN DOUBLE QUANTUM DOTS

Semiconductor quantum dot arrays defined electrostatically in a 2D electron gas provide a scalable platform for quantum information processing and quantum simulations. For the operation of quantum dot arrays, appropriate voltages need to be applied to the gate electrodes that define the quantum dot potential landscape. Tuning the gate voltages has proven to be a time-consuming task, because of initial electrostatic disorder and capacitive cross-talk effects. Here, we report on the automated tuning of the inter-dot tunnel coupling in gate-defined semiconductor double quantum dots. The automation of the tuning of the inter-dot tunnel coupling is the next step forward in scalable and efficient control of larger quantum dot arrays. This work greatly reduces the effort of tuning semiconductor quantum dots for quantum information processing and quantum simulation.

This chapter has been published as C. J. van Diepen, P. T. Eendebak, B. T. Buijtendorp, U. Mukhopadhyay, T. Fujita, C. Reichl, W. Wegscheider, and L. M. K. Vandersypen, Applied Physics Letters **113**, 033101 (2018).

4.1. INTRODUCTION

Electrostatically defined semiconductor quantum dots are actively studied as a platform for quantum computation [1–3] and quantum simulation [4, 5]. Control over the inter-dot tunnel coupling is a key ingredient for both applications. Via control over the tunnel coupling we have control over the exchange coupling, which is vital for realizing the various proposals for spin-based qubits [1, 6, 7]. Based on the natural description of semiconductor quantum dots in terms of the Fermi-Hubbard model, control over the tunnel coupling allows for analog simulations to explore the physics of interacting electrons on a lattice [8, 9].

An obstacle for the efficient use of semiconductor quantum dots are the background charged impurities and variations in the gate patterns, which lead to a disordered potential landscape. Initial disorder can be compensated for by applying individually adjusted gate voltages. Additionally, even though gates are designed to specifically control a chemical potential or a tunnel coupling, in practice capacitive coupling induces cross-talk from all gates to dot chemical potentials and tunnel couplings. The disorder and cross-talk increase the complexity of tuning up ever larger dot arrays. The effort of tuning can be reduced by automation based on image processing. Earlier work on automation of tuning for semiconductor quantum dots has shown that it is possible to automatically form double quantum dots with a sensing dot, and to find the single electron regime in the double dot, however without control of the inter-dot tunnel coupling [10]. More recently, such automated tuning routines were used to determine the initialization, read-out and manipulation points for a singlet-triplet qubit [11]. Machine learning was used for the automated tuning between an open channel, a single dot and a double quantum dot regime in a nanowire [12]. Automated control over the inter-dot tunnel coupling is an important next step forward in control for scaling up the number of spin qubits in semiconductor quantum dots.

In this Letter, we present a computer-automated algorithm for the tuning of the inter-dot tunnel coupling in semiconductor quantum dot arrays and demonstrate the algorithm on separate double dots. The algorithm consists of two parts. Part I determines a virtual barrier gate, which corresponds to a linear combination of voltages to apply on multiple gates in order to adjust the tunnel barrier without influencing the chemical potentials in the dots. To determine such a virtual barrier gate we model and fit the capacitive anti-crossings measured in charge stability diagrams. Part II tunes the tunnel coupling using a feed-back loop, which consists of stepping the virtual barrier gate value and measuring the tunnel coupling, until the tunnel coupling converges to a user-defined target value. To measure the tunnel coupling we use two methods. The first method is based on photon-assisted tunneling (PAT) [13], while the second method is based on the broadening of the inter-dot transition line [14]. We describe the algorithm and demonstrate its power by automatically tuning the tunnel coupling to a target value for two double dots. We show results for tuning both to higher and lower tunnel couplings for several different initial values, both for a single electron and for two electrons on the double dot.

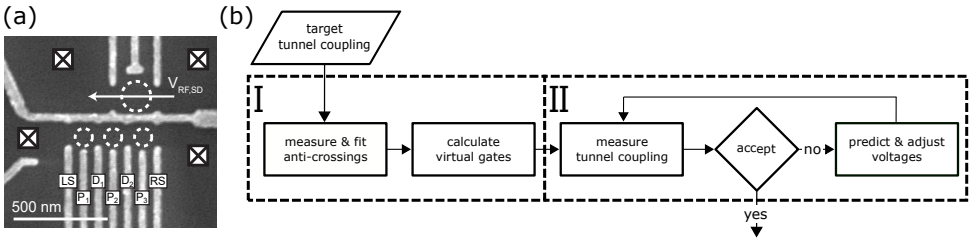

Figure 4.1: (a) A scanning electron microscopy image of a device nominally identical to the one used for the measurements. The three smaller dashed circles indicate the positions of the dots in the array. The larger dashed circle indicates the location of the sensing dot. Squares indicate Fermi reservoirs, which are connected to ohmic contacts. (b) A flowchart of the automated tunnel coupling tuning algorithm. The dashed boxes indicate the two parts of the algorithm.

4

4.2. DEVICE

The platform used for the demonstration of the algorithm is a linear triple quantum dot device [15]. A scanning electron microscopy image of a device similar to the one used in our experiment is shown in Fig. 4.1(a). By applying voltages on gate electrodes on the surface of a GaAs/AlGaAs heterostructure, we shape the potential landscape in the two-dimensional electron gas 85 nm below the surface. Gates LS and RS are designed to control the tunnel couplings to the left and right reservoir, respectively. Additionally, plunger gates, P_i, are designed to control the chemical potential of dot i, and barrier gates, D_i, are designed to control the inter-dot tunnel coupling between dot i and dot $i+1$. The device allows for the formation of three quantum dots in a linear configuration, which are indicated with three white dashed circles in the bottom part of Fig. 4.1(a). In the present work, we focus on two of the three dots at a time. There is one additional dot, indicated with the larger white dashed circle in the upper part, which we refer to as the sensing dot (SD), because it is operated as a charge sensor, utilizing its capacitive coupling to the three other quantum dots. One of the SD contacts is connected via a bias-tee to a resonator circuit, permitting fast read-out of the charge configuration in the bottom dots, by measuring the SD conductance with radio-frequency reflectometry. To optimize the sensitivity of the charge sensor, we operate the SD half-way on the flank of a Coulomb peak. Automation on the tuning of the sensing dot for read-out was already shown in Ref. 10. One of the bottom gates, P_2, is connected to a microwave source, used for PAT measurements.

As starting point for our algorithm, we assume that the device is tuned near an inter-dot charge transition. Such a starting point can be obtained from a computer-automated tuning algorithm [10]. We also require a rough estimate of the electron temperature for the modelling of charge transition line widths. For the PAT measurements, we calibrated the microwave power such that we only observe single-photon lines [13].

4.3. FIRST PART OF THE ALGORITHM

Part I of the algorithm, see Fig. 4.1(b), determines the virtual plunger and barrier gates by measuring the cross-capacitance matrix (see supplementary material 4.8.2), which describes the capacitive couplings from gates to dot chemical potentials. To determine

this matrix we measure charge stability diagrams with charge sensing and fit the avoided crossing with a classical model (see Fig. 4.4). The fitting of the anti-crossings is based on finding the minimum of the sum over all pixels of the difference between the processed data and a two-dimensional classical model of the avoided crossing (see supplementary material III). From the fit of the anti-crossing, we obtain the slopes of all five transition lines: four addition lines, where an electron moves between a reservoir and a dot, and the inter-dot transition line, where a charge moves from one dot to the other. We fit the anti-crossing to charge stability diagrams measured for any combination of P_i, P_{i+1} and D_i over a range of 40 mV around the starting point, to fill in the entries of the cross-capacitance matrix. From the inverse of this matrix we obtain both the virtual barrier, $\widetilde{D}_i$, and the virtual plungers, $\widetilde{P}_i$ and $\widetilde{P}_{i+1}$. The effectiveness of this basis transformation in voltage-space becomes clear from the right angles between addition lines in the charge stability diagram in the 2D-scan of $\widetilde{P}_i$ and $\widetilde{P}_{i+1}$ in Fig. 4.2(a). The anti-crossing fit also provides the voltages at the center position on the inter-dot transition line, indicated with the white dot. The white dotted line indicates the detuning axis, which will be used as a scanning axis in the second half of the algorithm.

4.4. TUNNEL COUPLING MEASUREMENTS

Before describing part II of the algorithm let us first explain the two methods we use to measure the tunnel coupling. The first method is PAT, see Fig. 4.2(b) and (e), which is based on the re-population of states induced by a microwave field. We can observe the re-population using the sensing dot, when the different states correspond to different charge configurations. While varying the frequency of the microwave source, we observe resonance peaks when the frequency is equal to the energy difference between two states. By scanning over the detuning axis and finding the resonance peaks we perform microwave spectroscopy to map out (part) of the energy level diagram, from which we determine the tunnel coupling. We obtain the tunnel coupling by using a fitting procedure that consists of three steps. First we process the data per microwave frequency, mainly subtracting a smoothed background signal taken when the microwave source is off. Second we find the extrema in this processed signal per microwave frequency and last we fit the curve(s) that connects the extrema using a model of the energy level diagram. For the PAT measurements with a single electron as shown in Fig. 4.2(b), we model the system in terms of two levels with energies as shown in Fig. 4.2(c). The resonance curve is then described by $hf = \sqrt{\varepsilon^2 + 4t^2}$, where h is Planck's constant, f the applied microwave frequency, t the inter-dot tunnel coupling and ε the detuning, which is given by $\alpha(\delta\widetilde{P}_i - \delta\widetilde{P}_{i+1})$, with α the lever arm, a conversion factor between voltage and energy scales [13]. If two electrons occupy the two tunnel coupled dots at zero magnetic field, there are three relevant energy levels at modest detuning, two corresponding to hybridized singlet states and the other to threefold degenerate triplet states, see Fig. 4.2(f) [2, 16]. This level structure results in three possible transitions, with corresponding energy differences between singlet and triplet states described by $hf = \pm\frac{\varepsilon}{2} + \frac{1}{2}\sqrt{\varepsilon^2 + 8t^2}$, indicated with respectively the green and blue wiggly arrows, and the energy difference between the two singlet states given by $hf = \sqrt{\varepsilon^2 + 8t^2}$, indicated

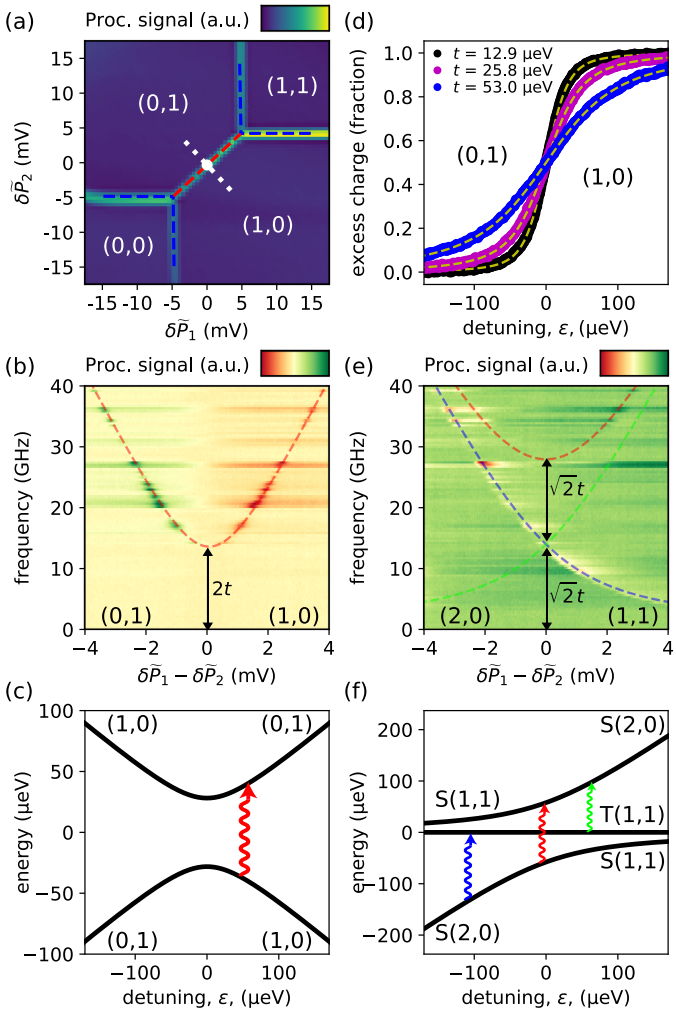

Figure 4.2: In all subfigures, (N_1, N_2) indicates charge occupation of the left and middle dot, with no dot formed on the right. (a) A double quantum dot charge stability diagram, showing the processed sensing dot signal as a function of virtual plunger gate voltages. The fitted anti-crossing model is indicated with dashed lines. The detuning axis is indicated with the white dotted line and the center point on the inter-dot transition line with a white dot. (b) Photon-assisted tunneling measurement showing the charge detector signal (background subtracted) as a function of frequency and inter-dot detuning at the (0,1) to (1,0) transition. The red dashed line is a fit of the form $hf = \sqrt{\varepsilon^2 + 4t^2}$. The detuning lever arm is extracted from the slope of the hyperbola in the large detuning limit. (c) The energy level diagram for one-electron occupation. The eigenenergies are $\pm\frac{1}{2}\sqrt{\varepsilon^2 + 4t^2}$. A microwave photon (red wiggly arrow) can induce a transition (and potentially tunnelling between the dots) when the difference between the energy levels corresponds to the photon energy (PAT). (d) Excess charge extracted from a fit to the sensing dot signal as a function of ε for different t, measured by scanning over the detuning axis for the single-electron occupation. The model used to fit to the SD signal is $V(\varepsilon) = V_0 + \delta V Q(\varepsilon) + \left[\frac{\delta V}{\delta\varepsilon}|_{Q=0} + \left(\frac{\delta V}{\delta\varepsilon}|_{Q=1} - \frac{\delta V}{\delta\varepsilon}|_{Q=0}\right) Q(\varepsilon)\right]\varepsilon$. Here V_0 is the background signal, δV is a measure of the charge sensitivity, Q the excess charge as a fraction of the electron charge and $\frac{\delta V}{\delta\varepsilon}$ the gate-sensor coupling when ε is varied [9]. (e) Photon-assisted tunneling measurement similar to (b) but for the inter-dot transition from (2,0) to (1,1). Coloured dashed lines are fits to the measured data. (f) The energy level diagram for the two electron transition. Coloured wiggly arrows indicate microwave photon excitations. The energy levels are given by $\frac{\varepsilon}{2} \pm \frac{1}{2}\sqrt{\varepsilon^2 + 8t^2}$ for the singlets and are 0 for the degenerate triplets.

with the red wiggly arrow. In the measurement shown in Fig. 4.2(e) we only observe two out of the three transitions. This we explain by observing that the thermal occupation of the lowest excited state is negligible. We note that some PAT transitions involve a spin-flip, which is mediated by spin-orbit interaction and a difference in the Overhauser fields between the two dots [17]. The variation in intensity for different horizontal lines in Fig. 4.2(b) and (e) is caused by the frequency dependence of the transmission of the high-frequency wiring. One could compensate for this by adjusting the output power of the microwave source per frequency. The white tails in Fig. 4.2(e) are caused by sweeping gate voltages at a rate which is of the same order of magnitude as the triplet-singlet relaxation rate. This was confirmed by inverting the sweep direction and observing that the white tails appear on the other side of the transition line.

The second method to measure the tunnel coupling is based on the broadening of the inter-dot transition line [14], see Fig. 4.2(d). The broadening reflects a smoothly varying charge distribution when scanning along the detuning axis, caused by the tunnel coupling via the hybridisation of the relevant states and the temperature through the thermal occupation of excited states. For the single-electron case, the average excess charge on the left (right) dot is given by

$$Q = \frac{1}{\mathcal{Z}} \sum_n (c_n e^{-E_n/k_B T_e}), \tag{4.1}$$

with $\mathcal{Z}$ the partition function, $c_n = \frac{1}{2} \mp \varepsilon/E_n$ the probability of finding the excess charge on the left (right) dot for the eigenstate with energy E_n and the thermal energy $k_B T_e \approx 10.5\,\mu\text{eV}$, with T_e the effective electron temperature. An analogous expression applies to the two-electron case, with $c_n = 0$ for the triplets and $c_n = \frac{1}{2}(1 \pm \varepsilon/\sqrt{\varepsilon^2 + 8t^2})$ for the hybridized singlets. The lever arm used for measuring the tunnel coupling from the broadening of the inter-dot transition line is obtained from PAT, but could also be measured with Coulomb diamonds or bias triangles [2]. Based on Eqn. 4.1 we obtain the model for the charge sensor response when scanning over the detuning axis, see the caption of Fig. 4.2 [9].

Here we compare the two methods for extracting the tunnel coupling. An advantage of the method based on the broadening of the inter-dot transition line is that it is about two orders of magnitude faster than PAT (see Table reftab:timings), because it is effectively a single scan over the detuning axis while PAT is a series of scans over the detuning axis for different microwave frequencies. Another difference is in the range of tunnel couplings over which the two methods work well. For PAT the upper limit depends on the maximum frequency that the microwave source can produce. We expect that the lower limit for PAT is determined by charge noise, resulting in broadening of the PAT peaks. With PAT, we were able to automatically measure tunnel coupling values as low as 5μeV. The lower limit for the inter-dot transition broadening method is set by the effective electron temperature, $k_B T_e$, here $\approx 10.5\,\mu\text{eV}$ [14]. The upper limit for this method is that for very large tunnel couplings, the broadening of the inter-dot transition line extends to the boundaries of the charge stability region. In the measurements shown here, we did not come close to this upper limit, but tunnel couplings up to 75 GHz $\approx 300\,\mu\text{eV}$ have been measured with the inter-dot transition line broadening method [9]. We observe that the two methods are in good correspondence with one an-

other, i.e. the difference between the two is smaller than 10% of their average value (see supplementary material 4.8.5). Measurement errors are usually smaller than the accuracy in target tunnel coupling we are interested in, while potential outliers will typically be caused by unpredictable charge jumps.

4.5. SECOND PART OF THE ALGORITHM

Now, let us describe part II of the algorithm, see Fig. 4.1(b), which performs a feedback loop. For each iteration the virtual barrier gate value, i.e. the linear combination of gate voltages as determined in part I, is adjusted and the tunnel coupling is measured. Before the first step of the algorithm we measure the tunnel coupling with PAT. For this initial measurement, we cannot rely on the (faster) method based on the broadening of the inter-dot transition, since at this stage the lever arm has not yet been determined. If we are not yet within 1 μeV, of the user-defined target tunnel coupling value, we step the virtual barrier gate value with step size equal to the maximal step size in the positive direction if the tunnel coupling is too low and vice versa. We limit the barrier gate step size to 20 mV such that the position of the anti-crossing can again be located automatically by fitting the anti-crossing model. For larger step sizes, the position of the anti-crossing becomes harder to predict due to non-linearities. After stepping the virtual barrier gate we measure the tunnel coupling again using PAT. Then we have measured the tunnel coupling for two settings and we determine the next step for the virtual barrier, by predicting the voltage required to reach the target value from an exponential fit [9, 18] to the measured tunnel couplings and their respective virtual barrier values (we thereby force the exponential to go to zero for very negative barrier voltages). After the tunnel coupling has been measured five times with PAT we also have five measured lever arm values for different gate voltages. The small differences in lever arm we interpret as caused by small shifts in the dot positions with the gate voltages. We predict the lever arm for other voltages using a linear approximation (see supplementary material 4.8.5). Using this knowledge of the lever arm, the algorithm can be sped up for the subsequent iterations by measuring the tunnel coupling from inter-dot transition broadening.

4.6. ALGORITHM AT WORK

Following the procedure described above the algorithm automatically tunes the inter-dot tunnel coupling to a target value, within the range of the measurable tunnel coupling values and the achievable values with our gate design and electron occupations. Fig. 4.3 shows the results of the tuning algorithm for various initial and target tunnel coupling values, indicated with different colours. The target tunnel coupling value are indicated with black dashed lines. We clearly see that the algorithm finds the gate voltages that bring the tunnel coupling to the target value, stepwise moving closer. In Fig. 4.3(a) results for the left pair of dots with a single electron are shown, while Fig. 4.3(b) shows results for an occupation with two electrons. We have obtained similar results for the second pair of neighbouring dots in the triple dot (see supplementary material 4.8.7). The duration of a run of the algorithm mainly depends on the difference between the initial and the final tunnel coupling value, because we limit the maximum step size. The time the tuning algorithm takes to tune an inter-dot tunnel coupling is in the order of 10

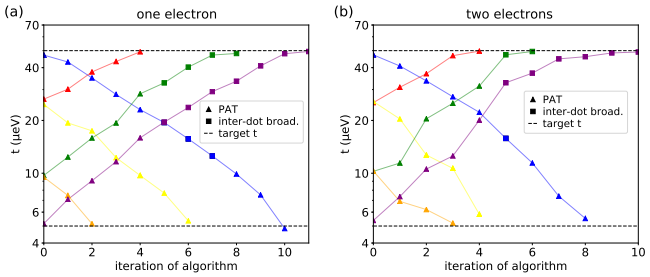

Figure 4.3: Results of the algorithm for a transition involving (a) single-electron states and (b) two-electron states. Each panel shows results for different runs of the algorithm indicated by different colors. Triangles indicate tunnel coupling values measured with PAT and squares indicate measurements based on inter-dot transition line broadening. Solid lines are added as a guide to the eye. The black dashed lines indicate the high and low target tunnel coupling values.

min (see supplementary material 4.8.6 for more details).

4.7. CONCLUSION

In conclusion, we have shown automation of the tuning of the tunnel coupling between adjacent semiconductor quantum dots. Key for this automation were image processing methods to automatically fit the shape of an anti-crossing and to find the shape of the resonance curve in a PAT measurement. The present methods for measuring inter-dot tunnel couplings and the feedback routine can be extended to larger quantum dot arrays, in the future including also two-dimensional arrays. When tuning multiple tunnel couplings, cross-talk effects from the tuning of one tunnel coupling on the values of nearby tunnel couplings will have to be compensated for, which so far was done by hand [9]. This work demonstrates further automated control over semiconductor quantum dots and is the next step forward in automated tuning of larger quantum dot arrays, necessary for scaling up the number of spin-based qubits implemented with semiconductor quantum dots.

See supplementary material for the explanation of the concept of virtual gates, details on the fitting routines, comparison between the two methods to measure the tunnel coupling, data on the automated tuning of another double dot and information about the time required for the tuning algorithm.

4.8. SUPPLEMENTARY MATERIAL

4.8.1. SOFTWARE AND ALGORITHMS

The software was developed using Python [19], SciPy [20] and the QCoDeS [21] framework. The image processing is performed in pixel coordinates. The parameters of algorithms are given in physical units such as mV. The corresponding parameter in pixel units is then determined by translating the value using the scan parameters. By specifying the parameters in physical units the algorithms remain valid also if scans are made with a different resolution. Of course making scans with a different resolution can lead to differences in rounding of numbers leading to slightly different results.

4.8.2. VIRTUAL GATES

Due to the capacitive coupling from gates to dot chemical potentials and tunnel barriers, changing the voltage applied on one of the gates influences not only one but all of the chemical potentials and tunnel barriers in the potential landscape. To compensate for the cross-talk from gates to chemical potentials we make use of a cross-capacitance matrix. The entries of this matrix correspond to the coupling strengths. The columns in the inverse of the cross-capacitance matrix contain the coefficients for the gate combinations defining the virtual gates. The virtual plungers, $\tilde{P}_i$, which are linear combinations of plungers, P_i, control the chemical potential in one dot while leaving the other chemical potentials unaffected. The virtual barrier, $\tilde{D}_i$, changes the inter-dot tunnel coupling without affecting the chemical potentials, hence contains compensation for the effect of the barrier, D_1, on the dot chemical potentials. An example of a measured cross-capacitance matrix is

$$\begin{pmatrix} \delta\widetilde{P}_1 \\ \delta\widetilde{P}_2 \\ \delta\widetilde{D}_1 \end{pmatrix} = \begin{pmatrix} 1.00 & 0.49 & 1.23 \\ 0.55 & 0.88 & 1.49 \\ 0.00 & 0.00 & 1.00 \end{pmatrix} \begin{pmatrix} \delta P_1 \\ \delta P_2 \\ \delta D_1 \end{pmatrix}. \tag{4.2}$$

The upper two rows are scaled such that the top-left entry is one. The left two entries of the bottom row describe the effect of the plunger gates on the tunnel barrier. These entries are set to zero because the PAT and inter-dot line broadening measurements are performed near an inter-dot transition, hence using these methods we could not independently measure the effect of plungers on the tunnel barrier. The last entry of the row for the couplings to the barrier is set to one as we chose the effect of the physical barrier on the virtual barrier to be one-to-one.

4.8.3. AVOIDED CROSSING MODEL

Here, we describe the fitting routine of an avoided crossing in a charge stability diagram, see Fig. 4.4(a). For this fitting we developed a two-dimensional, classical model of an avoided crossing which will be explained below. First we describe the processing of the measured data.

The first step in the processing is calculating a derivative of the image. This is done by applying a first order Gaussian filter. From the convoluted data we subtract a background signal. This background signal is a third order polynomial fit to the data, which was convoluted with the Gaussian filter. This background subtraction is done to remove

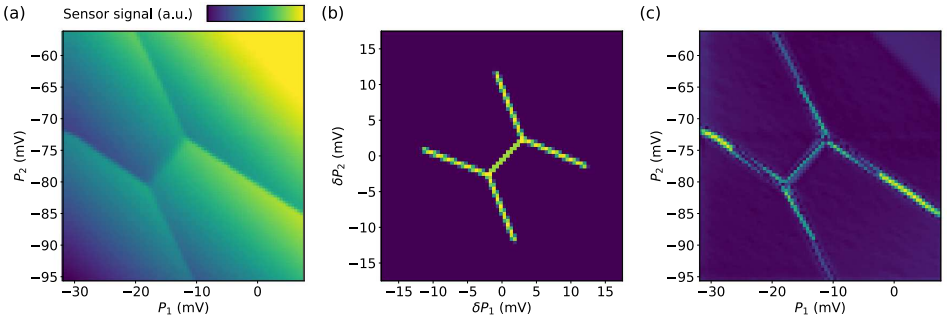

Figure 4.4: (a) A charge stability diagram with an avoided crossing, showing the unprocessed sensor signal. (b) The two-dimensional patch generated based on the classical model of the anti-crossing. (c) Processed sensor signal recorded during the charge stability measurement, from which the model fitted on the anti-crossing is subtracted.

the shape of the sensing dot Coulomb peak in the data. Next step is to straighten the measured data into a square image. This straightening ensures that horizontal and vertical directions are equally weighted in the fitting with the 2D model. Then we normalize the signal with its 99th percentile.

$$\text{proc. data} = \frac{\left(\text{conv. data}_{\text{pix.}} - \text{bg}_{\text{fit}}\right)}{p_{99}\left(\text{conv. data}_{\text{pix.}} - \text{bg}_{\text{fit}}\right)}. \tag{4.3}$$

We developed a classical model of an anti-crossing as observed in charge stability diagrams. The model consists of a two-dimensional patch, see Fig. 4.4(b). The line shapes in this model are based on a truncated cosine. The model has eight parameters, that need to be fit. Two parameters describe the center of the avoided-crossing, as indicated with a white dot in Fig. fig:models(a) in the main text, five parameters describe the angles of the four addition lines and the inter-dot transition line, and one parameter corresponds to the length of the inter-dot transition line. Additional to these eight parameters, which are to be fitted, there are two more parameters, which we fix before the fitting. The first is the typical width of an addition line, which is based on the effective electron temperature. The second parameter is the length of the four line pieces which we fit on the addition lines. These are chosen such that they are significantly larger than the effective electron temperature and smaller than the addition energy.

The anti-crossing is fit by minimizing the following cost function

$$\text{cost} = \sum_{\text{pixels}} \left[|\text{proc. data}| - \text{model}\right], \tag{4.4}$$

which is the sum over all pixel intensities of the processed data minus the 2D patch of the model. This fitting procedure results in a fit as shown in Fig. 4.4(c).

4.8.4. PHOTON ASSISTED TUNNELLING FITTING

Here we explain the fitting procedure for the photon assisted tunnelling measurements. The PAT fitting procedure consists of three steps: processing the data, detecting the de-

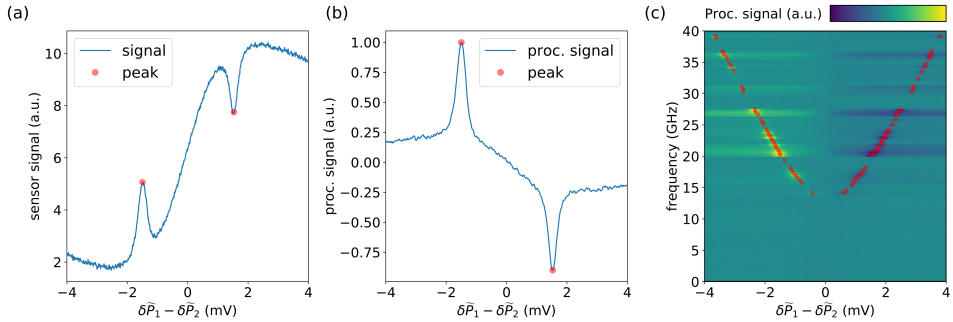

Figure 4.5: (a) Line cut of the sensing dot signal as a function of detuning with the microwave frequency, f, at 20 GHz. (b) At the same microwave frequency, but here showing the processed sensing dot signal, hence with the smoothed background subtracted and with the remaining signal normalized. (c) A PAT measurement, showing the processed sensing dot signal, with the red dots indicating the detected peaks.

4

tuning values of the resonance peaks per microwave frequency, see Fig. 4.5(a), and fitting the curve describing the energy difference to the detected peaks.

The processing of the data is done per horizontal line in a PAT measurement, i.e. per applied microwave frequency. The first step is the subtraction of a background signal. We measure the background signal with a scan over the detuning axis while the microwave source is off, note that this is the same scan we would do when we want to measure the tunnel coupling based on the broadening of the inter-dot transition line. Before subtracting the background signal we smoothen both the signal and the background signal with a Gaussian filter with σ set to five pixels. After the background subtraction we subtract the average of the signal and rescale it, resulting in the data as shown in Fig. 4.5(b).

We detect the resonance peaks as extrema in the processed signal. Just as for the processing of the data, the peak detection is done per horizontal line. First we find the

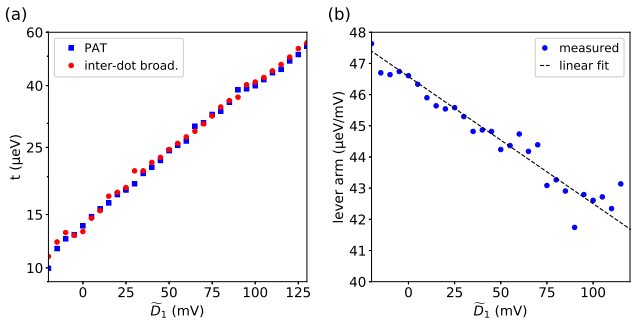

Figure 4.6: (a) The tunnel coupling plotted against the virtual barrier gate voltage. Blue triangles indicate measurements with PAT while filled red circles indicate measurements based on the broadening of the inter-dot transition line. The effective electron temperature used for the inter-dot line fitting is 10.5 μeV. (b) The lever arm measured with PAT plotted against the virtual barrier gate voltage. We fitted a linear relation to the observed trend, which indicates a slight decrease in lever arm as we increase the virtual barrier voltage.

Measurement	Time
Anti-crossing	5 s / 1 min
PAT	1 min
POL	2 s
Tuning alg.	10 min.

Table 4.1: The approximate time used per type of measurement. The fitting time is included in the shown durations.

maximum and minimum per horizontal line. We heuristically determined a threshold for the detected extrema based on the difference in signal for the two charge configurations and the noise level. We filter the extrema by only accepting the detected peaks which have an absolute value higher then the threshold, note here that we already normalized the processed signal.

To the filtered extrema, indicated with red dots in Fig. 4.5(c), we fit the energy transition model, which is described in the main text. This fitting procedure results in fits as shown in Fig. 4.2(b) and (e) in the main text.

4.8.5. COMPARE PAT AND INTER-DOT TRANSITION LINE BROADENING

We compare the tunnel coupling measurements based on PAT and those based on the inter-dot transition line broadening to check that they are in agreement with one another. We use both methods to measure the tunnel coupling over a range of tunnel coupling values for which both methods are reliable. These measurements were done in the single electron occupation regime. In Fig. 4.6 we show measured tunnel couplings by both the PAT method and the method based on broadening of the inter-dot line. The lever arm we used for the inter-dot line broadening measurement is taken from the PAT measurement at that virtual barrier gate voltage, see Fig. 4.6(b).

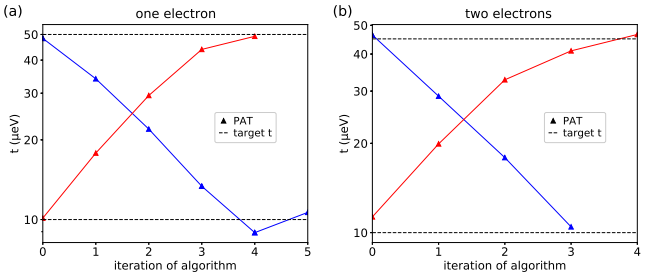

Figure 4.7: Results of the algorithm for a transition involving single-electron states (a) and (b) two-electron states. These results are for the automated tuning of the tunnel coupling between the pair of dots on the right side of the triple dot device. Each panel shows results for different runs of the algorithm indicated by different colors. Triangles indicate tunnel coupling values measured with PAT. Solid lines are added as a guide to the eye. In this case tune tuning algorithm converged to the target value before switching the inter-dot broadening method. The black dashed lines indicate the high and low target tunnel coupling values.

4.8.6. TIME REQUIRED TO RUN THE ALGORITHM

In Table 4.1 an overview is given with the approximate times used for the different routines of the tuning algorithm and the tuning algorithm itself. The measurement time for the anti-crossing measurement is lower if the gates on which the voltages are swept are connected to high-frequent lines, hence can be swept with an a.c. signal, or relatively longer if the voltages can only be changed by stepping a d.c. voltage. For the triple dot device used for the demonstration of the algorithm only the plunger gates were connected to high-frequent lines.

4.8.7. ADDITIONAL ALGORITHM RESULTS

In this section we present additional results of the computer automated tuning algorithm. Fig. 4.7 shows the results of the tuning algorithm on the tunnel coupling between the right pair of dots. Again, different colours indicate results of the algorithm for different initial and target tunnel coupling values. Fig. 4.7(a) shows results for the pair of dots with a single electron, while Fig. 4.7(b) shows results for an occupation with two electrons.

REFERENCES

[1] D. Loss and D. P. Divincenzo, *Quantum computation with quantum dots,* Physical Review A **57**, 120 (1998).

[2] R. Hanson, L. P. Kouwenhoven, J. R. Petta, S. Tarucha, and L. M. K. Vandersypen, *Spins in few-electron quantum dots,* Reviews of Modern Physics **79**, 1217 (2007).

[3] F. A. Zwanenburg, A. S. Dzurak, A. Morello, M. Y. Simmons, L. C. Hollenberg, G. Klimeck, S. Rogge, S. N. Coppersmith, and M. A. Eriksson, *Silicon quantum electronics,* Reviews of Modern Physics **85**, 961 (2013).

[4] T. Byrnes, N. Y. Kim, K. Kusudo, and Y. Yamamoto, *Quantum simulation of Fermi-Hubbard models in semiconductor quantum-dot arrays,* Physical Review B **78**, 075320 (2008).

[5] P. Barthelemy and L. M. K. Vandersypen, *Quantum Dot Systems: A versatile platform for quantum simulations,* Annalen der Physik **525**, 808 (2013).

[6] J. Levy, *Universal Quantum Computation with Spin-1/2 Pairs and Heisenberg Exchange,* Physical Review Letters **89**, 147902 (2002).

[7] D. P. DiVincenzo, D. Bacon, J. Kempe, G. Burkard, and K. B. Whaley, *Universal quantum computation with the exchange interaction,* Nature **408**, 339 (2000).

[8] S. Yang, X. Wang, and S. Das Sarma, *Generic Hubbard model description of semiconductor quantum-dot spin qubits,* Physical Review B **83**, 161301(R) (2011).

[9] T. Hensgens, T. Fujita, L. Janssen, X. Li, C. J. Van Diepen, C. Reichl, W. Wegscheider, S. Das Sarma, and L. M. K. Vandersypen, *Quantum simulation of a Fermi–Hubbard model using a semiconductor quantum dot array,* Nature **548**, 70 (2017).

[10] T. A. Baart, P. T. Eendebak, C. Reichl, W. Wegscheider, and L. M. K. Vandersypen, *Computer-automated tuning of semiconductor double quantum dots into the single-electron regime,* Applied Physics Letters **108**, 213104 (2016).

[11] T. Botzem, M. D. Shulman, S. Foletti, S. P. Harvey, O. E. Dial, P. Bethke, P. Cerfontaine, R. P. G. McNeil, D. Mahalu, V. Umansky, A. Ludwig, A. Wieck, D. Schuh, D. Bougeard, A. Yacoby, and H. Bluhm, *Tuning methods for semiconductor spin qubits,* Physical Review Applied **10**, 054026 (2018).

[12] S. S. Kalantre, J. P. Zwolak, S. Ragole, X. Wu, N. M. Zimmerman, M. D. Stewart, and J. M. Taylor, *Machine Learning techniques for state recognition and auto-tuning in quantum dots,* npj Quantum Information **5**, 6 (2019).

[13] T. H. Oosterkamp, T. Fujisawa, W. G. van der Wiel, K. Ishibashi, R. V. Hijman, S. Tarucha, and L. P. Kouwenhoven, *Microwave spectroscopy of a quantum-dot molecule,* Nature **395**, 873 (1998).

[14] L. DiCarlo, H. J. Lynch, A. C. Johnson, L. I. Childress, K. Crockett, C. M. Marcus, M. P. Hanson, and A. C. Gossard, *Differential charge sensing and charge delocalization in a tunable double quantum dot,* Physical Review Letters **92**, 226801 (2004).

[15] T. A. Baart, M. Shafiei, T. Fujita, C. Reichl, W. Wegscheider, and L. M. K. Vandersypen, *Single-Spin CCD,* Nature Nanotechnology **11**, 330 (2015).

[16] J. R. Petta, A. C. Johnson, J. M. Taylor, E. A. Laird, A. Yacoby, M. D. Lukin, C. M. Marcus, M. P. Hanson, and A. C. Gossard, *Coherent Manipulation of Coupled Electron Spins in Semiconductor Quantum Dots,* Science **309**, 2180 (2005).

[17] L. R. Schreiber, F. R. Braakman, T. Meunier, V. Calado, J. Danon, J. M. Taylor, W. Wegscheider, and L. M. K. Vandersypen, *Coupling artificial molecular spin states by photon-assisted tunnelling.* Nature Communications **2**, 556 (2011).

[18] C. B. Simmons, M. Thalakulam, B. M. Rosemeyer, B. J. Van Bael, E. K. Sackmann, D. E. Savage, M. G. Lagally, R. Joynt, M. Friesen, S. N. Coppersmith, and M. A. Eriksson, *Charge sensing and controllable tunnel coupling in a Si/SiGe double quantum dot,* Nano Letters **9**, 3234 (2009).

[19] *Python – Python Programming Language,* .

[20] *SciPy – Scientific computing tools for Python,* .

[21] *QCoDeS – Python-based data acquisition framework,* .

5

EFFICIENT ORTHOGONAL CONTROL OF TUNNEL COUPLINGS IN A QUANTUM DOT ARRAY

Electrostatically-defined semiconductor quantum dot arrays offer a promising platform for quantum computation and quantum simulation. However, crosstalk of gate voltages to dot potentials and inter-dot tunnel couplings complicates the tuning of the device parameters. To date, crosstalk to the dot potentials is routinely and efficiently compensated using so-called virtual gates, which are specific linear combinations of physical gate voltages. However, due to exponential dependence of tunnel couplings on gate voltages, crosstalk to the tunnel barriers is currently compensated through a slow iterative process. In this work, we show that the crosstalk on tunnel barriers can be efficiently characterized and compensated for, using the fact that the same exponential dependence applies to all gates. We demonstrate efficient calibration of crosstalk in a quadruple quantum dot array and define a set of virtual barrier gates, with which we show orthogonal control of all inter-dot tunnel couplings. Our method marks a key step forward in the scalability of the tuning process of large-scale quantum dot arrays.

This chapter has been published as T. K. Hsiao, C. J. van Diepen U. Mukhopadhyay, C. Reichl, W. Wegscheider, and L. M. K. Vandersypen, Physical Review Applied **13**, 054018 (2018).

5.1. INTRODUCTION

Electrostatically-defined semiconductor quantum dot arrays have great application potential in quantum computation [1–4] and quantum simulation [5]. In these arrays, the electrochemical potentials of dots and the tunnel coupling between neighboring dots are controlled electrostatically by applying gate voltages. By adjusting the dot potentials and tunnel couplings, also the exchange coupling between electron spins in the quantum dots can be tuned to perform spin-qubit operations [6–9]. In addition, the in-situ control of the parameters have allowed the use of quantum dot arrays for analog quantum simulation of Fermi-Hubbard physics [10, 11].

Crosstalk from capacitive coupling between gates and the quantum dot array causes a change in any of the gate voltages to affect not just one but multiple parameters. In the past, this crosstalk has been compensated through iterative adjustment of gate voltages to reach the target values. More recently, virtual gates have been introduced as linear combinations of physical gate voltages that enable orthogonal control of dot potentials [10, 12]. The virtual gates are obtained by inverting a crosstalk matrix that expresses by how much each physical gate shifts each of the electrochemical potentials. The technique of crosstalk compensation for dot potentials has become a standard and essential technique in multi-dot experiments [13–15]. However, the inter-dot tunnel coupling is approximately an exponential function of the gate voltages [10, 16, 17], and so far it has remained unclear how to incorporate this nonlinear dependence into the crosstalk matrix. Therefore, tuning of multiple tunnel couplings in a multi-dot device is mostly done by iteratively adjusting gate voltages using manual or computer-automated procedures [18, 19].

In this work, we achieve efficient orthogonal control of inter-dot tunnel couplings in a semiconductor quantum dot array. While the dependence of tunnel coupling on gate voltages is exponential, the exponent is still a linear combination of gate voltages. This allows us to extend the virtual gate matrix to include crosstalk on the tunnel barriers. Specifically, we first show how to efficiently obtain the elements of the virtual gate matrix from the derivatives of tunnel couplings with respect to gate voltages. Next, we test the use of the re-defined virtual barrier gates for orthogonal control of the tunnel couplings in a quadruple dot over a wide range of tunnel coupling values.

5.2. DEVICE AND EXPERIMENTAL APPROACH

5.2.1. QUADRUPLE QUANTUM DOT DEVICE

The experiment is carried out in an electrostatically-defined quantum dot array in a GaAs heterostructure (see Fig. 5.1(a) shows the relevant part of the device). Details of the fabrication and characterization of a nominally identical device are described in [13]. Quantum dots are formed by applying DC voltages to a set of plunger gates, P, and barrier gates, B. For brevity, we will also use the labels P and B to refer to the voltages applied to the corresponding gates. Each plunger gate, P_i, is designed to primarily control the electrochemical potential μ_i of dot i and each barrier gate, B_{ij}, is designed to mainly control the inter-dot tunnel couplings, t_{ij}, between neighboring dots i and j. Each P_i is connected to a bias-tee for additional fast control of the dot potential using an arbitrary waveform generator. In this experiment, up to four dots (a quadruple quantum dot) are

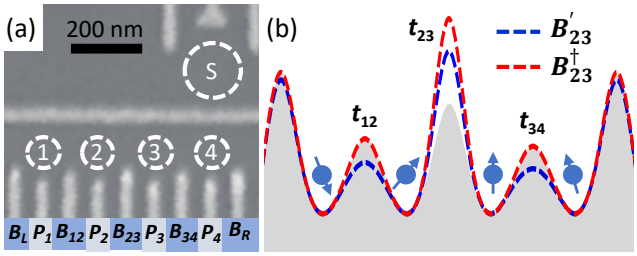

Figure 5.1: (a) A scanning electron microscope image of a device nominally identical to the one used here. The dashed circles indicate the intended positions of the quadruple dot and sensing dot. (b) Schematics illustrating the influence of changes in B'_{23} and $B^{\dagger}_{23}$ on the potential landscape of a quadruple quantum dot. The grey area denotes the original landscape, and the blue (red) dashed line indicates the landscape when B'_{23} ($B^{\dagger}_{23}$) is changed. B'_{23} controls the inter-dot tunnel coupling, t_{23}, while keeping the dot potentials fixed, but also influences t_{12} and t_{34}. In contrast, $B^{\dagger}_{23}$ controls t_{23} while affecting neither other tunnel couplings nor dot potentials.

5

formed, see Fig. 5.1(a). In addition, a sensing dot, S, is operated as a charge sensor. Due to capacitive coupling, the sensing dot potential and thus the conductance through the sensing dot depend on the number and position of the electrons in the quantum dot array [2]. The change in conductance is measured using radio-frequency reflectometry to achieve fast read-out of the charge configuration [20].

5.2.2. VIRTUAL BARRIER GATES

In the literature so far, the relationship between virtual plunger and barrier gates P' and B' and the physical plunger and barrier gates P and B is expressed via a crosstalk matrix of the form [10, 13, 14]

$$\begin{pmatrix} P'_1 \\ P'_2 \\ P'_3 \\ P'_4 \\ B'_{12} \\ B'_{23} \\ B'_{34} \end{pmatrix} = \begin{pmatrix} 1 & \alpha_{12} & \alpha_{13} & \alpha_{14} & \alpha_{15} & \alpha_{16} & \alpha_{17} \\ \alpha_{21} & 1 & \alpha_{23} & \alpha_{24} & \alpha_{25} & \alpha_{26} & \alpha_{27} \\ \alpha_{31} & \alpha_{32} & 1 & \alpha_{34} & \alpha_{35} & \alpha_{36} & \alpha_{37} \\ \alpha_{41} & \alpha_{42} & \alpha_{43} & 1 & \alpha_{45} & \alpha_{46} & \alpha_{47} \\ 0 & 0 & 0 & 0 & 1 & 0 & 0 \\ 0 & 0 & 0 & 0 & 0 & 1 & 0 \\ 0 & 0 & 0 & 0 & 0 & 0 & 1 \end{pmatrix} \begin{pmatrix} P_1 \\ P_2 \\ P_3 \\ P_4 \\ B_{12} \\ B_{23} \\ B_{34} \end{pmatrix}. \tag{5.1}$$

The matrix entries are measured using $\alpha_{ij} = \frac{\partial \mu_i}{\partial P_j} / \frac{\partial \mu_i}{\partial P_i}$ and similar ratios involving the B gates. By definition, then $\alpha_{ii} = 1$. The linear combination of P and B to orthogonally control the dot potentials is obtained from the inverse matrix. However, P'-B' do not compensate for the crosstalk on tunnel couplings, hence applying a voltage on B'_{ij} not only changes t_{ij} but also affects nearby tunnel couplings t_{kl}, as illustrated in Fig. 5.1(b) (blue dashed line).

To overcome this limitation, we note that t_{ij} can be approximated as an exponential

function [16, 17]

$$t_{ij} = t_0 \exp(\Phi_{ij}) = t_0 \exp\left(\sum_k \Lambda_k^{ij} P'_k + \sum_{kl} \Gamma_{kl}^{ij} B'_{kl}\right) \tag{5.2}$$

where Φ_{ij} is the integral of $-\sqrt{2m_e(V_{ij}(x)-E)}$ (m_e is the electron mass, $V_{ij}(x)$ is the potential of the barrier at a position x, and E is the energy of the tunneling electron). Our crucial assumption, which we will verify below, is that Φ_{ij} can be expressed as a linear combination of P' and B' with coefficients Λ and Γ respectively. A set of re-defined virtual gates, $P^\dagger$-$B^\dagger$, which includes the compensation for the crosstalk on tunnel couplings, is then constructed from

$$\begin{pmatrix} P_1^\dagger \\ P_2^\dagger \\ P_3^\dagger \\ P_4^\dagger \\ B_{12}^\dagger \\ B_{23}^\dagger \\ B_{34}^\dagger \end{pmatrix} = \begin{pmatrix} 1 & 0 & 0 & 0 & 0 & 0 & 0 \\ 0 & 1 & 0 & 0 & 0 & 0 & 0 \\ 0 & 0 & 1 & 0 & 0 & 0 & 0 \\ 0 & 0 & 0 & 1 & 0 & 0 & 0 \\ \beta_{51} & \beta_{52} & \beta_{53} & \beta_{54} & 1 & \beta_{56} & \beta_{57} \\ \beta_{61} & \beta_{62} & \beta_{63} & \beta_{64} & \beta_{65} & 1 & \beta_{67} \\ \beta_{71} & \beta_{72} & \beta_{73} & \beta_{74} & \beta_{75} & \beta_{76} & 1 \end{pmatrix} \begin{pmatrix} P'_1 \\ P'_2 \\ P'_3 \\ P'_4 \\ B'_{12} \\ B'_{23} \\ B'_{34} \end{pmatrix} \tag{5.3}$$

where $\beta_{51} = \Lambda_1^{12}/\Gamma_{12}^{12}$, $\beta_{52} = \Lambda_2^{12}/\Gamma_{12}^{12}$, $\beta_{56} = \Gamma_{23}^{12}/\Gamma_{12}^{12}$ and so on. The virtual barrier gates $B_{ij}^\dagger$ that orthogonally control Φ_{ij}, and hence also t_{ij} are obtained from the inverse matrix as a linear combination of P' and B'. Since P' and B' maintain the dot potentials fixed, $B^\dagger$ thus achieve orthogonal control of tunnel couplings while maintaining the dot potentials fixed as well, as depicted in Fig. 5.1(b) (red dashed line). Note that although t_{ij} scales exponentially with P' and B', as long as the factors Λ and Γ remain the same, orthogonal control with $B^\dagger$ remains valid for any value of tunnel couplings.

5.3. RESULTS AND DISCUSSION

5.3.1. EFFICIENT CROSSTALK CHARACTERIZATION

We first form a double dot with dots 2 and 3 to illustrate how to determine Γ from the derivatives of the tunnel couplings with respect to B', see Eq. (5.2). After the dots are formed, the crosstalk matrix from Eq. (5.1) is determined. Figure 5.2(a) shows the charge stability diagram of the double dot obtained when sweeping P'_2 and P'_3. The inter-dot tunnel coupling t_{23} is characterized near the (0,1)-(1,0) inter-dot transition by scanning the dot potentials along the detuning axis (the red dotted line in Fig. 5.2(a)), see Fig. 5.2(b). The gate voltages are converted to dot detuning using lever arms measured with photon-assisted tunneling (PAT) [21] (see Supplementary Material). The smooth variation in charge occupation is caused by thermal excitation and charge hybridization via the inter-dot tunnel coupling, and is fitted to a model described in [18], which is adapted from the one in [22], to obtain the value of the tunnel coupling. Utilising this method, the inter-dot tunnel coupling can be measured in approximately a second. Alternatively, the tunnel coupling can also be extracted from PAT measurements [21]. The crosstalk of B'_{kl} on t_{ij} can be characterized by varying the voltage on B'_{kl} and then measuring the change

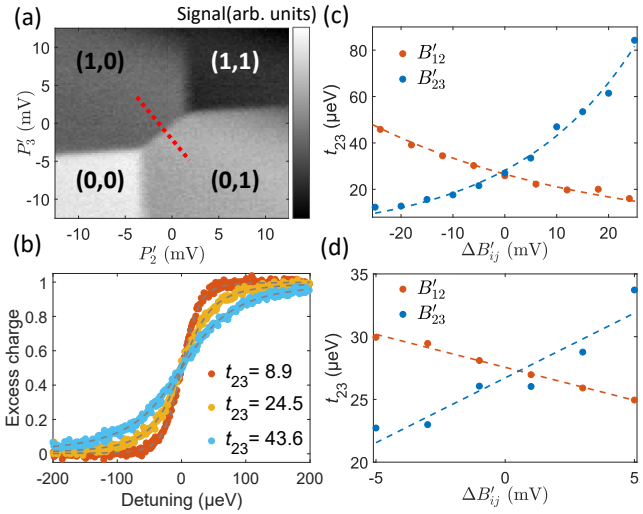

Figure 5.2: (a) Charge stability diagram showing the sensing-dot signal as a function of voltages on P_2' and P_3'. (N_2, N_3) indicates charge occupation of dot 2 and 3. The red dotted line indicates the inter-dot detuning axis. (b) Excess charge (in units of e) extracted from a fit to the sensing-dot signal as a function of detuning near the inter-dot transition in (a). Data (colored circles) for different t_{23} (in μeV) is shown together with the fitted curves (dashed lines). The model of the fit is described in [18]. t_{23} is obtained from the fit. (c) Measured tunnel coupling t_{23} as a function of barrier voltage B_{12}' and B_{23}', with an exponential fit to the data. (d) Same as (c) but with a smaller voltage variation in B_{12}' and B_{23}', plotted with a linear fit.

in t_{ij}. It is important to use the virtual barrier B_{kl}' instead of the physical barrier B_{kl} because varying B_{kl}' keeps the dot potentials unchanged so that they remain close to the inter-dot transition. Hence, inter-dot transition scans can be performed subsequently at different B_{kl}' without manually adjusting dot potentials. Note that similar methods for extracting tunnel couplings can also be used for higher electron occupations [18].

Figure 5.2(c) shows the measured t_{23} as a function of the corresponding barrier B_{23}' and the neighboring barrier B_{12}'. As B_{23}' becomes more positive, the potential barrier between dots 2 and 3 is lowered so t_{23} increases exponentially. As B_{12}' is increased, however, crosstalk makes t_{23} decrease exponentially. The crosstalk from B_{12}' to t_{23} can be understood by considering the following factors. First, increasing B_{12}' also increases B_{12}, which by itself increases t_{23}. Second, in order to keep dot potentials fixed, the voltage on P_2 is decreased to compensate the crosstalk from the increased voltage on B_{12} to the potential of dot 2. Decreasing P_2 reduces t_{23}. Finally, increasing B_{12}' may shift the wavefunction of the electron in dot 2 away from the electron in dot 3, hence reducing the tunnel coupling as well. Combining these factors leads to the negative crosstalk of B_{12}' on t_{23}.

By fitting the data in Fig. 5.2(c) to an exponential function $t_{23} = t_0 \exp\left(\Gamma_{kl}^{23} B_{kl}'\right)$, we obtain $\Gamma_{12}^{23} = -2.31 \pm 0.08 \times 10^{-2}\,\mathrm{mV}^{-1}$, $\Gamma_{23}^{23} = 4.26 \pm 0.17 \times 10^{-2}\,\mathrm{mV}^{-1}$ and the crosstalk ratio $r = |\Gamma_{12}^{23}/\Gamma_{23}^{23}| = 54 \pm 3\%$. In fact, the ratio between Γ_{12}^{23} and Γ_{23}^{23} can be obtained more easily by varying B_{12}' and B_{23}' in a small range and measuring $\frac{\partial t_{23}}{\partial B_{12}'}$ and $\frac{\partial t_{23}}{\partial B_{23}'}$ using a linear fit (see Fig. 5.2(d)). The fit gives $\frac{\partial t_{23}}{\partial B_{12}'} = -0.53 \pm 0.02\,\mu\mathrm{eV/mV}$, $\frac{\partial t_{23}}{\partial B_{23}'} = 1.03 \pm 0.18\,\mu\mathrm{eV/mV}$

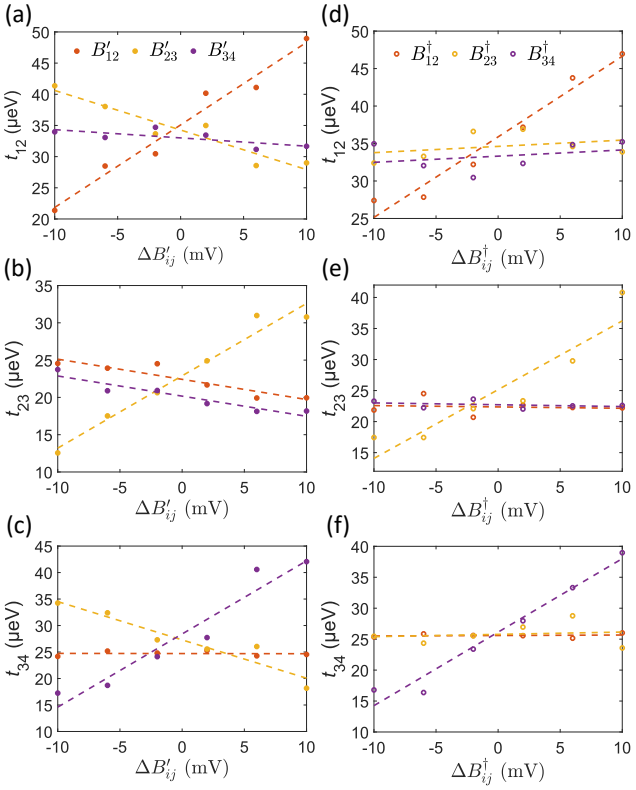

Figure 5.3: (a-c) Measured tunnel couplings as a function of B' for (a) t_{23}, (b) t_{12}, and (c) t_{34}. Dashed lines show linear fits to the data. (d-f) Measured tunnel couplings as a function of $B^\dagger$ for (d) t_{23}, (e) t_{12}, and (f) t_{34}. After calibration, each t_{ij} only depends on the corresponding $B^\dagger_{ij}$. Dashed lines show linear fits to the data.

and the crosstalk ratio $r' = |\frac{\partial t_{23}}{\partial B'_{12}} / \frac{\partial t_{23}}{\partial B'_{23}}| = 51 \pm 9\%$. From Eq. (5.2), one would expect that $\Gamma^{23}_{12}/\Gamma^{23}_{23} = \frac{\partial t_{23}}{\partial B'_{12}} / \frac{\partial t_{23}}{\partial B'_{23}}$, which is confirmed by the similar ratios r and r' from the two different measurements in Fig. 5.2(c) and (d). This result indicates that it is indeed sufficient to measure the derivatives of a tunnel coupling with respect to B' to efficiently characterize the ratios between Γ, which are used for defining the $B^\dagger$.

Note that in this work we do not characterize the factors Λ for P' in Eq. (5.2). To stay near the inter-dot transition, two neighboring P'_i and P'_j need to be varied together, therefore Λ^{ij}_i and Λ^{ij}_j cannot be independently measured using our method. However, this does not affect the orthogonal control of t_{ij} using $B^\dagger_{ij}$. In fact, the linear combination of gate voltages needed to orthogonally change $B^\dagger$ is independent of Λ. Of course, without knowing Λ (here set to 0), varying $P^\dagger$ will affect tunnel couplings, which we return to later.

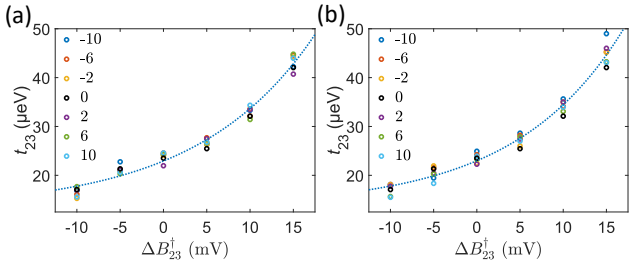

Figure 5.4: The experimentally measured tunnel coupling t_{23} as a function of $\Delta B^{\dagger}_{23}$ for different values of $\Delta B^{\dagger}_{12}$ (a) and $\Delta B^{\dagger}_{34}$ (b) (in mV), plotted with an exponential fit to the data. $\Delta B^{\dagger}_{ij}$ is the voltage relative to $B^{\dagger}_{ij}$ when $t_{ij} \sim 25\,\mu$eV. The exponential fit has an offset of 13 μeV. As observed in other works, the expression Eq. (5.2) is a good approximation over a finite range of gate voltages, for instance because of the presence of other tunnel barriers nearby.

5.3.2. ORTHOGONAL CONTROL OF TUNNEL COUPLINGS

Next, we demonstrate the crosstalk calibration and the orthogonal control of inter-dot tunnel couplings in a quadruple quantum dot, as shown in Fig. 5.1(a). A quadruple dot is formed and the capacitive coupling to dot potentials is characterized for an arbitrary initial condition, where $t_{12} = 33.4 \pm 1.0\,\mu$eV, $t_{23} = 23.2 \pm 0.4\,\mu$eV and $t_{34} = 25.6 \pm 0.4\,\mu$eV. P' and B' are defined with Eq. (5.1). The quadruple dot is then tuned to the (1,0,1,1)-(0,1,1,1) inter-dot transition to measure t_{12}, where (N_1,N_2,N_3,N_4) indicates the charge occupation on dots 1 to dot 4. The dependences of t_{12} on B' are shown in Fig. 5.3(a). As expected, t_{12} shows the largest dependence on the corresponding barrier gate voltage B'_{12}. From $\frac{\partial t_{12}}{\partial B'_{12}} = 1.32 \pm 0.12\,\mu$eV/mV and $t_{12} = 33.4 \pm 1.0\,\mu$eV, $\Gamma^{12}_{12} = 3.95 \pm 0.38 \times 10^{-2}$ mV^{-1}. Changing B'_{23} has a negative crosstalk effect on t_{12} ($\sim$ 50% compared with the effect from B'_{12}). The crosstalk from B'_{34} is weaker ($\sim$ 10%), which is expected, because B'_{34} is further away from B'_{12}. Note that the three fitted lines roughly intersect at $\Delta B'_{ij} = 0$ as expected. The deviations are caused by the error in measuring tunnel couplings. Similarly, the crosstalk on t_{23} and t_{34} is characterized by tuning the quadruple dot to the (1,1,0,1)-(1,0,1,1) and (1,1,1,0)-(1,1,0,1) transitions, respectively. In Fig. 5.3(b), t_{23} shows the largest dependence on B'_{23} ($\frac{\partial t_{23}}{\partial B'_{23}} = 0.97 \pm 0.09\,\mu$eV/mV) and $\Gamma^{23}_{23} = 4.18 \pm 0.39 \times 10^{-2}$ mV^{-1}. The crosstalk of B'_{12} and B'_{34} on t_{23} is about 30%. In Fig. 5.3(c), t_{34} shows the largest dependence on B'_{34} ($\frac{\partial t_{34}}{\partial B'_{34}} = 1.38 \pm 0.19\,\mu$eV/mV) and $\Gamma^{34}_{34} = 5.39 \pm 0.51 \times 10^{-2}$ mV^{-1}. The crosstalk of B'_{23} on t_{34} is about 50% and the crosstalk of B'_{12} is < 1%.

To achieve orthogonal control of the tunnel couplings, the characterized crosstalk ratios are placed into a new matrix including the tunnel-coupling crosstalk, as in Eq. (5.3), and $B^{\dagger}$ are defined. If desired, the crosstalk characterization can be repeated resulting in an updated set of $B^{\dagger}$ that further reduces the residual crosstalk (see Supplementary Material for the final full matrix we used to proceed). Fig. 5.3(d-f) show the tunnel couplings as a function of $B^{\dagger}$. As intended, each t_{ij} is only affected by the respective $B^{\dagger}_{ij}$ and crosstalk of other $B^{\dagger}$ is significantly suppressed, to < 8% for t_{12} and < 3% for t_{23} and t_{34}. The remaining crosstalk could be improved further by taking more data to ac-

curately measure the crosstalk (see Supplementary Material for summarized crosstalk values of B' and $B^\dagger$). This indicates that $B^\dagger$ orthogonally control the tunnel couplings in the quadruple dot. Using $B^\dagger$, we can quickly tune the quadruple dot to a desired configuration, for example, $t_{12} = t_{23} = t_{34} = 33\,\mu\text{eV}$ (see Supplementary Material).

We next verify whether $B^\dagger$ still compensate for crosstalk when changing the barrier gate voltages over a slightly wider range, where the exponential dependence of Eq. (5.2) is unmistakable. Starting from $t_{23} = 25.6 \pm 0.2\,\mu\text{eV}$, the dependence of t_{23} on $B^\dagger_{23}$ is measured for different values of $B^\dagger_{12}$ and $B^\dagger_{34}$. Fig. 5.4(a) and (b) show that, while changing $B^\dagger_{23}$ by 25 mV exponentially increases t_{23} over a range of 27 μeV, varying $B^\dagger_{12}$ and $B^\dagger_{34}$ by 20 mV only has a minor effect on t_{23} (crosstalk < 10% except for $\Delta B^\dagger_{23} = -7.5$ and -12.5 mV, where the small $\frac{\partial t_{23}}{\partial B^\dagger_{23}}$ results in a higher crosstalk ratio due to the uncertainty of the linear fit). This indicates that $B^\dagger$ compensate for the crosstalk in the exponent Φ rather than just compensate for the linearized dependence of tunnel couplings in a small range of gate voltages. As long as the crosstalk coefficients Γ for B' do not change, orthogonal control of tunnel couplings using $B^\dagger$ is effective for a large range of tunnel coupling values. We note that the range of effective $B^\dagger$ is ultimately limited by the voltage range where the positions of the electron wavefunctions are not changed too much (hence the capacitive couplings remain the same), and where the exponential dependence for t_{ij} holds [16].

Instead of calibrating crosstalk on all tunnel couplings in one go, we can also calibrate and compensate cross-talk one tunnel coupling at a time, as demonstrated in the Supplementary Material. This method is especially useful when some of the initial tunnel couplings are small, leading to large errors in the estimated crosstalk ratio.

Furthermore, we note that the spin exchange coupling between neighbouring spins, J_{ij}, is controlled by t_{ij} and the double dot detuning ϵ_{ij}. Since $B^\dagger_{ij}$ orthogonally controls t_{ij} while keeping the dot potentials fixed, $B^\dagger_{ij}$ thus also orthogonally controls J_{ij} [23].

As mentioned earlier, we did not characterize the crosstalk factors Λ for P' since Λ_i^{ij} and Λ_j^{ij} cannot be independently measured using the present method. Hence, varying $P^\dagger$ does affect tunnel couplings. To perform the most complete crosstalk calibration, one may measure either t_{ij} or J_{ij} as a function inter-dot detuning, hence of P'_i and P'_j independently, using a spin-funnel [8] or PAT measurement [21]. Then all the elements in the crosstalk matrix in Eq. (5.3) can be obtained, allowing fully orthogonal tuning of dot potentials and tunnel couplings.

5.4. CONCLUSION

In conclusion, we have achieved orthogonal control of tunnel couplings in a quadruple dot using re-defined virtual barrier gates $B^\dagger$. The crosstalk is calibrated efficiently with a differential method, which requires only a few measurements over a small range of tunnel coupling variation. We also showed that $B^\dagger$, calibrated at a certain condition, remain effective over a wide range of configurations. The demonstrated orthogonal control of tunnel couplings is an essential technique for configuring multi-dot devices to perform spin-qubit operations and analog quantum simulations.

Note Added: In the final stage of completing the manuscript, a report showing orthogonal control of J_{ij} appeared [23].

5.5. SUPPLEMENTARY MATERIAL

5.5.1. DETERMINING LEVER ARMS FROM PHOTON-ASSISTED TUNNELING

The energy difference between states with different charge occupations can be characterized using photon-assisted tunneling (PAT) [21], in which these states are re-populated by a resonant microwave signal. For example, at the (1,0,1,1)-(0,1,1,1) inter-dot transition and along the detuning axis where $\Delta P_1' = -\Delta P_2'$, the energy difference between (1,0,1,1) and (0,1,1,1) is described by $hf = \sqrt{\epsilon_{12}^2 + 4t_{12}^2}$, where h is Planck's constant, f is the frequency of the microwave signal, t_{12} is the inter-dot tunnel coupling, and ϵ_{12} is the detuning, which is given by $L_{12}(\Delta P_1' - \Delta P_2')$. L_{12} is the lever arm converting gate voltage to potential energy. Fig. 5.5 shows the processed PAT signal at the (1,0,1,1)-(0,1,1,1) inter-dot transition. The fit gives $t_{12} = 31.8 \pm 0.5\,\mu\text{eV}$ and $L_{12} = 175 \pm 2\,\mu\text{eV/mV}$. L_{12} is then used for measuring t_{12} from the inter-dot transition curve. By measuring the PAT signals at the (1,1,0,1)-(1,0,1,1) and (1,1,1,0)-(1,1,0,1) transitions, $L_{23} = 140 \pm 1\,\mu\text{eV/mV}$ and $L_{34} = 151 \pm 3\,\mu\text{eV/mV}$ are obtained, which are used for measuring t_{23} and t_{34} respectively.

5

5.5.2. CROSSTALK VALUES AND ERRORS

Table 5.1 summarizes the values and standard errors of crosstalk $\frac{\partial t_{ij}}{\partial B_{kl}'}$ and $\frac{\partial t_{ij}}{\partial B_{kl}^{\dagger}}$ (in μeV/mV) extracted from the slopes in Fig. 5.3.

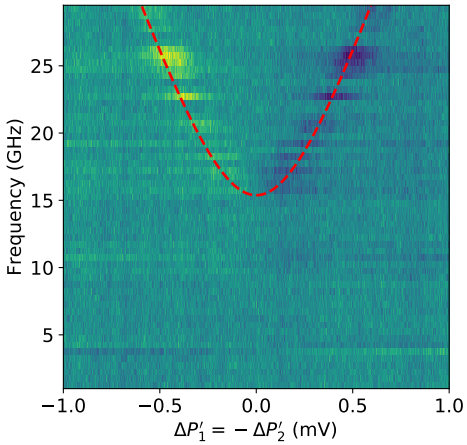

Figure 5.5: Photon-assisted tunneling measurement showing the sensor signal as a function of frequency and detuning at the (1,0,1,1)-(0,1,1,1) inter-dot transition, shown after background subtraction [18]. The red dashed line is the fit of the form $hf = \sqrt{\epsilon_{12}^2 + 4t_{12}^2}$.

	B'_{12}	B'_{23}	B'_{34}	$B^\dagger_{12}$	$B^\dagger_{23}$	$B^\dagger_{34}$
t_{12}	1.32 ± 0.12	-0.63 ± 0.11	-0.13 ± 0.12	1.06 ± 0.11	0.08 ± 0.11	0.08 ± 0.13
t_{23}	-0.27 ± 0.06	0.97 ± 0.09	-0.27 ± 0.05	-0.02 ± 0.08	1.11 ± 0.22	-0.03 ± 0.04
t_{34}	0 ± 0.03	-0.72 ± 0.12	1.38 ± 0.19	0 ± 0.02	0.04 ± 0.12	1.19 ± 0.11

Table 5.1: The crosstalk $\frac{\partial t_{ij}}{\partial B'_{kl}}$ and $\frac{\partial t_{ij}}{\partial B^\dagger_{kl}}$ (in μeV/mV) in Fig. 5.3.

5.5.3. FULL CROSSTALK MATRIX

The normalized crosstalk matrix, which defines $P^\dagger$-$B^\dagger$ in the P-B basis, is

$$\begin{pmatrix} P_1^\dagger \\ P_2^\dagger \\ P_3^\dagger \\ P_4^\dagger \\ B_{12}^\dagger \\ B_{23}^\dagger \\ B_{34}^\dagger \end{pmatrix} = \begin{pmatrix} 1 & 0.69 & 0.32 & 0.19 & 1.38 & 0.51 & 0.20 \\ 0.59 & 1 & 0.46 & 0.30 & 1.01 & 0.94 & 0.39 \\ 0.23 & 0.52 & 1 & 0.39 & 0.40 & 1.12 & 0.85 \\ 0.16 & 0.37 & 0.67 & 1 & 0.22 & 0.58 & 1.22 \\ 0 & 0 & 0 & 0 & 1 & -0.44 & -0.03 \\ 0 & 0 & 0 & 0 & -0.28 & 1 & -0.28 \\ 0 & 0 & 0 & 0 & 0.06 & -0.75 & 1 \end{pmatrix} \begin{pmatrix} P_1 \\ P_2 \\ P_3 \\ P_4 \\ B_{12} \\ B_{23} \\ B_{34} \end{pmatrix}$$

Note that, before defining $B^\dagger$, a set of intermediate virtual barrier gates is constructed, based on the measured crosstalk on tunnel couplings when using B'. The intermediate virtual barriers contain residual crosstalk on the tunnel couplings (< 25%) due to measurement uncertainty. $B^\dagger$ are obtained by measuring and compensating for this residual crosstalk, and are then employed to show the orthogonal control of tunnel couplings in Fig. 5.3(d-f).

5.5.4. TUNING TO A TARGET CONFIGURATION

Here, we demonstrate that tunnel couplings can be efficiently tuned to a target configuration using $B^\dagger$. As shown in Fig. 5.6(a), the initial configuration of tunnel couplings in μeV is $(t_{12}, t_{23}, t_{34}) = (33.4\pm1.0, 23.2\pm0.4, 25.6\pm0.4)$, where $\Delta B^\dagger$ (in mV) are defined as $(\Delta B^\dagger_{12}, \Delta B^\dagger_{23}, \Delta B^\dagger_{34}) = (0,0,0)$. We aim for a target configuration where all tunnel couplings ~ 33 μeV. According to the partial derivatives in Table 5.1, applying $(\Delta B^\dagger_{12}, \Delta B^\dagger_{23}, \Delta B^\dagger_{34}) = (0,9,6)$ will in principle make $(t_{12}, t_{23}, t_{34}) = (33.4, 33.2, 32.7)$. After applying $(\Delta B^\dagger_{12}, \Delta B^\dagger_{23}, \Delta B^\dagger_{34}) = (0,9,6)$, the measurement result in Fig. 5.6(b) shows $(t_{12}, t_{23}, t_{34}) = (32.7\pm0.8, 31.8\pm0.5, 32.8\pm0.5)$, which is very close to the target. This result indicates that by using $B^\dagger$ the tunnel couplings of a quantum dot array can efficiently be tuned to a target configuration.

5.5.5. STEPWISE TUNE-AND-CALIBRATE PROCEDURE

We here provide further details on the stepwise tune-and-calibrate procedure, which allows to systematically set the tunnel couplings in a large-scale quantum dot array from an arbitrary initial configuration to a target configuration and achieving orthogonal control at the same time.

The procedure consists of the following steps:

1. Form the quantum dot array and define P'-B' using the '$n+1$' method described

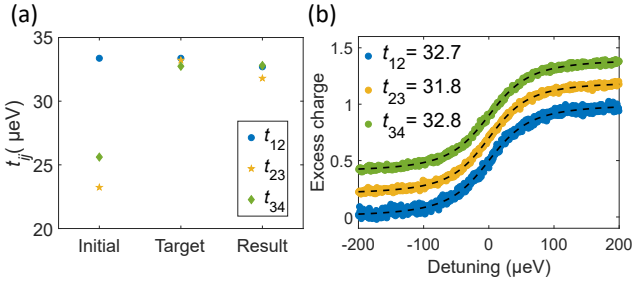

Figure 5.6: Tuning tunnel couplings using $B^{\dagger}$. (a) The tunnel couplings in the initial configuration where $(\Delta B^{\dagger}_{12}, \Delta B^{\dagger}_{23}, \Delta B^{\dagger}_{34}) = (0,0,0)$, the expected ('Target') and the measured ('Result') tunnel couplings in the target configuration where $(\Delta B^{\dagger}_{12}, \Delta B^{\dagger}_{23}, \Delta B^{\dagger}_{34}) = (0,6,9)$. (b) Excess charge (in units of e) as a function of detuning at the $(1,0,1,1)$-$(0,1,1,1)$ (green), $(1,1,0,1)$-$(1,0,1,1)$ (yellow) and $(1,1,1,0)$-$(1,1,0,1)$ (blue) inter-dot transitions, along with the measured tunnel couplings (in μeV), when $(\Delta B^{\dagger}_{12}, \Delta B^{\dagger}_{23}, \Delta B^{\dagger}_{34}) = (0,6,9)$. Offset in y axis is added to the data for clarity. The dashed lines show the fit to the data.

in [13].
2. Choose a t_{ij}, which can be chosen randomly, as the first inter-dot tunnel coupling to tune and calibrate.
3. Use the corresponding B'_{ij} to tune t_{ij} above a value (> 20 μeV in our case) at which the crosstalk on t_{ij} can be accurately obtained with the differential method. It is preferable to directly tune t_{ij} to the target value, if the target value is not too small for the differential method (otherwise see step 6).
4. Characterize the crosstalk of B' on t_{ij} and update the crosstalk matrix.
5. Use the updated matrix to define a new set of virtual barrier gates, B^{*1}, which compensate for the crosstalk on t_{ij}.
6. If t_{ij} is not yet the target value, tune t_{ij} to the target value using B^{*1}_{ij}.
7. Move to a t_{kl} which has not been included yet in the crosstalk compensation.
8. Use B^{*1}_{kl} to tune t_{kl} to a sufficiently high value. Note that t_{ij} will not be affected because B^{*1}_{kl} compensates for the crosstalk on t_{ij}.
9. Characterize the crosstalk of B^{*1} on t_{kl} and update the crosstalk matrix.
10. Define B^{*2}, which compensate for the crosstalk on t_{ij} and t_{kl}.
11. If t_{kl} is not yet the target value, tune t_{kl} to the target value using B^{*2}_{kl}.
12. Repeat steps 7–11 for the remaining tunnel couplings.
13. After going through all of the tunnel couplings, they are tuned to the target configuration, and the final virtual barrier gates, $B^{\dagger}$, orthogonally control the tunnel couplings.

We demonstrate this procedure on the quadruple dot to tune the tunnel couplings from an arbitrary initial configuration to a target configuration where all of the tunnel couplings ~ 25 μeV. The initial condition is $(t_{12}, t_{23}, t_{34}) = (6.1 \pm 0.4, 25.9 \pm 0.2, 8.8 \pm 0.4)$ μeV. After P'-B' are defined, the procedure is first carried out on t_{23}. Fig. 5.7(a) shows the crosstalk of B' on t_{23}. Based on the characterized crosstalk, B^{*1} are defined using a crosstalk matrix where the sub-matrix for the barrier gates is

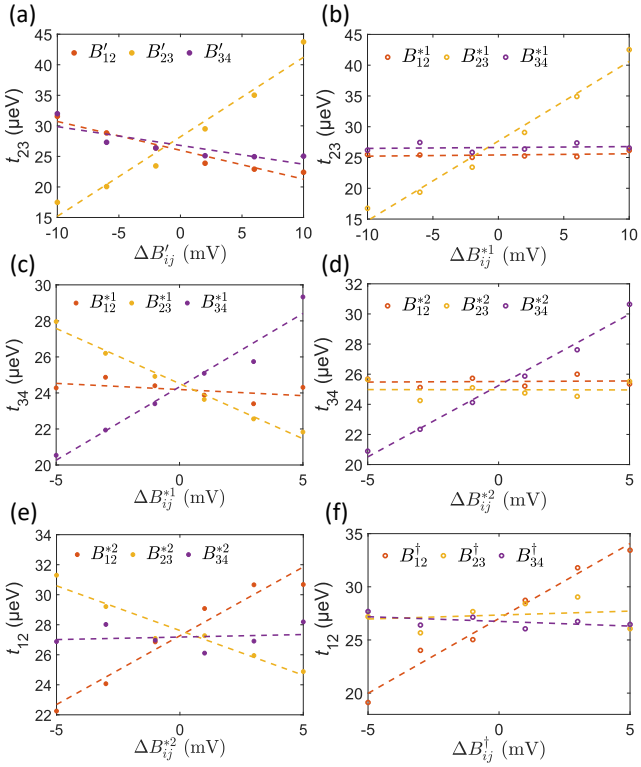

Figure 5.7: Stepwise tuning and calibration of tunnel couplings. t_{23} as a function of (a) B' and (b) B^{*1}. t_{34} as a function of (c) B^{*1} and (d) B^{*2}. t_{12} as a function of (e) B^{*2} and (f) $B^{\dagger}$.

$$\begin{pmatrix} B^{*1}_{12} \\ B^{*1}_{23} \\ B^{*1}_{34} \end{pmatrix} = \begin{pmatrix} 1 & 0 & 0 \\ -0.36 & 1 & -0.24 \\ 0 & 0 & 1 \end{pmatrix} \begin{pmatrix} B_{12} \\ B_{23} \\ B_{34} \end{pmatrix}$$

The physical gate voltages corresponding to B^{*1} are obtained from the inverse matrix. In Fig. 5.7(b), using B^{*1}, the crosstalk on t_{23} is reduced to below 2%, showing the compensation for the crosstalk. Subsequently, t_{34} is tuned to $24.7 \pm 0.2\,\mu$eV using B^{*1}_{34} ($\Delta B^{*1}_{34} = 105\,$mV). Interestingly, since B^{*1}_{34} includes the compensation for crosstalk on t_{23}, changing B^{*1}_{34} by 105 mV only affects t_{23} by $0.7\,\mu$eV (from $25.9 \pm 0.2\,\mu$eV to $26.6 \pm 0.3\,\mu$eV). This shows that t_{34} can be tuned using B^{*1}_{34} without disturbing t_{23}. The crosstalk of B^{*1} on t_{34} is shown in Fig. 5.7(c). The crosstalk matrix is updated by multiplying the matrix describing the crosstalk of B^{*1} on t_{34} by the current matrix used for defining B^{*1}, and then normalizing each row so that the diagonal elements are 1. The updated virtual barrier gates B^{*2}, which compensate for the crosstalk on t_{23} and t_{34}, are defined as

$$\begin{pmatrix} B_{12}^{*2} \\ B_{23}^{*2} \\ B_{34}^{*2} \end{pmatrix} = \begin{pmatrix} 1 & 0 & 0 \\ -0.36 & 1 & -0.24 \\ 0.23 & -0.64 & 1 \end{pmatrix} \begin{pmatrix} B_{12} \\ B_{23} \\ B_{34} \end{pmatrix}$$

In Fig. 5.7(d), using B^{*2}, the crosstalk on t_{34} is suppressed to below 1%. Next, t_{12} is tuned to $27.7 \pm 0.6\,\mu$eV using B_{12}^{*2} ($\Delta B_{12}^{*2} = 100$ mV). Again, since B_{12}^{*2} includes the compensation for crosstalk on t_{23} as well, changing B_{12}^{*2} by 100 mV only affects t_{23} by $2.4\,\mu$eV (from $26.6 \pm 0.3\,\mu$eV to $24.2 \pm 0.2\,\mu$eV). Repeating the crosstalk characterization on t_{12} in Fig. 5.7(e), $B^{\dagger}$, which include compensation for the crosstalk on all the tunnel couplings, are defined as

$$\begin{pmatrix} B_{12}^{\dagger} \\ B_{23}^{\dagger} \\ B_{34}^{\dagger} \end{pmatrix} = \begin{pmatrix} 1 & -0.84 & 0.20 \\ -0.36 & 1 & -0.24 \\ 0.23 & -0.64 & 1 \end{pmatrix} \begin{pmatrix} B_{12} \\ B_{23} \\ B_{34} \end{pmatrix}$$

In Fig. 5.7(f), using $B^{\dagger}$, the crosstalk on t_{12} are reduced to below 6%. The tunnel couplings have been tuned from an initial configuration where $(t_{12}, t_{23}, t_{34}) = (6.1 \pm 0.4, 25.9 \pm 0.2, 8.8 \pm 0.4)$ μeV to $(27.7 \pm 0.6, 24.2 \pm 0.2, 24.7 \pm 0.2)$ μeV, which is close to the target (25, 25, 25) μeV. Note that the gate voltages used in Fig. 5.7 and those in Fig. 5.3 are different. The different potential profiles caused by the gate voltages may explain the different crosstalk ratios in the two crosstalk matrices.

In summary, we have demonstrated the stepwise tune-and-calibrate procedure to tune the quadruple dot to a target configuration. In addition, $B^{\dagger}$ include the compensation for the crosstalk on all the tunnel couplings, so $B^{\dagger}$ can be used to orthogonally tune the tunnel couplings to other configurations provided that the crosstalk ratios remain the same.

REFERENCES

[1] D. Loss and D. P. DiVincenzo, *Quantum Computation with Quantum Dots,* Physical Review A **57**, 120 (1998).

[2] R. Hanson, L. P. Kouwenhoven, J. R. Petta, S. Tarucha, and L. M. K. Vandersypen, *Spins in few-electron quantum dots,* Reviews of Modern Physics **79**, 1217 (2007).

[3] F. A. Zwanenburg, A. S. Dzurak, A. Morello, M. Y. Simmons, L. C. Hollenberg, G. Klimeck, S. Rogge, S. N. Coppersmith, and M. A. Eriksson, *Silicon quantum electronics,* Reviews of Modern Physics **85**, 961 (2013).

[4] L. M. K. Vandersypen and M. A. Eriksson, *Quantum computing with semiconductor spins,* Physics Today **72**, 38 (2019).

[5] P. Barthelemy and L. M. K. Vandersypen, *Quantum Dot Systems: A versatile platform for quantum simulations,* Annalen der Physik **525**, 808 (2013).

[6] T. F. Watson, S. G. Philips, E. Kawakami, D. R. Ward, P. Scarlino, M. Veldhorst, D. E. Savage, M. G. Lagally, M. Friesen, S. N. Coppersmith, M. A. Eriksson, and L. M. K. Vandersypen, *A programmable two-qubit quantum processor in silicon,* Nature **555**, 633 (2018).

[7] D. M. Zajac, A. J. Sigillito, M. Russ, F. Borjans, J. M. Taylor, G. Burkard, and J. R. Petta, *Resonantly driven CNOT gate for electron spins,* Science **359**, 439 (2018).

[8] J. R. Petta, A. C. Johnson, J. M. Taylor, E. A. Laird, A. Yacoby, M. D. Lukin, C. M. Marcus, M. P. Hanson, and A. C. Gossard, *Coherent Manipulation of Coupled Electron Spins in Semiconductor Quantum Dots,* Science **309**, 2180 (2005).

[9] E. A. Laird, J. M. Taylor, D. P. DiVincenzo, C. M. Marcus, M. P. Hanson, and A. C. Gossard, *Coherent spin manipulation in an exchange-only qubit,* Physical Review B **82**, 075403 (2010).

[10] T. Hensgens, T. Fujita, L. Janssen, X. Li, C. J. Van Diepen, C. Reichl, W. Wegscheider, S. Das Sarma, and L. M. K. Vandersypen, *Quantum simulation of a Fermi-Hubbard model using a semiconductor quantum dot array,* Nature **548**, 70 (2017).

[11] J. P. Dehollain, U. Mukhopadhyay, V. P. Michal, Y. Wang, B. Wunsch, C. Reichl, W. Wegscheider, M. S. Rudner, E. Demler, and L. M. K. Vandersypen, *Nagaoka ferromagnetism observed in a quantum dot plaquette,* Nature **579**, 528 (2020).

[12] K. C. Nowack, M. Shafiei, M. Laforest, G. E. Prawiroatmodjo, L. R. Schreiber, C. Reichl, W. Wegscheider, and L. M. K. Vandersypen, *Single-shot correlations and two-qubit gate of solid-state spins,* Science **333**, 1269 (2011).

[13] C. Volk, A. M. J. Zwerver, U. Mukhopadhyay, P. T. Eendebak, C. J. van Diepen, J. P. Dehollain, T. Hensgens, T. Fujita, C. Reichl, W. Wegscheider, and L. M. K. Vandersypen, *Loading a quantum-dot based "Qubyte" register,* npj Quantum Information **5**, 29 (2019).

[14] A. R. Mills, D. M. Zajac, M. J. Gullans, F. J. Schupp, T. M. Hazard, and J. R. Petta, *Shuttling a single charge across a one-dimensional array of silicon quantum dots,* Nature Communications **10**, 1063 (2019).

[15] Y. P. Kandel, H. Qiao, S. Fallahi, G. C. Gardner, M. J. Manfra, and J. M. Nichol, *Coherent spin-state transfer via Heisenberg exchange,* Nature **573**, 553 (2019).

[16] M. Reed, B. Maune, R. Andrews, M. Borselli, K. Eng, M. Jura, A. Kiselev, T. Ladd, S. Merkel, I. Milosavljevic, E. Pritchett, M. Rakher, R. Ross, A. Schmitz, A. Smith, J. Wright, M. Gyure, and A. Hunter, *Reduced Sensitivity to Charge Noise in Semiconductor Spin Qubits via Symmetric Operation,* Physical Review Letters **116**, 110402 (2016).

[17] S. K. Bhattacharya and A. R. P. Rau, *Coulomb spectrum in crossed electric and magnetic fields: Eigenstates of motion in double-minimum potential wells,* Physical Review A **26**, 2315 (1982).

[18] C. J. Van Diepen, P. T. Eendebak, B. T. Buijtendorp, U. Mukhopadhyay, T. Fujita, C. Reichl, W. Wegscheider, and L. M. K. Vandersypen, *Automated tuning of inter-dot tunnel coupling in double quantum dots,* Applied Physics Letters **113**, 033101 (2018).

[19] A. R. Mills, M. M. Feldman, C. Monical, P. J. Lewis, K. W. Larson, A. M. Mounce, and J. R. Petta, *Computer-automated tuning procedures for semiconductor quantum dot arrays,* Applied Physics Letters **115**, 113501 (2019).

[20] C. Barthel, M. Kjærgaard, J. Medford, M. Stopa, C. M. Marcus, M. P. Hanson, and A. C. Gossard, *Fast sensing of double-dot charge arrangement and spin state with a radio-frequency sensor quantum dot,* Physical Review B **81**, 161308(R) (2010).

[21] T. H. Oosterkamp, T. Fujisawa, W. G. van der Wiel, K. Ishibashi, R. V. Hijman, S. Tarucha, and L. P. Kouwenhoven, *Microwave spectroscopy of a quantum-dot molecule,* Nature **395**, 873 (1998).

[22] L. DiCarlo, H. J. Lynch, A. C. Johnson, L. I. Childress, K. Crockett, C. M. Marcus, M. P. Hanson, and A. C. Gossard, *Differential Charge Sensing and Charge Delocalization in a Tunable Double Quantum Dot,* Physical Review Letters **92**, 226801 (2004).

[23] H. Qiao, Y. P. Kandel, K. Deng, S. Fallahi, G. C. Gardner, M. J. Manfra, E. Barnes, and J. M. Nichol, *Coherent multispin exchange coupling in a quantum-dot spin chain,* Physical Review X **10**, 031006 (2020).

6

ELECTRON CASCADE FOR DISTANT SPIN READOUT

The spin of a single electron in a semiconductor quantum dot provides a well-controlled and long-lived qubit implementation. The electron charge in turn allows to control the position of individual electrons in a quantum dot array, and enables charge sensors to probe the charge configuration. Here we show that the Coulomb repulsion allows an initial charge transition to induce subsequent charge transitions, inducing a cascade of electron hops, like toppling dominoes. A cascade can transmit information along a quantum dot array over a distance that extends by far the effect of the direct Coulomb repulsion. We demonstrate that a cascade of electrons can be combined with Pauli spin blockade to read out distant spins and show results with potential for high fidelity using a remote charge sensor in a quadruple quantum dot device. We implement and analyse several operating modes for cascades and analyse their scaling behaviour. We also discuss the application of cascade-based spin readout to densely-packed two-dimensional quantum dot arrays with charge sensors placed at the periphery. The high connectivity of such arrays greatly improves the capabilities of quantum dot systems for quantum computation and simulation.

This chapter has been published as C. J. van Diepen, T.-K. Hsiao, U. Mukhopadhyay, C. Reichl, W. Wegscheider, and L. M. K. Vandersypen, Nature Communications **12**, 77 (2021).

6.1. INTRODUCTION

Fault-tolerant quantum computation benefits from high connectivity, and requires fast and high-fidelity readout [1]. Qubit connectivity and density are severely limited when charge sensors need to be placed near all quantum dots in the qubit array. Not only the charge sensors themselves take space, but in addition they require a nearby electron reservoir which takes even more space. Several proposals for quantum processors based on gate-defined quantum dots, suggest gate-based readout of two-dimensional arrays to overcome this limitation [2–5]. The comparatively low signal-to-noise ratio (SNR) of this approach has hindered reaching the fidelity required for fault-tolerant quantum computation [6–9]. Signal enhancement has been achieved with a latching scheme [10–12], but does not enable the readout of dots far from the sensor. Readout based on shuttling [13] requires paths of empty dots to avoid that qubits are lost into the reservoirs, and the long-distance movement of electrons breaks qubit connectivity. Alternatively, readout via a sequence of swap operations is limited by the product of all the swap fidelities [14, 15].

We show that charge information can be transferred along a quantum dot array with a cascade, in which the spin-dependent movement of one electron induces the subsequent movement of other electrons. Cascades are used in various fields and technologies: stimulated emission [16] in lasers, secondary emission [17] in photomultiplier tubes, impact ionization in avalanche photodiodes [18], and neutron induced decay in nuclear fission [19]. A cascade has also been used to build classical logic with molecules in scanning-tunneling microscopes [20] and with excess electrons in cellular automata based on Al islands [21, 22].

6.2. DEVICE AND CASCADE CONCEPT

The prototype for cascade-based readout with quantum dots consists of a quadruple dot and a sensing dot. A scanning electron micrograph image of a device similar to the one used in the experiment is shown in Fig. 6.1a. The device is operated at 45 mK and without an external magnetic field, unless specified otherwise. By applying voltages on the electrodes on the surface we shape the potential landscape in a two-dimensional electron gas 90 nm below, formed in a silicon-doped GaAs/AlGaAs heterostructure. The plunger gates, labelled with P_i, control the electrochemical potentials of the dots, and the barrier gates control the tunnel couplings between dots or between a dot and a reservoir.

Figure 6.1b schematically illustrates the cascade-based readout concept. The first step of the protocol is to perform spin-to-charge conversion, based on Pauli spin blockade (PSB)[23], which induces an initial charge transition conditional on the spin state of the two leftmost electrons. This transition induces a chain reaction of charge transitions with a final charge transition nearby the sensor, which results in a large change in sensor signal. Resetting the cascade can be achieved by undoing the initial charge transition.

6.3. QUANTUM DOT TUNING AND CHARGE-STABILITY DIAGRAMS

Figure 6.2a shows a charge-stability diagram with transitions for the two dots on the left. Unless specified differently, the sensing dot is operated on the low-voltage flank of a Coulomb peak throughout this work. For the tuning and measurements, virtual plunger

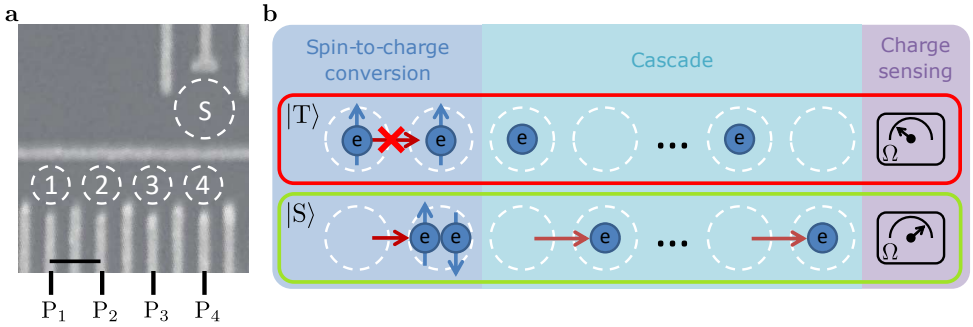

Figure 6.1: Device and cascade concept. a Scanning electron micrograph of a device nominally identical to the one used for the experiments. Dashed circles labelled with numbers indicate quantum dots in the array, and the dashed circle labelled with "S" is the sensing dot. The scale bar corresponds to 160 nm. **b** Schematic illustration of spin-to-charge conversion combined with a cascade for electron spin readout on dots far from the charge sensor.

gates $\widetilde{P_i}$ were used for electrochemical potentials [24–26] and virtual barrier gates for tunnel couplings [24, 27, 28]. The charge occupation of the four dots is indicated by the numbers in round brackets. The voltages were swept rapidly from right to left (left to right in panel c) and slowly from bottom to top. With these sweep directions, a white trapezoid caused by PSB is visible to the top-left of the inter-dot transition in the charge-stability diagram, with the sensor signal in between the signal for the (1100) and (0200) charge regions. The trapezoid is the region suited for PSB readout. The distance between the inter-dot line, which is the base of the trapezoid, and the top of the trapezoid, corresponds to the singlet-triplet energy splitting.

Cascade Pauli spin blockade (CPSB) is seen in the charge-stability diagram of Fig. 6.2b. The fourth dot is tuned close to a charge transition, such that the movement of an electron on the left pair induces a change in charge occupation of the fourth dot. See Supplementary Material 6.6.2 for details on the tuning of the fourth dot and the sensor for the different charge occupations. Supplementary Material 6.6.3 contains an analysis of the anti-crossing sizes.

The charge-stability diagram in Fig. 6.2c shows both the charge states for PSB and for CPSB readout. This diagram is obtained by varying the detuning of the left pair and the potential of the fourth dot. In this diagram there are three different regimes in $\Delta\widetilde{P}_4$. The left and right regions, with charge transitions indicated with a dashed line, can be used for PSB, with dot 4 unoccupied and occupied respectively. The middle region, with a charge transition indicated with a dotted line, can be used for CPSB.

The tuning requirements of the dot potentials for CPSB readout can be further understood from the ladder diagram in Fig. 6.2d. Dot 4 needs to be tuned such that $\mu_4(1101) < 0 < \mu_4(0201)$, with the electrochemical potential defined as $\mu_i(\ldots,N_i,\ldots) = E(\ldots,N_i,\ldots) - E(\ldots,N_i-1,\ldots)$, where E is the energy, N_i is the number of electrons on dot i, and the Fermi level in the reservoirs is by convention set to zero. This level alignment corresponds to the middle region in Fig. 6.2c, while the left (right) region corresponds to $\mu_4(1101)$ and $\mu_4(0201)$ both above (below) the Fermi level. Note that if $\mu_{2,S}(0201)$ is above $\mu_1(1101)$, the cascade in CPSB readout involves a co-tunnel process (see Supplementary

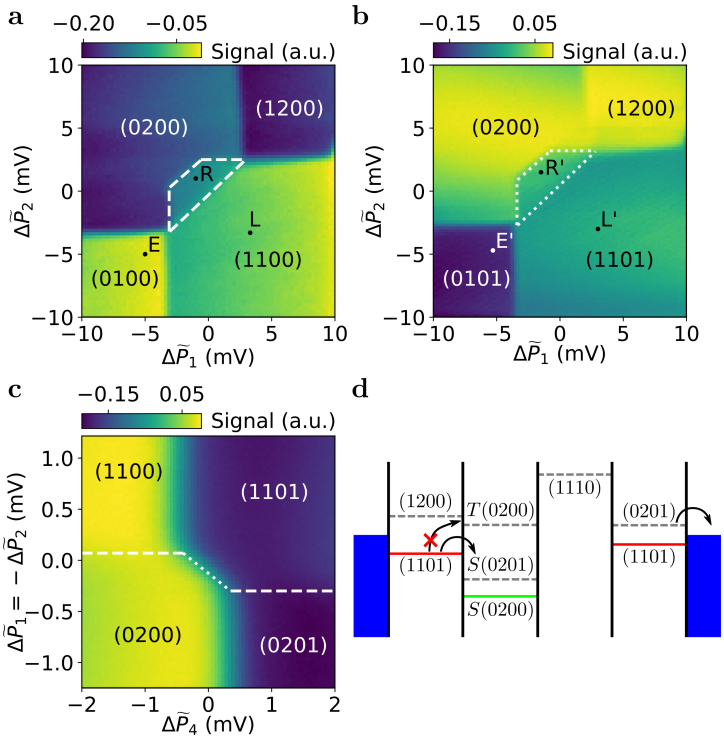

Figure 6.2: Quantum dot tuning for cascade-based readout. Numbers in round brackets indicate charge occupations of the dots. **a** Charge-stability diagram with transitions for dots 1 and 2. The white, dashed trapezoid on the top-left side of the inter-dot is the Pauli spin blockade (PSB) readout region. The black dots indicate the voltages for the PSB readout cycle: E(mpty), L(oad) and R(ead). **b** Charge-stability diagram similar to **a**, but with different occupations of the rightmost dot. The white, dotted trapezoid is the cascade Pauli spin blockade (CPSB) readout region. White and black dots labelled with E′, L′ and R′ indicate the pulse positions for the CPSB readout cycle. Note that the voltages at the origin are different from those in **a**. **c** Charge-stability diagram showing both the charge states for PSB and CPSB readout. Dashed (dotted) lines correspond to the charge transitions for the PSB (CPSB) readout regions. **d** Ladder diagram illustrating the alignment of the dot electrochemical potentials for the CPSB at the readout point. For a triplet state, the system remains in (1101) (red), whereas for as singlet state it transitions to (0201) and then (0200) (green).

Material 6.6.6). In an alternative implementation, we also perform CPSB readout with a charge transition between (1110) and (0201) (see data in Supplementary Material 6.6.5).

6.4. SINGLE-SHOT READOUT AND FIDELITY ANALYSIS

For single-shot PSB readout, voltage pulses are applied as indicated by the black circles in Fig. 6.2a. The pulse sequence starts in point E, where the charge occupation is (0100). Then the voltages are pulsed to point L, where an electron is loaded from the reservoir onto the leftmost dot reaching the (1100) charge occupation with random spin configuration. Finally, the voltages are pulsed to the readout point, R, where Pauli spin blockade forces a triplet to remain in the (1100) charge occupation while the singlet transitions to the (0200) charge occupation.

In Fig. 6.3a the results of 10,000 single-shot measurements are shown in a histogram. The integration time is $t_{int} = 1.5\,\mu s$. The peak at lower sensor signal corresponds to the (0200) charge occupation, and is assigned as singlet, while the peak at higher sensor signal corresponds to the (1100) charge occupation, which is assigned as a triplet. Residual overlap between the singlet and triplet distributions induces errors in the distinction of the two charge states, resulting in errors in the spin readout. The inset shows the signal averaged over the single-shot measurements as a function of the time stamp of the integration window. From an exponential fit, the relaxation time, $T_1 = 724(70)\,\mu s$, is obtained (see Supplementary Material 6.6.7).

For CPSB readout, a pulse cycle similar to that for PSB is used. The sensing dot is operated with comparable sensitivity as for PSB readout. The pulse voltages are indicated with white and black circles in Fig. 6.2b. The pulse sequence again consists of empty, E′, load, L′, and readout, R′. For CPSB, the charge occupation in E′ is (0101), and in L′, again an electron is loaded on the left dot forming the charge state (1101) with a random spin configuration. At the readout point, due to Pauli spin blockade, the two electrons on the left remain on separate dots if they are in a triplet state, which results in the charge state (1101). When the two electrons on the left form a singlet state the resulting charge state will be (0200), because the electron on the left dot moves one dot to the right, and the electron on the fourth dot is pushed off due to the cascade effect (here $\mu_1(1101) > \mu_{2,S}(0201)$, so the two charge transitions can occur sequentially, as discussed above).

Figure 6.3b shows a histogram of 10,000 CPSB single-shot measurements. The integration time, 1.5 µs, is the same as for the PSB single-shot data. The peak at lower sensor signal corresponds to the (1101) charge state, and is assigned as triplet, while the peak at higher sensor signal corresponds to the (0200) charge state, which is assigned as singlet. The residual overlap between the singlet and triplet distributions is strongly reduced for CPSB as compared to PSB. Again, from an exponential fit to the averaged single-shot measurements (inset Fig. 6.3b), the relaxation time, $T_1 = 680(3)\,\mu s$, is obtained.

The cascade enhances the signal-to-noise ratio for distinguishing between the singlet and triplet states by a factor of 3.5, extracted by comparing the histogram of CPSB to that of PSB. The SNR is defined as $|V_T - V_S|/\bar{\sigma}_{FWHM}$, with V_T and V_S the signals for a triplet and singlet state respectively, and $\bar{\sigma}_{FWHM}$ the average of the full width at half maximum of the singlet and the triplet probability distributions. Furthermore, Fig. 6.3 shows that for PSB the charge signal for the singlet is lower than that for a triplet, while

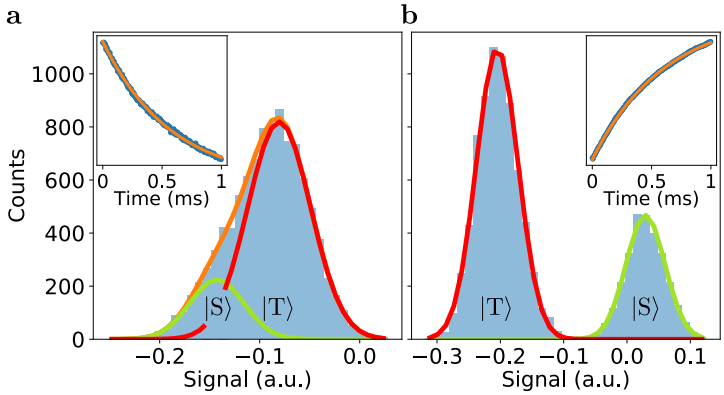

Figure 6.3: Single-shot readout. Histograms and fits of 10,000 single-shot measurements for **a** PSB readout and **b** CPSB readout. The integration time is t_{int} = 1.5µs. The orange lines are fits to the histograms [9, 23] and red and green solid lines correspond to respectively the triplet and singlet probability distributions. The left (right) inset shows the signal in arbitrary units averaged over the PSB (CPSB) single-shots as a function of wait time in the readout point, and an exponential fit to the data. **a** For PSB readout the singlet corresponds to charge occupation (0200) and the triplet to (1100). **b** For cascade PSB readout the singlet also corresponds to (0200) but the triplet corresponds to (1101), thus with an electron on dot 4.

for CPSB the charge signal for a singlet is actually higher than for a triplet. We note that changes in screening or shifts in dot positions, do not explain the sensor signals for the different charge occupations.

The enhanced SNR for CPSB readout arises from two contributions. The first contribution is directly due to the cascade, which maps a charge transition far from the sensor to a charge transition nearby the sensor. The longer the cascade, the larger the relative difference, because the final charge transition remains close to the sensor, while the initial transition is further away for a longer cascade, thus inducing a weaker sensor signal. The second contribution to the SNR enhancement is because the initial charge transition is an inter-dot transition, while the final transition induced by the cascade is a dot-reservoir transition, which has a stronger influence on the sensor.

As for which spin state produces the highest charge signal, for the case of PSB the singlet signal corresponds to a charge moving closer to the charge sensor, thus the sensor signal goes down. For CPSB a singlet outcome also causes a charge to move closer to the charge sensor, but on top of that a charge is pushed out of the fourth dot, reducing the total charge on the dot array and removing a charge which was very close to the sensor. In this case the two contributions to the signal partially cancel each other, but the resulting effect on the charge sensor is still stronger for CPSB than for conventional PSB. In Supplementary Material 6.6.5 CPSB is implemented such that the charge transition induced by the cascade corresponds to an electron moving closer to the sensor, by having an electron move from dot 3 to dot 4. In this case the signal was enhanced by a factor of 3.1 as compared to PSB. Here the effects on the charge sensor of the initial and the final charge transitions add up, but there is no second contribution to the signal enhancement as there is not a mapping of an inter-dot transition to a dot-reservoir transition.

The average spin readout fidelity with CPSB is potentially above 99.9%, and is achieved within the 1.7 µs readout time. The fidelity for conventional PSB with the same integration time is 85.6%. These fidelities are obtained by analysing different error sources: residual overlap, relaxation, and excitation, but do not include errors in the mapping from the (1101) spin states to the measurement basis at the readout point. Here, we provide details on the analysis for CPSB (see Supplementary Material 6.6.8 for details on PSB). The residual overlap between the charge signals and relaxation events during the integration time result in an error of $\eta_{hist} = 0.068\%$ for the average readout fidelity [9, 23], as determined from the fit to the single-shot histogram (See Supplementary Material 6.6.4). Relaxation during the arming time, $t_{arm} = 0.2\,\mu s$, contributes an error of 0.015%. During the arming time, which is the time between the start of the readout pulse and the start of the integration window, the signal is not analysed as it is still rising due to the limited measurement bandwidth. Excitation during the arming and integration time causes an error in the average readout fidelity of 0.014%, with the excitation time, $T_{exc} = 6.0(3)\,ms$ (see Supplementary Material 6.6.7). The spin readout fidelity will be affected by mapping errors, which can be caused by fluctuations in the hyperfine field (see Supplementary Material 6.6.9), high-frequent charge noise, leakage states, and relaxation and excitation during the voltage ramp. The spin readout fidelity including mapping errors can be obtained experimentally by performing high-fidelity deterministic state preparation. Supplementary Material 6.6.6 provides an analysis on scaling of the cascade.

6.5. DISCUSSION

A cascade can be implemented in various quantum dot array layouts. Figure 6.4a shows a schematic illustration of an example of cascade-based spin readout in a two-dimensional array. The quantum dots are filled in a chequerboard manner, compatible with the proposal in [4], and the sensor is placed at the periphery of the two-dimensional array, with sufficient space for reservoirs. The cascade is implemented by forming a path of dots which are each tuned close to a charge transition, while the dots outside the cascade path are tuned deep in Coulomb blockade so their occupations are unchanged. By tuning different cascade paths the same sensor can be used for the readout of spins at different locations in the quantum dot array. Cascades can also be designed in a fanout shape, as schematically illustrated in Fig. 6.4b. The ends of multiple cascade paths, both triggered by the same initial spin-dependent charge transition, converge at the same sensor, thus increasing the change in charge distribution in the vicinity of the sensor, which increases the SNR and the readout fidelity. Figure 6.4c shows another example of fanout of cascade paths, with at the end of each path a sensor. The signal from multiple sensors can be combined to achieve higher SNR and increased readout fidelity. The cascade-based readout can also be performed at higher filling, as schematically illustrated in Fig. 6.4d, in which each dot is occupied with an electron. The dot emptied by PSB enables the electrons in the cascade to move, which results in a charge moving away from the sensor. In this implementation the voltage pulse for PSB is first performed, and subsequently a voltage pulse is sent to tune the dot array to activate the cascade. This two-step procedure suppresses co-tunnelling from (111…) to (210…) without occupying (201…), which can be further suppressed by pulses that lower the relevant tun-

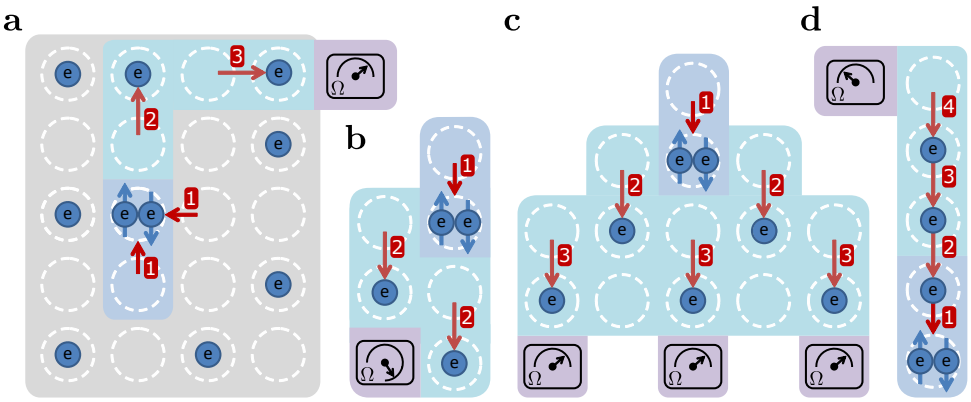

Figure 6.4: Cascade-based readout in 2D, fanout and a dense array. Schematic illustrations of cascade-based readout **a** in a two-dimensional quantum dot array, **b** using fanout of cascade paths that converge on a single sensor, **c** for fanout with multiple sensors, and **d** in a one-dimensional array with each dot occupied by an electron and where the electrons move away from the sensor. Coloured regions indicate the different aspects of the cascade-based spin readout, with the same colour coding as in Fig. 6.1b. Numbers indicate the order of the transitions. In **d** first PSB is performed, then the cascade is activated.

nel couplings. Accidental dot-reservoir transitions, particularly relevant for cascades at higher filling (see Supplementary Material 6.6.3), can be prevented by operating in an isolated regime [29, 30].

We end with a few important considerations on the usefulness of the cascade mechanism for spin readout. First, each electron along a cascade path can itself still be operated as a spin qubit, because phase shifts and reproducible (artificial or natural) spin-orbit induced rotations due to the motion of the electrons can be accounted for in hardware or software [31]. Second, as the length of the cascade path increases, both the spin readout fidelity and the timing of the motion of the electrons, can be largely maintained by allowing a cascade to propagate step-by-step using a series of voltage pulses applied to successive dots, see Supplementary Material 6.6.6. Third, the increased SNR from cascades, and the option of further increases through fanout, may enable high-fidelity readout with sensing dots at elevated temperatures [30, 32], because the enhanced signal compensates for the additional thermal noise, allowing higher cooling power and integration with cryogenic control or readout electronics [3]. Fourth, the cascade can also be performed with other spin-to-charge conversion methods, for example with energy-selective tunnelling [33]. Such readout with a cascade does not require a charge sensor nearby the spin to read out, but it does require a nearby reservoir for the initial charge transition. Last, when a quantum dot array is operated with cascade-based readout for qubits then extra caution should be taken for handling correlated errors as these may occur due to capacitive coupling between electrons inside and outside the cascade path.

In conclusion, we have demonstrated a cascade of electrons in a quantum dot array. We combined the cascade with Pauli spin blockade, and achieve spin readout fidelity potentially above 99.9% in 1.7 µs, even though the electrons were far from the charge sensor. We proposed that a cascade-based readout scheme will enable high-fidelity readout of spins in the interior of a two-dimensional quantum dot array, and that fanout

of cascades can be used to enhance the signal further. Other platforms, for example topological qubits, can also benefit from a cascade-based readout, when combined with parity-to-charge conversion [34]. The cascade of electrons opens up a new path for high-fidelity readout in large-scale quantum dot arrays, which is compatible with the established, high-sensitivity, charge sensor, paving the way for further progress in quantum computation and simulation with quantum dot arrays.

6.6. SUPPLEMENTARY MATERIAL

6.6.1. METHODS

DEVICE AND SET-UP

The material for the sample was grown with molecular beam epitaxy and consists of a GaAs/$Al_{0.3}Ga_{0.7}As$ heterostructure with a silicon doping layer of density 7×10^{12} cm^{-2} at 50 nm depth from the surface. A two-dimensional electron gas (2DEG) was formed at the interface, which is 90 nm below the surface. The mobility was 1.6×10^6 cm^2/Vs at an electron density of 1.9×10^{10} cm^{-2}, measured at 4 K. A single layer of metallic gates (Ti/Au) is defined by electron-beam lithography. The gate pattern was designed to define eight quantum dots and two sensing dots. The device was cooled inside an Oxford Kelvinox 400HA dilution refrigerator to a base temperature of 45 mK. To reduce charge noise, the sample was cooled with bias voltages on the gates varying between 100 and 200 mV. Gates P_1, P_2, P_3 and P_4 were connected to bias-tees ($RC = 470$ ms), enabling application of a d.c. voltage as well as high-frequency voltage pulses. Voltage pulses were generated with a Tektronix AWG5014. The sensing dot resistance was probed with radio-frequency reflectometry. The *LC* circuit for the reflectometry matched a carrier wave of frequency 97.2 MHz. The inductor, $L = 3.9$ µH, was a homebuilt, micro-fabricated NbTiN superconducting spiral inductor, and was wire-bonded to an ohmic contact. The reflected signal was amplified at 4 K with a Weinreb CITLF2 amplifier, and at room-temperature I/Q demodulated to baseband and filtered with a 10 MHz low-pass filter. Data acquisition was performed with a Spectrum M4i digitizer card. After digitization, the I and Q components of the signal were combined with inverse-variance weighting.

HIGH-FREQUENCY VOLTAGE CONTROL

The voltages for the charge-stability diagrams were simultaneously swept in 78 µs for the horizontal direction, and 6.2 ms for the vertical direction. The signal was averaged over 1,000 repetitions of such voltage scans. For the single-shot measurements the voltage pulse durations were 100 µs, 100 µs, and 1 ms for respectively the empty, load and read stage. After the read stage a compensation stage of 1 ms was performed to prevent accumulation of charge on the bias-tees.

SOFTWARE

The software modules used for data acquisition and processing were the open source python packages QCoDeS, which is available at https://github.com/QCoDeS/Qcodes, and QTT, which is available at https://github.com/QuTech-Delft/qtt.

READOUT ERRORS

The error in the average charge readout fidelity, caused by relaxation during the arming time is estimated to be below $\eta_{arm} = \frac{1}{2}\left(1 - \exp\left(-t_{arm}/T_1\right)\right) = 0.015\%$. The error due to excitation during the arming and integration time is estimated to be below $\eta_{exc} = \frac{1}{2}(1 - \exp(-(t_{arm} + t_{int})/T_{exc}) = 0.014\%$. The mapping error in spin readout due to charge non-adiabaticity (and slow subsequent charge relaxation) can be estimated with the Landau-Zener formula to $\eta_{LZ} = \exp\left(-\frac{2\pi\alpha^2\Delta t}{\hbar\Delta E}\right) = 10^{-9}\%$, with $\alpha = \sqrt{2}t_{c,12}$, and $t_{c,12} = 11.5$ µeV the tunnel coupling between dots 1 and 2, which is obtained from a spin funnel (see Supplementary Material 6.6.10), $\Delta t = 10$ ns is the ramp time of the pulse to the

readout point and $\Delta E \approx 1$ meV is the change in double dot detuning from the load to the readout point. Note that charge-noise can suppress the Landau-Zener transition probability, thus increasing the spin readout error due to charge non-adiabaticity.

6.6.2. SIGNAL IN CASCADE CSD

The signal for Fig. 6.2b was taken with the fourth dot and the sensor tuned such that all charge occupations result in clearly distinguishable signals. The signal for (1101) is higher than that for (0101), because the rightmost dot was close to the Fermi level for (1101), and thus only partially occupied. The signal for (1200) is higher than for (0200), because the signal for these occupations is from the high-voltage flank of a sensing dot Coulomb peak. The other relative signals are as intuitively expected, namely adding charges and bringing charges closer to the sensor both result in a reduced sensor signal.

6.6.3. OPERATING WINDOW FOR CASCADE READOUT

In order to get insight in the size of the operating window for PSB, CPSB and inter-dot CPSB (iCPSB), we start from the single-band Fermi-Hubbard Hamiltonian for the quantum dot array [24]:

$$H = -\sum_i \epsilon_i n_i + \sum_i \frac{U_i}{2} n_i(n_i - 1) + \sum_{ij, i\neq j} V_{ij} n_i n_j - \sum_{\langle i,j\rangle} t_{c,ij}\left(c_i^\dagger c_j + h.c.\right), \tag{6.1}$$

where ϵ_i is the single-particle energy offset, $n_i = c_i^\dagger c_i$ is the dot occupation, and $c_i^{(\dagger)}$ is the annihilation (creation) operator, U_i is the on-site Coulomb repulsion, and V_{ij} the inter-site Coulomb repulsion. For simplicity, we assume in what follows homogeneous Coulomb repulsion, thus $U_i = U$, $V_{i,i+1} = V$, $V_{i,i+2} = V'$, and $V_{i,i+3} = V''$, and neglect tunnel coupling. The shifts of charge transition lines due to capacitive couplings, and the tuning of dot potentials for each of the different readout schemes, namely PSB, CPSB and iCPSB, are obtained by solving sets of constraints. Note that, because the interaction strength decays with distance, the size of the operating window for a charge transition only depends on the occupation of nearby dots. This implies that the sizes of the operating windows remain constant as the length of the cascade is extended.

PAULI SPIN BLOCKADE

The on-site potential ϵ_1 must satisfy $\mu_1(1200) > 0 > \mu_1(1100)$, which yields $2V > \epsilon_1 > V$. The constraint for ϵ_2 follows from $E(1200) > E(1100) > E(0200)$, which yields $U + V > \epsilon_2 > \epsilon_1 + U - V$. From these constraints it follows that the shifts of the relevant charge transition lines due to capacitive couplings are V when projected onto ϵ_1 or ϵ_2. For the two dots on the right to remain empty $\mu_3(1010) > 0$ and $\mu_4(1001) > 0$, which respectively yield $\epsilon_3 < V'$ and $\epsilon_4 < V''$.

CASCADE WITH DOT-RESERVOIR

The constraint for dot 1 is now $\mu_1(1200) > 0 > \mu_1(1101)$, which yields $2V > \epsilon_1 > V + V''$. We also require $E(1200) > E(1101) > E(0200)$, which yields $\epsilon_4 + U + V - V' - V'' > \epsilon_2 > \epsilon_1 + \epsilon_4 + U - V - V' - V''$. For the rightmost dot, the cascade occurs when $\mu_4(0201) >$

$0 > \mu_4(1101)$, which yields $2V' > \epsilon_4 > V' + V''$. From these constraints it follows that the shifts of the relevant charge transition lines are $V - V''$ when projected onto ϵ_1 or ϵ_2, and $V' - V''$ when projected onto ϵ_4 or onto $\epsilon_1 - \epsilon_2$. For the third dot to remain empty $\mu_3(1110) > 0$, which yields $\epsilon_3 < V'$.

CASCADE WITH INTER-DOT

For the leftmost dot $\mu_1(1201) > 0 > \mu_1(1110)$, which yields $2V + V'' > \epsilon_1 > V + V'$. Another requirement is $E(1201) > E(1110) > E(0201)$, which yields $\epsilon_3 - \epsilon_4 + U + V'' > \epsilon_2 > \epsilon_1 + \epsilon_3 - \epsilon_4 + U - 2V + V'$. For the two dots on the right, the cascade effect takes place when $\mu_3(1110) < \mu_4(1101)$, which yields $\epsilon_3 - \epsilon_4 > V - V''$, and $\mu_3(0210) > \mu_4(0201)$, which yields $\epsilon_3 - \epsilon_4 < 2V - 2V'$. In addition, for the rightmost dot, we need $\mu_4(0201) < 0 < \mu_4(1111)$, which yields $2V' < \epsilon_4 < V + V' + V''$. From these constraints it follows that the shifts of the relevant charge transition lines are $V - V' + V''$ when projected onto ϵ_1 or ϵ_2, and $V - 2V' + V''$ when projected onto $\epsilon_1 - \epsilon_2$ or $\epsilon_3 - \epsilon_4$.

AT HIGHER FILLING

For the cascade-based readout in an array with all sites initially occupied the charge occupation after the cascade is $(1\ldots1)$ or $(21\ldots10)$. The electron-electron interaction decays with distance, thus may be too weak to prevent the $(1\ldots1)$ state from becoming a $(21\ldots1)$ state, while $(21\ldots10)$ is preserved, or similarly to prevent $(21\ldots10)$ from becoming $(21\ldots1)$, while $(1\ldots1)$ is preserved. The unwanted loading of electrons can be suppressed by operating the cascade with low couplings to reservoirs or in the isolated regime [29, 30].

6.6.4. SINGLE-SHOT HISTOGRAM

The single-shot histograms are modeled with [23]

$$N(x) = N_{\text{tot}} \left[P_S n_S(x) + (1 - P_S) n_T(x) \right] w_{\text{bin}} \tag{6.2}$$

with N_{tot} the total number of single-shot repetitions, P_S the average singlet probability over al single-shot outcomes, w_{bin} the bin width, and n_S and n_T the probability density distribution for the singlet and triplet states respectively. The probability density distributions are modeled by noise-broadened Gaussians as

$$n_S(x) = \frac{1}{\sqrt{2\pi}\sigma} e^{-(x-\mu_S)^2/2\sigma^2}, \tag{6.3}$$

and

$$n_T(x) = \frac{1}{\sqrt{2\pi}\sigma} \Big[e^{-t_{\text{int}}/T_1} e^{-(x-\mu_T)^2/2\sigma^2} + \frac{t_{\text{int}}}{T_1} \int_{\mu_T}^{\mu_S} \frac{1}{\mu_S - \mu_T} e^{-[(x'-\mu_T)/(\mu_S-\mu_T)](t_{\text{int}}/T_1)} e^{-(x-x')^2/2\sigma^2} dx' \Big], \tag{6.4}$$

where the second term accounts for relaxation during the integration time, where μ_S and μ_T are the means and σ the standard deviation of the gaussians for the singlet and triplet

density distributions respectively. T_1 is the triplet-singlet relaxation time obtained from an exponential fit to the averaged data as shown in the insets of Fig. 6.3, and t_{int} is the integration time.

From the probability density distributions we obtain the uncorrected readout fidelities as

$$F_S = 1 - \int_{V_T}^{\infty} n_S(x)\,dx, \qquad F_T = 1 - \int_{-\infty}^{V_T} n_T(x)\,dx, \tag{6.5}$$

with V_T the signal threshold, and $F_{\text{avg}} = \frac{1}{2}(F_S + F_T)$. These uncorrected readout fidelities include errors due to residual overlap of the histograms and relaxation during the integration time. We afterwards correct the readout fidelity for errors due to relaxation during the arming time, and errors due to excitation during the integration and arming time as described in the main text.

6.6.5. INTER-DOT CASCADE PAULI SPIN BLOCKADE

An alternative implementation for cascade-based readout in a quadruple dot is shown in Fig. 6.5. The additional electron moves from the third dot to the fourth dot, thus the cascade involves an inter-dot transition. The signal is from the left flank of a Coulomb peak of the sensing dot. The signal changes of the two charge transitions now add up, thus a singlet state corresponds, as with Pauli spin blockade, to the peak at lower signal and a triplet state corresponds to the peak at higher signal.

6.6.6. THEORY ON CASCADE SPEED AND SUCCESS PROBABILITY

In order to assess the scalability of the cascade-based readout, we analyse the speed and adiabaticity of the movement of charges in the cascade. The speed of the cascade is important since spin measurement must be faster than spin relaxation for achieving high-fidelity spin readout. Furthermore, spin readout must be faster than spin decoherence (with dynamical decoupling) for achieving fault-tolerance using feedback in quantum error correction. The adiabaticity with respect to charge is important when the Zeeman splitting is different between quantum dots. For different Zeeman splitting, the uncertainty in the electron position results in a phase error.

CO-TUNNEL CASCADE PAULI SPIN BLOCKADE

When the cascade is operated such that $E(S(0201)), E(1100) > E(1101)$, then the cascade occurs via a co-tunnel process, and the cascade can be operated adiabatically. For a quantum dot array with length four and when the cascade involves a dot-reservoir transition, the relevant charge states are (1101), (0200), (1100) and (0201). The Hamiltonian in this basis is

$$\begin{pmatrix} -\epsilon_1 - \epsilon_2 - \epsilon_4 + V + V' + V'' & 0 & -t_{c,4R} & -\widetilde{t}_{c,12} \\ 0 & -2\epsilon_2 + U & -\widetilde{t}_{c,12} & -t_{c,4R} \\ -t_{c,4R} & -\widetilde{t}_{c,12} & -\epsilon_1 - \epsilon_2 + V & 0 \\ -\widetilde{t}_{c,12} & -t_{c,4R} & 0 & -2\epsilon_2 - \epsilon_4 + U + 2V' \end{pmatrix}, \tag{6.6}$$

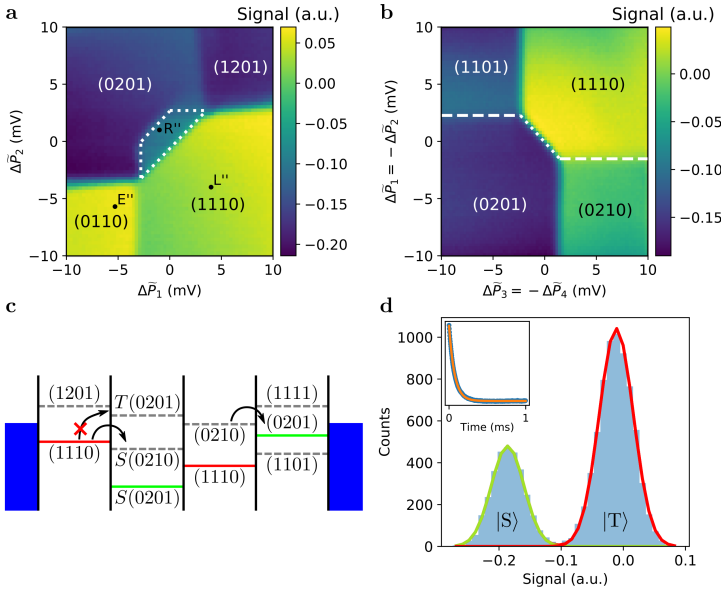

Figure 6.5: Cascade-based readout with inter-dot transition. Numbers in round brackets indicate charge occupations of the dots. **a** Charge-stability diagram as a function of the virtual plunger gates of dots 1 and 2. The trapezoid on the top-left side of the inter-dot transition is the inter-dot cascade Pauli spin blockade (iCPSB) window. The black dots indicate the voltages for the iCPSB readout cycle: E″(mpty), L″(oad) and R″(ead). **b** Charge-stability diagram showing the effect of the inter-dot transition for dots 1 and 2 on the inter-dot transition for dots 3 and 4. On the left and the right, the electron in dot 3 or 4 stays in place when an electron moves from dot 1 to dot 2. In the center, an electron moves from dot 3 to dot 4 when the electron on dot 1 is pushed to dot 2. This corresponds to an inter-dot cascade effect. **c** Ladder diagram corresponding to the readout point R″, illustrating the tuning of the dot potentials for the cascade Pauli spin blockade with inter-dot transition. Note that $\mu_{2,S}(0210)$ is drawn below $\mu_1(1110)$, but for the cascade it could also be above. **d** Histograms and fits of 10,000 single-shot measurements for iCPSB readout. The integration time is t_{int} = 1.5µs. Red and green solid lines correspond to the respectively triplet and singlet probability distributions, obtained from the fit to the histogram [9, 23]. For iCPSB readout the singlet corresponds to charge occupation (0201) and the triplet to (1110). The inset shows the signal averaged over the single-shots and an exponential fit, with T_1 = 75.0(2) µs.

with $\widetilde{t}_{c,12} = \sqrt{2}t_{c,12}$, and $t_{c,4R}$ the tunnel coupling between the rightmost dot and the right reservoir. Rewrite the Hamiltonian as

$$\begin{pmatrix} \frac{\widetilde{\epsilon}}{2} & 0 & -t_{c,4R} & -\widetilde{t}_{c,12} \\ 0 & -\frac{\widetilde{\epsilon}}{2} & -\widetilde{t}_{c,12} & -t_{c,4R} \\ -t_{c,4R} & -\widetilde{t}_{c,12} & \frac{V'-V''+\widetilde{\delta}}{2} & 0 \\ -\widetilde{t}_{c,12} & -t_{c,4R} & 0 & \frac{V'-V''-\widetilde{\delta}}{2} \end{pmatrix}, \tag{6.7}$$

with $\widetilde{\epsilon} = \epsilon - U + V + V' + V''$, and $\widetilde{\delta} = \delta - U + V - 2V'$, where $\epsilon = \epsilon_{12} + \epsilon_4$, and $\delta = \epsilon_{12} - \epsilon_4$, with $\epsilon_{12} = -\epsilon_1 + \epsilon_2$. By diagonalising this Hamiltonian, with approximation $|\widetilde{\epsilon}| \ll |V' - V'' \pm \widetilde{\delta}|$, the co-tunnel coupling between the eigenstates that are predominantly (1101) and (0200) is $t_{co} = \frac{\widetilde{t}_{c,12}t_{c,4R}}{\Delta_+} + \frac{\widetilde{t}_{c,12}t_{c,4R}}{\Delta_-}$, with $\Delta_\pm = \frac{V'-V''\pm\widetilde{\delta}}{2}$ [35].

CO-TUNNEL INTER-DOT CASCADE PAULI SPIN BLOCKADE

The analysis for a cascade involving co-tunnelling and only inter-dot transitions is very similar as for the co-tunnel cascade with a dot-reservoir transition. For cascade with an inter-dot transition, the relevant charge states are (1110), (0201), (1101) and (0210). The Hamiltonian in this basis is

$$\begin{pmatrix} -\epsilon_1 - \epsilon_2 - \epsilon_3 + 2V + V' & 0 & -t_{c,34} & -\widetilde{t}_{c,12} \\ 0 & -2\epsilon_2 - \epsilon_4 + U + 2V' & -\widetilde{t}_{c,12} & -t_{c,34} \\ -t_{c,34} & -\widetilde{t}_{c,12} & -\epsilon_1 - \epsilon_2 - \epsilon_4 + V + V' + V'' & 0 \\ -\widetilde{t}_{c,12} & -t_{c,34} & 0 & -2\epsilon_2 - \epsilon_3 + U + 2V \end{pmatrix}. \tag{6.8}$$

Rewrite the Hamiltonian as

$$\begin{pmatrix} \frac{\widetilde{\epsilon}}{2} & 0 & -t_{c,34} & -\widetilde{t}_{c,12} \\ 0 & -\frac{\widetilde{\epsilon}}{2} & -\widetilde{t}_{c,12} & -t_{c,34} \\ -t_{c,34} & -\widetilde{t}_{c,12} & \frac{V-2V'+V''+\widetilde{\delta}}{2} & 0 \\ -\widetilde{t}_{c,12} & -t_{c,34} & 0 & \frac{V-2V'+V''-\widetilde{\delta}}{2} \end{pmatrix}. \tag{6.9}$$

with $\widetilde{\epsilon} = \epsilon - U + 2V - V'$ and $\widetilde{\delta} = \delta - U - V + V' + V''$, where $\epsilon = \epsilon_{12} + \epsilon_{34}$, and $\delta = \epsilon_{12} - \epsilon_{34}$ with $\epsilon_{ij} = -\epsilon_i + \epsilon_j$. By diagonalising this Hamiltonian, with approximation $|\widetilde{\epsilon}| \ll |V - 2V' + V'' \pm \widetilde{\delta}|$, the co-tunnel coupling between the eigenstates that are predominantly (1110) and (0201) is $t_{co} = \frac{\widetilde{t}_{c,12}t_{c,34}}{\Delta_+} + \frac{\widetilde{t}_{c,12}t_{c,34}}{\Delta_-}$, with $\Delta_\pm = \frac{V-2V'+V''\pm\widetilde{\delta}}{2}$.

CONTROLLED PROPAGATION

The cascade can be implemented such that the propagation is controlled by a sequence of gate voltages. As example, we consider the cascade Pauli spin blockade as described in the main text. First, conventional PSB is performed with $\mu_4(0201) < 0$. The electron on

the fourth dot remains there. Next, gate voltages are changed such that $\mu_4(1101) < 0 < \mu_4(0201)$. Then the cascade will propagate and the electron on the fourth dot will move to the reservoir. A similar scheme can be designed for inter-dot cascade PSB. For a longer cascade path, which involves more than two charge transitions, the propagation could be controlled at each transition. The motivation for controlled propagation becomes clear in the next subsection.

LONGER CASCADE

We now discuss how the total duration of the cascade scales with the length of the cascade path for three different scenarios.

First we consider a cascade where all the charges are displaced in one single co-tunnel process. This involves N simultaneous tunnel events that are each energetically forbidden, but where the final state is lower in energy than the initial state. Then, for a chain with length $2N$ (with every other site occupied, except for the first two sites where the PSB mechanism is implemented), and homogeneous tunnel coupling, $t_{c,ij} = t_c$, and when the cascade involves only inter-dot transitions between neighbouring pairs, the co-tunnel coupling is [36]

$$t_{co} = N! \frac{\sqrt{2} t_c^N}{2V^{N-1}}, \tag{6.10}$$

where for simplicity we only included inter-site Coulomb repulsion between nearest-neighbour sites. Charge adiabaticity will require increasingly slower gate voltage changes, because $t_c < V$, thus t_{co} decreases exponentially with increasing cascade length. When the adiabaticity condition is not met, the cascade can get stuck along the way.

Next, for the sequential tunneling regime, thus with $E(11LL\ldots L) > E(02LL\ldots L) > E(02RL\ldots L) > \ldots > E(02RR\ldots R)$, with $L = 10$ and $R = 01$, the expected duration, assuming homogeneous tunnel rates, Γ, for the individual transitions is [37]

$$\langle \tau \rangle \sim \frac{N}{\Gamma}. \tag{6.11}$$

For the sequential regime, charge adiabaticity need not be preserved. Charge tunnelling is here a stochastic process and the duration only scales linearly with the length. Note that there is an intermediate regime, which does not fully rely on co-tunnelling, but is also not completely sequential. Theory on this regime is beyond the scope of this work.

Finally, both the charge adiabaticity and speed can be largely maintained in a cascade with controlled propagation. The total duration of the cascade increases linearly with the cascade length, similar to the sequential case, but now uncertainties in the timing of the charge movement can be suppressed, which is important when the Zeeman splittings are not homogeneous along the path.

Alternatively, co-tunnel, sequential, and cascades with controlled propagation could be combined, such that different parts of the cascade have different character.

SCALING OF SUCCESS PROBABILITY

Here we consider the probability density function for the total cascade duration and its scaling with cascade length in the context of charge getting stuck. The probability density function for the cascade duration with $N+1$ transitions, which each have decay rate

Γ, is given by the Erlang distribution [38]

$$P_N(t) = \frac{\Gamma^{N+1} t^N}{N!} e^{-\Gamma t}. \tag{6.12}$$

The probability for the cascade to take longer than time t is

$$\int_t^\infty P_N(t')\mathrm{d}t' = e^{-\tau} \sum_{n=0}^{N} \frac{\tau^n}{n!}, \tag{6.13}$$

with $\tau = \Gamma t$. We will show that the probability for a cascade with $N+1$ transitions to take longer than time τ_N decreases for increasing N given $\tau_N > \frac{N}{N-1}\tau_{N-1}$, with τ_i the time used to obtain the probability for the cascade of length $i+1$. From the constraint on τ_N it follows that $\tau_N \geq N\tau_1$, thus we consider $\tau_N = N\tau_1$, because if the scaling holds for this τ_N, then it will certainly hold for $\tau_N > N\tau_1$. The derivative of the probability with respect to N is

$$\frac{\mathrm{d}}{\mathrm{dN}}\left[e^{-\tau_N}\sum_{n=0}^{N}\frac{\tau_N^n}{n!}\right] = \frac{\mathrm{d}}{\mathrm{dN}}\left[e^{-N\tau_1}\sum_{n=0}^{N}\frac{N^n\tau_1^n}{n!}\right] = -\tau_1 e^{-N\tau_1}\frac{N^N\tau_1^N}{N!}. \tag{6.14}$$

Thus the probability decreases as function of cascade length, which shows that the time for a cascade to complete with a given probability scales sublinearly with respect to the cascade length. Alternatively formulated, the probability for a charge to get stuck and interrupt the cascade thus scales sublinearly with the cascade length.

6.6.7. RELAXATION AND EXCITATION TIME

The relaxation and excitation time are obtained from the signal averaged over the single-shot measurements, and as a function of time. This signal is fitted with an exponential [12]

$$V(t) = A\exp(-\Gamma t) + B, \tag{6.15}$$

with A a pre-factor,

$$\Gamma = \frac{T_1 + T_{exc}}{T_1 T_{exc}}, \tag{6.16}$$

and

$$B = \frac{1}{\Gamma}\left(\frac{V_T}{T_{exc}} + \frac{V_S}{T_1}\right), \tag{6.17}$$

where V_T and V_S are obtained from the fit to the histogram of the singlet-shot measurements.

6.6.8. FIDELITY ANALYSIS FOR PSB

From the fit to the histogram in Fig. 6.3a, the error due to overlap and relaxation during integration is $\eta_{hist} = 14.3\%$. The relaxation time is $T_1 = 724(70)\,\mu\mathrm{s}$, which results in an error of $\eta_{arm} = 0.014\%$. The excitation time is $T_{exc} = 2.8(11)\,\mathrm{ms}$, which results in an error of $\eta_{exc} = 0.030\%$. The error due to charge non-adiabaticity is the same as for CPSB, thus $10^{-9}\%$.

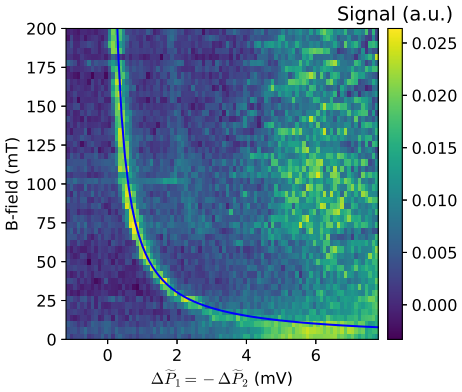

Figure 6.6: Spin funnel Higher signal corresponds to a higher triplet probability. For each data point the signal is averaged over 1,000 single-shot measurements. The wait time at the operating point, which is in the (1100) charge configuration for $\Delta\tilde{P}_1 > 0$, was 200 ns. The blue, solid line is a fit to $\frac{1}{2}\left(-\epsilon_{12} + \sqrt{8t_{c,12}^2 + \epsilon_{12}^2}\right)$, with $\epsilon_{12} = -\epsilon_1 + \epsilon_2$, the detuning, and $t_{c,12}$ the tunnel coupling between dots 1 and 2.

6

6.6.9. EFFECT OF HYPERFINE FIELD

The measurement basis for spin readout consists of the singlet and triplet states, which are the eigenstates of the Hamiltonian at the readout point. The voltage pulse from the loading point to the readout point, induces a mapping of the eigenstates at the loading point to the measurement basis. This mapping is determined by the pulse duration, the exchange coupling, and the hyperfine field, which is caused by the hyperfine interaction of the electron spins with the nuclear spins. The eigenstates at the loading point can vary between pulse cycles, due to fluctuations of the hyperfine field, thus changing the mapping to the measurement basis. In order to avoid unpredictable mappings, the exchange interaction must dominate the Hamiltonian. This can be done by increasing the exchange interaction or suppressing the hyperfine field fluctuations, either by feedback mechanisms based on dynamical nuclear polarization [39] or by using isotopically purified ^{28}Si[40].

6.6.10. SPIN FUNNEL

The strength of the tunnel coupling between dots 1 and 2, $t_{c,12}$, is obtained from a so-called spin funnel measurement, which is shown in Fig. 6.6. For the spin funnel, a pulse cycle with three stages is executed [41]. The first stage is deep in the (0200) charge region to initialise a singlet state. Then the voltages are pulsed towards the (1100) region, and then into the readout region in (0200). Such a pulse cycle is repeated for varying depths in the (1100) region and varying external magnetic fields. The magnetic field is converted to an energy scale with the g-factor, $|g| = 0.44$, and the Bohr magneton. From a fit to the funnel, the tunnel coupling $t_{c,12} = 11.5\,\mu$eV is obtained. The detuning is obtained from the change in virtual gate voltages by multiplying with the lever arms, which were

obtained with photon-assisted tunnelling measurements [28].

REFERENCES

[1] A. G. Fowler, A. M. Stephens, and P. Groszkowski, *High-threshold universal quantum computation on the surface code,* Physical Review A **80**, 052312 (2009).

[2] M. Veldhorst, H. G. Eenink, C. H. Yang, and A. S. Dzurak, *Silicon CMOS architecture for a spin-based quantum computer,* Nature Communications **8** (2017).

[3] L. M. K. Vandersypen, H. Bluhm, J. S. Clarke, A. S. Dzurak, R. Ishihara, A. Morello, D. J. Reilly, L. R. Schreiber, and M. Veldhorst, *Interfacing spin qubits in quantum dots and donors—hot, dense, and coherent,* npj Quantum Information **3**, 34 (2017).

[4] R. Li, L. Petit, D. P. Franke, J. P. Dehollain, J. Helsen, M. Steudtner, N. K. Thomas, Z. R. Yoscovits, K. J. Singh, S. Wehner, L. M. K. Vandersypen, J. S. Clarke, and M. Veldhorst, *A crossbar network for silicon quantum dot qubits,* Science Advances **4**, eaar3960 (2018).

[5] B. Buonacorsi, Z. Cai, E. B. Ramirez, K. S. Willick, S. M. Walker, J. Li, B. D. Shaw, X. Xu, S. C. Benjamin, and J. Baugh, *Network architecture for a topological quantum computer in silicon,* Quantum Science and Technology **4**, 025003 (2019).

[6] P. Pakkiam, A. V. Timofeev, M. G. House, M. R. Hogg, T. Kobayashi, M. Koch, S. Rogge, and M. Y. Simmons, *Single-Shot Single-Gate rf Spin Readout in Silicon,* Physical Review X **8**, 41032 (2018).

[7] M. Urdampilleta, D. J. Niegemann, E. Chanrion, B. Jadot, C. Spence, P. A. Mortemousque, C. Bäuerle, L. Hutin, B. Bertrand, S. Barraud, R. Maurand, M. Sanquer, X. Jehl, S. De Franceschi, M. Vinet, and T. Meunier, *Gate-based high fidelity spin readout in a CMOS device,* Nature Nanotechnology **14**, 737 (2019).

[8] A. West, B. Hensen, A. Jouan, T. Tanttu, C. H. Yang, A. Rossi, M. F. Gonzalez-Zalba, F. Hudson, A. Morello, D. J. Reilly, and A. S. Dzurak, *Gate-based single-shot readout of spins in silicon,* Nature Nanotechnology **14**, 437 (2019).

[9] G. Zheng, N. Samkharadze, M. L. Noordam, N. Kalhor, D. Brousse, A. Sammak, G. Scappucci, and L. M. K. Vandersypen, *Rapid gate-based spin read-out in silicon using an on-chip resonator,* Nature Nanotechnology **14** (2019).

[10] S. A. Studenikin, J. Thorgrimson, G. C. Aers, A. Kam, P. Zawadzki, Z. R. Wasilewski, A. Bogan, and A. S. Sachrajda, *Enhanced charge detection of spin qubit readout via an intermediate state,* Applied Physics Letters **101**, 233101 (2012).

[11] T. Nakajima, M. R. Delbecq, T. Otsuka, P. Stano, S. Amaha, J. Yoneda, A. Noiri, K. Kawasaki, K. Takeda, G. Allison, A. Ludwig, A. D. Wieck, D. Loss, and S. Tarucha, *Robust Single-Shot Spin Measurement with 99.5% Fidelity in a Quantum Dot Array,* Physical Review Letters **119**, 017701 (2017).

[12] P. Harvey-Collard, B. D'Anjou, M. Rudolph, N. Tobias Jacobson, J. Dominguez, G. A. Eyck, J. R. Wendt, T. Pluym, M. P. Lilly, W. A. Coish, M. Pioro-Ladrière, and M. S. Carroll, *High-Fidelity Single-Shot Readout for a Spin Qubit via an Enhanced Latching Mechanism,* Physical Review X **8**, 021046 (2018).

[13] T. A. Baart, M. Shafiei, T. Fujita, C. Reichl, W. Wegscheider, and L. M. K. Vandersypen, *Single-Spin CCD,* Nature Nanotechnology **11**, 330 (2016).

[14] A. J. Sigillito, M. J. Gullans, L. F. Edge, M. Borselli, and J. R. Petta, *Coherent transfer of quantum information in a silicon double quantum dot using resonant SWAP gates,* npj Quantum Information **5**, 110 (2019).

[15] Y. P. Kandel, H. Qiao, S. Fallahi, G. C. Gardner, M. J. Manfra, and J. M. Nichol, *Coherent spin state transfer via Heisenberg exchange,* Nature **573**, 553 (2019).

[16] A. Einstein, *Strahlungs-emission und -absorption nach der quantentheorie,* Verhandlungen der Deutschen Physikalischen Gesellschaft **18**, 318 (1916).

[17] R. Kollath, *Secondary electron emission of solids induced by electron bombardment,* Encyclopedia of physics **21**, 232 (1956).

[18] P. Webb, R. McIntyre, and J. Conradi, *Properties of avalanche photodiodes,* R.C.A. Review **35**, 234 (1974).

[19] V. Von Halban, F. Joliot, and L. Kowarski, *Number of neutrons liberated in the nuclear fission of uranium,* Nature **143**, 680 (1939).

[20] A. J. Heinrich, C. P. Lutz, J. A. Gupta, and D. M. Eigler, *Molecule cascades,* Science **298**, 1381 (2002).

[21] C. S. Lent, P. D. Tougaw, W. Porod, and G. H. Bernstein, *Quantum cellular automata,* Nanotechnology **4**, 49 (1993).

[22] I. Amlani, *Digital logic gate using quantum-dot cellular automata,* Science **284**, 289 (1999).

[23] C. Barthel, D. J. Reilly, C. M. Marcus, M. P. Hanson, and A. C. Gossard, *Rapid single-shot measurement of a singlet-triplet qubit,* Physical Review Letters **103**, 160503 (2009).

[24] T. Hensgens, T. Fujita, L. Janssen, X. Li, C. J. Van Diepen, C. Reichl, W. Wegscheider, S. Das Sarma, and L. M. K. Vandersypen, *Quantum simulation of a Fermi-Hubbard model using a semiconductor quantum dot array,* Nature **548**, 70 (2017).

[25] C. Volk, A. M. J. Zwerver, U. Mukhopadhyay, P. T. Eendebak, C. J. van Diepen, J. P. Dehollain, T. Hensgens, T. Fujita, C. Reichl, W. Wegscheider, and L. M. K. Vandersypen, *Loading a quantum-dot based "Qubyte" register,* npj Quantum Information **5**, 29 (2019).

[26] A. R. Mills, D. M. Zajac, M. J. Gullans, F. J. Schupp, T. M. Hazard, and J. R. Petta, *Shuttling a single charge across a one-dimensional array of silicon quantum dots,* Nature Communications **10**, 1063 (2019).

[27] H. Qiao, Y. P. Kandel, S. K. Manikandan, A. N. Jordan, S. Fallahi, G. C. Gardner, M. J. Manfra, and J. M. Nichol, *Conditional teleportation of quantum-dot spin states,* Nature Communications **11**, 3022 (2020).

[28] T.-K. Hsiao, C. J. van Diepen, U. Mukhopadhyay, C. Reichl, W. Wegscheider, and L. M. K. Vandersypen, *Efficient orthogonal control of tunnel couplings in a quantum dot array,* Physical Review Applied **13**, 054018 (2020).

[29] B. Bertrand, H. Flentje, S. Takada, M. Yamamoto, S. Tarucha, A. Ludwig, A. D. Wieck, C. Bäuerle, and T. Meunier, *Quantum Manipulation of Two-Electron Spin States in Isolated Double Quantum Dots,* Physical Review Letters **115**, 096801 (2015).

[30] C. H. Yang, R. C. C. Leon, J. C. C. Hwang, A. Saraiva, T. Tanttu, W. Huang, J. C. Lemyre, K. W. Chan, K. Y. Tan, F. E. Hudson, K. M. Itoh, A. Morello, M. Pioro-Ladrière, A. Laucht, and A. S. Dzurak, *Silicon quantum processor unit cell operation above one Kelvin,* Nature **580**, 350 (2020).

[31] T. F. Watson, S. G. Philips, E. Kawakami, D. R. Ward, P. Scarlino, M. Veldhorst, D. E. Savage, M. G. Lagally, M. Friesen, S. N. Coppersmith, M. A. Eriksson, and L. M. K. Vandersypen, *A programmable two-qubit quantum processor in silicon,* Nature **555**, 633 (2018).

[32] L. Petit, H. G. J. Eenink, M. Russ, W. I. L. Lawrie, N. W. Hendrickx, J. S. Clarke, L. M. K. Vandersypen, and M. Veldhorst, *Universal quantum logic in hot silicon qubits,* Nature **580**, 355 (2020).

[33] J. M. Elzerman, R. Hanson, L. H. W. van Beveren, B. Witkamp, L. M. K. Vandersypen, and L. P. Kouwenhoven, *Single-shot read-out of an individual electron spin in a quantum dot,* Nature **430**, 431 (2004).

[34] D. Aasen, M. Hell, R. V. Mishmash, A. Higginbotham, J. Danon, M. Leijnse, T. S. Jespersen, J. A. Folk, C. M. Marcus, K. Flensberg, and J. Alicea, *Milestones toward Majorana-based quantum computing,* Physical Review X **6**, 031016 (2016).

[35] F. R. Braakman, P. Barthelemy, C. Reichl, W. Wegscheider, and L. M. K. Vandersypen, *Long-distance coherent coupling in a quantum dot array,* Nature Nanotechnology **8**, 432 (2013).

[36] D. V. Averin and A. A. Odintsov, *Macroscopic quantum tunneling of the electric charge in small tunnel junctions,* Physics Letters A **140**, 251 (1989).

[37] M. Buttiker, *Coherent and Sequential Tunneling in Series Barriers.* IBM Journal of Research and Development **32**, 63 (1988).

[38] B. D'Anjou and W. A. Coish, *Enhancing qubit readout through dissipative sub-Poissonian dynamics,* Physical Review A **96**, 052321 (2017).

[39] H. Bluhm, S. Foletti, D. Mahalu, V. Umansky, and A. Yacoby, *Enhancing the coherence of a spin qubit by operating it as a feedback loop that controls its nuclear spin bath,* Physical Review Letters **105**, 216803 (2010).

[40] M. Veldhorst, J. C. C. Hwang, C. H. Yang, A. W. Leenstra, B. de Ronde, J. P. Dehollain, J. T. Muhonen, F. E. Hudson, K. M. Itoh, A. Morello, and A. S. Dzurak, *An addressable quantum dot qubit with fault-tolerant control-fidelity,* Nature Nanotechnology **9**, 981 (2014).

[41] J. R. Petta, A. C. Johnson, J. M. Taylor, E. A. Laird, A. Yacoby, M. D. Lukin, C. M. Marcus, M. P. Hanson, and A. C. Gossard, *Coherent Manipulation of Coupled Electron Spins in Semiconductor Quantum Dots,* Science **309**, 2180 (2005).

7

QUANTUM SIMULATION OF ANTIFERROMAGNETIC HEISENBERG CHAIN WITH GATE-DEFINED QUANTUM DOTS

Quantum-mechanical correlations of interacting fermions result in the emergence of exotic phases. Magnetic phases naturally arise in the Mott-insulator regime of the Fermi-Hubbard model, where charges are localized and the spin degree of freedom remains. In this regime the occurrence of phenomena such as resonating valence bonds, frustrated magnetism, and spin liquids are predicted. Quantum systems with engineered Hamiltonians can be used as simulators of such spin physics to provide insights beyond the capabilities of analytical methods and classical computers. To be useful, methods for the preparation of intricate many-body spin states and access to relevant observables are required. Here we show the quantum simulation of magnetism in the Mott-insulator regime with a linear quantum dot array. We characterize the energy spectrum for a Heisenberg spin chain, from which we can identify when the conditions for homogeneous exchange couplings are met. Next, we study the multi-spin coherence with global exchange-oscillations in both the singlet and triplet subspace of the Heisenberg Hamiltonian. Last, we adiabatically prepare the low-energy global singlet of the homogeneous spin chain, and probe it with two-spin singlet-triplet measurements on each nearest-neighbour pair and the correlations therein. The methods and control presented here open new opportunities for the simulation of quantum magnetism benefiting from the flexibility in tuning and layout of gate-defined quantum dot arrays.

This chapter has been published as C. J. van Diepen*, T.-K. Hsiao*, U. Mukhopadhyay, C. Reichl, W. Wegscheider, and L. M. K. Vandersypen, Physical Review X **11**, 041025 (2021).

7.1. INTRODUCTION

Analog quantum simulations of magnetism [1] have been performed with a rich variety of experimental platforms, ranging from ultra-cold atoms in optical lattices [2–7] to trapped ions [8, 9], scanning tunnelling microscopy of atoms on metallic surfaces [10], and superconducting circuits [11]. A recent addition is the use of gate-defined quantum dots as platform for quantum simulation of the Fermi-Hubbard model. The abilities to independently control the filling of the array, the local electrochemical potentials and the hopping energy between sites, are complemented with methods to probe the charge configuration across an array, spin states, the electrical susceptibility as well as transport through the system [12]. These already enabled the observation of the transition from Coulomb blockade to collective Coulomb blockade [13] and the observation of Nagaoka ferromagnetism [14], a form of purely itinerant ferromagnetism which occurs at doping with a single hole.

In the Mott-insulator regime, where all sites are occupied by one electron, magnetism is governed by the Heisenberg exchange interaction [15], which favors antiferromagnetic spin alignment. Earlier studies on quantum dot arrays in this regime have demonstrated the sequential control of exchange couplings enabling coherent state transfer [16], and a method to handle crosstalk in simultaneous control of exchange couplings [17]. In order to study the many-body properties of this system, novel methods are needed for state preparation in the presence of disorder and temperature, as well as for probing spin correlations. Preparation of the Heisenberg ground state is both a useful and exciting goal, because of its potential applications such as quantum information transfer [18–22] and quantum simulation of magnetic phases [23–25].

In this work we simulate the antiferromagnetic Heisenberg spin chain in a gate-defined quadruple quantum dot. For this purpose we develop experimental techniques based on energy spectroscopy and coherent oscillations of the global spin state. These include methods for many-body spin-state preparation and singlet-triplet correlation measurements, which form a powerful probe for the characterization of a many-body spin state [26]. We use these methods to engineer a chain with homogeneous exchange couplings. Finally, we adiabatically prepare the low-energy singlet eigenstate of the homogeneous Heisenberg chain and characterize the state with single-shot singlet-triplet readout on all nearest-neighbour pairs.

7.2. HEISENBERG SPIN CHAIN

The Heisenberg isotropic exchange Hamiltonian, while giving rise to rich emergent phenomena, has a simple form:

$$H_{heis} = \sum_{\langle i,j \rangle} J_{ij} \left(\vec{S}_i \cdot \vec{S}_j - \frac{1}{4} \right), \tag{7.1}$$

with J_{ij} the exchange coupling between spins on sites i and j, $\vec{S}_i$ the vector of spin operators for site i, and the summation over nearest-neighbours only. The conventional $-\frac{1}{4}$ offset ascertains that the two-spin triplets have zero energy contribution in the absence of an external field. For quantum dot systems the exchange coupling is typically positive [27], thus neighbouring spins prefer to anti-align, or more precisely tend to form

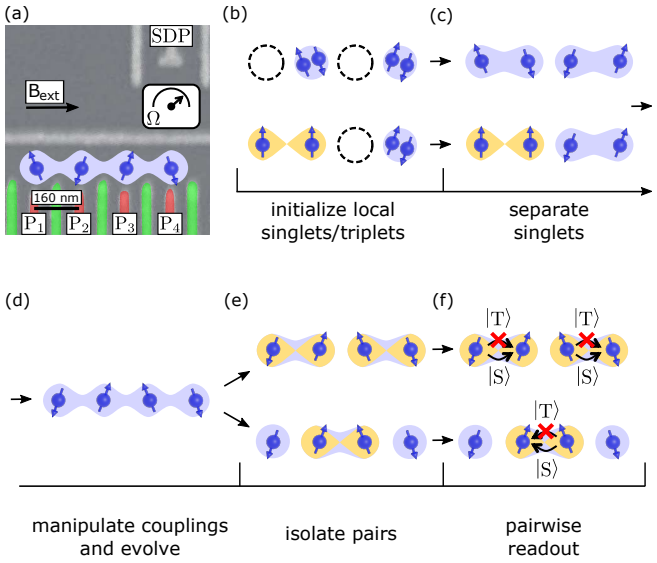

Figure 7.1: Device and spin-chain operation. (a) False-coloured scanning electron micrograph of a device nominally identical to the one used for the experiments. The resistance meter, indicated with Ω, shows the location of the sensing dot. Plunger gates for the dots are coloured in red and labelled with P_i, and the plunger for the sensing dot is labelled with SDP. (b)-(f) Schematic illustration of the experimental sequence for the spin chain, consisting of five stages: initialization of local singlets or triplets, separation of singlets, manipulation of exchange couplings and time evolution, isolation of either the left and the right pair or the middle pair by switching off specific exchange couplings, and pairwise singlet-triplet readout.

local singlets. In addition, a Zeeman splitting can be induced with an external magnetic field, which energetically splits spin states according to their magnetization as

$$H_{ext} = g\mu_B B_{ext} \sum_i \hat{S}_i^z, \tag{7.2}$$

with g the Landé g-factor, μ_B the Bohr magneton, and B_{ext} the external magnetic field.

The properties of a Heisenberg spin chain have theoretically been studied extensively, with as most famous result the exact solution of the energy spectrum and eigenstates of the homogeneous chain using the Bethe ansatz [28]. Intuitive insights can be obtained from the symmetries of the Heisenberg Hamiltonian, due to which the Hilbert space can be separated into subspaces, which are eigenspaces for the total spin operator, $\hat{S}^2$, with eigenvalues $S(S+1)$, and the spin operator in the z-direction, $\hat{S}^z$, with eigenvalues $m_S \in [-S,\ldots,S]$. The dimensions for these subspaces can be obtained from the Clebsch-Gordan decomposition. For four spins this results in two global singlet states for which $S=0$, nine global triplet states for which $S=1$ and five states with $S=2$, which form a quintuplet. The triplets are separated into three three-dimensional subspaces, and are denoted by T_k^α, with the subspace magnetization $\alpha \in [-,0,+]$ and k labelling the energy level, where $k=0$ for the state with lowest energy in the respective subspace. Similarly, the singlets are denoted by S_k, and the quintuplets by Q^β with $\beta \in [--,-,0,+,++]$.

The global spin states can be characterized in terms of the probabilities to measure either two-spin singlets, $|S_{ij}\rangle = \frac{1}{\sqrt{2}}\left(|\uparrow_i\downarrow_j\rangle - |\downarrow_i\uparrow_j\rangle\right)$, or triplets, $|T_{ij}^+\rangle = |\uparrow_i\uparrow_j\rangle$, $|T_{ij}^0\rangle =$

State	(S, m_S)	Left and right pair basis	Middle and outer pair basis
$Q^{\pm\pm}$	$(2,\pm2)$	$\lvert T^{\pm}_{12}T^{\pm}_{34}\rangle$	$\lvert T^{\pm}_{23}T^{\pm}_{14}\rangle$
$Q^{\pm}$	$(2,\pm1)$	$\frac{1}{\sqrt{2}}\left(\lvert T^{0}_{12}T^{\pm}_{34}\rangle+\lvert T^{\pm}_{12}T^{0}_{34}\rangle\right)$	$\frac{1}{\sqrt{2}}\left(\lvert T^{0}_{23}T^{\pm}_{14}\rangle+\lvert T^{\pm}_{23}T^{0}_{14}\rangle\right)$
Q^{0}	$(2,0)$	$\frac{1}{\sqrt{6}}\left(\lvert T^{+}_{12}T^{-}_{34}\rangle+\lvert T^{-}_{12}T^{+}_{34}\rangle+2\lvert T^{0}_{12}T^{0}_{34}\rangle\right)$	$\frac{1}{\sqrt{6}}\left(\lvert T^{+}_{23}T^{-}_{14}\rangle+\lvert T^{-}_{23}T^{+}_{14}\rangle+2\lvert T^{0}_{23}T^{0}_{14}\rangle\right)$
$T^{\pm}_{k}$	$(1,\pm1)$	$\lvert 2_{T^{\pm}}\rangle=\frac{1}{\sqrt{2}}\left(\lvert T^{0}_{12}T^{\pm}_{34}\rangle-\lvert T^{\pm}_{12}T^{0}_{34}\rangle\right)$ $\lvert 1_{T^{\pm}}\rangle=\lvert T^{\pm}_{12}S_{34}\rangle$ $\lvert 0_{T^{\pm}}\rangle=\lvert S_{12}T^{\pm}_{34}\rangle$	$\frac{1}{\sqrt{2}}\left(\lvert S_{23}T^{\pm}_{14}\rangle+\lvert T^{\pm}_{23}S_{14}\rangle\right)$ $\frac{1}{2}\left(\lvert S_{23}T^{\pm}_{14}\rangle-\lvert T^{\pm}_{23}S_{14}\rangle+\lvert T^{\pm}_{23}T^{0}_{14}\rangle-\lvert T^{0}_{23}T^{\pm}_{14}\rangle\right)$ $\frac{1}{2}\left(\lvert S_{23}T^{\pm}_{14}\rangle-\lvert T^{\pm}_{23}S_{14}\rangle-\lvert T^{\pm}_{23}T^{0}_{14}\rangle+\lvert T^{0}_{23}T^{\pm}_{14}\rangle\right)$
T^{0}_{k}	$(1,0)$	$\frac{1}{\sqrt{2}}\left(\lvert T^{+}_{12}T^{-}_{34}\rangle-\lvert T^{-}_{12}T^{+}_{34}\rangle\right)$ $\lvert T^{0}_{12}S_{34}\rangle$ $\lvert S_{12}T^{0}_{34}\rangle$	$\frac{1}{\sqrt{2}}\left(\lvert S_{23}T^{0}_{14}\rangle+\lvert T^{0}_{23}S_{14}\rangle\right)$ $\frac{1}{2}\left(\lvert S_{23}T^{0}_{14}\rangle-\lvert T^{0}_{23}S_{14}\rangle-\lvert T^{+}_{23}T^{-}_{14}\rangle+\lvert T^{-}_{23}T^{+}_{14}\rangle\right)$ $\frac{1}{2}\left(\lvert S_{23}T^{0}_{14}\rangle-\lvert T^{0}_{23}S_{14}\rangle+\lvert T^{+}_{23}T^{-}_{14}\rangle-\lvert T^{-}_{23}T^{+}_{14}\rangle\right)$
S_{k}	$(0,0)$	$\lvert 1_S\rangle=\frac{1}{\sqrt{3}}\left(\lvert T^{+}_{12}T^{-}_{34}\rangle+\lvert T^{-}_{12}T^{+}_{34}\rangle-\lvert T^{0}_{12}T^{0}_{34}\rangle\right)$ $\lvert 0_S\rangle=\lvert S_{12}S_{34}\rangle$	$\frac{\sqrt{3}}{2}\lvert S_{23}S_{14}\rangle+\frac{1}{2\sqrt{3}}\left(\lvert T^{0}_{23}T^{0}_{14}\rangle-\lvert T^{+}_{23}T^{-}_{14}\rangle-\lvert T^{-}_{23}T^{+}_{14}\rangle\right)$ $\frac{1}{2}\left(\lvert S_{23}S_{14}\rangle-\lvert T^{0}_{23}T^{0}_{14}\rangle+\lvert T^{+}_{23}T^{-}_{14}\rangle+\lvert T^{-}_{23}T^{+}_{14}\rangle\right)$

Table 7.1: Four-spin shared eigenstates of $\hat{S}^2$ and $\hat{S}^z$ expressed in a basis of two-spin singlets and triplets on either the left and right, or middle and outer pair. States in the rightmost column are the same as states on the same row in the column to the left of it. The four-spin states shown here are in general not eigenstates of the Heisenberg Hamiltonian, but the Hamiltonian does operate within a specific (S, m_S) subspace.

$\frac{1}{\sqrt{2}}\left(\lvert\uparrow_i\downarrow_j\rangle+\lvert\downarrow_i\uparrow_j\rangle\right)$, $\lvert T^{-}_{ij}\rangle=\lvert\downarrow_i\downarrow_j\rangle$, where i and j indicate the site. The simultaneous eigenstates of $\hat{S}^2$ and $\hat{S}^z$ for four-spin states can be expressed in this pairwise singlet-triplet basis as shown in Table 7.1. Appendix 7.8.1 discusses the limitations of singlet-triplet measurements to distinguish spin states.

Alternatively we can characterize the Heisenberg spin chain via its energy spectrum. Based on the symmetries of the Hamiltonian, for four spins the global singlet states form a two-dimensional subspace. For this subspace the Heisenberg Hamiltonian is

$$H_{(0,0)}=\begin{pmatrix}-J_{12}-\frac{1}{4}J_{23}-J_{34} & \frac{\sqrt{3}}{4}J_{23}\\ \frac{\sqrt{3}}{4}J_{23} & -\frac{3}{4}J_{23}\end{pmatrix}, \tag{7.3}$$

with as basis states $\lvert 0_S\rangle$ and $\lvert 1_S\rangle$ from Table 7.1. This subspace has been proposed as a singlet-only exchange-only qubit implementation, which offers increased coherence due to the reduced influence of nuclear spins [29].

For the global triplet states, the three three-dimensional subspaces are identical in terms of energy splittings. The Heisenberg Hamiltonian for each of these triplet subspaces is

$$H_{(1,1)}=\begin{pmatrix}-J_{12}-\frac{1}{4}J_{23} & -\frac{1}{4}J_{23} & -\frac{1}{2\sqrt{2}}J_{23}\\ -\frac{1}{4}J_{23} & -\frac{1}{4}J_{23}-J_{34} & -\frac{1}{2\sqrt{2}}J_{23}\\ -\frac{1}{2\sqrt{2}}J_{23} & -\frac{1}{2\sqrt{2}}J_{23} & -\frac{1}{2}J_{23}\end{pmatrix}, \tag{7.4}$$

with as basis $|0_{T^+}\rangle$, $|1_{T^+}\rangle$, $|2_{T^+}\rangle$ from Table 7.1. The quintuplet states have zero energy contribution from the Heisenberg Hamiltonian, but can be energetically split with an external magnetic field.

The energy differences in the subspaces reveal information about the exchange coupling strengths, and characteristic features can be identified. For the singlet subspace the energy splitting is $\frac{1}{2}\sqrt{(2J_{12}+2J_{34}-J_{23})^2+3J_{23}^2}$. It follows that given $J_{12}=J_{34}$, the energy splitting is minimized when $J_{23}=J_{12}=J_{34}$, thus for homogeneous exchange couplings. For the triplet subspace the energy difference between the two lowest-energy states is minimized if $J_{12}=J_{34}$. If $J_{12}=J_{23}=J_{34}$ the triplet states are equally spaced in energy (see Appendix 7.8.2 for simulated energy diagrams). These characteristic features for the energy spectrum of the Heisenberg Hamiltonian will be experimentally identified, but first we introduce the quantum dot device and the experimental operation.

7.3. DEVICE AND EXPERIMENTAL OPERATION

The prototype for the simulation of an antiferromagnetic Heisenberg spin chain consists of a quadruple dot and a sensing dot, which are formed in a device nominally identical to that shown in Fig. 7.1(a) (see Appendix 7.8.3 for details). The device is based on a GaAs/AlGaAs heterostructure, since this was the only technology in which we were able to fabricate high-quality and well-controlled quantum dot arrays. The exchange couplings are induced by electron wave function overlap, which we here control by detuning the potentials of neighbouring dots, such that one electron shifts towards the other [30] (we note that independent control of the exchange couplings can also be achieved by adjusting the tunnel couplings [13, 17, 31]). In order to control the detuning between one pair of dots without affecting the detuning between other pairs, we define the detunings ε_{ij} as

$$\begin{pmatrix}\varepsilon_{12}\\ \varepsilon_{23}\\ \varepsilon_{34}\end{pmatrix}=\begin{pmatrix}-1 & 1 & 1 & 1\\ 1 & 1 & -1 & -1\\ -1 & -1 & -1 & 1\end{pmatrix}\begin{pmatrix}\varepsilon_1\\ \varepsilon_2\\ \varepsilon_3\\ \varepsilon_4\end{pmatrix}, \tag{7.5}$$

where ε_i is the negative local energy offset for site i, and $\varepsilon_{ij}=0$ at the inter-dot transition between charge occupations (1111) and (0211), (1201), (1102) for ε_{12}, ε_{23}, ε_{34} respectively. The ε_i are independently controlled using virtual plunger gates, which are linear combinations of the voltages applied to the gates P_i [13] (In the figures below, we express ε_{ij} in units of mV. In Appendix 7.8.3, we specify the conversion factor between energy and the applied voltage). The dependence of exchange couplings on detunings can be modelled as [32]

$$J_{ij}=\frac{1}{2}\left(\varepsilon_{ij}+\sqrt{8t_{ij}^2+\varepsilon_{ij}^2}\right), \tag{7.6}$$

with t_{ij} the tunnel coupling between dots i and j. In this way, the exchange couplings can be set independently with the detunings, and increasing detuning results in increasing exchange strength. There is no obstacle to implementing this method in larger chains

of quantum dots.

The experimental sequence used to operate the quantum-dot spin chain is schematically depicted in Fig. 7.1(b)-(f), and will be described step-by-step here (charge-stability diagrams and sequence details are provided in Appendix 7.8.3). Initially, the quadruple dot is tuned in either the (0202) or (1102) charge occupation. For the (0202) case, we load local singlets in the second and fourth dot, by allowing tunnelling or cotunnelling between dots and the reservoirs. For the (1102) configuration, we load a thermal mixture of two-spin states on the left pair and post-select for triplet loading (see Appendix 7.8.3), and load a singlet on dot four. Next, the electrons are separated to obtain (1111) charge occupation. The global spin state remains a product of local spin pairs, because the left and right pair exchange remain large compared to the hyperfine field from the nuclear spins, and the middle pair exchange coupling is kept small. Then, during the manipulation stage the exchange couplings are diabatically or adiabatically changed by applying gate voltage pulses with variable rise time. In this work the pulses are always diabatic with respect to anti-crossings between states with different magnetization. Subsequently, the four-spin state evolves under the newly set exchange couplings. Finally, the spin pair(s) to be measured is(are) diabatically isolated from the other spins and measured with single-shot singlet-triplet readout based on Pauli spin blockade (PSB) [33]. Here either the left and right pair are sequentially read out, while parking the other pair to avoid capacitive crosstalk [34], or the middle pair is read out.

In the remainder of this work, we focus on realizing homogeneous exchange couplings throughout the spin chain. In principle, this could have been achieved by calibrating the exchange couplings one at a time [17] and extrapolating to the required tuning while compensating for crosstalk. Instead, we have developed a two-step spectroscopy method from which we identify directly when the condition of homogeneous exchange couplings is met.

7.4. ENERGY SPECTROSCOPY

For gate-defined quantum dots, information about the energy level spectrum can be obtained from the degeneracies between spin states with different magnetization. This so-called spin funnel method has been used extensively in quantum dots arrays of various lengths [30, 35, 36]. Here we use the same underlying principles in a novel method for simultaneously characterizing multiple exchange coupling strengths in the spin chain. In addition, since the system size is small enough to allow classical numerical computation of its energy level spectrum, we can validate the quantum simulator by comparing the measured energy spectrum to the numerically computed spectrum.

For the energy spectroscopy measurements, we prepare spin singlets on the left and right dot pairs [see Fig. 7.1(b)] (i.e. we prepare in the low-energy global singlet $|0_S\rangle$), diabatically pulse the exchange couplings, allow the system to evolve for 100 ns, and read out the left and right pair. The duration of 100 ns is chosen to allow the coherent time evolution kick-started by the pulse to have largely damped out. This measurement gives access to correlations in the singlet-triplet occupations, $P_{ST}, P_{TT}, P_{TS}, P_{SS}$, where the left (right) sub-index corresponds to the left (right) pair outcome. Decreased P_{SS} indicates mixing of the low-energy global singlet with one of the triplet or quintuplet states. Such mixing occurs most manifestly at anti-crossings between the low-energy global singlet

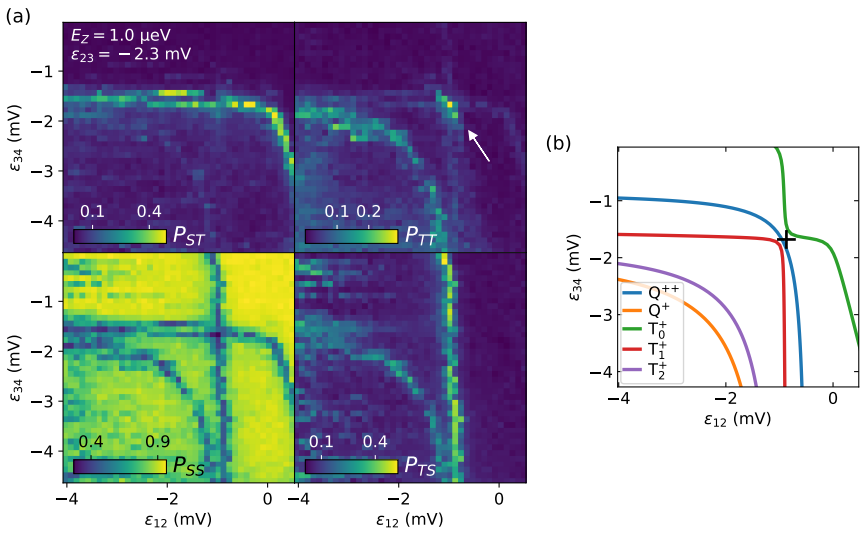

Figure 7.2: Energy spectroscopy as function of left and right pair detunings. (a) Left and right pair correlated singlet-triplet probabilities from independent single-shot Pauli spin blockade readout. A decrease in singlet-singlet probability and an increase in one of the other probabilities corresponds to an anti-crossing between the low-energy global singlet state and a polarized state. (b) Numerical simulation of the outer pair detunings for which the low-energy global singlet state is degenerate with a polarized state. The parameters for the numerical simulation are obtained from separate spin funnel measurements for the left and right exchange coupling (see Appendix 7.8.3) and from the Fourier transform in Fig. 7.4(d). The energy of the low-energy global singlet state is set to zero as a reference. Points in (b) and Fig. 7.3(b) with the same detunings and magnetic field are indicated with a "+".

state and the polarized states with $m_S = 1,2$, induced by the gradients of the hyperfine field and the spin-orbit interaction. Depending on which of the other probabilities increases, we can infer information on the nature of the polarized state involved in that specific anti-crossing.

We now examine and interpret the spectra in detail. For the measurement shown in Fig. 7.2(a) the left and right pair detunings during the manipulation stage were varied in the presence of a 40 mT magnetic field. The middle pair detuning is kept fixed and such that the middle exchange coupling is small compared to the outer exchange couplings, thus the low-energy global singlet state remains almost fully $|S_{12}S_{34}\rangle$, with $|S_{ij}\rangle = \frac{1}{\sqrt{2}}\left(|\uparrow_i\downarrow_j\rangle - |\downarrow_i\uparrow_j\rangle\right)$. Figure 7.2(b) shows the result of a corresponding numerical simulation, which helps to interpret the data. The detunings for the anti-crossing between the low-energy singlet and the T_1^+, are either vertical, where $T_1^+ \approx |T_{12}^+ S_{34}\rangle$ with $|T_{ij}^+\rangle = |\uparrow_i\uparrow_j\rangle$, or horizontal, where $T_1^+ \approx |S_{12}T_{34}^+\rangle$, over a large range of detunings. This demonstrates the independent control of J_{12} and J_{34} with the detunings ε_{12} and ε_{34} respectively. For higher ε_{12} (ε_{34}) the horizontal (vertical) T_0^+ line bends away towards lower ε_{34} (ε_{12}), which is a manifestation of the capacitive coupling between the left and right pair of dots: the singlet energy on one pair is lowered when the charge occupa-

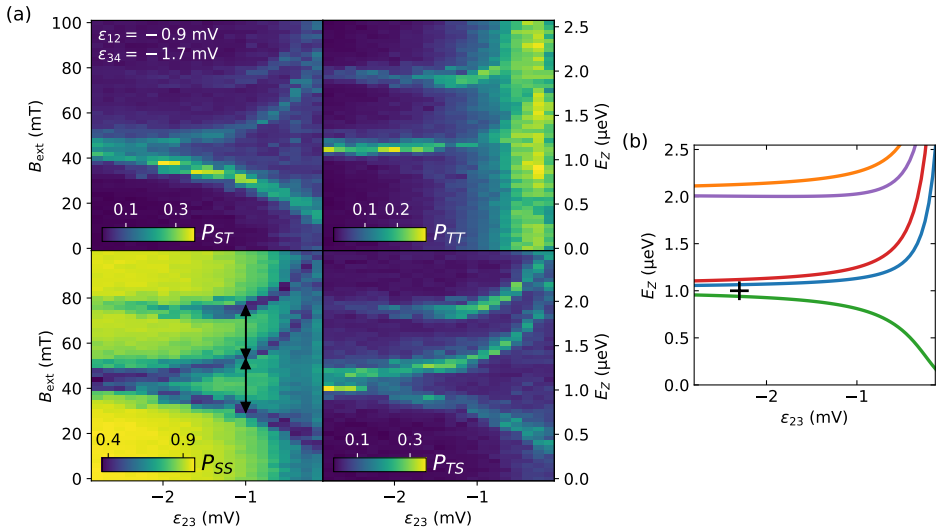

Figure 7.3: Energy spectroscopy as function of magnetic field and middle pair detuning. (a) Left and right pair correlated singlet-triplet probabilities from independent single-shot Pauli spin blockade readout. A decrease in singlet-singlet probability and an increase in one of the other probabilities corresponds to an anti-crossing between the low-energy global singlet state and a polarized state. The right axis shows the calculated Zeeman splitting taking a Landé g-factor of -0.44. (b) Numerical simulation of the middle pair detuning and Zeeman splitting for which the low-energy global singlet state is degenerate with a polarized state. The diagram only shows the energies for the polarized states for which the magnetic field lowers the energy. The energy of the low-energy global singlet state is set to zero as a reference. Points in (b) and Fig. 7.2(b) with the same detunings and magnetic field are indicated with a "+". The legend for (b) is the same as for Fig. 7.2(b).

tion for a singlet on the other pair becomes more (02)-like [34]. The capacitive coupling is modelled by adding $-DJ_{12}J_{34}$ to the diagonal matrix element for $|S_{12}S_{34}\rangle = |0_S\rangle$ in eqn. (7.3), with $D = 0.015\mu\text{eV}^{-1}$ a pre-factor for the interaction strength of the singlet dipoles [34, 37]. At the left and right detunings for which the anti-crossings with T_0^+ and T_1^+ are closest together, the condition $J_{12} = J_{34} = E_Z$ is reached, with E_Z the Zeeman splitting set by the magnetic field.

The coupling between the singlet state and the quintuplet states is of second order in the hyperfine gradients, hence the mixing between them is less efficient. The corresponding lines, such as the blue line in Fig. 7.2(b), are most visible when the quintuplet state energy is closest to a triplet state energy (see the white arrow), since the triplet states mediate the second order coupling (see Appendix 7.8.4).

Figure 7.3(a) shows the measured energy level diagram for which the middle pair detuning and magnetic field were varied. The left and right pair detunings were fixed, and such that $J_{12} = J_{34} = E_Z$, as identified in Fig. 7.2(a). Figure 7.3(b) shows the corresponding numerical simulation. As ε_{23} is increased, the energy splitting between T_0^+ and T_1^+ increases due to increased middle-pair exchange. We experimentally reach the condition $J_{12} = J_{23} = J_{34} = E_Z$ at the middle pair detuning for which the energy level spacing between T_2^+ and T_1^+ is equal to that for T_1^+ and T_0^+, which is indicated by the two equal

length double arrows in the bottom-left panel.

7.5. GLOBAL COHERENT OSCILLATIONS

Before we further characterize the homogeneously coupled spin chain, we will first demonstrate the coherent nature of the coupled four-spin system. Figure 7.4 shows global coherent oscillations, during which the full four-spin system evolves, along with Fourier transforms of those oscillations. Due to the symmetries of the Heisenberg Hamiltonian, time evolution occurs within the subspaces of fixed total spin and magnetization. Since we will initialize in either only local singlets or at most one local triplet, the subspaces here consist of global singlet states or triplet states respectively. The insets in each panel show numerical simulations based on time evolution under a single-band Fermi-Hubbard model [13] without decoherence effects (see Appendix 7.8.5). We note that the condition of homogeneous exchange couplings can be extracted from the coherent oscillations as well.

To observe global coherent oscillations, the spin chain is again operated as depicted in Fig. 7.1(b)-(f). A magnetic field of 200 mT is applied here and in the subsequent measurements, to suppress leakage to states with different magnetization during the manipulation stage. For the data shown in Fig. 7.4(a)-(d) a triplet state is initialized on the left pair and a singlet on the right pair. The detunings are rapidly pulsed such that the exchange couplings diabatically change and the system evolves coherently under the Heisenberg Hamiltonian during the manipulation stage. This evolution results in oscillations in the singlet-triplet probabilities of the left and right pair readout.

Figure 7.4a shows a Chevron pattern from coherent oscillations between the global triplet states for varying differences between the left and right pair detuning and fixed middle pair detuning. The Fourier transform of these oscillations is shown in Fig. 7.4(b). In line with the discussion in Section 7.2, for fixed J_{23} the energy difference between the two lowest-energy triplet states, and thus the oscillation frequency, is minimized if $J_{12} = J_{34}$. We point out that all three exchanges are activated in this measurement, so all four spins coherently evolve together.

Figure 7.4(c) shows global coherent oscillations in the triplet subspace for varying middle pair detuning, and with the left and right pair detuning such that $J_{12} = J_{34}$, as obtained from Fig. 7.4(a),(b). In Fig. 7.4(d) the Fourier transform of these oscillations is shown. The middle pair detuning for which $J_{12} = J_{23} = J_{34}$, indicated by the white dotted line, can be identified from this Fourier transform as the point where the faint vertical line meets the other more visible line. Here the triplets with identical magnetization are equidistant in energy ($J_{hom}/\sqrt{2}$), thus reaching the condition of a spin chain with homogeneous exchange couplings, as described in Section 7.2. In both the experimental and numerical Fourier transform data shown in Fig. 7.4(b),(d), one frequency component is typically much more visible than the others. This is caused by the fact that the initial state overlaps mostly with just two of the three eigenstates, hence the energy difference between these two eigenstates dominates the time evolution.

For the measurements in Fig. 7.4(e) a product of singlets is initialized and the middle pair is read out. As described in Section 7.2, the energy splitting in the singlet subspace, given $J_{12} = J_{34}$, is minimized when $J_{23} = J_{12} = J_{34}$. Figure 7.4(f) shows the Fourier transform of the oscillations in the singlet subspace. The ε_{23} value for the frequency

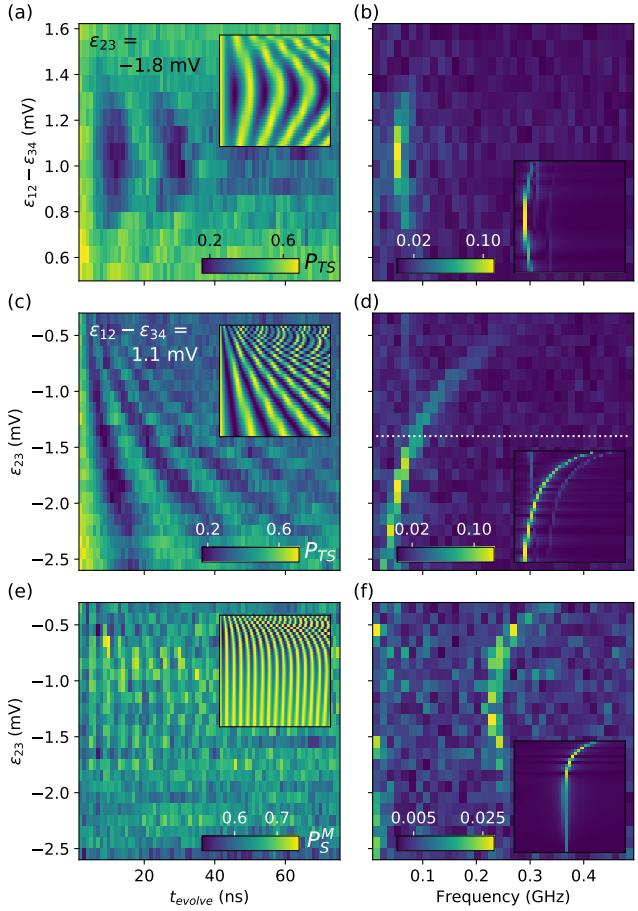

Figure 7.4: Global coherent exchange oscillations. Coherent oscillations (a), (c) within the triplet subspaces and (e) within the singlet subspace. In (a) the difference in outer pair detunings is varied and in (c), (e) the middle pair detuning is varied (with $J_{12} = J_{34}$). (b) Fourier transform of the data in panel (a). The frequency minimum corresponds to $J_{12} = J_{34}$. (d) Fourier transform of the data in panel (c). At $J_{12} = J_{23} = J_{34} = J_{\text{hom}}$, indicated by the white dotted line, the most visible frequency is equal to $J_{\text{hom}}/\sqrt{2}$. (f) Fourier transform of the data in panel (e). The frequency minimum corresponds to $J_{12} = J_{23} = J_{34} = J_{\text{hom}}$ and is equal to $\sqrt{3}J_{\text{hom}}$. Insets in all panels show numerical simulations of the experiment.

minimum cannot be precisely identified due to the limited frequency resolution, but an approximate identification is in agreement with the value of ε_{23} corresponding to homogeneous exchange couplings from Fig. 7.4(d). Also the ratio of the observed oscillation frequencies in the triplet and the singlet subspace at this value of ε_{23} is consistent with theory.

The observation of global coherent oscillations demonstrates the coherent nature of the four-spin system. The coherence is limited by hyperfine and charge noise, of which the first can be strongly reduced by working with (isotopically purified) silicon or germanium as host materials [38]. The latter can be largely mitigated when simulating spin models at half filling (one electron per site) by operating at a so-called sweet spot [39, 40]. Magnetic field gradients, such as due to hyperfine fields, can also induce leakage out of the fixed total spin and magnetization subspace. For the evolution this can result in damping of the oscillations towards an offset that corresponds to the leakage state(s) [41], but this effect is strongly suppressed when exchange couplings dominate the hyperfine fields. The optimal visibility of the oscillations is in general lower than one, because the eigenstates partially overlap with the readout basis. The measured visibility is further lowered by relaxation during readout (which can be accounted for, see Appendix 7.8.3), leakage and partial adiabaticity of state preparation and transition to the readout configuration, which will be further discussed in the next section.

7.6. PROBING THE LOW-ENERGY SINGLET

We finally turn to the preparation and characterization of the Heisenberg spin chain with homogeneous exchange couplings. The ground state of the Heisenberg spin chain, in the absence of an external magnetic field, is the low-energy singlet eigenstate. For homogeneous exchange couplings, $J_{ij} = J_{hom}$, the low-energy singlet eigenstate, S_0, written in the singlet-triplet basis for the left and right pair, is

$$|S_0\rangle \propto (2\sqrt{3}+3)\,|S_{12}S_{34}\rangle + |T^0_{12}T^0_{34}\rangle - |T^+_{12}T^-_{34}\rangle - |T^-_{12}T^+_{34}\rangle\,, \tag{7.7}$$

with normalization factor $\frac{1}{2\sqrt{3(\sqrt{3}+2)}}$. Upon measurement in the two-spin singlet-triplet basis for the left and right pair, we thus have a $\frac{1}{4}\left(2+\sqrt{3}\right) \approx 0.93$ singlet-singlet probability and ≈ 0.07 triplet-triplet probability. Alternatively, the same global singlet state written in a basis given by the middle and outer pair is

$$|S_0\rangle = \frac{1}{\sqrt{2}}S_{14}S_{23} - \frac{1}{\sqrt{6}}T^0_{14}T^0_{23} + \frac{1}{\sqrt{6}}T^+_{14}T^-_{23} + \frac{1}{\sqrt{6}}T^-_{14}T^+_{23}, \tag{7.8}$$

which indicates a fifty-fifty probability to measure a singlet or a triplet on the middle pair. When quasi-static hyperfine and charge noise are included (see Appendix 7.8.5), then numerical simulations result in probabilities of $P^M_S = 0.50$, $P^M_T = 0.50$, $P_{SS} = 0.91$, $P_{ST} = 0.01$, $P_{TS} = 0.01$, and $P_{TT} = 0.07$, which indicates that the noise in the device does not form a direct bottleneck for the quantitative characterization of the spin chain ground state.

Quantitative two-spin singlet-triplet characterization of the low-energy singlet eigenstate, S_0, is facilitated by state preparation that is adiabatic with respect to the exchange couplings. Starting from singlets on the left and right pair of dots, the detunings are

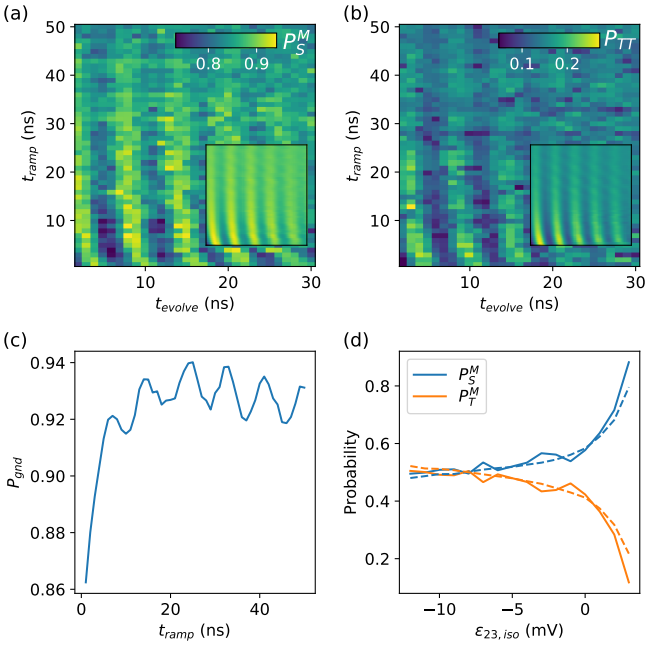

Figure 7.5: Adiabaticity of state preparation and readout. (a) Singlet probability for middle pair readout as function of ramp-in time and evolution time. (b) Triplet-triplet probability for left and right pair readout as function of ramp-in time and evolution time. Insets in (a) and (b) show numerical simulations of the experiment. (c) Numerical simulation of the overlap, $P_{gnd} = |\langle\psi|S_0\rangle|^2$, between the state at the manipulation stage, $|\psi\rangle$, and the low-energy singlet eigenstate, $|S_0\rangle$, as function of ramp-in time. The overlap is an indication for the success of the state preparation. (d) Middle pair singlet and triplet probabilities from experiment (solid lines) and numerical simulations (dashed lines) as function of middle pair detuning for the isolation stage after the manipulation. The experimentally obtained probabilities were corrected for relaxation during the readout time (see Appendix 7.8.3).

slowly varied using voltage ramps to increase the middle pair exchange while reducing the outer pair exchanges. Ideally, the singlet product state evolves to the instantaneous low-energy singlet eigenstate of the Hamiltonian at the manipulation stage. Conversely, projection in the singlet-triplet basis for readout requires a diabatic transition from the manipulation to the readout stage.

Figure 7.5(a) shows the singlet probability for the middle pair readout and Fig. 7.5(b) shows the triplet-triplet probability for the left and right pair readout as function of ramp-in time and evolution time. As expected, we observe oscillations with a decreasing visibility as the ramp-in time increases, as a result of the more adiabatic character of the state preparation. We note that for the measurements shown in Fig. 7.5(a)-(c) during the manipulation stage, the middle exchange, $J_{23} \approx 175\,\text{MHz}$, is made larger than the outer exchanges, $J_{12} = J_{34} \approx 85\,\text{MHz}$, in order to increase the visibility of the oscillations, so we can best evaluate the adiabaticity of the state preparation. For shorter ramp-in time the oscillations bend towards longer evolution time, which is due to the evolution during the ramp-in, thus at the start of the evolution stage the state has already evolved further

for longer ramp-in time. Figure 7.5(c) shows the numerically simulated overlap with the low-energy singlet eigenstate at the manipulation point as function of ramp-in time, indicating > 92% overlap for 12 – 36 ns ramp-in time. For longer ramp-in time leakage to quintuplet and triplet states will start to dominate.

We next study how to maximize the degree of diabaticity for the readout pulses with respect to the exchange couplings, in order to acquire the singlet-triplet probabilities for the state at the end of the manipulation stage. To increase the diabaticity given the finite rise time of the arbitrary waveform generator, an isolation stage is added between the manipulation stage and the readout stage for the case where we aim to read the middle pair. In the isolation stage, the voltages are pulsed deep into the (1201) charge region, such that the voltage step is steeper, which makes the pulse more diabatic.

Figure 7.5(d) shows the singlet and triplet probability for the middle pair readout as a function of $\varepsilon_{23,iso}$, the middle pair detuning (relative to the readout position) for the isolation stage. The state is prepared with $t_{ramp} = 25$ ns, and with homogeneous exchange couplings at the manipulation stage. As discussed previously, for this condition the low-energy singlet eigenstate ideally has equal two-spin singlet and triplet probability on the middle pair. We see in Fig. 7.5(d) that the measured two-spin singlet and triplet probabilities gradually approach each other as $\varepsilon_{23,iso}$ is made more negative, pulsing deeper in the (1201) charge region, indicating that the isolation becomes more diabatic in exchange couplings. Pushing $\varepsilon_{23,iso}$ even further, the singlet-triplet probabilities for the middle pair pass slightly beyond 50/50%, which we can trace back to an artefact from the digital filter in the arbitrary waveform generator. Specifically, we measured the detailed rising flank of the arbitrary waveform generator which shows an undershoot just before the rising flank and ringing after the rising flank, and numerically simulated its effect on the measured singlet-triplet probabilities (see Appendix 7.8.5).

Based on these findings, we set in what follows the ramp-in time to 26 ns when aiming to adiabatically prepare the low-energy singlet eigenstate. Numerical simulations similar to Fig. 7.5(c) show that an overlap of 95.5% with the low-energy singlet state is expected for the homogeneous spin chain. For readout of the middle pair, the middle pair isolation detuning was set to $\varepsilon_{23,iso} = 10$ mV.

Figure 7.6 shows the singlet-triplet probabilities for the spin chain as a function of middle pair detuning (with fixed $J_{12} = J_{34} \approx 85$ MHz) during the manipulation stage. The exchange couplings are calibrated to be homogeneous at $\varepsilon_{23} = -1.8$ mV based on measurements of coherent oscillations similar to Fig. 7.4. The exchange coupling favors two-spin singlet formation on every pair, but due to the monogamy of entanglement, there cannot simultaneously exist such singlets on overlapping pairs. Away from homogeneous exchange couplings, we see in Fig. 7.6(a) that for increasing ε_{23}, thus increasing J_{23}, the singlet probability on the middle pair increases, as expected. Conversely, in Fig. 7.6(b) we observe that as ε_{23} decreases (J_{23} decreases), P_{SS} (P_{TT}) increases (decreases), because the singlets on the left and right pair become energetically increasingly favourable compared to the middle pair singlet. For higher ε_{23} also P_{TS} and P_{ST} increase, which is caused by leakage out of the singlet subspace, due to decreasing energy splitting between the global singlet states and other $m_S = 0$ states.

The experimentally measured numbers are in good agreement with the predicted probabilities based on equations (7.7) and (7.8), and numerical simulations including

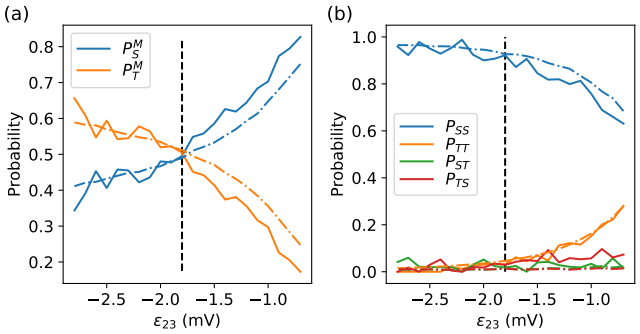

Figure 7.6: Probing the low-energy singlet eigenstate of the homogeneous spin chain. (a) Singlet and triplet probability for middle pair readout, and (b) singlet-triplet correlated probabilities from left and right pair readout as function of middle pair detuning and with $J_{12} = J_{34}$. Experimental data are shown as solid lines and the results from numerical simulations as dashed-dotted lines. Vertical dashed lines indicate the middle pair detuning for which the exchange couplings are calibrated to be homogeneous. The experimentally obtained probabilities were corrected for relaxation during the readout time (see Appendix 7.8.3).

noise. Both the qualitative trend and quantitative comparison between experiment and simulation indicate high-fidelity preparation of the low-energy singlet eigenstate for the homogeneously coupled spin chain, and a high-fidelity characterization method based on singlet-triplet readout and correlations therein.

7.7. CONCLUSION AND OUTLOOK

In summary, we have implemented a quantum simulation of a quantum coherent antiferromagnetic Heisenberg spin chain. For this purpose, we have developed energy spectroscopy methods to identify the condition of homogeneous exchange couplings. Furthermore, we have devised methods to prepare the global ground state of the homogeneous Heisenberg spin chain Hamiltonian, and to probe this state via local measurements in the singlet-triplet basis and correlations of such measurements. We find both qualitative and quantitative agreement between experiment and numerical simulation. Finally, coherent oscillations of the full four-spin system indicate the coherent nature of the system, despite the presence of hyperfine noise in the GaAs host material.

Future quantum magnetism simulation experiments with quantum dots may leverage the recent developments of (isotopically purified) silicon and germanium as host materials, due to the lower concentration of nuclear spins, which further enhances coherence and facilitates high-resolution spectroscopy. The demonstrated control of exchange couplings, as facilitated by the independent control with virtual gates, is a powerful technique for quantum simulations in larger systems. The techniques demonstrated here also pave the way for quantum magnetism simulations in other lattice configurations, such as square and triangular ladders for which simulations of respectively resonating valence bonds and frustrated magnetism are now within the capabilities of gate-defined quantum dots.

The data reported in this paper, and scripts to generate the figures are uploaded to Zenodo: [42].

7.8. SUPPLEMENTARY MATERIAL

7.8.1. LIMITATION FOR DISTINGUISHING STATES WITH TWO-SPIN SINGLET-TRIPLET MEASUREMENTS

The two-spin singlet and triplet projection operators are

$$P_{S_{ij}} = \frac{1}{4} - \vec{S}_i \cdot \vec{S}_j, \tag{7.9}$$

$$P_{T_{ij}} = 1 - P_{S_{ij}}. \tag{7.10}$$

The global spin raising operator, $\hat{S}^+ = \sum_i \hat{S}_i^+$, with $\hat{S}_i^+ = \hat{S}_i^x + i\hat{S}_i^y$, commutes with the singlet and triplet projection operators.

In addition, the spin raising operator commutes with the Heisenberg Hamiltonian

$$[H_{heis}, \hat{S}^+] = 0, \tag{7.11}$$

thus the spin raising and lowering operators map between states in the same eigenspace of the Hamiltonian.

From the commutativity it follows that two-spin singlet-triplet measurements cannot distinguish states in the same eigenspace for the Heisenberg Hamiltonian, and those states can be mapped onto one another with spin raising or lowering operators.

7.8.2. GLOBAL TRIPLET ENERGIES

Figure 7.7 shows the triplet energies as a function of $J_{12} - J_{34}$ and as a function of J_{23} with $J_{12} = J_{34}$.

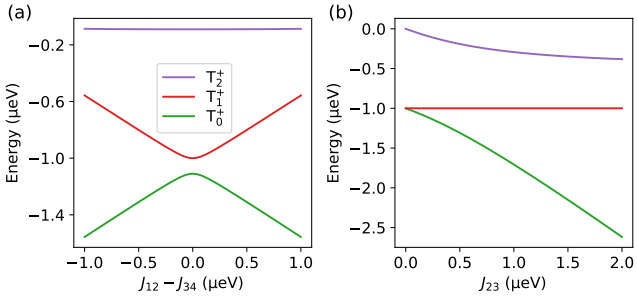

Figure 7.7: Triplet energies. (a) Energies of global triplet states as function of $J_{12} - J_{34}$, with $J_{23} = 0.2\,\mu\text{eV}$ and $J_{12} + J_{34} = 2\,\mu\text{eV}$, revealing a minimum in energy difference at $J_{12} = J_{34}$ for T_0^+ and T_1^+. (b) Triplet energies as function of J_{23} with $J_{12} = J_{34} = 1\,\mu\text{eV}$, showing that at $J_{12} = J_{23} = J_{34}$ the energy spacings are equal. The legend for (b) is the same as for (a). An external magnetic field would result in an overall offset, thus not change the triplet energy differences.

7.8.3. EXPERIMENTAL METHODS

DEVICE

The quadruple quantum dot and sensing dot are formed in a device designed for eight dots and two sensors. A scanning electron micrograph image of the active region of a

Stage	Duration	Description
Initialization (L)	100 µs	Exchange electrons with the reservoir, either in the (0202) charge region for a singlet-singlet state or in (1102) for a triplet-singlet state.
Readout initial (R)	20 µs	Readout of the left and the right pair (each 10 µs) for post-selection, and for background signal subtraction for the final readout to correct for low-frequency charge-noise.
Separate (S)	2 ns	Separate electrons into (1111) charge region.
Ramp detunings	0-50 ns	Ramp the voltages to the operation point (O).
Evolve (O)	2-100 ns	Let the spin state evolve under the exchange couplings.
Isolate (I/S)	2 ns	Isolate the pair(s) for readout.
Readout final (R)	20 µs	Readout the middle pair or the left and right pair (each 10 µs).
Compensate	< 50 µs	Discharge the capacitors in the bias-tee's.

Table 7.2: Details on the stages for the pulse sequence with the durations and descriptions as used for the spin-chain operation. The total duration of the pulse sequence is below 191 µs, including the compensation stage.

device similar to the one used in the experiment is shown in Fig. 7.1(a). The device is mounted in a dilution refrigerator, which resulted in an electron reservoir temperature of about (100 mK) (roughly 10 µeV). By applying voltages on the electrodes on the surface we shape the potential landscape in a two-dimensional electron gas 90 nm below the surface, formed in a silicon-doped GaAs/AlGaAs heterostructure. The plunger gates, labelled P_i [red in Fig. 7.1(a)] for the spin-chain dots and SDP for the sensing dot, control the electrochemical potentials, and the barrier gates [green in Fig. 7.1(a)] control the tunnel couplings between dots or between a dot and a reservoir. When an external magnetic field is applied, it is oriented in the plane of the 2D electron gas.

Table 7.2 shows an overview of the pulse sequence, with the durations and descriptions of the pulse stages.

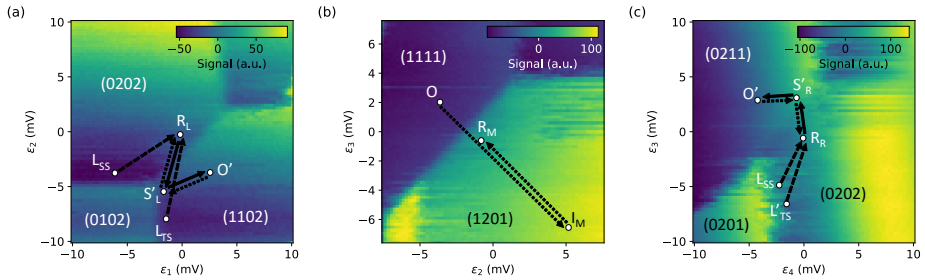

Figure 7.8: Charge-stability diagrams for nearest-neighbour pairs, with (a) left, (b) middle and (c) right. Pulse positions are indicated with small white circles, and are labelled with a letter corresponding to the pulse stage in Table 7.2. Primes are added to characters for which the indicated voltage position is a projection, because the true position is in a different charge occupation, which is outside the respective two-dimensional plane in the four-dimensional charge-stability space. Solid arrows represent the part of the pulse sequence for which only one variant is used, though the operation voltage position, O, is varied throughout the experiments. Dashed arrows correspond to sequences for initialization of either a singlet-singlet, L_{SS}, or triplet-singlet, L_{TS}. Dotted arrows correspond to sequences for readout (and isolation) of either the middle pair, R_M (I_M), or readout (and isolation) of the left pair, R_L (S'_L), and the right pair, R_R (S'_R).

VIRTUAL GATES

For the independent control of site-specific offsets [43] the crosstalk was compensated with the matrix transformation

$$\begin{pmatrix}\varepsilon_1\\ \varepsilon_2\\ \varepsilon_3\\ \varepsilon_4\end{pmatrix} = \begin{pmatrix}1 & 0.539 & 0.203 & 0.145\\ 0.542 & 1 & 0.538 & 0.223\\ 0.181 & 0.5 & 1 & 0.507\\ 0.100 & 0.242 & 0.522 & 1\end{pmatrix}\begin{pmatrix}P_1\\ P_2\\ P_3\\ P_4\end{pmatrix}. \tag{7.12}$$

The lever arms for the single-particle energy offsets are $[76, 81, 87, 84]\,\mu\mathrm{eV\,mV^{-1}}$, which were obtained with photon-assisted tunnelling [31, 44].

CHARGE-STABILITY DIAGRAMS WITH SEQUENCE DETAILS

Figure 7.8 shows charge-stability diagrams for the nearest-neighbour pairs in the quadruple dot. Typical pulse voltage positions and the order of the pulse sequence are indicated. The compensation and the parking for the readout of the left and right pair are not displayed to preserve clarity.

POST-SELECTION FOR STATE PREPARATION

Figure 7.9 shows single-shot results of readout directly after initialization. The data for the readout after the evolution stage is post-selected by thresholding the signal from the readout after initialization. The signal is also used for background subtraction to suppress the effect of low-frequency charge noise on the signal for the final readout. Errors in initialization for both the singlet-singlet product state and the triplet-singlet product state can occur because of the finite dot-reservoir tunnel rate, due to which the target charge state (0202) and (1102) respectively is not occupied at the end of the initialization stage. These errors result in the counts in the top half regions of Fig. 7.9(a) and (b). Such

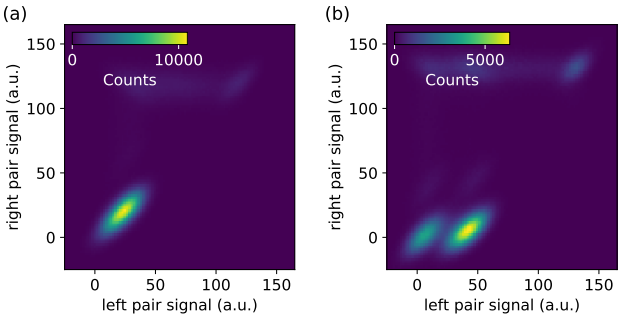

Figure 7.9: Histograms of correlated left and right pair readout directly after initialization of (a) the singlet-singlet product state and (b) the triplet-singlet product state. For both the left and the right pair readout the integration time was 8 µs and the bin width was [1.9, 1.9] a.u.

errors can be reduced by increasing the duration of the initialization stage or increasing the dot-reservoir tunnel rate. Additionally, errors in the triplet-singlet product initialization can be caused by thermal excitations, due to which a singlet-singlet product state in the (1102) charge occupation can be occupied, which results in the bottom-left peak in Fig. 7.9(b). This error can be reduced by increasing the magnetic field strength.

SEPARATE EXCHANGE COUPLING MEASUREMENTS

Fig. 7.10 shows separate exchange coupling measurements for each of the neighbouring pairs. For the spin funnel measurements for the left and right pair the middle exchange coupling is set to be small. The spin funnels are fitted with the exchange model in eqn. (7.6). For the middle pair the Fourier transform of coherent oscillations in the triplet-subspace is used. The model for the Fourier transform follows from eqn. (7.4), and is $\frac{1}{2}\left(J_{23} - J_{hom} + \sqrt{J_{23}^2 + J_{hom}^2}\right)$, with $J_{hom} = J_{12} = J_{34} = 125\,\text{MHz}$, the homogeneous exchange coupling as obtained from Fig. 7.4. From these three separate fits the tunnel couplings are extracted as 8.5 µeV, 7.5 µeV, and 11.9 µeV for the left, middle and right pair respectively. These tunnel coupling values are used for the numerical simulations of the experiment.

READOUT WITH RELAXATION AND HISTOGRAM MODELS

Single-shot readout characteristics for each of the nearest-neighbour pairs are shown in Fig. 7.11. The data in panels (b) and (d) is from the data for Fig. 7.6(a), and the data from panel (e) is from part of the data for Fig. 7.2(a).

The effect on the probabilities of relaxation during the readout is taken into account by modelling the single-shot data with a histogram. For readout on a single pair the model for the histogram has been described in [33, 45]. For the singlet-triplet correlation measurements the two-dimensional single-shot histograms are modelled with

$$N(\mathbf{x}) = N_{tot} \sum_{i,j \in [S,T]} P_{ij}\, n_{ij}(\mathbf{x})\, w_1\, w_2, \tag{7.13}$$

with N_{tot} the number of single-shot repetitions, P_{ij} the average probability for outcome ij, n_{ij} the probability density distribution, and w_i the bin widths.

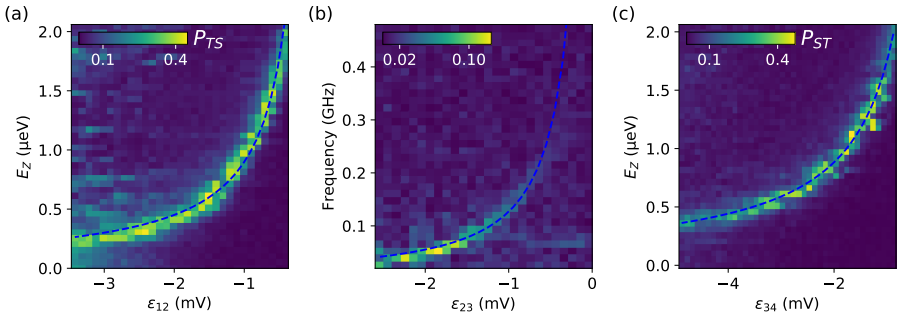

Figure 7.10: Separate exchange coupling measurements. The dashed blue lines are fits to the data. (a) Spin funnel on left pair, (b) Fourier transform of triplet-subspace coherent oscillations shown in Fig. 3(c), (c) Spin funnel on right pair.

The readout of the left and right pair of spins is performed with the same sensing dot, thus noise on the sensor signal can induce correlations between the two readouts. Low-frequency noise, which causes signal differences between repetitions, is taken into account by the subtraction of the sensor signal from the readout directly after the initialization. Correlations in the sensor signals due to higher frequency noise remain, which results in the diagonally elongated signal peaks in the two-dimensional readout histogram as shown in Fig. 7.11(e). The effect of the correlations is incorporated in the model for the two-dimensional Gaussian histogram by modelling the Gaussian peaks with rotated ellipses.

The two-dimensional Gaussian is

$$g_{2D}(\mathbf{x},\mu) = \frac{1}{2\pi\sigma_1\sigma_2} e^{-\left[a(x_1-\mu_1)^2+2b(x_1-\mu_1)(x_2-\mu_2)+c(x_2-\mu_2)^2\right]}, \tag{7.14}$$

with μ the mean coordinates, and where the parameters for the shapes of the Gaussian peaks are

$$a = \frac{\cos^2\theta}{2\sigma_1^2} + \frac{\sin^2\theta}{2\sigma_2^2}, b = -\frac{\sin 2\theta}{4\sigma_1^2} + \frac{\sin 2\theta}{4\sigma_2^2}, c = \frac{\sin^2\theta}{2\sigma_1^2} + \frac{\cos^2\theta}{2\sigma_2^2}, \tag{7.15}$$

with θ the rotation angle of the ellipsoidal shape of the Gaussian peaks, and σ_1 and σ_2 describe the ellipse width and length. In the experiment the first and second readout signals are integrated for equal durations, which sets $\theta = \pi/4$, which means that the one-dimensional histograms for the left and right pair readout have the same Gaussian widths. In the extreme when there are no noise correlations, then $\sigma_1 = \sigma_2$ and in the other extreme where the noise would be fully correlated the histogram effectively is a one-dimensional Gaussian.

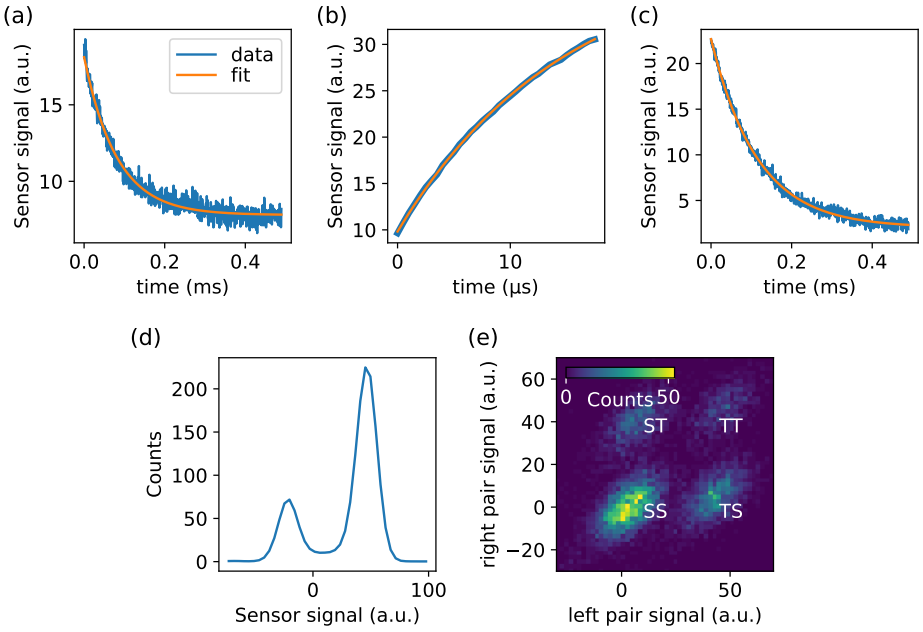

Figure 7.11: Readout characteristics (a), (b), (c), show relaxation curves for the Pauli spin blockade readout of the left, middle and right pair respectively. The corresponding T_1 values are 80.9 µs, 25.0 µs and 114.8 µs. (d) Histogram of middle pair readout with 8 µs integration time, bin width 4.375 a.u., and the counts are in thousands. (e) Histogram of correlated left and right pair readout. For both readouts the integration time was 8 µs and the bin width was [2.0, 2.0] a.u.

7

The probability distributions for the correlated singlet-triplet outcomes are

$$n_{SS}(\mathbf{x}) = g_{2D}(\mathbf{x}, \mu_{SS}), \tag{7.16}$$

$$n_{ST}(\mathbf{x}) = e^{-\alpha_R} g_{2D}(\mathbf{x}, \mu_{ST}) + \alpha_R \int_0^1 dz e^{-z\alpha_R} g_{2D}(\mathbf{x}, z(\mu_{ST} - \mu_{SS}) + \mu_{SS}), \tag{7.17}$$

$$n_{TS}(\mathbf{x}) = e^{-\alpha_L} g_{2D}(\mathbf{x}, \mu_{TS}) + \alpha_L \int_0^1 dz e^{-z\alpha_L} g_{2D}(\mathbf{x}, z(\mu_{TS} - \mu_{SS}) + \mu_{SS}), \tag{7.18}$$

$$\begin{aligned} n_{TT}(\mathbf{x}) = {} & e^{-(\alpha_L+\alpha_R)} g_{2D}(\mathbf{x}, \mu_{TT}) + e^{-\alpha_R} \alpha_L \int_0^1 dz e^{-z\alpha_L} g_{2D}(\mathbf{x}, z(\mu_{TT} - \mu_{ST}) + \mu_{ST}) \\ & + e^{-\alpha_L} \alpha_R \int_0^1 dz e^{-z\alpha_R} g_{2D}(\mathbf{x}, z(\mu_{TT} - \mu_{TS}) + \mu_{TS}) \\ & + \alpha_L \alpha_R \int_0^1 \int_0^1 dz dz' \left[e^{-(z\alpha_L + z'\alpha_R)} g_{2D}(\mathbf{x}, (z(\mu_{T,L} - \mu_{S,L}) + \mu_{S,L}, z'(\mu_{T,R} - \mu_{S,R}) + \mu_{S,R})) \right], \end{aligned} \tag{7.19}$$

with $\alpha_i = t_i / T_{1,i}$, which is the ratio between the signal integration time, t_i, and the relaxation time, $T_{1,i}$, for the left pair or the right pair. In n_{TT} the first term corresponds to states which do not decay during both readouts, the second term to states which decay

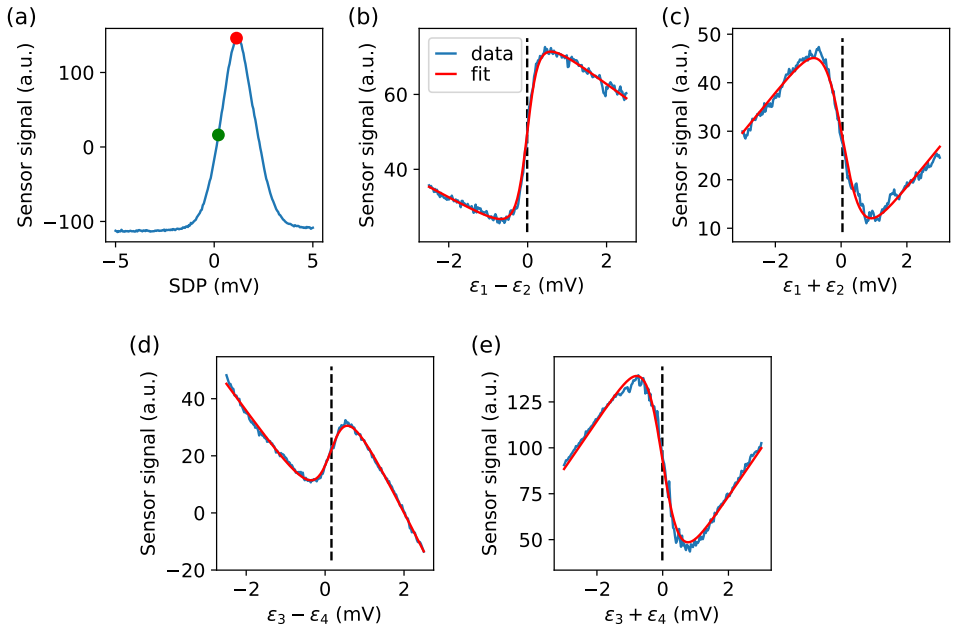

Figure 7.12: Automatic calibration of pulse voltage offsets. (a) Sensing dot calibration, with the red marker corresponding to the top of the Coulomb peak, and the green marker is the half-height on the rising flank, (b) inter-dot transition between (0202)-(1102), (c) dot-reservoir transition between (0202)-(1202), (d) inter-dot transition between (0202)-(0211), (e) dot-reservoir transition between (0202)-(0212). The traces are not centred at the same voltages, but voltage offsets are added for each scan based on the previous calibration.

during the left pair readout but not the right pair readout, the third term to states which do not during the left pair readout but do decay during the right pair readout, and the last term corresponds to states which decay during both readouts.

For the fitting procedure first the histogram of single-shot results for all pulse setpoints is fitted to obtain the Gaussian widths and peak positions, and then the histogram for each pulse setpoint is separately fitted to obtain the probability amplitudes.

AUTOMATIC PULSE OFFSET CALIBRATION

The spin-chain operation of the device was automatically re-calibrated on a daily basis to correct for the effect of irregular charge jumps. The results of the calibration were incorporated as offsets for the pulse voltages. The static voltage on the sensing dot plunger was sometimes adjusted between measurements, but all other d.c. voltages were left untouched to avoid introducing instabilities of the device.

Figure 7.12 shows the result of the daily automatic re-calibration, which consists of five traces. These traces are a sweep of the sensing dot plunger gate voltage, and four one-dimensional cuts through the charge-stability space of the quadruple quantum dot. The sensing dot scan is performed to calibrate the gate voltage for the position on the flank of the sensing dot Coulomb peak. The four one-dimensional cuts are performed to

locate the gate voltages corresponding to specific charge transitions. The gate voltages for these transitions form a reference for the voltages used in the pulsed control of the spin chain, such that electrostatic shifts of the device are corrected for.

The analysis procedures for the Coulomb peak and the dot-reservoir transition are based on Ref. [46], and the inter-dot transition fitting is from Ref. [44]. The automatic calibration routine takes in total approximately 30 seconds. Occasionally, large charge jumps required coarse manual tuning of the device, after which the automatic calibration routine was used for refinement.

7.8.4. HYPERFINE GRADIENT COUPLINGS

The effect of the nuclear spins in the material environment on the electron spins in the quantum dots can effectively be described by hyperfine fields [32] as

$$H_{hf} = g\mu_B \sum_i \vec{h}_i \cdot \vec{S}_i, \tag{7.20}$$

with $\vec{h}_i$ the local hyperfine field for dot i. The hyperfine term breaks the conservation of total spin and spin-z of the Heisenberg Hamiltonian, and has been studied extensively experimentally and theoretically for two-spin systems [32, 47]. For the energy spectroscopy of the four-spin system as shown in Fig. 7.2 and Fig. 7.3 the couplings between the singlet-subspace and the polarized states are given by the hyperfine matrix, which in the basis $(Q^{++}, Q^{+}, |2_{T^+}\rangle, |1_{T^+}\rangle, |0_{T^+}\rangle, |1_S\rangle, |0_S\rangle)$ is

$$\begin{pmatrix}
\frac{B_{z,sum}}{2} & \frac{B_{x,sum}-iB_{y,sum}}{4} & \frac{dB_{-,14}+dB_{-,23}}{2} & \frac{-dB_{-,12}}{\sqrt{2}} & \frac{-dB_{-,34}}{\sqrt{2}} & 0 & 0 \\
\frac{B_{x,sum}+iB_{y,sum}}{4} & \frac{B_{z,sum}}{4} & \frac{-dB_{z,12}-dB_{z,34}}{2} & \frac{dB_{z,12}}{\sqrt{2}} & \frac{dB_{z,34}}{\sqrt{2}} & 0 & 0 \\
\frac{dB_{+,14}+dB_{+,23}}{2} & \frac{-dB_{z,12}-dB_{z,34}}{2} & \frac{B_{z,sum}}{4} & \frac{dB_{z,12}}{\sqrt{2}} & \frac{-dB_{z,12}}{\sqrt{2}} & \frac{dB_{-,14}+dB_{-,23}}{\sqrt{3}} & 0 \\
\frac{-dB_{+,12}}{\sqrt{2}} & \frac{dB_{z,12}}{\sqrt{2}} & \frac{dB_{z,12}}{\sqrt{2}} & \frac{B_{z,3}+B_{z,4}}{2} & 0 & \frac{dB_{-,12}}{\sqrt{6}} & \frac{-dB_{-,34}}{\sqrt{2}} \\
\frac{-dB_{+,34}}{\sqrt{2}} & \frac{dB_{z,34}}{\sqrt{2}} & \frac{-dB_{z,34}}{\sqrt{2}} & 0 & \frac{B_{z,1}+B_{z,2}}{2} & \frac{dB_{-,34}}{\sqrt{2}} & \frac{-dB_{-,12}}{\sqrt{6}} \\
0 & 0 & \frac{dB_{+,14}+dB_{+,23}}{\sqrt{3}} & \frac{dB_{x+,12}}{\sqrt{6}} & \frac{dB_{+,34}}{\sqrt{2}} & 0 & 0 \\
0 & 0 & 0 & \frac{-dB_{+,34}}{\sqrt{2}} & \frac{-dB_{+,12}}{\sqrt{6}} & 0 & 0
\end{pmatrix}, \tag{7.21}$$

with $dB_{+,ij} = dB_{x,ij} + idB_{y,ij}$ and $dB_{-,ij} = dB_{x,ij} - idB_{y,ij}$, where $dB_{\alpha,ij} = (B_{\alpha,i} - B_{\alpha,j})/2$, and $B_{\alpha,sum} = \sum_i B_{\alpha,i}$.

From the hyperfine matrix it follows that for any state in the singlet subspace, $|S_k\rangle$, the first-order coupling to a quintuplet is $\langle S_k | H_{hf} | Q^{++} \rangle = \langle S_k | H_{hf} | Q^{+} \rangle = 0$. The coupling between the singlet and the quintuplet(s) as visible in the energy spectroscopy in Fig. 7.2(a) and Fig. 7.3(a), can be explained by a second order effect where the singlet state couples to a triplet state, which in turn couples to a quintuplet state. The second-order coupling only becomes effective when the singlet and quintuplet state energies are near the energy of a coupling-mediating triplet state. This is observed in the energy spectroscopy where the coupling of the singlet to the Q^{++} state decreases as the singlet energy differs more from the T_0^+ and T_1^+ energies.

Note that the spin-orbit interaction can induce couplings between states with different charge occupation [48, 49], which can contribute to the signal for the anti-crossings in the energy spectroscopy.

7.8.5. NUMERICAL SIMULATION

The time evolution simulations are based on the single-band Fermi-Hubbard model

$$H_{FH} = -\sum_i \epsilon_i n_i + \sum_i \frac{U_i}{2} n_i(n_i - 1) + \sum_{ij, i\neq j} V_{ij} n_i n_j - \sum_{\langle i,j\rangle} t_{ij}\left(c_i^\dagger c_j + h.c.\right), \tag{7.22}$$

where ϵ_i is the negative single-particle energy offset, $n_i = c_i^\dagger c_i$ is the dot occupation, and $c_i^{(\dagger)}$ is the annihilation (creation) operator, U_i is the on-site Coulomb repulsion, V_{ij} the inter-site Coulomb repulsion and t_{ij} the inter-dot tunnel coupling. The parameter values for the simulations were $U_i = 3\,\text{meV}$, $V_{i,i+1} = 0.5\,\text{meV}$, $V_{i,i+2} = 0.1\,\text{meV}$, $V_{i,i+3} = 20\,\mu\text{eV}$, and $[t_{12}, t_{23}, t_{34}] = [8.5, 7.5, 11.9]\,\mu\text{eV}$. The tunnel coupling values were experimentally obtained from fits to spin funnels for the left and right pair and from a fit of the Fourier transform in Fig. 7.4(d) (see Appendix 7.8.3). Differences between the experimental and simulation values for the interaction parameters are accounted for in the simulations with offsets in the single-particle energies. The Hamiltonian matrix for the simulation is generated with QuTip [50]. The charge configurations used for the simulations are (1111), (0211), (1201), (1102) and (0202). The spin subspace which is used for the simulation of Fig. 7.4(a)-(d) is the four-spin T^+ subspace, while for Fig. 7.4(e),(f) the global singlet subspace is used. For the numerical simulations in Fig. 7.5 and 7.6 the set of states for the simulation consists of the global singlet subspace, and all other $m_S = 0$ states, thus the four-spin T^0 subspace and Q^0.

For the simulation the same sequence was followed as the experimental sequence for the spin chain, which is shown in Fig. 7.1(b)-(f) and detailed in Table 7.2. Time evolution of the states is computed using an in-house density matrix solver package [51]. The simulated probabilities shown in the figures in the main text are the probabilities at the isolation stage after the evolution. In order to simulate the adiabaticity of the experimental sequence, the voltage pulse shape for the simulation is based on the experimental voltage pulse shape from the arbitrary waveform generator (AWG). The simulated shape is obtained from the Fourier transform of the ideal pulse shapes and the subsequent inverse Fourier transform with the experimentally measured frequency response of the AWG. The Fourier component amplitudes are corrected for the finite sampling rate, $f_s = 1\,\text{GHz}$, of the AWG by dividing with $\text{sinc}\left(f/f_s\right)$, where f is the frequency of the Fourier component.

The effects of charge noise and quasi-static hyperfine noise were included for the simulations in the main text, except for Fig. 7.4. The quasi-static hyperfine noise is considered by repeating the simulation, and for each repetition taking a sample from a Gaussian distribution with a root mean square of 3.2 mT, which was experimentally obtained from the amplitude decay of the global exchange oscillations. The power spectral density of the charge noise is modelled with A/f^α, with A=0.26 μeV^2/Hz and $\alpha = 0.79$, which are obtained from a charge noise measurement. The charge noise was measured from 1 Hz to 5 kHz. For the simulations a charge-noise frequency range from 0.1 Hz to 100 GHz was used, where noise on a timescale longer than a single-shot of the experimental sequence is integrated and added as quasi-static noise.

REFERENCES

[1] I. M. Georgescu, S. Ashhab, and F. Nori, *Quantum simulation,* Reviews of Modern Physics **86**, 153 (2014).

[2] J. Simon, W. S. Bakr, R. Ma, M. E. Tai, P. M. Preiss, and M. Greiner, *Quantum simulation of antiferromagnetic spin chains in an optical lattice,* Nature **472**, 307 (2011).

[3] S. Nascimbène, Y. A. Chen, M. Atala, M. Aidelsburger, S. Trotzky, B. Paredes, and I. Bloch, *Experimental realization of plaquette resonating valence-bond states with ultracold atoms in optical superlattices,* Physical Review Letters **108**, 205301 (2012).

[4] D. Greif, T. Uehlinger, G. Jotzu, L. Tarruell, and T. Esslinger, *Short-range quantum magnetism of ultracold fermions in an optical lattice,* Science **340**, 1307 (2013).

[5] S. Murmann, F. Deuretzbacher, G. Zürn, J. Bjerlin, S. M. Reimann, L. Santos, T. Lompe, and S. Jochim, *Antiferromagnetic heisenberg spin chain of a few cold atoms in a one-dimensional trap,* Physical Review Letters **115**, 215301 (2015).

[6] A. Mazurenko, C. S. Chiu, G. Ji, M. F. Parsons, M. Kanász-Nagy, R. Schmidt, F. Grusdt, E. Demler, D. Greif, and M. Greiner, *A cold-atom Fermi-Hubbard antiferromagnet,* Nature **545**, 462 (2017).

[7] G. Salomon, J. Koepsell, J. Vijayan, T. A. Hilker, J. Nespolo, L. Pollet, I. Bloch, and C. Gross, *Direct observation of incommensurate magnetism in Hubbard chains,* Nature **565**, 56 (2019).

[8] A. Friedenauer, H. Schmitz, J. T. Glueckert, D. Porras, and T. Schaetz, *Simulating a quantum magnet with trappedions,* Nature Physics **4**, 757 (2008).

[9] J. G. Bohnet, B. C. Sawyer, J. W. Britton, M. L. Wall, A. M. Rey, M. Foss-Feig, and J. J. Bollinger, *Quantum spin dynamics and entanglement generation with hundreds of Trapped Ions,* Science **352**, 1297 (2016).

[10] R. Toskovic, R. Van Den Berg, A. Spinelli, I. S. Eliens, B. Van Den Toorn, B. Bryant, J. S. Caux, and A. F. Otte, *Atomic spin-chain realization of a model for quantum criticality,* Nature Physics **12**, 656 (2016).

[11] M. W. Johnson, M. H. Amin, S. Gildert, T. Lanting, F. Hamze, N. Dickson, R. Harris, A. J. Berkley, J. Johansson, P. Bunyk, E. M. Chapple, C. Enderud, J. P. Hilton, K. Karimi, E. Ladizinsky, N. Ladizinsky, T. Oh, I. Perminov, C. Rich, M. C. Thom, E. Tolkacheva, C. J. Truncik, S. Uchaikin, J. Wang, B. Wilson, and G. Rose, *Quantum annealing with manufactured spins,* Nature **473**, 194 (2011).

[12] R. Hanson, L. P. Kouwenhoven, J. R. Petta, S. Tarucha, and L. M. K. Vandersypen, *Spins in few-electron quantum dots,* Reviews of Modern Physics **79**, 1217 (2007).

[13] T. Hensgens, T. Fujita, L. Janssen, X. Li, C. J. Van Diepen, C. Reichl, W. Wegscheider, S. Das Sarma, and L. M. K. Vandersypen, *Quantum simulation of a Fermi-Hubbard model using a semiconductor quantum dot array,* Nature **548**, 70 (2017).

[14] J. P. Dehollain, U. Mukhopadhyay, V. P. Michal, Y. Wang, B. Wunsch, C. Reichl, W. Wegscheider, M. S. Rudner, E. Demler, and L. M. K. Vandersypen, *Nagaoka ferromagnetism observed in a quantum dot plaquette,* Nature **579**, 528 (2020).

[15] A. Auerbach, *Interacting Electrons and Quantum Magnetism,* Springer (1994).

[16] Y. P. Kandel, H. Qiao, S. Fallahi, G. C. Gardner, M. J. Manfra, and J. M. Nichol, *Coherent spin state transfer via Heisenberg exchange,* Nature **573**, 553 (2019).

[17] H. Qiao, Y. P. Kandel, K. Deng, S. Fallahi, G. C. Gardner, M. J. Manfra, E. Barnes, and J. M. Nichol, *Coherent multi-spin exchange in a quantum-dot spin chain,* Physical Review X **10**, 31006 (2020).

[18] S. Bose, *Quantum communication through spin chain dynamics : an introductory overview,* Contemporary Physics **48**, 13 (2007).

[19] L. Campos Venuti, C. Degli Esposti Boschi, and M. Roncaglia, *Qubit Teleportation and Transfer across Antiferromagnetic Spin Chains,* Physical Review Letters **99**, 060401 (2007).

[20] S. Oh, Y.-P. Shim, J. Fei, M. Friesen, and X. Hu, *Resonant adiabatic passage with three qubits,* Physical Review A **87**, 022332 (2013).

[21] U. Farooq, A. Bayat, S. Mancini, and S. Bose, *Adiabatic many-body state preparation and information transfer in quantum dot arrays,* Physical Review B **91**, 134303 (2015).

[22] Y. P. Kandel, Q. Haifeng, S. Fallahi, G. C. Gardner, M. J. Manfra, and J. M. Nichol, *Adiabatic quantum state transfer in a semiconductor quantum-dot spin chain,* Nature Communications **12**, 1256 (2021).

[23] P. W. Anderson, *The Resonating Valence Bond State in La_2CuO_4 and Superconductivity,* Science **235**, 1196 (1987).

[24] S. Sachdev, *Quantum magnetism and criticality,* Nature Physics **4**, 173 (2008).

[25] L. Balents, *Spin liquids in frustrated magnets,* Nature **464**, 199 (2010).

[26] J. Gray, A. Bayat, R. K. Puddy, C. G. Smith, and S. Bose, *Unravelling quantum dot array simulators via singlet-triplet measurements,* Physical Review B **94**, 195136 (2016).

[27] G. Burkard, D. Loss, and D. P. Divincenzo, *Coupled quantum dots as quantum gates,* Physical Review B **59**, 2070 (1999).

[28] H. Bethe, *Zur theorie der metalle,* Zeitschrift für Physik **71**, 205 (1931).

[29] A. Sala and J. Danon, *Exchange-only singlet-only spin qubit,* Physical Review B **95**, 241303 (2017).

[30] J. R. Petta, A. C. Johnson, J. M. Taylor, E. A. Laird, A. Yacoby, M. D. Lukin, C. M. Marcus, M. P. Hanson, and A. C. Gossard, *Coherent Manipulation of Coupled Electron Spins in Semiconductor Quantum Dots,* Science **309**, 2180 (2005).

[31] T.-K. Hsiao, C. J. van Diepen, U. Mukhopadhyay, C. Reichl, W. Wegscheider, and L. M. K. Vandersypen, *Efficient orthogonal control of tunnel couplings in a quantum dot array,* Physical Review Applied **13**, 054018 (2020).

[32] J. M. Taylor, J. R. Petta, A. C. Johnson, A. Yacoby, C. M. Marcus, and M. D. Lukin, *Relaxation, dephasing, and quantum control of electron spins in double quantum dots,* Physical Review B **76**, 035315 (2007).

[33] C. Barthel, D. J. Reilly, C. M. Marcus, M. P. Hanson, and A. C. Gossard, *Rapid single-shot measurement of a singlet-triplet qubit,* Physical Review Letters **103**, 160503 (2009).

[34] M. D. Shulman, O. E. Dial, S. P. Harvey, H. Bluhm, V. Umansky, and A. Yacoby, *Demonstration of entanglement of electrostatically coupled singlet-triplet qubits,* Science **336**, 202 (2012).

[35] J. Medford, J. Beil, J. M. Taylor, E. I. Rashba, H. Lu, A. C. Gossard, and C. M. Marcus, *Quantum-dot-based resonant exchange qubit,* Physical Review Letters **111**, 050501 (2013).

[36] F. K. Malinowski, F. Martins, T. B. Smith, S. D. Bartlett, A. C. Doherty, P. D. Nissen, S. Fallahi, G. C. Gardner, M. J. Manfra, C. M. Marcus, and F. Kuemmeth, *Spin of a Multielectron Quantum Dot and Its Interaction with a Neighboring Electron,* Physical Review X **8**, 11045 (2018).

[37] D. Buterakos, R. E. Throckmorton, and S. Das Sarma, *Simulation of the coupling strength of capacitively coupled singlet-triplet qubits,* Physical Review B **100**, 075411 (2019).

[38] G. Scappucci, *Semiconductor materials stacks for quantum dot spin qubits,* arXiv:2102.10897 (2021).

[39] M. D. Reed, B. M. Maune, R. W. Andrews, M. G. Borselli, K. Eng, M. P. Jura, A. A. Kiselev, T. D. Ladd, S. T. Merkel, I. Milosavljevic, E. J. Pritchett, M. T. Rakher, R. S. Ross, A. E. Schmitz, A. Smith, J. A. Wright, M. F. Gyure, and A. T. Hunter, *Reduced Sensitivity to Charge Noise in Semiconductor Spin Qubits via Symmetric Operation,* Physical Review Letters **116**, 110402 (2016).

[40] F. Martins, F. K. Malinowski, P. D. Nissen, E. Barnes, S. Fallahi, G. C. Gardner, M. J. Manfra, C. M. Marcus, and F. Kuemmeth, *Noise Suppression Using Symmetric Exchange Gates in Spin Qubits,* Physical Review Letters **116**, 116801 (2016).

[41] J. Medford, J. Beil, J. M. Taylor, S. D. Bartlett, A. C. Doherty, E. I. Rashba, D. P. Divincenzo, H. Lu, A. C. Gossard, and C. M. Marcus, *Self-consistent measurement and state tomography of an exchange-only spin qubit,* Nature Nanotechnology **8**, 654 (2013).

[42] https://doi.org/10.5281/zenodo.4541301.

[43] T. A. Baart, M. Shafiei, T. Fujita, C. Reichl, W. Wegscheider, and L. M. K. Vandersypen, *Single-Spin CCD,* Nature Nanotechnology **11**, 330 (2015).

[44] C. J. van Diepen, P. T. Eendebak, B. T. Buijtendorp, U. Mukhopadhyay, T. Fujita, C. Reichl, W. Wegscheider, and L. M. K. Vandersypen, *Automated tuning of inter-dot tunnel coupling in double quantum dots,* Applied Physics Letters **113**, 033101 (2018).

[45] C. J. van Diepen, T.-K. Hsiao, U. Mukhopadhyay, C. Reichl, W. Wegscheider, and L. M. K. Vandersypen, *Electron cascade for distant spin readout,* Nature Communications **12**, 77 (2021).

[46] T. A. Baart, P. T. Eendebak, C. Reichl, W. Wegscheider, and L. M. K. Vandersypen, *Computer-automated tuning of semiconductor double quantum dots into the single-electron regime,* Applied Physics Letters **108**, 1213104 (2016).

[47] A. C. Johnson, J. R. Petta, A. Yacoby, M. D. Lukin, C. M. Marcus, M. P. Hanson, and A. C. Gossard, *Triplet – singlet spin relaxation via nuclei in a double quantum dot,* Nature **435**, 925 (2005).

[48] L. R. Schreiber, F. R. Braakman, T. Meunier, V. Calado, J. Danon, J. M. Taylor, W. Wegscheider, and L. M. K. Vandersypen, *Coupling artificial molecular spin states by photon-assisted tunnelling,* Nature Communications **2**, 556 (2011).

[49] J. M. Nichol, S. P. Harvey, M. D. Shulman, A. Pal, V. Umansky, E. I. Rashba, B. I. Halperin, and A. Yacoby, *Quenching of dynamic nuclear polarization by spin-orbit coupling in GaAs quantum dots,* Nature Communications **6**, 7682 (2015).

[50] J. R. Johansson, P. D. Nation, and F. Nori, *QuTiP: An open-source Python framework for the dynamics of open quantum systems,* Computer Physics Communications **183**, 1760 (2012).

[51] https://github.com/stephanlphilips/dm_solver.

8

LONG-RANGE ELECTRON-ELECTRON INTERACTION IN GATE-DEFINED QUANTUM DOTS

Long-range interactions play an important role in a variety of physical phenomena. Such phenomena could be studied with quantum simulators to gain insights where classical numerical simulations fail. Gate-defined quantum dots have been established as a platform for quantum simulations of Fermi-Hubbard physics. However, long-range electron-electron interactions have not been used as ingredient for those simulations so far. Here we show the experimental characterization of the electron-electron interaction in an array of gate-defined quantum dots. The interaction is found to be measurable between electrons that are up to four sites away, thus considered to be long-range. The interaction is modelled with both the Yukawa potential and a potential based on the method of image charges with the gate metal acting as screening layer. These results pave the way for quantum dots as quantum simulators of phenomena involving long-range electron-electron interactions. Furthermore, they have implications for the operation of quantum dot arrays with spin qubits, for example when using shared control.

The results in this chapter are being prepared for publication.

8.1. INTRODUCTION

Electron-electron interactions are a key ingredient to describe quantum chemistry [1], Wigner crystallization [2], exciton formation [3], and even high-temperature superconductivity [4]. Quantum simulators could provide insights where classical numerical simulations become intractable [5, 6], but interactions in simulators are often only short-ranged. Semiconductor quantum dots are a promising platform for analog quantum simulation of Fermi-Hubbard physics [6–8]. Simulations have addressed the transition from Coulomb blockade to collective Coulomb blockade [9], itinerant ferromagnetism when doping with a single hole [10], and Heisenberg magnetism arising in the Mott-insulator regime [11]. Long-range electron-electron interactions have not yet been used as ingredient for simulations with gate-defined quantum dots, and their effect was previously either tuned away or remained as an unwanted disturbance.

Transport measurements on double quantum dots more than two decades ago [12] already revealed interactions between electrons on nearest-neighbour sites. In more recent work, these interactions have been used to induce entanglement between qubits on separate double dots [13]. The charge sensor performance has been assessed based on the coupling to the sensed dot [14]. For readout of spins distant from the charge sensor, a cascade of electrons was induced, which made use of the interactions between electrons on either one or two sites away [15]. However, a detailed study of the electron-electron interaction as a function of distance has not yet been performed. Such characterization is challenging because it demands control over the potential landscape over sufficient distance, such as for the formation and homogeneous tuning of a multi-dot array. More specifically, the electron-electron interaction can be accurately characterized with a multi-dot array that is sufficiently large to offer adequate coverage over the range of interactions. The recent development of a tuning strategy for a multi-dot array [16], and the efficient compensation for tunnel coupling tuning crosstalk [17] facilitate the formation of a large and homogeneously tunnel coupled multi-dot array.

In this work, we report the characterization of the electron-electron interaction in a semiconductor quantum dot array. For this purpose, we tuned a homogeneously tunnel coupled linear array of six quantum dots with two charge sensors. A large set of charge-stability diagrams is taken, which contains a diagram for each pair in the dot array, thus including non-nearest neighbours. From these pairwise diagrams the long-range interaction elements were extracted. The electron-electron interaction is found to be measurable between electrons that are up to four sites away, thus considered to be long-range. The decay of the interaction strength is heuristically modelled with a Yukawa potential [18], and with a model based on the method of image-charges with the gate metal acting as screening layer.

8.2. DEVICE AND CONCEPT

The quantum dot array for our characterization consists of six quantum dots and two sensing dots, which are formed in a GaAs/AlGaAs heterostructure. Figure 8.1(a) shows a scanning electron micrograph image of the active region of a device similar to the one used in this experiment, and which has previously been operated as a Heisenberg spin chain [11]. At the GaAs/AlGaAs interface, 90 nm below the surface, which is 40 nm be-

low a silicon doping layer, a two-dimensional electron gas (2DEG) forms. The potential landscape for the 2DEG is shaped by applying voltages on the gates at the surface. The plunger gates, labelled in Fig. 8.1(a) as P_i for the dots in the main channel and SP_i for the sensing dots, control the electrochemical potentials, and barrier gates, B_{ij}, B_L, and B_R, control the tunnel couplings between dots and to the reservoirs. The device is cooled in a dilution refrigerator, which results in an electron reservoir temperature of about 100 mK (roughly 10 μeV).

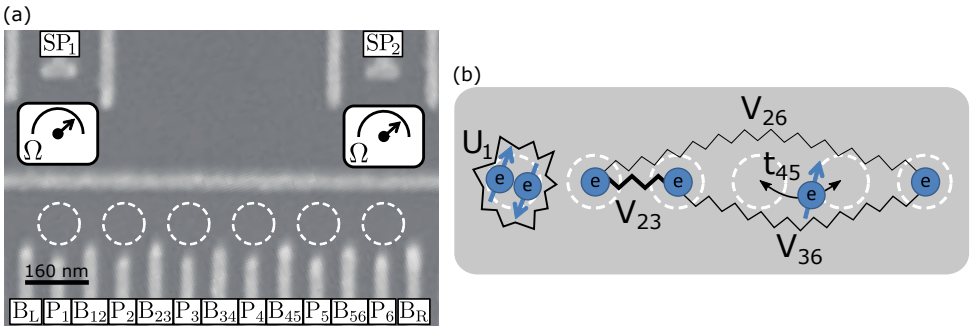

Figure 8.1: (a) Scanning electron micrograph of a nominally identical device. Dot locations are indicated with dashed circles, and the charge sensors are indicated by resistance meters labelled with Ω. (b) Schematic to illustrate the on-site interaction, U_i, inter-site interaction, V_{ij}, and tunnelling, t_{ij}, in a quantum dot array.

The long-range interaction between electrons on a quantum dot array is schematically depicted in Figure 8.1(b). These electron-electron interactions are captured with an extended form of the single-band Fermi-Hubbard model [9, 19, 20]

$$H_{FH,ext} = -\sum_i \varepsilon_i n_i + \sum_i U_i n_{i\uparrow} n_{i\downarrow} + \sum_{i\neq j} V_{ij} n_i n_j - \sum_{\langle i,j\rangle,\sigma} t_{ij}\left(c^\dagger_{i\sigma} c_{j\sigma} + h.c.\right), \tag{8.1}$$

with $n_i = n_{i\uparrow} + n_{i\downarrow}$ the dot occupation for site i where $n_{i\sigma} = c^\dagger_{i\sigma} c_{i\sigma}$ with $c^{(\dagger)}_{i\sigma}$ the annihilation (creation) operator for an electron with spin σ, and with ε_i the local energy offset, U_i the on-site interaction, V_{ij} the inter-site interaction, and t_{ij} the tunnel coupling.

8.3. CHARGE-STABILITY DIAGRAMS

The quantum dot array is characterized based on charge-stability diagrams for each pair of dots. For six quantum dots the full set contains fifteen diagrams, such as shown in Fig. 8.2. Interestingly, such a full set of diagrams also reveals occasionally overlooked crosstalk for chemical potentials of non-nearest neighbours, but which is relevant for the operation with virtual gates [9, 16, 21, 22]. This crosstalk has already been corrected for here, thus no longer present in the set of diagrams. Before the diagrams are measured, the voltages are tuned to the center of the charge region with one electron per dot. From that configuration, for each diagram only the voltages on the two virtual plungers for that pair are temporarily changed. Each diagram is measured with an additional voltage offset on that pair of virtual plungers to center at the anti-crossing.

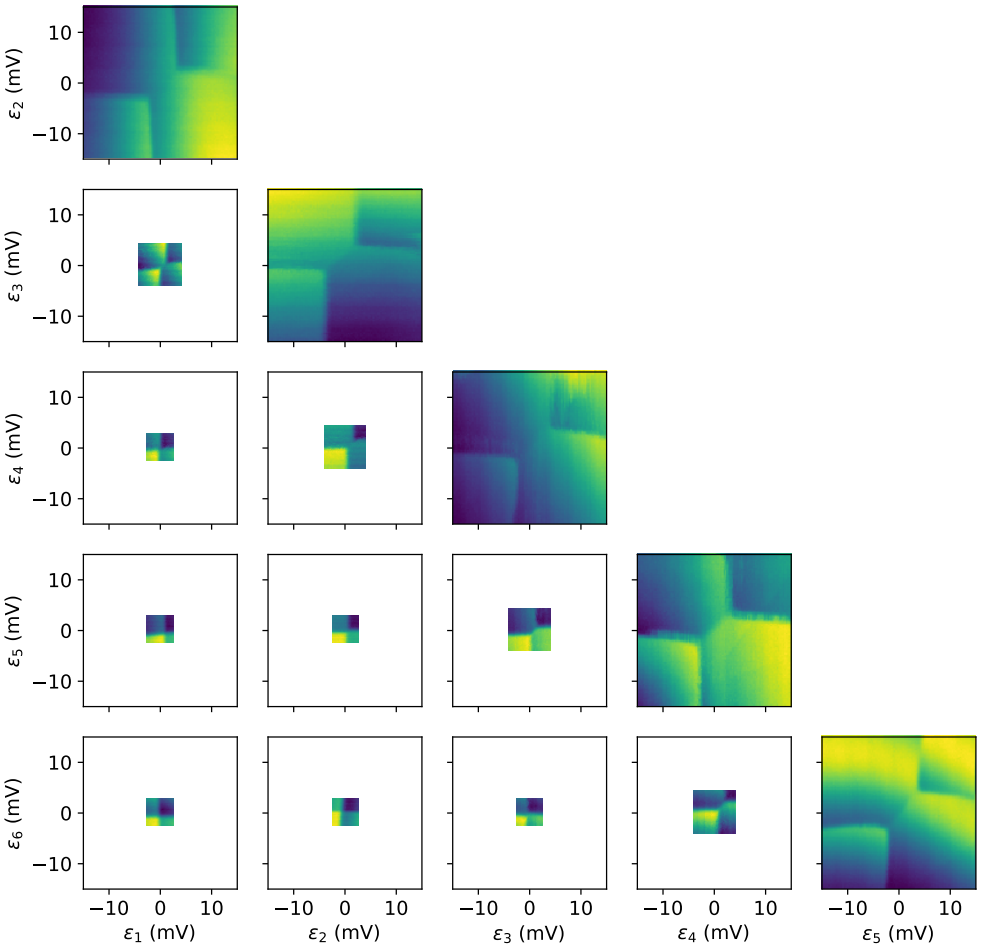

Figure 8.2: Charge-stability diagrams for each pair of dots along a linear array of six quantum dots. For each of the diagrams the charge occupation in the bottom-left corner is (111111), and the diagrams are centred at the (12)-(21) anti-crossing for the measured pair of dots. Latching hindered efficient acquisition and analysis for the case when all dots were empty in the bottom left corner of the diagram, i.e. for diagrams centred at the (10)-(01) anti-crossing. For pairs which are further apart, a smaller voltage range is used to obtain higher resolution at the anti-crossing without increasing the measurement time. The signals from both sensors are combined to obtain sufficient signal-to-noise for each dot.

8.4. MICROSCOPIC MODEL

The interaction elements and tunnel couplings can be expressed based on a microscopic model as

$$V_{ij} = \int\int \mathrm{d}^2\mathbf{r}\,\mathrm{d}^2\mathbf{r}'\, n_i(\mathbf{r}) V(\mathbf{r},\mathbf{r}') n_j(\mathbf{r}'), \quad U_i = V_{ii}, \tag{8.2}$$

and

$$t_{ij} = \int \mathrm{d}^2\mathbf{r}\,\psi_i^*(\mathbf{r})\left[-\frac{\hbar^2\nabla^2}{2m_{\mathrm{eff}}} + V^{\mathrm{ext}}(\mathbf{r})\right]\psi_j(\mathbf{r}), \tag{8.3}$$

with $m_{\mathrm{eff}} = 0.067 m_e$ the effective electron mass for GaAs, $V^{\mathrm{ext}}(\mathbf{r})$ the confinement potential, $n_i(\mathbf{r}) = \psi_i^*(\mathbf{r})\psi_i(\mathbf{r})$ the probability density with ψ_i the electron wavefunction, and $V(\mathbf{r},\mathbf{r}')$ the interaction. For a quantum dot with an isotropic and parabolic confinement potential, thus a two-dimensional harmonic oscillator, the ground state wavefunction is

$$\psi_i(\mathbf{r}) = \frac{1}{\sqrt{\pi}\Delta}\exp\left\{-\frac{(\mathbf{r}-\mathbf{r}_i)^2}{2\Delta^2}\right\}, \tag{8.4}$$

with $\mathbf{r}_i$ the coordinates for the center of the dot, and Δ the spread of the wavefunction. The multi-dot confinement potential can be modelled with a combination of harmonic oscillator potentials as [20]

$$V^{\mathrm{ext}}(\mathbf{r}) = \frac{m_{\mathrm{eff}}}{2}\,\mathrm{Min}\left[\sum_i \omega_i^2|\mathbf{r}-\mathbf{r}_i|^2\right], \tag{8.5}$$

with ω_i the harmonic oscillator frequency for dot i. This potential landscape will partially differ from the actual landscape, because it has kinks in the profile of the inter-dot barriers while the actual barriers are expected to be smooth. Nevertheless, this simple model is expected to be adequate for the description of the electron-electron interactions. Note that the harmonic oscillator eigenfunctions are in general not eigenfunctions of the multi-dot potential, thus can have overlap, which becomes in particular relevant at short distances. Here only pairwise anti-parallel spin configurations are included, which is consistent with the single-band approximation, and results in that wavefunctions are orthogonal due to their different spin component.

The Coulomb interaction modified by a homogeneous screening layer can be modelled based on the method of image-charges [23, 24], and can be expressed as

$$V_{\mathrm{im}}(\mathbf{r},\mathbf{r}') = A\frac{f_{\mathrm{im}}(|\mathbf{r}-\mathbf{r}'|)}{|\mathbf{r}-\mathbf{r}'|}, \quad f_{\mathrm{im}}(r) = 1 - \frac{r}{\sqrt{r^2+4d^2}}, \tag{8.6}$$

with $A = e^2/(4\pi\varepsilon\varepsilon_0)$, where ε_0 is the dielectric constant, $\varepsilon \approx 13$ the relative dielectric constant for (Al)GaAs, and $d = 90\,\mathrm{nm}$ the distance to the screening layer.

Alternatively, the screened interaction can be heuristically modelled with the Yukawa potential [18]

$$V_{\mathrm{yuk}}(\mathbf{r},\mathbf{r}') = A\frac{e^{-|\mathbf{r}-\mathbf{r}'|/\gamma}}{|\mathbf{r}-\mathbf{r}'|} \tag{8.7}$$

with γ the screening length. An advantage of the Yukawa potential is that the screening length offers a more intuitive interpretation for the decay of the interaction.

8.5. THE LONG-RANGE INTERACTION

The inter-site interaction elements, V_{ij}, are extracted by modelling the anti-crossings in the charge-stability diagrams with [9]

$$\delta\varepsilon_i + \delta\varepsilon_j = \pm\left(V_{ij} + \sqrt{(\delta\varepsilon_i - \delta\varepsilon_j)^2 + 4t_{ij}^2}\right). \tag{8.8}$$

The anti-crossing model is converted into a two-dimensional patch, which is fitted onto the charge-stability diagrams using an edge detection algorithm.

Figure 8.3 shows charge-stability diagrams, which each involve the leftmost dot. The on-site interaction is obtained from the spacing between the first and second dot-reservoir transition line, such as shown in Fig. 8.3(a). The inter-site interactions are obtained from the anti-crossing fits to the diagrams in Fig. 8.3(b)-(f), which represent the same data as the leftmost column of diagrams in Fig. 8.2. All the interaction elements for the array of six dots dots are plotted as a function of distance in Fig. 8.3(g). The interaction data shows a clear decay with distance, but is measurable up to four sites away, which confirms that electrons in the quantum dot array are subjected to long-range interactions.

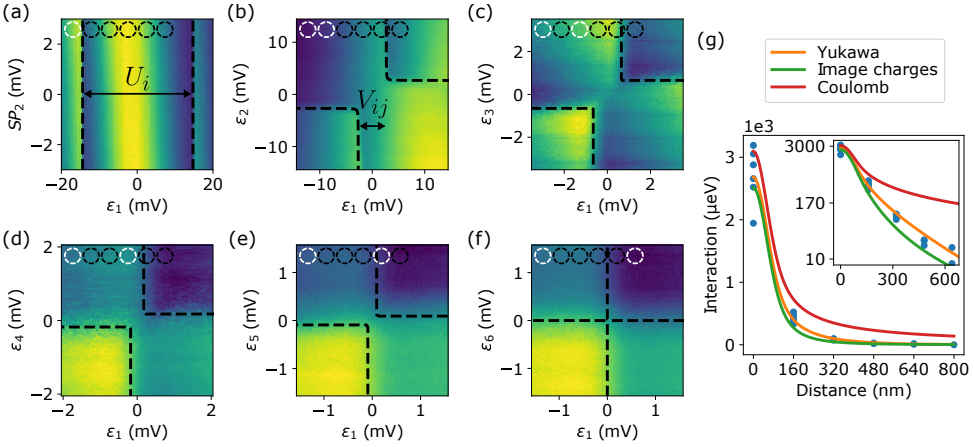

Figure 8.3: Charge-stability diagrams for the dots highlighted by the white dashed circles. (a) For the leftmost dot as measured relative to the plunger gate for the rightmost sensor. This gate here acts as a dummy, because it has negligible effect on both the leftmost dot and the signal from the left sensor. The broad vertical band is a Coulomb peak for the left sensor, which appears due to crosstalk from ε_1. For the leftmost dot in combination with a dot (b) one, (c) two, (d) three, (e) four, and (f) five sites away. Black dashed lines are fits to the anti-crossings, and are used to extract the interaction elements. For this the voltages are converted to energies with the lever arms $[105, 94, 104, 86, 104, 95]$ $\mu\text{eV}\,\text{mV}^{-1}$, which were obtained with photon-assisted tunnelling [25]. (g) Interaction versus distance with blue dots the experimentally obtained interaction elements and the solid lines fits based on the Yukawa potential, the method of image-charges and the normal Coulomb potential. The inset shows the interaction and fits on a logarithmic scale.

In Fig. 8.3(g) the interaction potentials are shown for a fitted dot size, where for the Yukawa potential the screening length is used as an additional fitting parameter, and the Coulomb potential is not fitted but based on the dot size from the other fits. The fitted dot size is $\Delta = 45\,\text{nm}$ for both models. The fitted screening length is $\gamma = 250\,\text{nm}$, thus larger than the spacing between dots. The fitting was facilitated by analytical simplification of the interaction integrals (see Supplementary material).

Both the Yukawa potential and that obtained from the method of image charges are in reasonable agreement with the data. The models both capture the fact that the interaction strength decays more rapidly than for normal Coulomb repulsion, which is explained by screening. As a self-consistency check, the experimentally set values of $t_{ij} \approx 20\,\mu\text{eV}$ are compared with the numerically calculated values of $12\,\mu\text{eV}$ based on

equation (8.3) and the dot sizes from the fits to the interaction data. The discrepancy between these two values can be explained by that the profile of the multi-dot potential landscape in eqn. (8.5) can especially differ from the barriers in the actual potential landscape. The barrier shape has a strong influence on the tunnel couplings, thus the experiment and the numerical simulation are still considered to be in reasonable agreement.

8.6. DISCUSSION AND CONCLUSION

The dominant source for screening of the interaction in our device is the metal of the fine gates in the surface area above the quantum dots. For depletion mode devices such as that used here, only side gates suffice to form a quantum dot array, thus the surface area directly above the quantum dot is not covered with metal. Therefore, the method of image charges overestimates the screening, which is expected to be the strongest for the on-site interaction, thus the actual dot sizes are expected to be larger than those obtained from the fit. For accumulation mode devices, such as those based on silicon and germanium, there usually is metal on the surface directly above the quantum dot in order to pull charges into it, which will result in stronger screening. In addition, due to the higher effective mass in silicon, the formation of a multi-dot array requires a multi-layer gate stack, thus more coverage with metal, which enhances the screening. Furthermore, in SiMOS devices the distance to the screening layer is much smaller, because gates are separated from the dots by only a few nanometres of dielectric, which will also result in stronger screening. Besides the gate metal there are several other sources which can contribute to screening, such as the surrounding 2DEG, dopants, and impurities, but these are expected to have much smaller contributions.

In conclusion, we have characterized the electron-electron interactions in a gate-defined quantum dot array. The interactions were found to be measurable between electrons up to four sites away, thus are considered to be long-range. The interaction as a function of distance is described with a microscopic model of the quantum dot array combined with either the Yukawa potential, or a potential based on the method of image charges where the gate metal is acting as screening layer. The character of the long-range electron-electron interaction is relevant for the operation of quantum dot arrays with spin qubits, for example when implementing shared control [26]. In addition, our study of the long-range character for the electron-electron interactions opens the way for future quantum simulations with quantum dot arrays, because it is a key ingredient for quantum chemistry [1], Wigner crystallization [27], exciton formation [3], and high-temperature superconductivity [4, 7].

8.7. SUPPLEMENTARY MATERIAL

8.7.1. SIMPLIFICATION OF INTERACTION INTEGRAL

To simplify the integral expressions in eqn. (8.2) and reduce the numerical calculation time, it is useful to observe that the interaction, $V(\mathbf{r},\mathbf{r}')$, only depends on the distance, thus can be replaced with $V(|\mathbf{r}-\mathbf{r}'|)$. This brings eqn. (8.2) in a form to which the convolution theorem can be applied. which relates the Fourier transform of a convolution of two functions to the product of their Fourier transforms. For the interaction elements this results in

$$V_{kl} = \int\int \mathrm{d}^2\mathbf{r}\,\mathrm{d}^2\mathbf{r}'\, n_k(\mathbf{r})\, V(|\mathbf{r}-\mathbf{r}'|)\, n_l(\mathbf{r}') \tag{8.9}$$

$$= \int \mathrm{d}^2\mathbf{r}\, n_k(\mathbf{r})\, (V * n_l)\,(\mathbf{r}) \tag{8.10}$$

$$= \int \mathrm{d}^2\mathbf{r}\, n_k(\mathbf{r}) F^{-1}\left[F(V)\cdot F(n_l)\right](\mathbf{r}), \tag{8.11}$$

with F the Fourier transform operator. With Plancherel's theorem the spatial integrals can be converted into momentum integrals as

$$V_{kl} = \int \mathrm{d}^2\mathbf{q}\, \tilde{n}_k(\mathbf{q})\, V(|\mathbf{q}|)\, \tilde{n}_l(-\mathbf{q}), \tag{8.12}$$

with $\tilde{f} = F(f)$, and $V(|\mathbf{q}|)$ the Fourier transform of the interaction. For harmonic oscillator eigenfunctions the interaction elements are

$$V_{kl} = \frac{1}{4\pi^2} \int \mathrm{d}^2\mathbf{q}\, e^{-i|k-l|aq_1}\, e^{-|\mathbf{q}|^2\Delta^2/2}\, V(|\mathbf{q}|), \tag{8.13}$$

with $a = 160\,\mathrm{nm}$ the lattice constant for the quantum dot array. Transformation to polar coordinates in momentum space results in

$$V_{kl} = \frac{1}{4\pi^2} \int\int \mathrm{d}q\mathrm{d}\theta\, q \cos\left[|k-l|aq\cos\theta\right] e^{-q^2\Delta^2/2}\, V(q). \tag{8.14}$$

The Fourier transforms for the potentials of the normal Coulomb repulsion, the image-charge based method, and the Yukawa model are

$$V_{\mathrm{coul}}(q) = \frac{2\pi A}{q}, \quad V_{\mathrm{im}}(q) = \frac{2\pi A}{q}\left(1 - e^{-2dq}\right), \quad V_{\mathrm{yuk}}(q) = \frac{2\pi A}{\sqrt{q^2 + (1/\gamma)^2}}. \tag{8.15}$$

REFERENCES

[1] J. Argüello-Luengo, A. González-Tudela, T. Shi, P. Zoller, and J. I. Cirac, *Analogue quantum chemistry simulation,* Nature **574**, 215 (2019).

[2] E. Wigner, *On the interaction of electrons in metals,* Physical Review **46**, 1002 (1934).

[3] J. Frenkel, *On the transformation of light into heat in solids. I,* Physical Review **37**, 17 (1931).

[4] P. W. Anderson, *Twenty-five years of high-temperature superconductivity - A personal review,* Journal of Physics: Conference Series **449**, 012001 (2013).

[5] J. I. Cirac and P. Zoller, *Goals and opportunities in quantum simulation,* Nature Physics **8**, 264 (2012).

[6] I. M. Georgescu, S. Ashhab, and F. Nori, *Quantum simulation,* Reviews of Modern Physics **86**, 153 (2014).

[7] E. Manousakis, *A quantum-dot array as model for copper-oxide superconductors: A dedicated quantum simulator for the many-fermion problem,* Journal of Low Temperature Physics **126**, 1501 (2002).

[8] T. Byrnes, N. Y. Kim, K. Kusudo, and Y. Yamamoto, *Quantum simulation of Fermi-Hubbard models in semiconductor quantum-dot arrays,* Physical Review B **78**, 075320 (2008).

[9] T. Hensgens, T. Fujita, L. Janssen, X. Li, C. J. Van Diepen, C. Reichl, W. Wegscheider, S. Das Sarma, and L. M. K. Vandersypen, *Quantum simulation of a Fermi-Hubbard model using a semiconductor quantum dot array,* Nature **548**, 70 (2017).

[10] J. P. Dehollain, U. Mukhopadhyay, V. P. Michal, Y. Wang, B. Wunsch, C. Reichl, W. Wegscheider, M. S. Rudner, E. Demler, and L. M. K. Vandersypen, *Nagaoka ferromagnetism observed in a quantum dot plaquette,* Nature **579**, 528 (2020).

[11] C. J. van Diepen, T.-K. Hsiao, U. Mukhopadhyay, C. Reichl, W. Wegscheider, and L. M. K. Vandersypen, *Quantum simulation of antiferromagnetic Heisenberg chain with gate-defined quantum dots,* Physical Review X **11**, 041025 (2021).

[12] W. G. van der Wiel, S. De Franceschi, J. M. Elzerman, T. Fujisawa, S. Tarucha, and L. P. Kouwenhoven, *Electron transport through double quantum dots,* Reviews of Modern Physics **75**, 1 (2003).

[13] M. D. Shulman, O. E. Dial, S. P. Harvey, H. Bluhm, V. Umansky, and A. Yacoby, *Demonstration of entanglement of electrostatically coupled singlet-triplet qubits,* Science **336**, 202 (2012).

[14] D. M. Zajac, T. M. Hazard, X. Mi, E. Nielsen, and J. R. Petta, *Scalable Gate Architecture for a One-Dimensional Array of Semiconductor Spin Qubits,* Physical Review Applied **6**, 054013 (2016).

[15] C. J. van Diepen, T.-K. Hsiao, U. Mukhopadhyay, C. Reichl, W. Wegscheider, and L. M. K. Vandersypen, *Electron cascade for distant spin readout,* Nature Communications **12**, 77 (2021).

[16] C. Volk, A. M. J. Zwerver, U. Mukhopadhyay, P. T. Eendebak, C. J. van Diepen, J. P. Dehollain, T. Hensgens, T. Fujita, C. Reichl, W. Wegscheider, and L. M. K. Vandersypen, *Loading a quantum-dot based "Qubyte" register,* npj Quantum Information **5**, 29 (2019).

[17] T.-K. Hsiao, C. J. van Diepen, U. Mukhopadhyay, C. Reichl, W. Wegscheider, and L. M. K. Vandersypen, *Efficient orthogonal control of tunnel couplings in a quantum dot array,* Physical Review Applied **13**, 054018 (2020).

[18] H. Yukawa, *On the Interaction of Elementary Particles,* Proceedings of the Physico-Mathematical Society of Japan **17**, 48 (1935).

[19] M. Imada, A. Fujimori, and Y. Tokura, *Metal-insulator transitions,* Rev. Mod. Phys. **70**, 1039 (1998).

[20] S. Yang, X. Wang, and S. Das Sarma, *Generic Hubbard model description of semiconductor quantum-dot spin qubits,* Physical Review B **83**, 161301 (2011).

[21] K. C. Nowack, M. Shafiei, M. Laforest, G. E. D. K. Prawiroatmodjo, L. R. Schreiber, C. Reichl, W. Wegscheider, and L. M. K. Vandersypen, *Single-Shot Correlations and Two-Qubit Gate of Solid-State Spins,* Science **333**, 1269 (2011).

[22] A. R. Mills, D. M. Zajac, M. J. Gullans, F. J. Schupp, T. M. Hazard, and J. R. Petta, *Shuttling a single charge across a one-dimensional array of silicon quantum dots,* Nature Communications **10** (2019).

[23] L. D. Hallam, J. Weis, and P. A. Maksym, *Screening of the electron-electron interaction by gate electrodes in semiconductor quantum dots,* Physical Review B **53**, 1452 (1996).

[24] T. Byrnes, P. Recher, N. Y. Kim, S. Utsunomiya, and Y. Yamamoto, *Quantum simulator for the hubbard model with long-range coulomb interactions using surface acoustic waves,* Physical Review Letters **99**, 016405 (2007).

[25] C. J. Van Diepen, P. T. Eendebak, B. T. Buijtendorp, U. Mukhopadhyay, T. Fujita, C. Reichl, W. Wegscheider, and L. M. K. Vandersypen, *Automated tuning of inter-dot tunnel coupling in double quantum dots,* Applied Physics Letters **113**, 033101 (2018).

[26] R. Li, L. Petit, D. P. Franke, J. P. Dehollain, J. Helsen, M. Steudtner, N. K. Thomas, Z. R. Yoscovits, K. J. Singh, S. Wehner, L. M. K. Vandersypen, J. S. Clarke, and M. Veldhorst, *A crossbar network for silicon quantum dot qubits,* Science Advances **4**, eaar3960 (2018).

[27] D. Vu and S. Das Sarma, *Collective ground states in small lattices of coupled quantum dots,* Physical Review Research **2**, 023060 (2020).

9

CONCLUSION

This chapter puts the results of the previous chapters into perspective. After that, a more general conclusion for this thesis is drawn, accompanied with comments about the status and prospects for the research field of gate-defined quantum dots.

9.1. PER CHAPTER

This thesis reports developments for gate-defined quantum dots as platform for quantum simulation. The developments consist of various results, which are summarized per chapter in this section, and put into broader perspective with additional comments.

AUTOMATED TUNING

In Chapter 4 automated tuning of the inter-dot tunnel coupling was demonstrated. This result builds on the previously demonstrated automated tuning of double quantum dots [1]. These automated tuning routines make use of a computer to extract relevant parameters from experimental data, for example with image processing techniques and/or by fitting the data with a model.

- Acquisition of statistics on devices will benefit from automated tuning, and in particular for measurements on (1) multiple devices cooled down simultaneously and controlled via a multiplexer [2], (2) a full wafer of devices directly cooled down and measured with a cryoprober, and (3) devices with many single dots or small clusters of dots.
- For multi-dot and multi-qubit devices, automated tuning schemes can be used for the initial tune-up, but in the coming years will be most helpful for re-calibration after device jumps such as caused by charge rearrangements.
- Manual tuning strategies are typically based on human observations, which are useful for qualitative judgements and efficient coarse tuning of the device. However, computers are much more skilled at quantitative judgements, thus computer-assisted tuning can result in a higher level of device control, such as improved precision for Hamiltonian engineering and higher fidelities for qubit initialization, manipulation and readout.
- Reduced disorder and improved stability shift the focus from automated to efficient tuning strategies. Currently, it seems unlikely that in the foreseeable future quantum dot devices will arise which have negligible disorder and instability, such that they could be operated with pre-calculated settings and without additional re-tuning.

EFFICIENT CONTROL

The tuning of tunnel couplings was further discussed in Chapter 5. It is common practice in research with gate-defined quantum dots to independently control chemical potentials with virtual gates, which incorporate compensation for crosstalk effects. However, the control of multiple tunnel couplings has remained largely uncharted territory, because disorder and crosstalk have hindered the operation of multi-dot devices. Chapter 5 reports an efficient calibration scheme for enhanced virtual gates with which independent control of tunnel couplings is achieved.

- Independent control of tunnel couplings facilitates Hamiltonian engineering for quantum simulation.

- The implementation of gate operations in quantum dot devices with multiple qubits is expected to benefit from independent tunnel coupling control. For example, to perform two-qubit gates in parallel, to suppress residual exchange with spins that should not be influenced by the gate operation, and to prevent leakage out of the computational subspace due to unwanted changes in tunnel couplings to other dots or reservoirs.

SCALABLE READOUT

After tuning the tunnel couplings, the next step was measurement of the electron spin. While discussing in the lab about the measurement of spins at a distance from the charge sensor, a new readout scheme was invented, which was demonstrated in Chapter 6. As the sensing is based on Coulomb repulsion, which decays with distance (see also Chapter 8), only readout of the spin of an electron close to the sensor has sufficient signal-to-noise ratio to result in a reliable outcome. However, inspired by the effect of toppling dominoes, a cascade of hopping electrons, induced by Coulomb repulsion, can effectively convert the information about motion of a distant charge to the motion of a charge close to the sensor. The benefit of cascade-based readout was demonstrated by comparing the readout fidelities with or without the cascade activated for singlet-triplet measurements based on Pauli spin blockade [3, 4].

- With cascade-based readout a single sensor can be used to readout many different electron spins.
- Cascade-based schemes are a promising approach for readout in densely-packed quantum-dot arrays. For example, the readout of spins in the interior of a two-dimensional dot array while sensors are only placed at the periphery, thus maintaining the level of qubit-connectivity.
- Cascades can enable the tune-up of dots without a nearby sensor.
- Caution should be taken for unwanted rotations of the spins for both electrons moving between dots, and for electrons in Coulomb blockade, due to changes in their electrostatic environment.
- Fanout of cascades can enable further enhancement of the readout signal.

QUANTUM MAGNETISM SIMULATION

With the measurement of spin, all the basic building blocks were examined for the most involved experiment of this thesis, which was presented in Chapter 7. This experiment was a proof-of-principle quantum simulation of Heisenberg magnetism. Note that quantum simulation in this regime requires access to states with energy splitting much smaller than that for previous quantum simulations with quantum dots. Previously, the energy splitting was dominated by either the on-site interaction [5] or the tunnel coupling [6], while for Heisenberg quantum magnetism it is the exchange coupling which sets the energy scale.

In this experiment, a linear array of four quantum dots was tuned as a spin chain with control over each of the exchange couplings. For this purpose, spin readout for

each of the nearest-neighbour pairs was configured, of which the outcomes and correlations therein are used as a probe of the spin states. With these spin measurements, energy spectroscopy was performed for the spin chain, based on which the exchange couplings were tuned. In particular, the voltage settings could be identified for homogeneous exchange couplings. In addition, the coherence was demonstrated via global coherent oscillations of the coupled spin system. Specifically, global coherent oscillations were observed in different subspaces for the Heisenberg Hamiltonian.

To characterize the ground state of the Heisenberg model, and to go beyond qualitative features, careful analysis and optimization of the adiabaticity for the state preparation and readout were performed, which were supported by numerical simulations of the time evolution. Finally, the low-energy singlet state of the homogeneous Heisenberg chain was adiabatically prepared and probed with diabatic singlet-triplet measurements on all nearest-neighbour pairs. This completed the proof-of-principle experiment with operation of a multi-dot array as quantum simulator of Heisenberg magnetism.

- Adiabatic state preparation and diabatic readout of many-body states becomes challenging when anti-crossings between states are not Landau-Zener like, or when multiple anti-crossings are involved.

- Coherent control in Hamiltonian subspaces of multi-spin systems is largely unexplored, while it can offer beneficial properties, such as protection against decoherence, full-electrical control, and multi-level systems to encode qudits (such as a qutrit with a triplet subspace).

- For quantum simulation of low-energy properties it is important to study the effective temperature and coherence of many-body states in a multi-dot array. In turn, obtained insights can serve as input for improvements to the experimental set-up for the quantum simulator.

LONG-RANGE ELECTRON-ELECTRON INTERACTION

After the quantum magnetism simulation, which revolved around the spin-spin interaction, the focus shifted to the electron-electron interaction at a distance. For gate-defined quantum dots, the Coulomb repulsion, in addition to on-site interaction, typically also results in the long-range interaction between electrons on different sites [7]. In Chapter 8 the characterization of the electron-electron interaction as function of distance was presented. The decay of the interaction was captured by either a Yukawa type potential or a model based on the method of image charges, with the gate metal as source of screening. The characterization of the long-range electron-electron interaction is not only relevant for the operation of multi-dot arrays with spin qubits, but it also forms the basis for further quantum simulations, which range from bonding energies in quantum chemistry [8], to phenomena such as exciton formation [9], and charge-ordering [10].

- Proximity and coverage of metal from the gates result in screening, thus the gate pattern could be optimized to reduce or enhance the long-range electron-electron interaction.

- Long-range interaction can complicate the operation of multi-dot arrays with shared control [11], as it induces a difference in chemical potentials for dots with a different charge distribution in their environment. For example, such differences are relevant for the edges when homogeneously filling a two-dimensional array, or when charge is moved in an array.

9.2. IN GENERAL

Gate-defined quantum dots have momentum as a platform for quantum simulation and computation. In the coming decade or so, spin qubits in quantum dots could catch up, in terms of qubit numbers and gate performance, with the currently most advanced platforms, such as that based on superconducting qubits [12]. For quantum simulation, the development in terms of numbers is currently almost hand-in-hand with that for spin qubits. However, scaling to larger quantum dot arrays while sacrificing the requirement of high-fidelity qubit control will benefit the momentum for quantum simulations. Further comments are presented point-by-point below.

- The community has successfully shifted to silicon and germanium as host materials [13] which offer a magnetically quiet environment that enables longer coherence times [14, 15].
- Charge-noise mitigation [16, 17] is of increasing importance for high-fidelity gates and scaling up.
- Spin qubits are at the verge of a new period in development, enabled by the demonstrations of high-fidelities and short durations for single-qubit [18] and two-qubit gates [19–22], initialization and readout [23, 24].
- Scaling in 1D and quasi-2D to tens of dots is within reach and scaling to few hundreds of dots is feasible with the currently demonstrated techniques.
- Scaling up quantum dots into densely-packed 2D arrays is an open and exciting challenge, in particular for quantum simulation. For quantum computation, alternatives, such as sparse arrays [25, 26], could be more favourable as they replace some of the stringent requirements in crosstalk mitigation for spin-qubits, with potentially more lenient requirements for long-range couplers and footprint.
- Substantial reduction or mitigation of electrostatic disorder is key for further scaling of quantum dots arrays.
- Gate-defined quantum dots offer versatility in layout for dot arrays based on revisions of the gate pattern, but in practice it can be time consuming to develop a suitable gate pattern and tuning strategy.
- Further development of quantum dots as a platform for quantum simulations will benefit from active involvement of condensed-matter theorists to guide experimentalists towards the parameter regime of interest, and where numerical methods fail.

In conclusion, this thesis reports on the development of quantum dot arrays as platform for quantum simulation. The main result establishes quantum dot arrays as quantum simulator of Heisenberg magnetism, thus manifests access to the regime where only the spin degree of freedom remains. In addition, the long-range nature of the electron-electron interaction was characterized in a multi-dot array, which opens up further directions for quantum simulation. Other parts of this thesis demonstrate automated tuning, independent control and scalable readout techniques, which facilitate scaling up to arrays of tens or even hundreds of quantum dots. The development is hindered by electrostatic disorder, even though it can be mitigated with tuning, and could form a bottleneck for scaling to even larger arrays. On a positive note, development is stimulated by the involvement of (semi-)industrial parties (such as Intel, IBM, Imec, CEA-Leti, TNO), as they introduce new insights and means to the research field, which may result in progress that seems improbable at the time of writing.

REFERENCES

[1] T. A. Baart, P. T. Eendebak, C. Reichl, W. Wegscheider, and L. M. K. Vandersypen, *Computer-automated tuning of semiconductor double quantum dots into the single-electron regime,* Applied Physics Letters **108**, 213104 (2016).

[2] B. Paquelet Wuetz, P. L. Bavdaz, L. A. Yeoh, R. Schouten, H. van der Does, M. Tiggelman, D. Sabbagh, A. Sammak, C. G. Almudever, F. Sebastiano, J. S. Clarke, M. Veldhorst, and G. Scappucci, *Multiplexed quantum transport using commercial off-the-shelf CMOS at sub-kelvin temperatures,* npj Quantum Information **6**, 43 (2020).

[3] K. Ono, D. G. Austing, Y. Tokura, and S. Tarucha, *Current rectification by Pauli exclusion in a weakly coupled double quantum dot system,* Science **297**, 1313 (2002).

[4] C. Barthel, D. J. Reilly, C. M. Marcus, M. P. Hanson, and A. C. Gossard, *Rapid single-shot measurement of a singlet-triplet qubit,* Physical Review Letters **103**, 160503 (2009).

[5] T. Hensgens, T. Fujita, L. Janssen, X. Li, C. J. Van Diepen, C. Reichl, W. Wegscheider, S. Das Sarma, and L. M. K. Vandersypen, *Quantum simulation of a Fermi–Hubbard model using a semiconductor quantum dot array,* Nature **548**, 70 (2017).

[6] J. P. Dehollain, U. Mukhopadhyay, V. P. Michal, Y. Wang, B. Wunsch, C. Reichl, W. Wegscheider, M. S. Rudner, E. Demler, and L. M. K. Vandersypen, *Nagaoka ferromagnetism observed in a quantum dot plaquette,* Nature **579**, 528 (2020).

[7] W. G. van der Wiel, S. De Franceschi, J. M. Elzerman, T. Fujisawa, S. Tarucha, and L. P. Kouwenhoven, *Electron transport through double quantum dots,* Reviews of Modern Physics **75**, 1 (2003).

[8] J. Argüello-Luengo, A. González-Tudela, T. Shi, P. Zoller, and J. I. Cirac, *Analogue quantum chemistry simulation,* Nature **574**, 215 (2019).

[9] J. Frenkel, *On the transformation of light into heat in solids. I,* Physical Review **37**, 17 (1931).

[10] M. Imada, A. Fujimori, and Y. Tokura, *Metal-insulator transitions,* Rev. Mod. Phys. **70**, 1039 (1998).

[11] R. Li, L. Petit, D. P. Franke, J. P. Dehollain, J. Helsen, M. Steudtner, N. K. Thomas, Z. R. Yoscovits, K. J. Singh, S. Wehner, L. M. K. Vandersypen, J. S. Clarke, and M. Veldhorst, *A crossbar network for silicon quantum dot qubits,* Science Advances **4**, eaar3960 (2018).

[12] F. Arute *et al.*, *Quantum supremacy using a programmable superconducting processor,* Nature **574**, 505 (2019).

[13] G. Scappucci, *Semiconductor materials stacks for quantum dot spin qubits,* arXiv:2102.10897 (2021).

[14] M. Veldhorst, J. C. C. Hwang, C. H. Yang, A. W. Leenstra, B. de Ronde, J. P. Dehollain, J. T. Muhonen, F. E. Hudson, K. M. Itoh, A. Morello, and A. S. Dzurak, *An addressable quantum dot qubit with fault-tolerant control-fidelity,* Nature Nanotechnology **9**, 981 (2014).

[15] N. W. Hendrickx, W. I. Lawrie, L. Petit, A. Sammak, G. Scappucci, and M. Veldhorst, *A single-hole spin qubit,* Nature Communications **11**, 3478 (2020).

[16] M. D. Reed, B. M. Maune, R. W. Andrews, M. G. Borselli, K. Eng, M. P. Jura, A. A. Kiselev, T. D. Ladd, S. T. Merkel, I. Milosavljevic, E. J. Pritchett, M. T. Rakher, R. S. Ross, A. E. Schmitz, A. Smith, J. A. Wright, M. F. Gyure, and A. T. Hunter, *Reduced Sensitivity to Charge Noise in Semiconductor Spin Qubits via Symmetric Operation,* Physical Review Letters **116**, 110402 (2016).

[17] F. Martins, F. K. Malinowski, P. D. Nissen, E. Barnes, S. Fallahi, G. C. Gardner, M. J. Manfra, C. M. Marcus, and F. Kuemmeth, *Noise Suppression Using Symmetric Exchange Gates in Spin Qubits,* Physical Review Letters **116**, 116801 (2016).

[18] J. Yoneda, K. Takeda, T. Otsuka, T. Nakajima, M. R. Delbecq, G. Allison, T. Honda, T. Kodera, S. Oda, Y. Hoshi, N. Usami, K. M. Itoh, and S. Tarucha, *A quantum-dot spin qubit with coherence limited by charge noise and fidelity higher than 99.9%,* Nature Nanotechnology **13**, 102 (2018).

[19] W. Huang, C. H. Yang, K. W. Chan, T. Tanttu, B. Hensen, R. C. Leon, M. A. Fogarty, J. C. Hwang, F. E. Hudson, K. M. Itoh, A. Morello, A. Laucht, and A. S. Dzurak, *Fidelity benchmarks for two-qubit gates in silicon,* Nature **569**, 532 (2019).

[20] M. T. Mądzik, S. Asaad, A. Youssry, B. Joecker, M. Kenneth, E. Nielsen, K. C. Young, T. J. Proctor, A. D. Baczewski, V. Schmitt, F. E. Hudson, K. M. Itoh, A. M. Jakob, C. Brett, D. N. Jamieson, A. S. Dzurak, C. Ferrie, R. Blume-kohout, and A. Morello, *Precision tomography of a three-qubit electron-nuclear quantum processor in silicon,* arXiv:2106.03082v2 (2021).

[21] X. Xue, M. Russ, N. Samkharadze, B. Undseth, A. Sammak, G. Scappucci, and L. M. K. Vandersypen, *Computing with spin qubits at the surface code error threshold,* arXiv:2107.00628 (2021).

[22] A. Noiri, K. Takeda, T. Nakajima, T. Kobayashi, A. Sammak, G. Scappucci, and S. Tarucha, *Fast universal quantum control above the fault-tolerance threshold in silicon,* arXiv:2108.02626 (2021).

[23] P. Harvey-Collard, B. D'Anjou, M. Rudolph, N. Tobias Jacobson, J. Dominguez, G. A. Eyck, J. R. Wendt, T. Pluym, M. P. Lilly, W. A. Coish, M. Pioro-Ladrière, and M. S. Carroll, *High-Fidelity Single-Shot Readout for a Spin Qubit via an Enhanced Latching Mechanism,* Physical Review X **8**, 021046 (2018).

[24] C. J. van Diepen, T.-K. Hsiao, U. Mukhopadhyay, C. Reichl, W. Wegscheider, and L. M. K. Vandersypen, *Electron cascade for distant spin readout,* Nature Communications **12**, 77 (2021).

[25] L. M. K. Vandersypen, H. Bluhm, J. S. Clarke, A. S. Dzurak, R. Ishihara, A. Morello, D. J. Reilly, L. R. Schreiber, and M. Veldhorst, *Interfacing spin qubits in quantum dots and donors—hot, dense, and coherent,* npj Quantum Information **3**, 34 (2017).

[26] J. M. Boter, J. P. Dehollain, J. P. Van DIjk, T. Hensgens, R. Versluis, J. S. Clarke, M. Veldhorst, F. Sebastiano, and L. M. K. Vandersypen, *A sparse spin qubit array with integrated control electronics,* in *Proceedings IEEE International Electron Devices Meeting (IEDM)* (2019).

A

VIDEOMODE CHARGE-STABILITY DIAGRAMS

The tuning of a multi-dot device typically requires many measurements of charge-stability diagrams. From these diagrams, the settings for the gate voltages are identified with which the target tuning is achieved. Radio-frequency reflectometry has enabled an increase of the measurement bandwidth to few or even tens of MHz, which enabled high-fidelity single-shot readout in the order of microseconds or even below (see Chapter 6).

The increased measurement bandwidth also enabled the development of the videomode, which is depicted in Fig. A.1. For the videomode, voltage sweeps are created with an arbitrary waveform generator to perform charge-stability measurements, which are acquired and visualized in real-time. The videomode is commonly operated at refresh rates of a few to few tens of hertz for two-dimensional charge-stability diagrams. This corresponds to about two orders of magnitude faster acquisition as compared to the previous measurements which involved stepping DC voltages. For the videomode diagrams, the voltage sweep durations were typically below ten milliseconds for the slow axis, and about ten microseconds for the fast axis. The full voltage sweep would be repeated, and the data averaged for a few to few tens of repetitions to achieve the desired signal-to-noise ratio (SNR).

The videomode shown in Fig. A.1 is based on the initial implementation in Delft from 2017, which was developed together with Pieter Eendebak. That implementation uses the AWG5014 from Tektronix to perform the gate voltage sweeps and a FPGA to record the data, which was later replaced by a digitizer. The fast visualization is based on the software package pyqtgraph. The videomode was first demonstrated with a Josephson parametric amplifier connected to a superconducting cavity, which was in turn connected to the source contact of a semiconductor nanowire hosting a double quantum dot [1].

A great benefit of the videomode is that the effect of a change in DC voltage can be observed in real-time. To give an example, double dot charge-stability diagrams can be acquired with the videomode while observing the effect of changes to the DC gate volt-

A

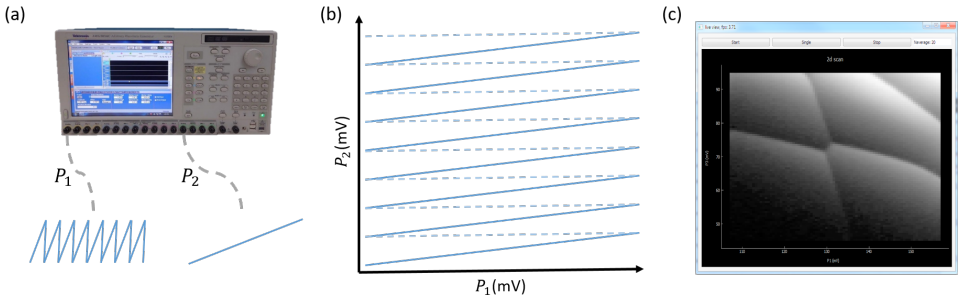

Figure A.1: (a) Schematic of voltage sweeps for two plunger gates, P_1 and P_2, generated by the Tektronix arbitrary waveform generator. (b) Visualization of how the combined voltage sweeps realize a two-dimensional scan. Along the solid lines the data is acquired for the measurement. For common operation, typically about a hundred horizontal sweeps are performed during one vertical sweep. (c) Snip-it of the videomode graphical-user interface, which shows a charge-stability diagram for a triple quantum dot, with buttons to start and stop the videomode, save the data for a single frame, and the change the number of averages.

ages of the inter-dot tunnel barrier, changing the DC voltages for the plungers to explore other electron occupations, or while tuning up an additional dot. Below are further comments, which can be helpful for working with the videomode.

- Tuning for Pauli spin blockade can be easier with the videomode, because blockade triangles appear when relaxation times are longer than measurement times.
- Latching effects depend on the sweep direction, hence can be identified by inverting the sweep direction or by switching the fast and slow sweep direction.
- The range for the voltage sweeps influences the observed latching effects, because a change in range indirectly also changes the sweep rate, and possibly also which states are accessed.
- To improve the SNR, either the number of averages or the integration time per pixel can be increased. Which of the two is preferred is typically decided taking into account that changing the integration time per pixel changes the sweep rate, which in turn influences latching effects and can induce charging effects of the bias-tee.

REFERENCES

[1] J. Stehlik, Y. Y. Liu, C. M. Quintana, C. Eichler, T. R. Hartke, and J. R. Petta, *Fast charge sensing of a cavity-coupled double quantum dot using a Josephson parametric amplifier*, Physical Review Applied **4**, 014018 (2015).

ACKNOWLEDGEMENTS

Many people have contributed to the research in this thesis and have been a key part in making the PhD a great experience. Having this thesis is in particular a great opportunity for putting my gratitude to all of you in writing.

First of all, **Lieven**, thanks for the opportunity and supervision. The freedom you offered has allowed my PhD to be a fun and challenging adventure. Speaking of adventure: I still remember that conference in Trieste were you kindly invited me to join for dinner with a group of professors. The restaurant had a beautiful view over the sea and a lower-lying harbour with sailing boats. We enjoyed dinner outside under the clear blue sky. However, when the sun had set and it was time to return to the accommodation, the weather abruptly started to turn. We decided not to wait for a taxi, but to take our chances and went for it, which resulted in us running through pouring rain and thunder.

Thanks **Menno** for being my copromotor and our occasional lunch discussions. Also thanks to the other committee members, **Sougato**, **Servaas**, **John**, and **Sander** for being part of the final stage of my PhD, and opposing me during the defence. Thanks **Gary** for being a reserve member, and for our helpful discussion.

Another two people part of the final stage are my paranymphs. **Willem**, our paths began to strongly overlap since our studies in Utrecht. Besides taking courses together, we were also volleyball team mates, and even neighbours, as we lived in student rooms directly above each other (it actually seems a bit creepy when making it all explicit). Then starting the PhD in the same building as you helped me feel comfortable and in place. Having you as paranymph just seemed so natural. **Tzu-Kan**, having you join my project has probably been the best choice during my PhD. Your patience and the combination of our creativity have allowed us to generate several results. I wish you all the best with the remainder of your postdoc and am curious about your next steps. It's a pleasure to end the PhD with you as paranymph.

Then to all the current group members who I have had the pleasure spending time with. **Stephan**, the combination of your creativity, ambition and intelligence will surely lead to something magical. Great to see things coming together on the multi-qubit project. **Xiao**, the many chats we have had were both stimulating and entertaining, whether it was about gossip or quantum physics. Your productivity, but also literature knowledge and encyclopaedic overview of quantum scientists are impressive. Looking forward to having some more sushi together. **Anne-Marije**, it feels like we have had the most overlap, which made it especially interesting to notice the differences in how we handled things. Special thanks for all your initiatives on organizing group activities. **Alice**, congrats on beating me with getting a date for the defence. **Florian**, you make an interesting combination of head-first and hands-on. I am happy to have entrusted the wet fridge to you. **Jurgen**, you always seem patient and modest, and have already achieved beautiful work. Have fun with the PhD. **Pablo**, you combine charm and creativity with a solid level of physics intuition. That surely makes a fruitful combination and I look

forward to your results. **Oriol**, we first met at a gardening/permaculture course, which made it particularly nice to see you join the spin-qubit group. Good luck with the hot qubits and cold electronics. **Sergey**, I enjoyed being your mostly absent office mate. You manage to nicely balance pessimism and optimism. Good luck with continuing to produce great devices. **Max**, soon after you started the experimentalists already knew how to find you for help with theory and numerical simulations. All the best with your next steps. **Mateusz**, the multi-qubit project nicely started coming together since you arrived. Have fun with the great results. **Xin**, it was nice to see you join the project. Good luck quantum simulating.

Not forgotten are the former group members. **Tobias**, you brought so much joy to the work environment, and I could not have wished for a more fun lab neighbour. Especially thinking of all our coffee breaks at the dewar bar. I admire your generosity and social antenna. All the best in Zürich and I look to forward to catching up. **Patrick**, you seemed active in every aspect of our group and always made time for extensive discussions to share your experiences. **Guoji**, a nose for free food and eye for opportunity will hopefully turn out to be fulfilling. I imagine that you overtaking me just before the finish of the Golden Ten Loop surely was. **Jelmer**, your openness, whether about something you criticized or appreciated, is admirable. Your focused and down-to-earth attitude were often a valuable perspective for my own working style. Thanks for organizing group trips and taking the group members for running. **Kostas**, your cheerfulness and enthusiasm were very enjoyable and I regretted your premature leave. **Christian**, I admire your friendliness and helpfulness, and am happy the qubyte project turned into a nice result. **Udi**, thanks for providing me with devices, even when multiple got damaged you anyway continued to help me out. The passion and emotion you put into work were moving and stimulating. Special thanks for organizing the Iceland trip and the great time we had at conferences. **JP**, thanks for all the spiritual guidance, squash games, physics discussions, and great fun. **Toivo**, a boiling pot of enthusiasm and creativity. Thanks for the inspiration and all the suggestions for projects. **Takafumi**, thanks for all your patience despite my ignorance. **Tim**, you were the first who made me seriously consider a PhD in spin qubits, thanks for that. **Nodar**, the mysterious and friendly giant who just makes me smile. Good luck with scaling up the spin qubits. Also thanks to the other former post-docs in our group: **Tom**, **Gabriel**, **Andrea**, **Nima**, **Vincent**, and **Oscar**.

Besides the above group members there are several others who made the spin-qubit group a great team. **Pieter**, thanks for guiding and supporting me during my first steps into the working life. Both inside and outside work we get along well, and I look forward to keeping in touch. **Floor**, we shared the new step of moving to Delft and taking up a new job. I admire your courage and how you speak up. **Sander**, you boosted the software quality in the group. Thanks for that and for all the enjoyable chats. **Luc**, thanks for helping out with software challenges, and being curious about the experiments.

In addition to Lieven's group there are many others working on spin qubits and quantum dots in Delft who I had the pleasure to spend time with. **Will**, thanks for being office mates, and your always cheerful and open attitude. **Brian**, I enjoyed our discussions, but am still waiting for that time when you join for volleyball practice. **Giordano**, your materials have formed the basis for great spin-qubit devices and a big step forward. And thanks to all the others: **Delphine, Luca, Nico, Gertjan, Hanifa, Chien-An, Mar-**

cel, Maxim, David, Marco, Roy, Mohammad, Luka, Brian, Alberto, Mario, Amir, Diego, LaReine.

During the final period of my PhD I have enjoyed collaborating with **Johannes**, which provided welcome variation during the final period. I am glad it is turning into a nice result. All the best in Zürich.

During the PhD I've had the opportunity to supervise several students: **Bruno**, you always showed enthusiasm and perseverance. Thanks for your dedication and good luck with your PhD. **Steven**, you showed great independence, and took a lot of initiative, such as contacting other researchers for discussions. Thanks for programming simulations and measurement routines. **Carlijn**, you demonstrated great physics intuition and eye for detail, whether it was with measurements or making schematics. Thanks for the various discussions and working together in the lab.

Thanks to my fellow Uitje committee members: **Maarten, Victoria, Marta, Christian**. It was great fun to organize the best Uitje ever with you, and to visit Texel beforehand. Thanks to my office mates **Job** and **Pascal**, for turning my work environment into an enjoyable chaos.

Thanks to **Marja**, **Chantal**, **Jenny**, and the other management assistants, for all their support, and organizing the Kavli trips, summer BBQ's and Christmas parties, and what not. Thanks to **Aletta**, **Aldo**, and **Suzanne** for the help with generating outreach. Thanks to all the cryo- and general techs: **Olaf** for help with the fridges and the down-to-earth coffee chats, **Jason** for help on so many different aspects and enthusiastic lunch chats, **Matt** for designing a sandwich with chips, **Mark** for being so very friendly and helpful, **Remco** for balancing safety and pragmatism, **Nico** for always delivering more quickly than I expected, **Peter** for the numerous talks on campers, holiday plans, family visits, and more personal subjects, and also thanks to **Siebe**, **Jelle**, and **Roy** for all the technical support. More generally speaking, your help has been of great value, whether it was with hail coming out of air-conditioners, a popped cooling water connection due to which the floor of the lab got covered with water, or a burning transformer in tube lights, which resulted in a team of firemen occupying the small wet fridge lab despite Corona regulations. Thanks to the **Raymond's**, **Marijn**, and **Roy** for all the insightful electronics discussions and the welcoming atmosphere. Thanks to the DEMO team, including **Jack**, **Hans**, **Erik**, and **Kees**, of course for providing electronics, but also for the many pleasant chats.

There are still so many more others not yet mentioned here who made the work environment a nice place to be at and who have directly or indirectly contributed to my research. Thanks to all of you for that.

Welcome distraction from the research was offered by my **volleyball team**, thanks for that and for tolerating my occasional mental absence. Thanks to my neighbours, **Jim** and **Eleanor**, for making Delft feel like home quickly, and being so very interested and thoughtful. Thanks to my **friends** and **family** for showing interest and putting trust in me.

Last, **Berber**, it is with great pleasure that my thesis ends with words addressing you. Thanks for all those times when you pulled me away from my computer, when I could not manage to take distance from work myself. But also for making me more relaxed and showing me another perspective on things. I look forward to making new steps together.

Curriculum Vitæ

Cornelis Jacobus van Diepen

August 23, 1990 Born in Alkmaar, The Netherlands.

Education

2002–2008 Secondary school
GSG Schagen, Schagen, The Netherlands

2008–2012 Bachelor of Science in Mathematics
Utrecht University, Utrecht, The Netherlands

2008–2012 Bachelor of Science in Physics and Astronomy
Utrecht University, Utrecht, The Netherlands

2009–2011 Honours programme in Philosophy of Science
Utrecht University, Utrecht, The Netherlands

2009–2011 Honours Programme in Experimental Physics
Utrecht University, Utrecht, The Netherlands
Research internship at FOM Rijnhuizen on plasma-surface interactions
Supervisors: Dr. G. De Temmerman and Dr. J. J. Zielinski

2012–2016 Master of Science in Theoretical Physics
Utrecht University, Utrecht, The Netherlands
Thesis title: The stability of a magnon Bose-Einstein condensate in YIG
Supervisors: Prof. dr. R. A. Duine and Dr. B. Flebus

2017–2021 Doctorate in Experimental Quantum Physics
Delft University of Technology, Delft, The Netherlands
Thesis title: Quantum simulation with electron spins in quantum dots
Promotor: Prof. dr. ir. L. M. K. Vandersypen

WORK EXPERIENCE

2016-2017 Research Scientist
Intelligent Imaging
TNO, The Hague, The Netherlands

List of Publications

Journal papers and preprints

8. *Long-range electron-electron interaction in gate-defined quantum dots* (preliminary title)
C. J. van Diepen, *et al.*,
Manuscript in preparation.

7. *Quantum simulation of antiferromagnetic Heisenberg chain with gate-defined quantum dots*
C. J. van Diepen*, T.-K. Hsiao*, U. Mukhopadhyay, C. Reichl, W. Wegscheider, and L. M. K. Vandersypen,
Physical Review X **11**, 041025 (2021) [Featured in Physics].

6. *Electron cascade for distant spin readout*
C. J. van Diepen, T.-K. Hsiao, U. Mukhopadhyay, C. Reichl, W. Wegscheider, and L. M. K. Vandersypen,
Nature Communications **12**, 77 (2021).

5. *Efficient orthogonal control of tunnel couplings in a quantum dot array*
T.-K. Hsiao, **C. J. van Diepen**, U. Mukhopadhyay, C. Reichl, W. Wegscheider, and L. M. K. Vandersypen,
Physical Review Applied **13**, 054018 (2020).

4. *Loading a quantum-dot based "Qubyte" register*
C. Volk, A. M. J. Zwerver, U. Mukhopadhyay, P. T. Eendebak, **C. J. van Diepen**, J. P. Dehollain, T. Hensgens, T. Fujita, C. Reichl, W. Wegscheider, and L. M. K. Vandersypen,
npj Quantum Information **5**, 29 (2019).

3. *Automated tuning of inter-dot tunnel coupling in double quantum dots*
C. J. van Diepen, P. T. Eendebak, B. T. Buijtendorp, U. Mukhopadhyay, T. Fujita, C. Reichl, W. Wegscheider, and L. M. K. Vandersypen,
Applied Physics Letters **113**, 033101 (2018) [Editor's Pick].

2. *Quantum simulation of a Fermi-Hubbard model using a semiconductor quantum dot array*
T. Hensgens, T. Fujita, L. Janssen, Xiao Li, **C. J. van Diepen**, C. Reichl, W. Wegscheider, S. Das Sarma, and L. M. K. Vandersypen,
Nature **548**, 70 (2017).

1. *ELM simulation experiments on Pilot-PSI using simultaneous high flux plasma and transient heat/particle source*
G. De Temmerman, J. J. Zielinski, **C. J. van Diepen**, L. Marot, and M. Price,
Nuclear Fusion **51**, 073008 (2011).

Patent applications

2. *Controlling tunnel couplings in a quantum dot array*
C. J. van Diepen, T.-K. Hsiao, and L. M. K. Vandersypen
Patent pending (European patent application No. 2024724)

1. *Readout of a quantum state in an array of quantum dots*
   C. J. van Diepen, and T.-K. Hsiao
   Patent pending (European patent application No. 2024580)

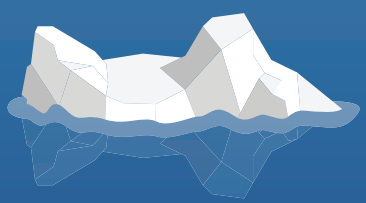

Casimir PhD series 2021-32
ISBN: 978-90-8593-498-1